Atmospheric Thermal Properties of Venus and Mars

–

Investigation of CO_2 Absorption Lines using Ground-Based Mid-Infrared Heterodyne Spectroscopy

Inaugural - Dissertation
zur
Erlangung des Doktorgrades
der Mathematisch-Naturwissenschaftlichen Fakultät
der Universität zu Köln

vorgelegt von

Tobias Stangier

aus Köln

Berichterstatter: Prof. Dr. L. Labadie
Prof. Dr. S. Crewell

Tag der mündlichen Prüfung: 13. Oktober 2014

Contents

List of Figures

List of Tables

Kurzzusammenfassung

Die thermischen Eigenschaften verschiedener atmosphärischer Höhenlagen erdähnlicher Planeten können aus druckverbreiterten Molekülübergängen ermittelt werden. Mittels bodengebundener Heterodynspektroskopie werden einzelne solcher druckverbreiterten CO_2-Absorptionslinien bei 10 µm Wellenlänge auf der Nachtseite des Planeten Venus beobachtet. Außerdem wird ein Spektrum von der Tagseite des Mars untersucht, welches ebenfalls eine verbreiterte Absorptionslinie aufweist. Infrarot-Heterodynspektroskopie ist auf die atmosphärischen Schichten sensitiv, in denen die Absorption stattfindet. Auf der Venus entspricht dies Höhenlagen in der Mesosphäre zwischen $\sim$60–95 km. Auf dem Mars findet die Absorption in der Troposphäre zwischen der Oberfläche und einer Höhe von $\sim$35 km statt.

Die atmosphärischen Parameter werden mit einer auf dem Levenberg-Marquard-Optimierungsalgorithmus basierenden Rückwärtsroutine erlangt. Diese vergleicht iterativ die Beobachtungsdaten mit Planetenspektren, welche mit Hilfe eines Strahlungstransportmodells unter Berücksichtigung des irdischen spektralen Transmissionsgrads in der obersten planetaren Atmosphäre errechnet wurden. Ein detaillierter *proof of concept* wird durchgeführt, um den Einfluss der Höhenauflösung zu untersuchen und um die Verlässlichkeit der neu entwickelten Routine zu bestätigen.

Während zweier Beobachtungskampagnen, die im März und im Mai 2012 stattgefunden haben, sind vier verschiedene Positionen auf der Nachtseite der Venus beobachtet worden. In dieser Arbeit werden erstmalig die an den jeweiligen Positionen erlangten Temperaturprofile präsentiert. Die Höhenauflösung der erhaltenen Profile beträgt $\sim$4.5 km. Die so erhaltenen Profile werden mit bereits bekannten Temperaturmessungen anderer luft- und bodengebundener Beobachtungsmethoden, sowie mit der *Venus International Reference Atmosphere* verglichen. Die gemessenen Temperaturen stimmen gut mit den gefundenen Daten anderer Beobachtungstechniken überein. Ein besonderes Augenmerk liegt auf dem Vergleich der an einer speziellen Beobachtungsposition erhaltenen Temperaturen

mit denen, die zeitgleich während einer koordinierten Messreihe im Mai 2012 mit dem *Venus Express Radio Science Experiment* gemessen worden sind. Zusätzlich zu existierenden Beobachtungstechniken können nunmehr heterodyne Infrarot-Beobachtungen von hochaufgelösten Spektrallinien Temperaturmessungen von der Nachtseite der Venus liefern.

Die Untersuchung von verbreiterten CO_2-Absorptionslinien auf der Tagseite vom Mars wurde an einem Spektrum durchgeführt, das während einer Beobachtungskampagne im Jahr 2010 aufgenommen wurde. Die vorläufigen Ergebnisse des erhaltenen Temperaturprofils werden hier nun präsentiert. Das erhaltene Profil wird mit einer Vorhersage aus der *Mars Climate Database* verglichen, zu der eine zufriedenstellende Übereinstimmung gefunden werden kann. Ein weiterer, ausführlicher *proof of concept* wird durchgeführt, um die besonderen atmosphärischen Bedingungen für den Mars zu berücksichigen und um den Beitrag der, da durch Sonneneinstrahlung hervorgerufen nur auf der Tagseite präsenten, nichtthermischen Emissionslinien auf die Auswerteroutine zu untersuchen. Die Auswertung von atmosphärischen Temperaturen auf der Tagseite des Mars unterliegt zusätzlichen Einschränkungen, die in erster Linie von der dünnen Atmosphäre und der vielfältigen Topografie der Marsoberfläche herrühren.

Abstract

Atmospheric thermal properties of different altitude layers of terrestrial planets can be deduced from pressure-broadened molecular transition features. Ground-based heterodyne spectroscopy is used to observe the nightside of Venus by probing single pressure-broadened CO_2 absorption lines at around 10 µm. In addition, a dayside spectrum of Mars, also containing a pressure-broadened absorption feature was investigated. Infrared heterodyne spectroscopy is sensitive to those atmospheric layers, which can be identified as the absorption line formation region. These layers correspond to an altitude range in the Venusian mesosphere between $\sim$60 and $\sim$95 km. On Mars, the line formation region is located in the troposphere between the surface and an altitude of $\sim$35 km.

Retrieval of atmospheric parameters is based on a Levenberg-Marquard χ^2 optimization that iteratively compares observed data to telluric transmittance corrected planetary top-of-atmosphere spectra calculated using a radiative transfer algorithm. A sophisticated proof of concept is performed to investigate the influence of the altitude resolution and to demonstrate the reliability of the newly developed retrieval technique.

During two observing campaigns in March and May 2012, four different locations on the Venusian nightside hemisphere were investigated. In this thesis, the retrieval of vertical temperature profiles in the nightside atmosphere of Venus using mid-infrared heterodyne spectroscopy is reported for the first time. The retrieval can be deduced with an altitude resolution of $\sim$4.5 km. The retrieved profiles are compared to existing space- and ground-based observations as well as to the Venus International Reference Atmosphere. The temperatures found are in good agreement to other retrieval techniques. Emphasis is given to the comparison of the temperatures from one specific location to thermal profiles simultaneously obtained with the Venus Express Radio Science Experiment during a coordinated observing campaign in May 2012. Sub-Doppler resolution infrared heterodyne observations can now provide temperature measurements on the dark side of Venus that complement those techniques.

Analysis of a broad CO_2 absorption feature obtained at the Martian dayside during an observing campaign in 2010 is performed and a preliminary temperature profile is retrieved. This profile is compared to predictions from the Mars Climate Database and found to be in satisfactory agreement. A further detailed poof of concept is provided, addressing the specific preconditions of the Martian atmosphere and analyzing the contribution of the solar induced non-thermal CO_2 emission on the retrieval method. It is found, that the deduction of atmospheric dayside temperatures on Mars is subject to additional restrictions, which are due to the thin atmosphere and the multifarious topography.

Chapter 1

"Anybody who has been seriously engaged in scientific work of any kind realizes that over the entrance to the gates of the temple of science are written the words: 'Ye must have faith.'"
(Max Planck)

Introduction

Comparative climatology of terrestrial planets is a subject of high impact for many researchers. The climate change on Earth has brought the topic also to public awareness, which promotes significant interest in the atmospheric processes of our - and other - planets. A better understanding of the physical and chemical processes in the atmospheres of the terrestrial planets contributes to gain insights into the evolution and development of our solar system.

The biggest question for mankind has always been: are we alone in the universe? Besides the philosophical and theological approach, science can provide hints to answer this question by finding tracers of life. The most appropriate candidate to host life in our solar system is Mars. A strong release of the trace gas methane into the Martian atmosphere (CH_4) in 2003 [1, 2] was controversially discussed to be of biogenic production [3], especially, since the event has not been observed afterwards [4, 5]. The environmental conditions, however, could have been favorable for life to evolve on Mars in the past [6]. It is nowadays believed, that the early atmospheres of Venus, Earth and Mars began under similar conditions [7] and have now estranged, due to the respective orbital location or geology.

The investigation of the terrestrial planets' atmospheres in our own solar system is crucial to explore and understand the boundaries of the so-called habitable zone. The circumstellar habitable zone is the region around the central star, where the ambient conditions for a planet are such, that liquid water could be present on the surface [8]. Unsurprisingly, planets are orbiting stars everywhere in our galaxy. The proof was given in 1990's when first evidences for exoplanets were found [9]. Today, there are over 1800 confirmed detection of extra-solar planets [10], and the number is increasing continuously. Thanks to the Kepler observations, the threshold of finding a planet similar to ours has been crossed and a numerous amount of Earth-like planets were found in the habitable zones around other stars [11–13]. The habitable zone is colloquially called the "Goldilocks zone": the first is too hot, the other too cold, but the third one is just right!
The inner edge of the habitable zone in our solar system is populated by Venus. Despite the fact that Venus' surface temperature is now far too hot to hold liquid water, the initial composition of Venus included enough water to form an ocean [14]. Nevertheless, Venus has lost its oceans and the liquid water has vaporized into the atmosphere, where it is continuously dissociate by ultraviolet (UV) radiation in the past hundreds of millions of years [15]. By now, Venus' climate is dominated by a strong greenhouse effect, which heats the surface to a temperature of $\sim 740\,\mathrm{K}$ [16].
Mars, in contrast, resides at the outer edge of the habitable zone. It is believed, that Mars used to hold surface oceans, too [17]. These oceans have also evaporated into the atmosphere, but opposite to Venus, the water has not contributed to a condensation of the atmosphere. The lack of a magnetic field makes Mars susceptible to the influences of the solar wind, which has eroded the uppermost atmospheric layers, leading to a depletion of light molecules [7].
Despite the undoubtedly existing commonalities, the three terrestrial planets differ a lot from each other and every single one of them possesses its unique characteristics. Their atmospheric thermal structure and composition provides insights into the evolution of the planet. When mankind is searching for Earth-like planets, it is most likely, that it will also find Venus- or Mars-like planets. Therefore, it is important to understand, why and how the climate evolution of the terrestrial planets in the habitable zone around our sun is so diverge. Especially, since their atmospheric structure varies only through different input parameters like i.a. solar insulation or molecular abundances. However, modeling planetary atmospheres is not trivial and observations are essential to improve the basic understanding of the unequal conditions.

The atmospheric molecules yield a manifold of physical parameters, representing the local state of the observed atmosphere. This encourages scientists to make use of remote sensing techniques to reveal their properties. First sophisticated

spectroscopic observations to investigate the thermal properties of Mars and Venus from Earth were conducted in 1923 by *Pettit and Nicholson* [18, 19]. In the past 50 years, space exploration missions to Venus and Mars have contributed significantly to our knowledge about Earth's neighbor planets. Especially the atmosphere of Mars is undoubtedly the most studied extraterrestrial atmosphere. 28 current and past missions have been successfully accomplished since the 1964 Mariner 4 flyby [20]. In the last decade, the National Aeronautic and Space Administration (NASA) missions Mars Global Surveyor (MGS) [21], Mars Climate Orbiter (MCO) [22], Mars Odyssey (MO) [23], Mars Reconnaissance Orbiter (MRO) [24] and Mars Science Laboratory (MSL) [25] as well as the European Space Agency's (ESA) Mars Express mission [26] have continuously provided information about the processes and the structure of Mars' atmosphere. In contrast, 16 missions dedicated to Venus have been performed since 1961 [20] and only the ESA spacecraft Venus Express [27] is currently orbiting the planet. Since the space exploration of Venus suffers a diminution in the next years, the importance of ground-based observations increases significantly.

Ground-based observations of fully spectrally resolved molecular transitions in terrestrial planets' atmospheres require ultra high spectral resolution with $\frac{\nu}{\Delta\nu} \geq 10^7$. In the mid-infrared (mid-IR) wavelength region around 10 µm, this can only be provided by using the heterodyne technique. CO_2 is the most abundant molecule in the atmospheres of Venus and Mars and the atmospheric window in the telluric transmission at 10 µm, in combination with the ultra-high frequency resolution of infrared (IR) heterodyne instruments, allows the detection of single Doppler-shifted molecular lines. In recent years, heterodyne spectroscopy has been applied to investigate a variety of physical conditions on different planets, moons and the sun [28]. The technique was used to gain knowledge about the dynamical properties [29–32] and thermal conditions [33–35] around the Venusian mesopause, to measure winds [36–40] and temperatures [41] in the mesosphere of Mars, as well as to investigate abundances of minor species like ozone [42–44] or methane [4] in the Martian atmosphere. In addition, observations were performed to determine ethane abundances [45, 46] and the dynamical [47] and thermal structure [48, 49] on the Saturnian moon Titan and to investigate species abundances in the atmosphere of the gas giant Jupiter [50]. Recently, first observations of the telluric atmosphere were performed in solar occultation, to derive stratospheric dynamics from ozone and to obtain the Earth's atmospheric transmission [51].

Up to now, temperatures of Venus' and Mars' atmospheres have been investigated by analyzing the solar induced CO_2 emission line, which occurs only at very low pressure (1 µbar $\hat{=}$ 0.001 hPa). There, the molecules are not in local thermodynamic equilibrium (LTE) and the line shape is purely Doppler-broadened. This

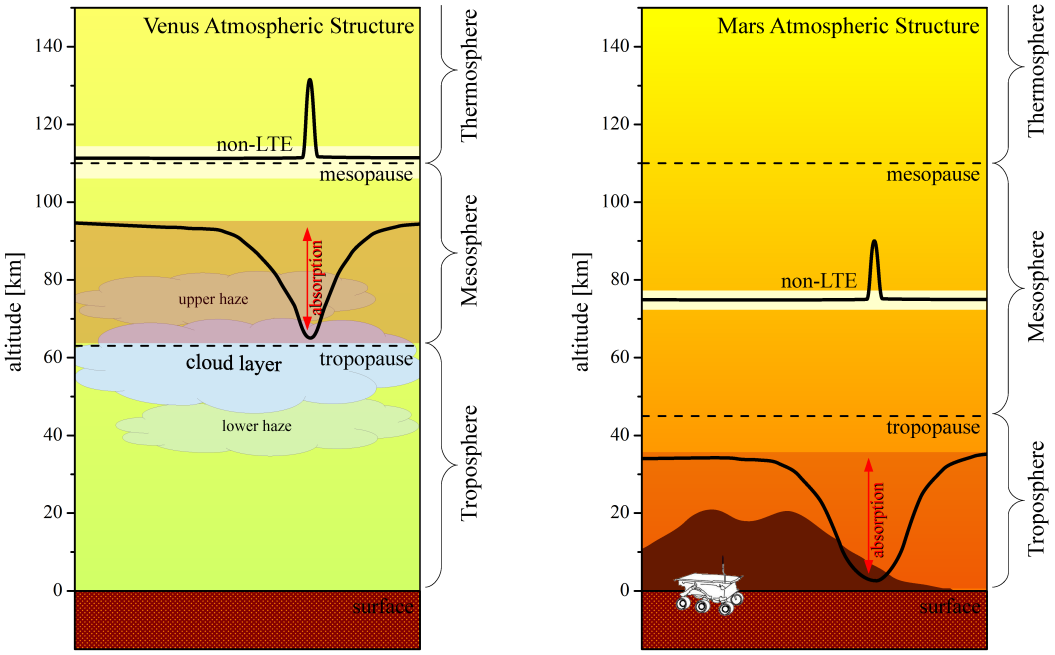

(a) *On Venus, the background radiation emerges from the main cloud layer. At an altitude of ∼ 63 km the atmosphere becomes opaque for IR radiation.*

(b) *On Mars, the background radiation emerges from the surface. Due to the multifarious Martian topography, the surface pressure can strongly vary.*

Figure 1.1: *Illustration of the atmospheric structure of Venus and Mars. The redish area represents the absorption line formation region. Note that the contribution of the altitude layers to the line formation is turned upside down. The continuum is defined by the background radiance, whereas the line center is formed in the higher altitudes. The non-LTE emission line occurs only on the sunlit sides of the planets and in only one pressure layer around 0.001 hPa, indicated by the yellow bar. The resulting spectra are a superposition of the two features. On the nightside, only the absorption feature can be observed. (Stangier 2014 [52])*

low-pressure layer corresponds to an altitude of ∼ 110 km in the Venusian and to ∼ 75 km in the Martian atmosphere [53]. In lower altitudes, the CO_2 molecules absorb the background radiation emerging from the surface of Mars or the clouds of Venus, forming a broad absorption line. The basic structure of the atmosphere of Venus and Mars and the line forming region on the respective planet is illustrated in Fig. 1.1. The non-LTE emission occurring in higher altitudes on the dayside is superimposed to the underlaying LTE absorption feature in the finally detected spectrum. A typical spectrum from the Martian dayside is shown in Fig. 1.2(b). On the nightside, no solar pumped emission exists and only the LTE feature is

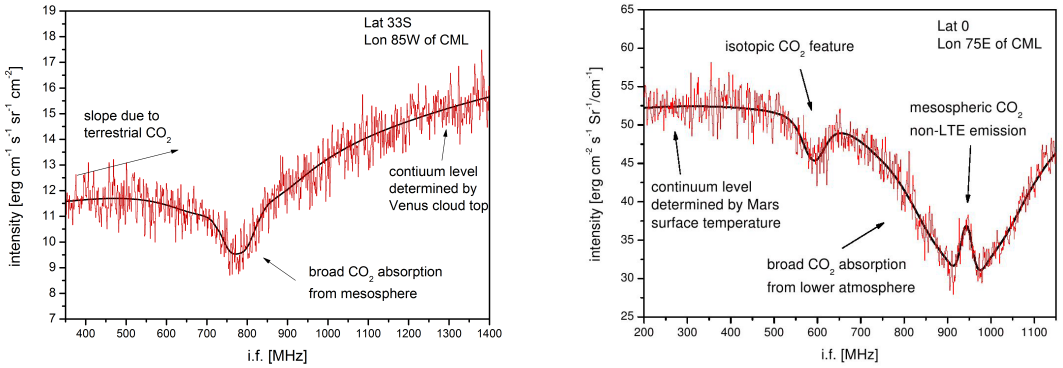

(a) *Venus nighhtside: No narrow non-LTE emission can be observed. Data were obtained in 2012, probing the CO_2 P(12) transition. See Chap. 4 for details.*

(b) *Mars dayside: The narrow non-LTE emission line can be observed. Data were obtained in 2005, probing the CO_2 P(2) transition. From Sonnabend et al. [55].*

Figure 1.2: *Typical IR heterodyne spectra from Venus and Mars. Both spectra contain a broad absorption feature, originating from the respective altitudes indicated in Fig. 1.1.*

detected. An example of a nightside spectrum of Venus is given in Fig. 1.2(a). Analysis of the broad CO_2 LTE features is performed for the first time. This expands the probing region into deeper altitude levels, significantly widening the field of application for infrared heterodyne spectroscopy. The line forming region was found to be in an altitude region between ~ 60 km and ~ 95 km on Venus and between the surface at 0 km and ~ 35 km on Mars. The shape of the absorption line is primarily depending on the thermal properties in the different altitudes. Hence, an inverse retrieval algorithm can reduce the local temperature profile in these atmospheric layers. This describes a completely new approach for dealing with ultra high resolution spectra obtained in the mid-IR [54]. In addition to expanding the probing altitude, the analysis of observed spectra on the planets' nightside enables access to a hemisphere that was not approached by investigations with IR heterodyne spectroscopy up to now. Thus, the investigation of the Venusian nightside spectra is of high interest and will be the main subject of this work.

In this thesis, the development and application of a completely new retrieval technique for thermal profiles from data obtained with infrared heterodyne spectroscopy is presented. In Chap. 2 the principles of the heterodyne technique and the instruments used for observations are presented.
The newly developed inverse fitting routine (IFR) is discussed in detail together with a proof of concept in Chap. 3. By investigating synthetic heterodyne spectra, created to simulate observations, it is shown, that the IFR can reliably retrieve

temperatures when applied to spectra deduced on the Venusian nightside, containing CO_2 absorption lines.
Emphasis is given to the analysis of measured data from Venus, obtained during two different observing campaigns in 2012, and to their comparison to a variety of other temperature profiles from space- and ground-based observations and model predictions in Chap. 4. The temperatures found are in good agreement to other observational profiles.
The atmosphere of Mars differs to that of Venus in terms of molecular abundances. Although the volume-mixing-ratio of CO_2 is almost identical, the column density and thus the surface pressure on Mars is of magnitude 10^{-4} smaller than on Venus. The thin Martian atmosphere and the variable topography yield more complications for the retrieval of thermal profiles. In addition, the orbital constellation between Earth and Mars constrains the observations to the Martian dayside, where a non-LTE emission line is superimposed to the broad absorption feature. These changing external preconditions and their effect on the retrieval algorithm, as well as preliminary results from one observed spectrum are presented in Chap. 5.
Besides Venus and Mars, other terrestrial planets exist in our solar system. An outlook on the potential of the IFR to retrieve temperatures on Titan and the most terrestrial planet - the Earth - is discussed in Chap. 6, before, finally, a summary is provided.

Chapter 2

"And in the end, it's heterodyning or die."
(Parody of the Song "Golden Eye")

Infrared Heterodyne Spectroscopy

Heterodyne spectroscopy is a powerful tool to observe the atmospheres of terrestrial planets. It provides ultra high spectral resolution of $\frac{\nu}{\Delta\nu} \geq 10^7$, yielding the capability to resolve single molecular transition features. Fully resolved molecular transitions provide information about physical parameters, like temperatures, abundances or dynamical properties. The heterodyne technique is most commonly applied in the radio and sub-mm regime of the electromagnetic spectrum. However, in recent years, this technique has been established to derive ground-based direct wind and temperature measurements by remote sensing of Doppler-shifted and -broadened molecular transitions also in the mid-IR wavelength regime.

In the following, the heterodyne technique will be introduced in Sec. 2.1. In Sec. 2.2 the sensitivity of the receivers is described and characterized briefly. A short introduction on the spectroscopic line broadening effects is given Sec. 2.3, and in the last part of this chapter, the instruments used for observations are presented (Sec. 2.4).

2.1 Heterodyne Technique

Heterodyning is the superposition of two transversal polarized, planar electromagnetic (EM) waves. In Fig. 2.1 a schematic overview of a heterodyne receiver is displayed.

In a heterodyne receiver, the radiation emerging from the object to be analyzed is coherently superimposed to a well-known reference radiation provided by the so-called local oscillator (LO). Various beam combining elements can be used for superposition. Most commonly, beam splitters, Fabry-Pérot resonators or waveguides are used. In the IR, waveguides are not as advanced yet, but first efforts were made towards a miniature IR heterodyne receiver using waveguides as beam combiner [56].

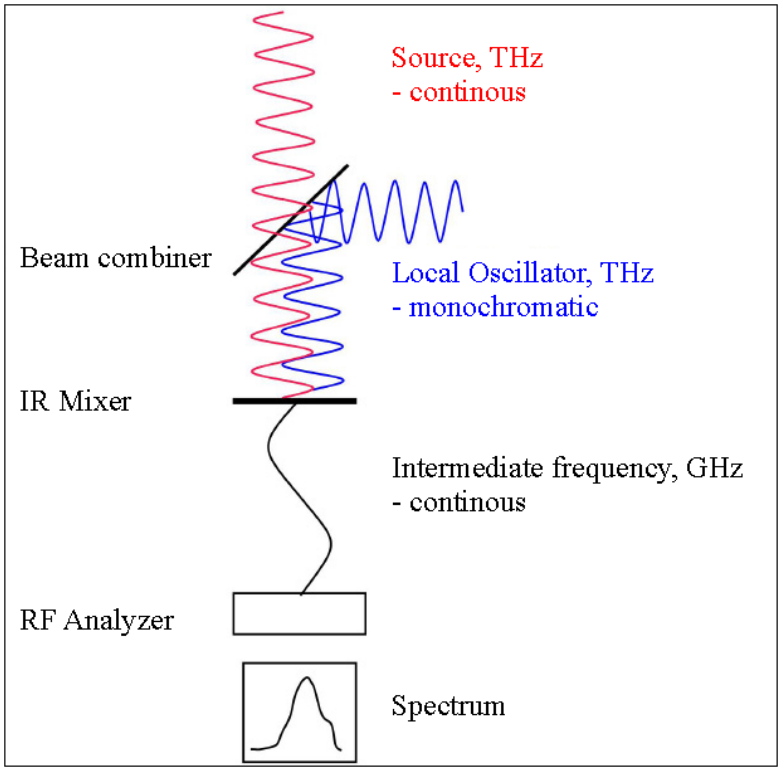

Figure 2.1: *Schematic view on the heterodyne principle. Two planar EM-waves are superimposed by a beam combining element. The spatial superposition is detected by a photomixer which converts the THz radiation down to few GHz. The radio frequency (RF) is then analyzed by standard RF components. From Stupar [41].*

After superposition, the combined beam is detected by a detector, commonly called (photo-)mixer. The mixer must possess a non-linear characteristic in order to mix the high frequency signals from the source and the LO. Due to the mixing process, new frequencies of few GHz are generated. These frequencies can now be analyzed and processed using standard radio spectroscopic devices. The spatial superposition can be described by the summation of their electric fields $E_{LO,sig}$ so that the electric field at the detector is

$$E_{det} = E_{LO}\, cos(\omega_{LO}\, t + \Phi_{LO}) + \sum_k E_{sig,k}\, cos(\omega_{sig,k}\, t + \Phi_{sig,k}) \tag{2.1}$$

where $\omega_{LO,sig}$ is the output frequency of the LO and of the signal, respectively. It has to be noted, that the electric field of the signal E_{sig} consists of several spatial modes and thus has to be treated as the sum of the individual components k. The incident power on the photomixer P_{det} is proportional to the intensity of the radiation I_{det}, which can be expressed as the square of the electric field

$$I_{det} \propto E_{det}^2 \tag{2.2}$$

defining

$$P_{det} = \frac{1}{\eta_q} \frac{h\nu}{e_0}\, I_{det} \tag{2.3}$$

with

$$I_{det} = I_{LO} + \sum_k I_{sig,k} + 2\eta_{het} \sum_k \sqrt{I_{LO}\, I_{sig,k}}\, cos(\|\omega_{LO} - \omega_{sig,k}\|\, t + \triangle\Phi_k) \tag{2.4}$$

where $\triangle\Phi_k$ is a constant phase shift between the LO and the signal. $\eta_{het} = \eta_q + \eta_{mix}$ is the heterodyne efficiency, which takes the quantum efficiency of the detector η_q and optical losses, i.e. at the beam combiner, η_{mix} into account. The initial and the sum frequencies are to high and cannot be processed. They are represented by the DC components $I_{LO} + \sum_k I_{sig,k}$ and result in an averaged photo current. Only the difference frequency $\triangle\omega_k = \|\omega_{LO} - \omega_{sig,k}\|$ between the detected signals, called intermediate frequency (IF) is detected. The IF spectrum contains all original spectral information. The spectral size of the IF spectrum depends on the bandwidth of the applied photomixer and is typically of few GHz.

Due to the symmetry of the cosine function two valid solutions for $\triangle\omega$ can be found. All frequencies $\omega_{sig,k} < \omega_{LO}$ originate in the lower side band (LSB), frequencies $\omega_{sig,k} > \omega_{LO}$ originate in the upper side band (USB) of the so-called double side band (DSB) spectrum. In the resulting IF spectrum, a distinction between LSB and USB cannot be made. The DSB is simply the sum of the individual contributions. In Fig. 2.2 the various steps from a direct detection to a DSB heterodyne spectrum are illustrated.

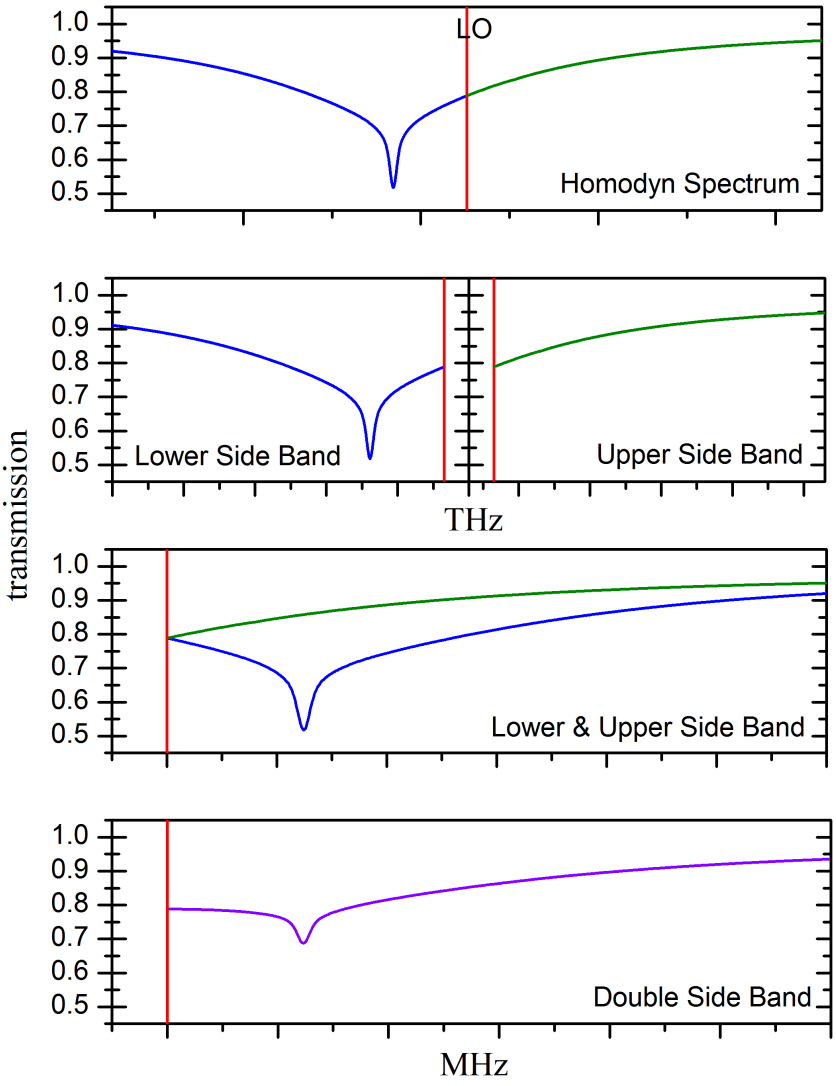

Figure 2.2: *Steps from a homodyne to a heterodyne spectrum. Top: the homodyne spectrum of an atmospheric absorption feature in the THz region. Center top: The same atmospheric feature divided into the LSB and USB. Center bottom: USB and mirrored LSB in the IF bandwidth. Bottom: resulting heterodyned DSB spectrum in the IF bandwidth.*

2.2 Sensitivity

Comparison of the sensitivity between heterodyne and direct detection methods is not trivial. A detailed investigation was made by *Krötz* [34]. In radio astronomy, the system temperature T_{sys} is commonly used to describe the noise equivalent power (NEP) of a heterodyne receiver. This notation allows the direct comparison of various heterodyne instruments and is adapted to infrared heterodyne receivers [55]. The NEP is the minimum detectable power with a given post detection bandwidth of 1 Hz and can be written in terms of T_{sys} as

$$NEP = \sqrt{\frac{8\,\delta_{res}^2}{\delta_{fl}}}\,k_B\,T_{sys} \tag{2.5}$$

with the Boltzmann constant k_B, the resolution bandwidth δ_{res} and the fluctuation bandwidth δ_{fl} of the system. In order to characterize the resolution of an acousto-optical spectrometer (AOS, as used for signal analysis in the receiver, comp. Subsec. 2.4.3) the Rayleigh criterion is conventional. It describes two monochromatic frequencies as resolved, when the first maximum of the diffraction image of the second component coincides with the first null of the diffraction image of the first component. Their spectral distance is the fluctuation bandwidth δ_{fl} [57].

2.2.1 System Temperature

The system temperature T_{sys} is convenient to characterize the noise of a heterodyne receiver. It has to be noted, that

$$T_{sys} = T_{ant} + T_{rec} \tag{2.6}$$

divides into two components [58]. The antenna temperature T_{ant} is a measure for the noise of the detected signal and the transmission line. The receiver temperature T_{rec} in contrast, represents the intrinsic noise contribution, originating from the various devices of the receiver. It includes all losses in the instruments' optics but mainly depends on the mean quantum efficiency η_q of the mixer. η_q describes the ratio of detected signal photons to generated electrons. Even in the ideal case of $\eta_{het} = 1$ (see Eq. (2.4)), a minimum noise contribution is indispensable. Hence, the ideal system temperature is limited by the so-called quantum limit. It can be written as

$$T_{ql} = \frac{h \cdot \nu}{k_B} \tag{2.7}$$

where h is the Planck quantum and ν the observing frequency. The quantum limit T_{ql} represents the minimal system temperature for a purely shot noise limited receiver.

To determine the receiver temperature, two well-known reference signals are compared. In contrast to radio or sub-mm observations, the noise contribution of the transmission line's thermal radiation is negligible. The incident power is directly proportional to the system temperature. Here, T_{ant} can be identified as the well defined surface brightness temperature of corresponding calibration sources, called hot H and cold C. The surface brightness temperature can be calculated according to Planck's Law. Thus, the incident power of the calibration sources can be expressed as

$$H = \alpha(T_{rec} + T_H) \text{ and } C = \alpha(T_{rec} + T_C) \tag{2.8}$$

where α is the unknown amplification of the system. The ratio of the incident power $Y = \frac{H}{C}$ terminates the dependency on the amplification and reveals the receiver temperature:

$$T_{rec} = \frac{T_H - Y \cdot T_C}{Y - 1}. \tag{2.9}$$

It is crucial to generate a high contrast between the two calibration signals. In IR heterodyne receivers, the hot load is usually a blackbody radiator, whereas the cold load is an absorber at room temperature.

2.2.2 Radiometer Equation and Noise Amplitude

An important parameter to describe the sensitivity of a heterodyne receiver is the noise amplitude. To retrieve information on the noise amplitude, analysis of the signal's variance is important. A frequency independent noise amplitude is common for white noise. The radiometer equation describes the decrease of the frequency independent noise amplitude of a constant signal in time:

$$\sigma^2(\tau) = \frac{T_{sys}}{\sqrt{\delta_{fl} \cdot \tau}} \tag{2.10}$$

where σ^2 is the root mean square error (RMS) in K, T_{sys} is the system temperature, δ_{fl} is the fluctuation bandwidth of the back-end filter [59].

To obtain the resulting spectrum, the ratio of the incident signals from all observed sources is determined (comp. Eq. (2.8)):

$$F = \frac{S - R}{H - C} \tag{2.11}$$

with H: hot calibration load, C: cold calibration load, S: sky signal, R: sky reference. The radiometer equation Eq. (2.10) is valid for the integration on each source. To optimize the signal-to-noise ratio (SNR) it is necessary to minimize the RMS of the retrieved spectrum in Eq. (2.11), which can be calculated according to the error propagation law. Thus, as shown in Appendix A the RMS can be expressed in dependence on the whole exposure time τ and the temperature of the observed sources:

$$\sigma^2(\tau, F) = \frac{T_{rec}}{\sqrt{\delta_{fl}\tau}} \cdot \frac{T_S + T_R + F(T_H + T_C)}{T_H - T_C} \tag{2.12}$$

For more information on the sensitivity of a heterodyne receiver please also refer to *Abbas et al.* [60], *Schmülling* [61] and *Krötz* [34].

2.3 Line Broadening Effects

For the investigation of absorption features, it is essential to understand the processes, responsible for the shape of the observed molecular transition lines. In the following the basic effects, leading to a broadening of spectral lines are discussed. The descriptions below are following along the lines of *Bernath* [62].

The energy of photons traveling through a group of molecules can be either absorbed or induce stimulated or spontaneous emission. Considering a finite volume of molecules and an incident photon flux, Beer's law describes that the intensity of the incident radiation I_0 abates exponentially with distance l and can be described as

$$I(l) = I_0 e^{-\alpha l} \tag{2.13}$$

where α the so-called absorption coefficient in cm^{-1} and is depending on the absorption cross-section of the molecule and its concentration in the probed volume.

The rotational structure of a dipole, vibrating in a particular mode, is called band. These rotational-vibrational (ro-vibrational) bands are composed of single transitions, called lines. A typical molecular spectrum of the CO_2 antisymmetric stretching mode is illustrated in Fig. 2.3. To resolve one single ro-vibrational transition, ultra high frequency resolution is required. Usually, the shape of these lines can be described by line-shape functions, which are classified into homogeneous and inhomogeneous functions. The distinction is due to the properties of the molecules. A homogeneous line shape occurs, when all molecules are subject to equal ambient conditions, i.e. the surrounding pressure. Consequently, an inhomogeneous line shape is assumed for varying molecular properties, i.e. the velocity

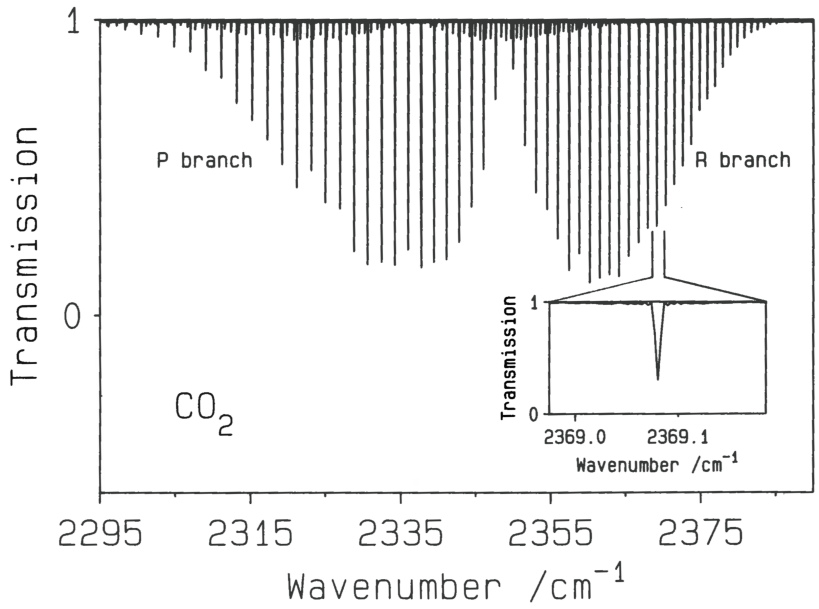

Figure 2.3: *A typical molecular spectrum of the antisymmetric stretching mode of CO_2. One vibrational mode contains a complete band of rotational transitions. In the insert graphic, one ro-vibrational transition line is shown in absorption. From Bernath [62]*

of the single molecules which is Maxwell-Boltzmann distributed. This broadening effect is called Doppler-broadening.

2.3.1 Natural Lifetime Broadening

Each molecular transition possesses an intrinsic broadening effect, which is due to the finite lifetime (τ_{LT}) of the excited energy level. This effect is called natural lifetime broadening. In quantum mechanics, the energy state of a molecule is described by a time-dependent wavefunction. The Fourier transformation of an infinite wavefunction yields the frequency of the wave as a sharp delta peak. However, since the excited state decays into a lower state by spontaneous emission after a while, a finite lifetime of the excited state exists and the wavefunction is not infinite. The Fourier transformation of a transition with a certain decay rate gives the homogeneous line-shape function. The function represents a statistical distribution around the centroid frequency and can be described by a Lorentzian function with a full width at half maximum (FWHM) given by

$$\triangle\nu_{\mathrm{FWHM}} = \frac{1}{2\pi\tau_{LT}} \tag{2.14}$$

This FWHM is often called natural line width and can also be regarded as a consequence of the Heisenberg uncertainty principle.

2.3.2 Pressure Broadening

Pressure broadening occurs due to collisions between molecules and is thus also called collisional broadening. To understand the process, we consider a transition from a higher to a lower state, which can be described by a wavefunction. The dipole moment of the molecule oscillates at a certain frequency except for time of collision. Then, the wavefunction is disrupted and the dipole moment is altered. This disruption leads to a finite length of the wavefunction and the Fourier transformation of the divided wave yields, similar to the natural lifetime broadening, a homogeneous line-shape function, which can be described by a Lorentzian distribution. The FWHM of the curve is proportional to the reciprocal of the average time T_c between two collisions. Increasing the ambient pressure, decreases the time between two collisions. Hence, the FWHM of the line can be given in terms of the pressure as

$$\triangle\nu_{\mathrm{FWHM}} = b \cdot p \tag{2.15}$$

where b is identified as the substance-specific pressure-broadening coefficient. The encounter of two molecules is depending on the interaction of their potentials, and cannot be exactly determined in a group of three or more, thus, the derivation of the pressure-broadened line shape is a difficult task and the pressure-broadening coefficients are experimentally determined. For CO_2, the self-broadening coefficient is $\sim 7.6\,\mathrm{MHz/Torr}$ [63].

2.3.3 Doppler-Broadening

Gas in a finite volume contains a certain amount of molecules, which are all moving in a different direction. This varying motion of the molecules provokes a small scale frequency shift of the incident radiation, resulting in many, natural lifetime broadened homogeneous line shapes. The envelope of this set of lines is an inhomogeneously broadened line and can be described by a Gaussian distribution (comp. Fig. 2.4). The FWHM of the Doppler-broadened line is depending on the mass m of the molecules at a given temperature T and can be written as

$$\triangle\nu_D = \frac{\nu_0}{c}\sqrt{\frac{8k_BTln(2)}{m}} \tag{2.16}$$

where ν_0 is the centroid frequency of the line, c is the speed of light and k_B the Boltzmann constant. From Eq. (2.16) the kinetic temperature of the observed

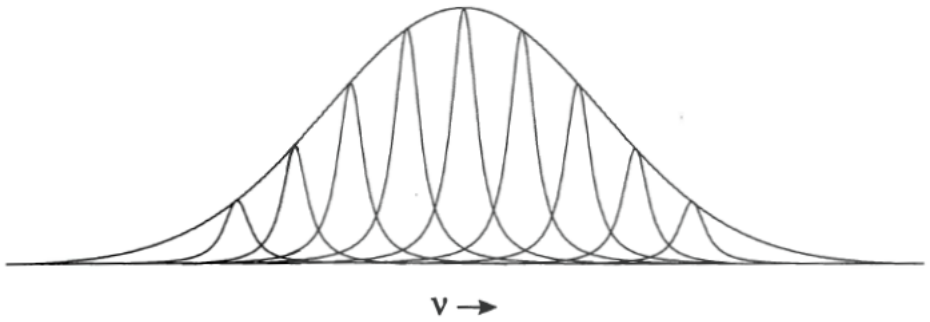

Figure 2.4: *An inhomogeneously broadened line (Gaussian distributed) made up of many homogeneously broadened components (Lorentzian distributed). From Bernath [62]*

molecule can be retrieved, if the width of the line is given. Hence, fitting a Gaussian function to a purely Doppler-broadened line shape reveals the kinetic temperature of the molecule.

In case the molecules are subject to both broadening mechanisms, the resulting line-shape function must be described as a convolution of a Gaussian and a Lorentzian distribution function. This convolution is called Voigt line-shape function.

In planetary atmospheres, the pressure decreases with altitude, since the molecules are gravitationally forced towards the surface. The line forms either between the surface or the altitude, where the pressure is low enough for the atmosphere to be not optically thick anymore and the altitude where the pressure is high enough for the pressure broadening to exceed the Doppler broadening. In this region, the energy emerging from the background radiation source, is absorbed and re-emitted as traveling along the path of ray. Therefore, one Voigt profile is not sufficient to describe an atmospheric absorption line. Thus, a full radiative transfer calculation has to be performed, which accounts for the varying pressure in the atmosphere. Details on the radiative transfer code I used for the work herein are given in the next chapter, Chap. 3.

2.4 Instrumentation

Infrared heterodyne spectrometer are still rare and only few instruments exist worldwide. The first heterodyne receiver was developed at the University of California (UC) in Berkeley in the early 1970s, to measure CO_2 emission lines in the atmosphere of Mars and Venus [64–67]. The biggest instrument nowadays that uti-

lizes the IR heterodyne method is the Infrared Spatial Interferometer (ISI), which was developed by the group of the UC Berkeley around *Betz, Johnson and Towns* [68]. ISI is a high spatial resolution interferometer, consisting of three movable 1.65 m telescopes. Each of them heterodynes the incoming radiation with a CO_2 laser emission [69]. The combination of interferometry and heterodyning creates a unique way to achieve high spatial and spectral resolution. ISI's main field of application, however, is the investigation of stellar environments [69].

In middle of the 1970s a group at the NASA Goddard Space Flight Center developed the Infrared Heterodyne Spectrometer (IRHS), used for planetary observations in the mid-IR wavelength region [70, 71]. At first, it was permanently mounted at the Mc-Math Pierce Solar Telescope (McMath) in Arizona, USA, before it was relocated to the NASA Infrared Telescope Facility (IRTF) on Hawaii. At the end of the 1990s, the instrument was disassembled and substituted by the newer and more flexible Heterodyne Instrument for Planetary Winds And Compositions (HIPWAC) [72]. HIPWAC was the first transportable infrared heterodyne receiver in the world.

Around the beginning of the century, a second transportable instrument, the Cologne Tuneable Heterodyne Infrared Spectrometer (THIS), was assembled. The instrument is in operation since 2002 [73, 74].

In recent years, more mid-infrared heterodyne receivers were developed. In Cologne, a second instrument called iCHIPS (infrared Compact Heterodyne Instrument for Planetary Science) was built, intended as a breadboard for laboratory measurement and terrestrial observations [51]. In addition, a Japanese group is about to start observations with their newly developed instrument at the PLANETS telescope on Haleakala, Hawaii [75]. Besides the mid-IR receivers, a couple of near-IR instruments exist and have been successfully applied for observations. However, these instruments are less advanced and have mainly been used for terrestrial observations [76, 77].

THIS and HIPWAC are still operating and have been used for the observations within this thesis. In the following, they will be presented in more detail. A description of the receivers setup and most important components is given for each instrument, to point out the major differences and commonalities. An overview of some characteristics and specifications can be found at end of the chapter in Tab. 2.2.

2.4.1 THIS

Spectrometer Setup

The beam path in THIS is displayed in Fig. 2.5. A picture of the receiver is shown in Fig. 2.6(a). The instrument was designed to fit in a two-story aluminum framework. The receivers dimensions are $80 \times 60 \times 42\,\mathrm{cm}^3$ and it weighs approximately 80 kg. The inner part of the cube is indicated as the *LO deck* in the scheme in

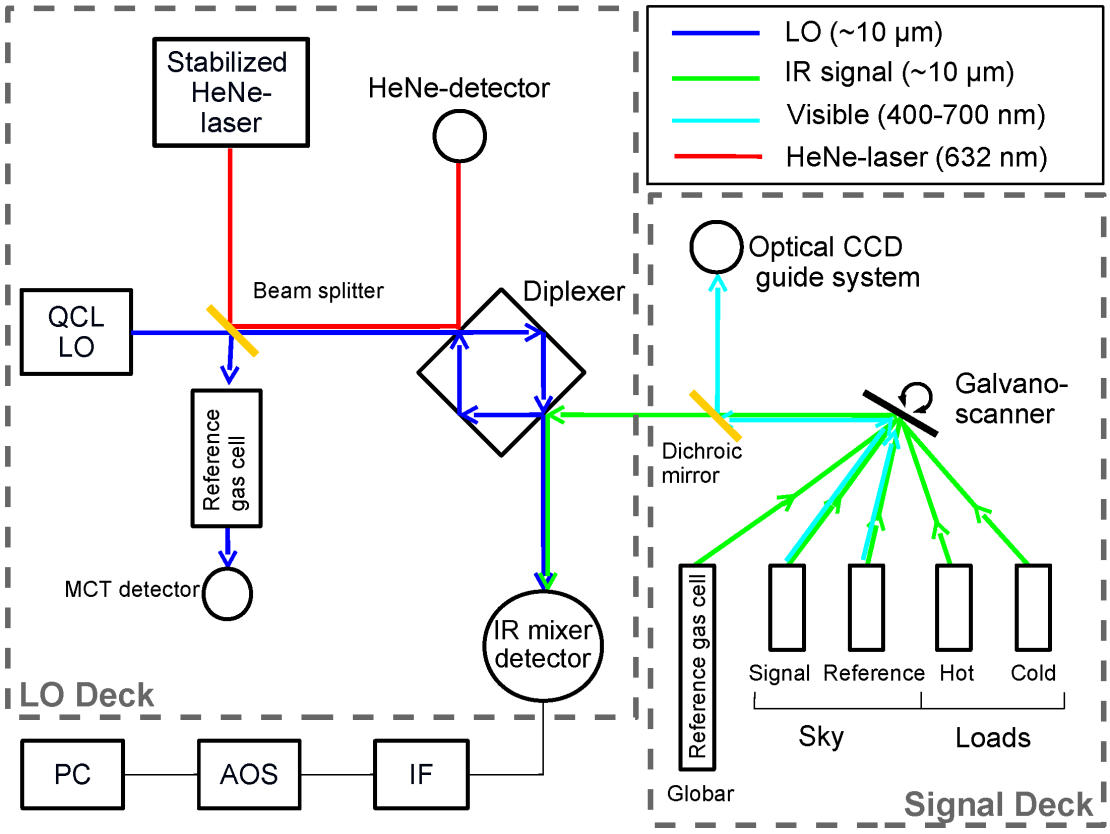

Figure 2.5: *Schematic view on the beam path in* THIS. *The broadband IR signal (green) coming from the various radiation sources is injected into the spectrometers optical path by a high speed galvano scanner. The radiation from the sky is split into its optical (light blue) and its IR component by a dichroic mirror. The optical light is detected by a CCD for guiding purposes. The IR signal is fed into the diplexer and heterodyned to the LO beam (blue). A fraction of the LO power is routed through a reference gas cell onto a MCT (HgCdTe) detector to monitor the output frequency of the LO. A stabilized HeNe laser (red) is also injected into the diplexer in order to lock the LO frequency onto a specific resonator fringe. (Sonnabend et al. [55])*

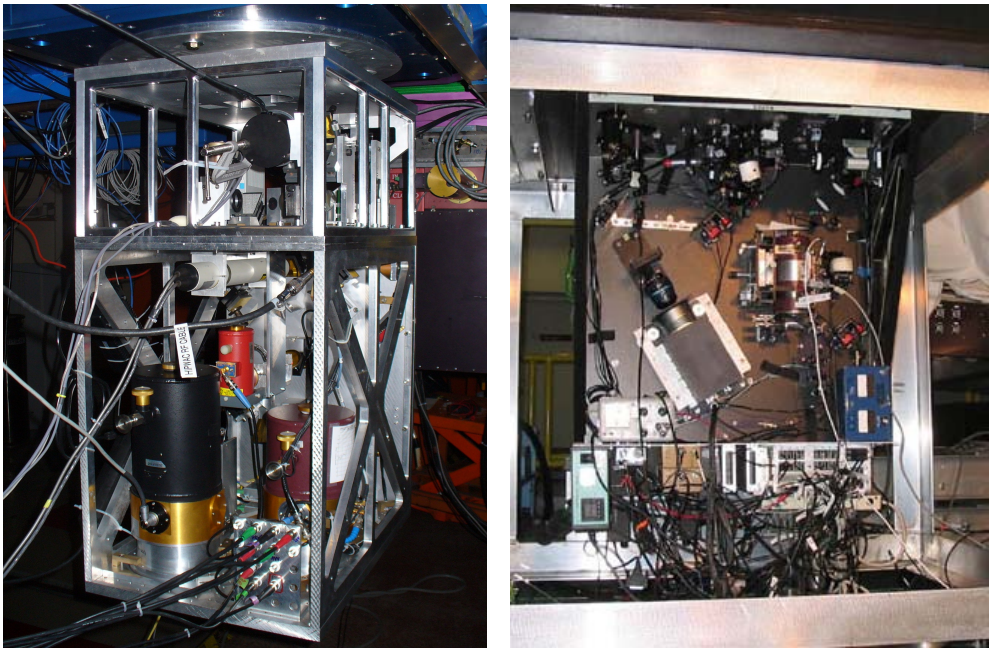

(a) THIS: *dimension 80 x 60 x 42 cm*^{3} **(b)** HIPWAC: *dimension 75 x 80 x 137 cm*^{3}

Figure 2.6: *Photos of the two receivers.*

Fig. 2.5. The LO deck contains the beam combining optics, the detector and the LO. In addition, all components required for frequency stabilization are mounted inside the LO deck. The upper part of the receiver contains all the optics necessary for matching the instrument to different telescopes with different F# [55]. It is marked as the *signal deck* in Fig. 2.5. Besides the IR signal and calibration components, an indispensable optical guide system is located on the signal deck. All electronic components, needed for operation are mounted into two separate 19" racks which makes it convenient for transportation and handling.

The Local Oscillator - QCL

THIS is the first infrared heterodyne receiver that uses quantum cascade lasers (QCLs) as LO. QCLs are semiconductor lasers and have been developed in 1994 by *Faist et al.* [78]. In these types of lasers, photon emission is obtained by optical transitions of electrons between confined energy levels [79]. The transitions take place between intersubbands in a multi-quantum-well structure. In Fig. 2.7 the scheme of a QCL with the concept of alternating wells and barriers is on display.

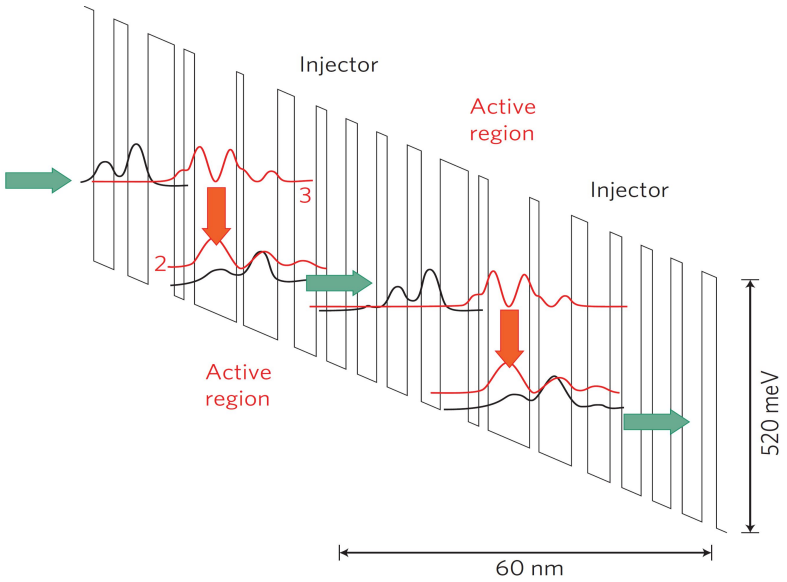

Figure 2.7: *Energy diagram of a QCL from Yao et al. [80]. The laser transition takes place in the active region between sub-band 3 and 2. The sub-bands contain alternating structure of quantum-wells and barriers in order to force stimulated emission.*

The advantage of QCLs compared to other lasing devices, i.e. diode lasers, are their high continuous wave (CW) output power and spectral tuning range. A QCL is a multi layer semiconductor usually made out of GaInAs/AlInAs heterostructures. The emission frequency of the laser is depending on the layer structure and can be tailored over a wide range by changing only the thicknesses. Hence, a manifold of QCLs are available in the mid-IR wavelength regime between 3 µm–25 µm [80]. However, two kinds of QCLs have to be distinguished. The multi-mode Fabry-Perot (FP) devices and the distributed feedback (DFB) QCLs. DFB-QCLs possess an incorporated internal grating which allows monochromatic single-mode operation with a narrow linewidth [81, 82]. Despite the narrow linewidth, DFB-QCLs provide a spectral tuning range of approximately 1% around the central wavenumber [78]. Tuning of the device can be achieved by either changing the applied current or the operation temperature. The former results in a fast, the latter, due to a longer thermal relaxation time, in a slow tuning effect. This provides a

#	λ_{peak}		tuning range		operating temperature
	µm	cm^{-1}	µm	cm^{-1}	K
1	10.54	948.63	10.51–10.57	947–951.5	187–243

Table 2.1: *QCL mounted in* THIS *during observations for this work.*

common tuning range of 6–10 cm^{-1}. Initially, QCLs had to be liquid nitrogen (LN) cooled to be operated at low temperatures. In recent years, the development was successfully driven towards devices that could be operated at room temperature [79]. LN cooled DFB-QCLs are used in THIS. Mostly, the devices are heated additionally, in order to increase their tunability. A list of the important parameters of the device used in THIS during observations for this work is given in Tab. 2.1.

The Beam Combiner - Diplexer

A confocal FP ring resonator, called diplexer, is used as the beam combining element. Two focusing mirrors, with a focal length of 30 mm each, are placed in the respective opposed focal spot. The beams are injected into the resonator through two highly reflective beam splitters. The transmission in the diplexer follows the Airy function and, assuming a good alignment, the maxima are separated by $\triangle\nu = c/2 \cdot l$, with l the length of the resonator. The suppression of side modes from the QCL and the avoidance of accidental reflective feedback are two advantages of the setup. To assure optimal amplification in the cavity, one mirror can be modulated by a piezo actuator at a frequency of a few hundred Hz. This way, the diplexer can serve also for frequency stabilization purposes. The LO can be stabilized to the maximum of a resonator fringe with an accuracy of ~ 1 MHz. Further information can be found in the work of *Wirtz* [83], *Sonnabend* [73], *Sonnabend et al.* [55] and *Sornig* [84].

Beam Selection and Signal Calibration

In Sec. 2.2.2, we learned from Eq. (2.11), that for obtaining a calibrated spectrum it is necessary to observe four different input signals. To select the different radiation sources a galvano scanner is implemented into the spectrometer (comp. Fig. 2.5). The scanner switches between the calibration loads Hot, $Cold$ and the beam from the sky provided at the on-source $Signal$ and the off-source $Reference$ port. In THIS, the hot load is a black body radiation source at 673 K and the cold load a room temperature absorber. In addition, a steady state emitter, observed through a reference gas cell, is introduced as a fifth source, required for monitoring the frequency position and stabilization of the LO. The galvano scanner enables high speed switching between the various positions within only a few milliseconds. It injects the required broadband signal beam by rotating into the accurate angular position. Its high switching frequency can be precisely synchronized with the observing procedure. This enables the measuring of the loads and the source within the short period of one observing cycle.

2.4.2 HIPWAC

Spectrometer Setup

The setup of HIPWAC is displayed in Fig. 2.8 and a picture of the instrument can be found in Fig. 2.6(b). The size of the receiver is $75 \times 80 \times 137\,\mathrm{cm}^3$. It weighs approximately 90 kg. In contrast to THIS, the optical components in HIPWAC

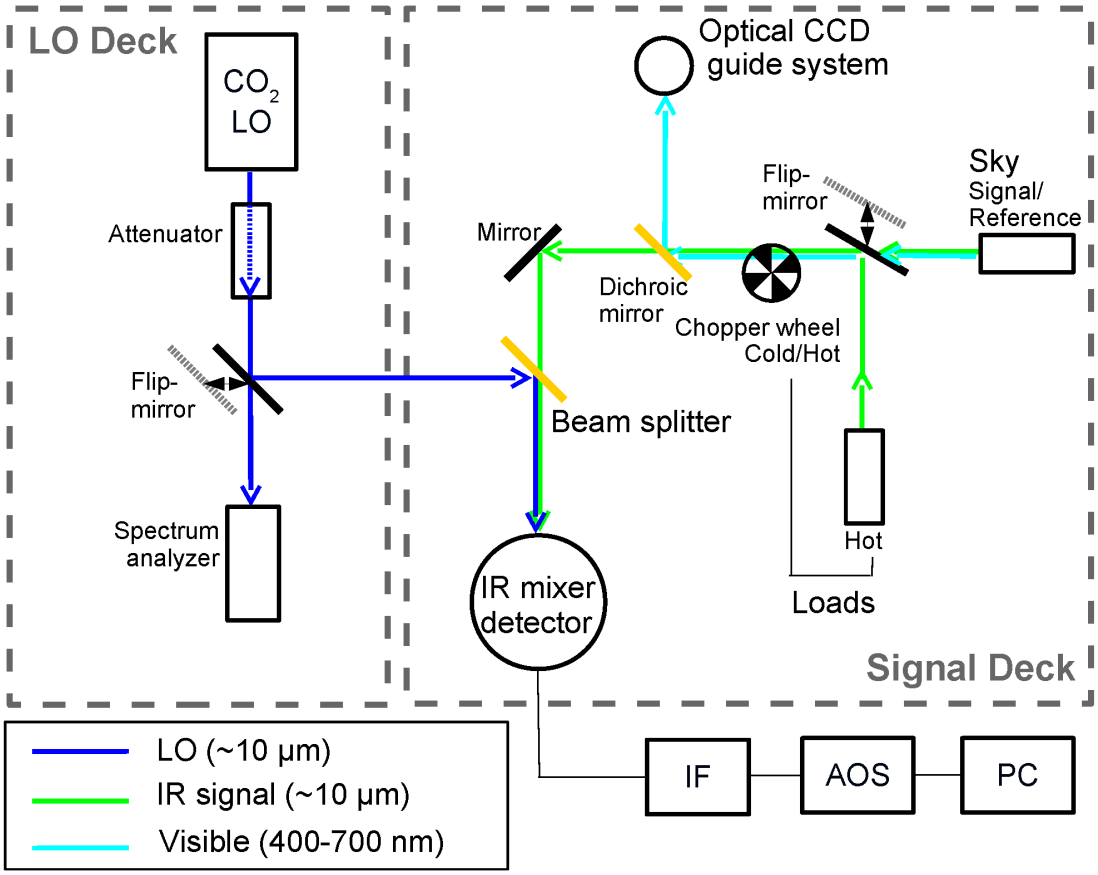

Figure 2.8: *Schematic view on the beam path in* HIPWAC. *The broadband signal coming from the sky is split into its visible (light blue) and its IR (green) component by a dichroic mirror. The visible light is detected by a CCD for guiding purposes. To select the hot load, a flip mirror can be introduced into the beam path. A chop between the hot and the cold load is achieved by a chopper wheel. The IR signal is superimposed to the LO beam (blue) on a beam splitter. The LO output power can be reduced in the attenuator. By removing a flip mirror, the LO output frequency can be monitored in a spectrum analyzer. The heterodyned beam is detected by the IR mixer and finally analyzed. (Stangier 2014 [52])*

are vertically aligned and the two decks are mounted to the opposed sides of an upright optical plate. The receivers framework is made of carbon fibers. The *LO deck* contains the LO, an attenuator and a spectrum analyzer. On the *signal deck* the calibration loads, the beam combining element and an optical guide system are located. In addition, the optical components which are needed for telescope adaption can be found on the signal deck. The broadband signal coming from the sky is fed into the instrument from the top, through a hole in the lid. The IF signal provided by the mixer can not only be analyzed with an AOS, but also with a high-resolution filter bank [45], which is omitted in the scheme in Fig. 2.8, since it was not used for data acquisition in this work.

The Local Oscillator - CO_2 Gas Laser

In HIPWAC the LO signal is provided by a CO_2 gas laser. In order to increase the spectral coverage of the instrument, two different laser gain tubes can be selected. Each laser gain tube contains different CO_2 isotopes, yielding a manifold of transitions around the $^{12}C^{16}O_2$ I-, and II-band centered at 10.4 µm and 9.4 µm, respectively. The desired transition can be selected by tuning the cavity length of the gain tube. This can be achieved by changing the angle of incidence of an incorporated diffraction grating on one end of the tube. In gas lasers, though, tunability is limited and the monochromatic LO output frequency is restricted to a small bandwidth around the energy peak of the specific transition. To guarantee a stable output frequency, the laser is locked to the peak of the gain profile [85].

The advantage of CO_2 gas lasers is their high output power. To ensure a constant power for the various transitions and to avoid signal saturation on the back-end detection devices an attenuator is introduced in the LO beam path (comp. Fig. 2.8). The spectrum analyzer serves for monitoring the selected transition of the laser.

Beam Selection and Signal Calibration

HIPWAC cannot be applied as flexible as THIS. Since it is not equipped with an appliance to switch between signal and reference, the instrument must rely on telescopes which are capable of chopping the beam on the sky, e.g. the IRTF. The hot load can be observed by introducing a flip mirror into the beam path. The flip mirror is electronically controlled in order to obtain a calibration measurement remotely. A chopper wheel is then used to chop between the hot and the cold load. The cold load in HIPWAC is represented by the filled areas of the chopper wheel, which are kept at room temperature. The hot load is a black body radiator with

a surface temperature of 1273 K. In HIPWAC the calibration procedure cannot be implemented into the observing procedure as it is in THIS. Therefore, it has to be done after each measuring cycle.

The various broadband signals are heterodyned to the LO signal on the beam combining element, which is a $2 \times 3\,\text{inch}^2$ ZnSe beam splitter. The beam splitter has a special IR coating which reflects 10 % and transmits 90 % of the signal.

	THIS	**HIPWAC**
Local oscillator	QCL	CO_2-Laser
Operating wavelength	7.8–11.2 µm (tunable)	~ 10 µm (CO_2-band)
Beam combiner	Diplexer	Beam splitter
Receiver Dimensions	$80 \times 60 \times 42\,\text{cm}^3$, 80 kg	$75 \times 80 \times 137\,\text{cm}^3$, 90 kg
AO-Spectrometer	3 GHz, 6000 channels	1.6 GHz, 3000 channels
Spectral Stability	~ 0.3 MHz	≤ 0.01 MHz
Maximum Resolution $\frac{\nu}{\Delta\nu}$	$\geq 10^7$, adjustable	
Sensitivity	$T_{sys} \leq 3000$ K at 10 µm	

Table 2.2: *List of important specifications for* THIS *and* HIPWAC.

2.4.3 IR Mixer and AOS

Both instruments use an mercury-cadmium-telluride (HgCdTe or MCT) IR detector. In each case, it is a doped semiconductor *pin*-photodiode optimized for heterodyne detection between 7.6 µm and 12.0 µm. It consists of four single detector chips, each of them embodies one *pin*-photodiode buried in an optical cavity. The incorporated resonator creates a standing wave pattern within the HgCdTe material to optimize sensitivity of each chip to different wavelengths [86]. The resonator increases the quantum efficiency η_q to ~ 80 %. The photomixers have to be LN cooled and their 3 dB cutoff is at ~ 3 GHz.

The back-end spectrometers used for signal analysis are AO-spectrometers. AOS were developed and assembled at our institute [57] and have been applied successfully for various purposes in the field of radio-astronomy and spectroscopy for many years [74, 87, 88]. The two AOS applied in the instruments are slightly different. Both possess a fluctuation bandwidth δ_{fl} of 1.3 MHz. The AOS used in THIS has an IF bandwidth B of 3 GHz, the one in HIPWAC of 1.5 GHz, respectively, limiting the IF bandwidth of the entire instrument.

In an acousto-optical spectrometer, the IF photons of the signal to be analyzed, excite grating vibrations of a Bragg crystal. These vibrations modulate the refrac-

tive index of the crystal. A laser beam is routed through the crystal and collimated onto a linear CCD. This enables the simultaneous detection of the broadband IF signal, since the modulated dispersion of the crystal, caused by the spectral distribution of the IF, leads to a spatial refraction of the AOS laser. The amount of channels of the CCD defines the bandwidth B of the AOS. In THIS, the AOS-CCD has 6000 channels and in HIPWAC 3000, respectively. For more detailed information on the functionality of an AOS, please refer to the work of *Schieder et al.* [57], *Siebertz* [89] or *Olbrich* [90]. Further analysis and data processing is performed by a PC.

2.4.4 Spectral Stability

One important factor for observations requiring long integration times is the spectral stability of the receiver. The importance even increases for ultra high spectral resolution. To claim a spectral resolution of $\sim 1\,\mathrm{MHz}$ is only valuable, if the spectral stability is guaranteed to be less or equal to this value. The spectral stability of the AOS can be assumed as given, as it was proven several times in the past [57, 89, 90]. Additionally, a comb generator with defined spectral distance of 50 MHz between the comb emission lines, is implemented into the IF processing box in order to calibrate the AOS-CCD precisely. Hence, all potentially slow and long term drifts of the back-end spectrometer, caused by varying ambient temperatures can be ruled out.

In THIS, the spectral stability was tested by observing a well known molecular transition feature of a reference gas in absorption. The pressure of the gas must be low enough to obtain an only Doppler-broadened line shape. Commonly, a pressure of less than $\sim 5\,\mathrm{hPa}$ is sufficient [55]. A Gaussian distribution is fitted to the absorption line, yielding the IF center frequency of the feature. The procedure was repeated every 30 s for 4500 s, simulating real observing conditions. A typical result of such a stability measurement is shown in Fig. 2.9. The obtained standard deviation of the IF frequency position of the line, which directly correlates to the output frequency stability of the LO, is 0.3 MHz. The slight slope, that can be observed in Fig. 2.9(b) is due to the thermal properties of the QCL. However, these long term drifts can be neglected, since an absorption line is frequently measured during the observing procedure, for LO frequency calibration purposes.

In HIPWAC, an additional load for monitoring the spectral stability of the receiver is abdicated. The CO_2 gas lasers are assumed to provide a stable output frequency over the observing period. The laser can only emit at the rest frequency of the selected transition to which it is locked. The transition is selected by changing

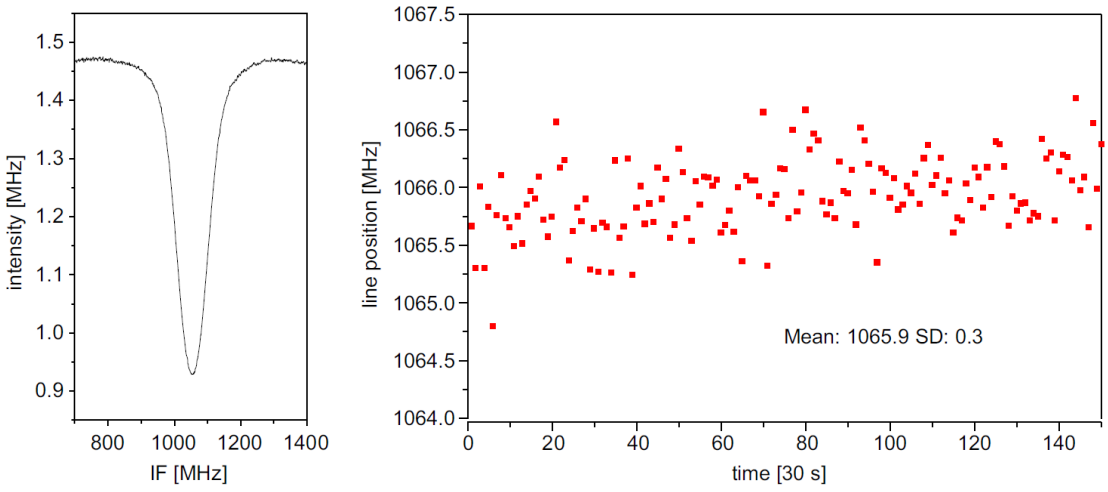

Figure 2.9: *Spectral stability of* THIS *from Sonnabend et al. [55]. IF line center frequency variation over time. The inset values in (b) are the mean value and the standard deviation (SD) given in MHz.*

the resonator length. The rest frequency is independent from external parameters such as ambient pressure or temperature. The resonator length however, can vary due to external influences and must be stabilized to keep the output frequency constant. This is achieved by a piezo actuator, controlling the incorporated grating at the end of the laser gain tube. Hence, the LO output frequency can only be slightly tuned within a small bandwidth around the very narrow emission peak of less than 10 kHz. This can only result into a potential frequency drift which is two magnitudes smaller than the resolution bandwidth of the AOS and thus negligible. In case of a major deviation, the stabilization circuit would be truncated and the incident would be indicated on the electronic control rack.

2.4.5 Allan Variance Measurement

A key factor for astronomical and terrestrial observations is the amplitude stability of the receiver. Its variance, σ, must decrease with increasing integration time, τ (comp. Eq. (2.10), radiometric behavior) [91]. The Allan variance method, a common procedure to investigate the accuracy of time and frequency standards [92], is used to demonstrate the radiometric decrease of the noise amplitude. The minimum of the Allan variance can be determined using a power law, where frequency drifts are proportional to τ^{β} and the white noise contribution is proportional to $\frac{1}{\tau}$

[93]. It can be written as:

$$\sigma_A^2(\tau) = \frac{a}{\tau} + b\tau^\beta \text{ with } \beta \geq 1 \tag{2.17}$$

Hence, when the variance is plotted on a logarithmic scale, the -1 slope defines the time interval in which the radiometer equation must be valid and only white noise contributes to the spectrum. This time interval can be individually determined for each receiver and defines the maximal integration time for one cycle τ_{cyc}, the so-called Allan-time. During that time, all individual sources need to be observed. To obtain the resulting spectrum, the single cycles are stacked, conserving the pure white noise contribution. In THIS the Allan-time is $\sim 60\,\mathrm{s}$ [73].

Chapter 3

"A thermometer is a device that measures temperature or a temperature gradient using a variety of different principles."
(Oxford English Dictionary)

Retrieval Method

In recent years, the dark side of Venus was observed with IR heterodyne technique. Unsurprisingly, broad CO_2 absorption lines were detected. These observations posed the question: is it possible to retrieve thermal profiles from these CO_2 absorption features, which are seen not only on the Venusian nightside but also on the Martian dayside? If affirmative, which altitude region would they probe?

First steps of analyzing the CO_2 absorption features on Venus with IR heterodyne spectroscopy were performed a long time ago in the early 1980s by *Deming et al.* [94]. However, spectroscopy technology and atmospheric models were not as advanced as they are nowadays and no further effort was put into these studies ever since.

Subject of this work is to use a radiative transfer model to create an inverse fitting routine, capable to extract pressure-temperature profiles from measured spectra. Initially, a nominal profile was used as an input parameter for the model in order to simulate the local atmospheric conditions.

In this chapter, the model (Sec. 3.1) and the inversion routine (Sec. 3.2) are presented in detail. In Sec. 3.3 the altitude resolution for the retrieval method will be explained and in Sec. 3.4 a proof of concept is given.

3.1 The Model CoDAT

Infrared heterodyne spectroscopy produces sub-Doppler resolution spectra that need a specialized analysis utility. The infrared heterodyne group of the NASA Goddard Space Flight Center developed a model for an accurate representation of the spectra of planetary atmospheres acquired with IR ground based heterodyne observations at telescopes with a finite aperture. The model allows a beam integrated radiative transfer calculation over various parameters such as species abundances, dynamics and thermal properties distributed over the field of view (FoV). The measured true line shapes include information on the abundance and temperature structure in the region of spectral line formation. The radiative transfer code, called Composition and Dynamics Analysis Tools (CoDAT), was specifically developed to model and fit such highly resolved line spectra.

CoDAT is an atmospheric molecular line-by-line radiative-transfer modeling engine that can also integrate spatially variable properties of the target's atmosphere in sub-resolution elements across the spectrometer beam, if needed. The engine can incorporate perturbations to the line shape that result from varying viewing angle due to the finite size of the diffraction limited telescope beam projected on the planet. This beam-integrated technique is vital to the uniqueness of the retrieval and confidence in the derived atmospheric properties, especially when the viewing geometry is such that the instrument beam captures contributions from a range of planetary longitudes and viewing angles. CoDAT accounts for all these effects directly in the analysis. All relevant information concerning the model and radiative transfer code can be found in more detail in the work of *Hewagama et al.* [95].

3.1.1 Geometrical Segmentation of the Beam

The radiative transfer calculation of CoDAT is based on the basic geometric formalism for beam integrated spectra that was developed by *Goldstein* [96] in the late 1980s. The mathematical formalism describes the projection from a thin spherical shell to a two-dimensional circular area. The geometrical input parameters are important for dividing the tangential vector to the spherical shell into the components parallel and perpendicular to the line-of-sight (LoS). These parameters are also needed for calculating the latitudinal and longitudinal position relative to the observer. However, to transform the projections into relative coordinates, only the axis tilt between the planetary and the celestial north pole (called inclination, β) as well as between the planetary north pole and the plane of the sky (called azimuth, α) has to be taken into account. The viewing angle is defined as the inclination

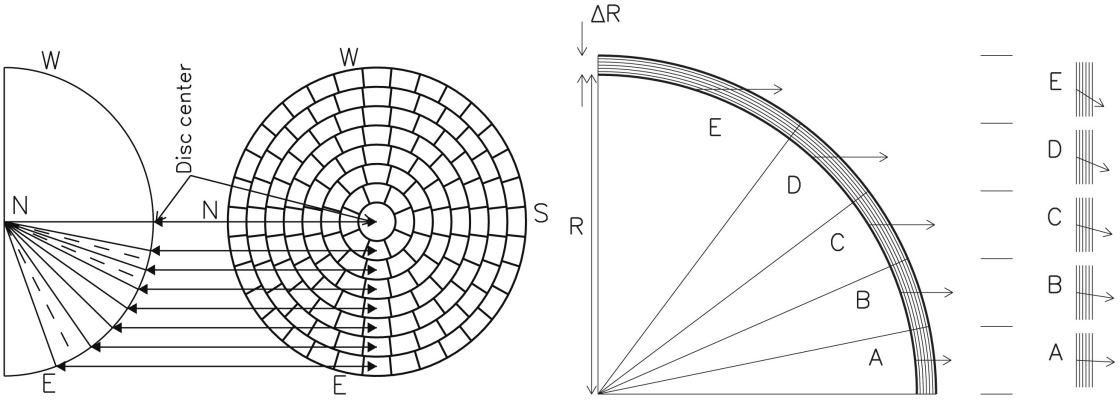

(a) *Top of the atmosphere projection of a planet viewed from the north to a disk on the sky plane which is rotated around the EW axis by 90°. The sky plane represents an example of a possible fragmentation into a sub-resolution grid.*

(b) *The cross-section of atmospheric shells for a circular symmetry is shown on the left, including the illustration of a ray emerging from the bottom of the atmosphere. The shaded area represents the geometrically thin shells. These shells are assumed to be semi-infinite plane parallel layers as shown on the right.*

Figure 3.1: *Illustrations of the geometrical conditions for the model in the case where the FoV is equal to the apparent planetary disk from Hewagama et al. [95].*

between the local radius vector and the LoS. It has to be noted, that the viewing angle increases for observing positions along an arbitrary line, originating in the center of the apparent disk (the sub-observer point (SOP)) towards the limb. This is illustrated in Fig. 3.1(a) for the case of a planetary disk equal in size to the FoV. In addition, Fig. 3.1(a) represents the two-dimensional circularly symmetric grid which is used to divide the planetary disk for beam integrated calculations. The grid displayed in Fig. 3.1(a) is an example of a possible segmentation of the beam. For CoDAT, various beam models using different grids are at hand.

A higher viewing angle results in a longer ray path through the atmosphere. Thus, a ray penetrating the atmosphere will encounter varying conditions (thermal structure, wind shears, etc.) caused by the curvature of the planet. CoDAT does not account for the curvature in terms of regarding the changing external conditions. It only considers the longer ray path through the atmosphere within the FoV by tilting the LoS to the viewing angle as it is indicated in Fig. 3.1(b). The portion of the atmosphere associated with a beam element is represented by geometrically thin ($\triangle R \ll R$) shells. The shell segments are approximated by a set of semi-infinite plane parallel layers. It has to be pointed out, that the illustrations in Fig. 3.1(a) and Fig. 3.1(b) are examples of the previously assumed case of an apparent planetary disk size equal to the FoV.

For a single-element beam CoDAT assumes a ray path through the atmosphere as

it is indicated by case A in Fig. 3.1(b) even at the limb, meaning the curvature is completely neglected. This is also true for a multi-element beam at the limb, in the case where the apparent disk is much bigger than the FoV. The importance of dividing the beam into smaller portions increases significantly when the ratio between FoV and apparent disk is ~ 1. Thus, the sub-resolution beam segmentation is necessary for analyzing the atmosphere of small terrestrial bodies like Titan. However, on Venus, for example, especially when it is close to inferior conjunction, the FoV/apparent disk ratio is $\ll 1$, since the apparent disk is more than one order of magnitude bigger than the diffraction limited FoV of the telescope. In that case, a single-element beam is a sufficient approximation of the observation. This approximation improves computational efficiency while employing the geometry calculations incorporated in the modeling code.

3.1.2 Radiative Transfer through the Atmosphere

Infrared thermal radiation forms in planetary atmospheres over a wide range of atmospheric parameters, such as the thermal and species composition as well as the pressure level corresponding to the altitudes. For example, the continuum radiation of Mars emerging from the warm surface suffers absorption by CO_2 molecules in the overlaying atmosphere. IR heterodyne technique provides ultra high frequency resolution of $\sim 1\,\mathrm{MHz}$. Thus, a pressure broadened single ro-vibrational transition can be measured. For analysis, however, the radiative transfer model must provide spectral calculations which are commensurate with the observed data. For most applications, a $\sim 1\,\mathrm{MHz}$ frequency grid is applied to match the instruments frequency resolution. The frequency grid though, can be adapted to a possible resampling of the acquired spectra to lower resolution. The grid is chosen in a way, that it symmetrically matches the IF bandwidth around the LO frequency which was used for observations. In other words, the spectral grid has to be centered around the LO frequency.

The radiation transport through the atmosphere is assumed to be time independent. The radiative transfer is approximated with the use of homogeneous semi-infinite plane parallel atmospheric layers as described above. Each layer possesses an abrupt boundary condition. Furthermore, the atmosphere is assumed to be isotropic and dominated by absorption/emission processes; i.e. scattering is neglected. The engine provides a monochromatic transfer for each frequency in the previously chosen grid. The transfer can then be calculated for a given viewing angle by cumulating the line-by-line contributions of transitions from all constituents in the remote atmosphere. A nominal coarse layering and composition distribution for the molecule of interest is presented in the algorithm. On Venus and Mars,

the only relevant constituent is CO_2 and affects due to trace molecular species are neglected. In Chap. 4 and Chap. 5 more information on the composition of the observed planetary atmospheres can be found. Assuming hydrostatic equilibrium and the ideal gas law, the model constructs a set 1000 plane parallel vertically stratified layers. Each layer is chosen to be optically thin, isothermal and homogeneous. The thickness of a layer is typically $\sim 10\,\mathrm{m}$. For a single layer, local thermodynamical equilibrium is assumed. Thus, each layer is a small black body radiator, emitting thermal radiation according to the Planck law. The whole atmospheric transfer is thus simulated by calculating the influence of the radiation from the adjacent layer to the next in a bottom to top stratification.

The frequencies of the specific molecular transition is provided by either the HITRAN [97] or the GEISA [98] line atlas. The monochromatic spectral calculations are performed at the corresponding frequency grid, using a Voigt line shape.

The top-of-the atmosphere planetary spectrum is further modulated by telluric extinction before reaching the ground-based telescope. A correction for the terrestrial atmosphere is thus included into the engine. The contribution of Earth's atmosphere is modeled using a modified version of the NCAR GENLN2 (National Center for Atmospheric Research General Line-by-Line atmospheric transmittance and radiance model) terrestrial atmospheric transmittance and radiance modeling algorithm [99, 100].This package includes standard atmosphere models by region and season for the gases of significance in our spectral region. It calculates the atmospheric transmission on the basis of the given input parameters, such as target elevation or observer altitude. This contribution from the Earth's atmosphere is analytically removed in the modeling and analysis. Since heterodyning is a spatial coherent detection method, scattering or stray light in the terrestrial atmosphere have minimal influence on the spectra and are neglected.

3.1.3 Simulating the Observed Spectra

The CODAT package has been used extensively in the past as a forward model for analyzing atmospheric data from ground based IR heterodyne observations [42, 43, 45–48, 50]. In these cases, all relevant atmospheric parameters have been included into the code to accurately model the radiative transfer at the corresponding observing site. These parameters include the planetary aspect data, such as the apparent angular disk or the SOP and sub-solar point (SSP) in longitude and latitude. Furthermore, the beam position on the apparent disk has to be marked, given in relative coordinates on the planet in respect to the equator and the central meridian longitude (CML). In this notation, sky north and sky west have a

positive whereas sky south and sky east a negative sign. However, for clarity the relative planetary coordinates, necessary to indicate the beam position, will be given in celestial directions north (N), west (W), south (S) and east (E) in the further text.

In addition to the geometrical constrains, the Doppler frequency shift has to be taken into account. The relative velocity between the target and the observer defines the spectral shift of the observed transition relative to the rest frequency in a stationary reference system. This shift is known as the relative Doppler shift. An additional shift, originating by the angular velocity of the targets circulating atmosphere and the observers locations angular velocity is called differential Doppler. The differential Doppler shift is of magnitudes smaller than the relative Doppler shift. However, given a rotational movement in the targets atmosphere the differential Doppler must be taken into account when analyzing the dynamics of the planets atmosphere but will be neglected for investigations of the thermal properties further on.

The whole fitting section, indispensable when using CoDAT as a forward model, is generally not of any interest for the retrieval algorithm and will not be discussed here in detail. Retrieved temperatures are still influenced by two critical parameters: absolute calibration of radiance and spectral line shape position. The former is represented by the scale factor which must be estimated during observations. The scale factor represents the accuracy of the adaption of the instrument to the telescope. It also includes all optical coupling losses of the signal. The scale factor is an important quantity and its influence, properties and behavior will be discussed in Subsec. 3.4.1. The line position can be calculated from the relative Doppler shift between target and observer, however, due to winds in the target's atmosphere, a small frequency variation is possible. For analyzing spectra where a non-LTE emission line is superimposed to the broad absorption line, i.e. dayside measurements of Mars, the code provides the possibility to add an auxiliary line profile to the spectrum. The auxiliary line is represented by a Gaussian distribution function and the intensity, the width and the frequency position can be fitted in order to derive information on the present dynamics and temperatures in the low pressure region of 10^{-3} hPa. This analysis of the non-LTE emission has been the main task of CoDAT in the past.

3.2 Extracting Thermal Profiles

The intension of the newly developed retrieval algorithm was to create the IFR, capable of extracting these atmospheric parameters from the measurement, which

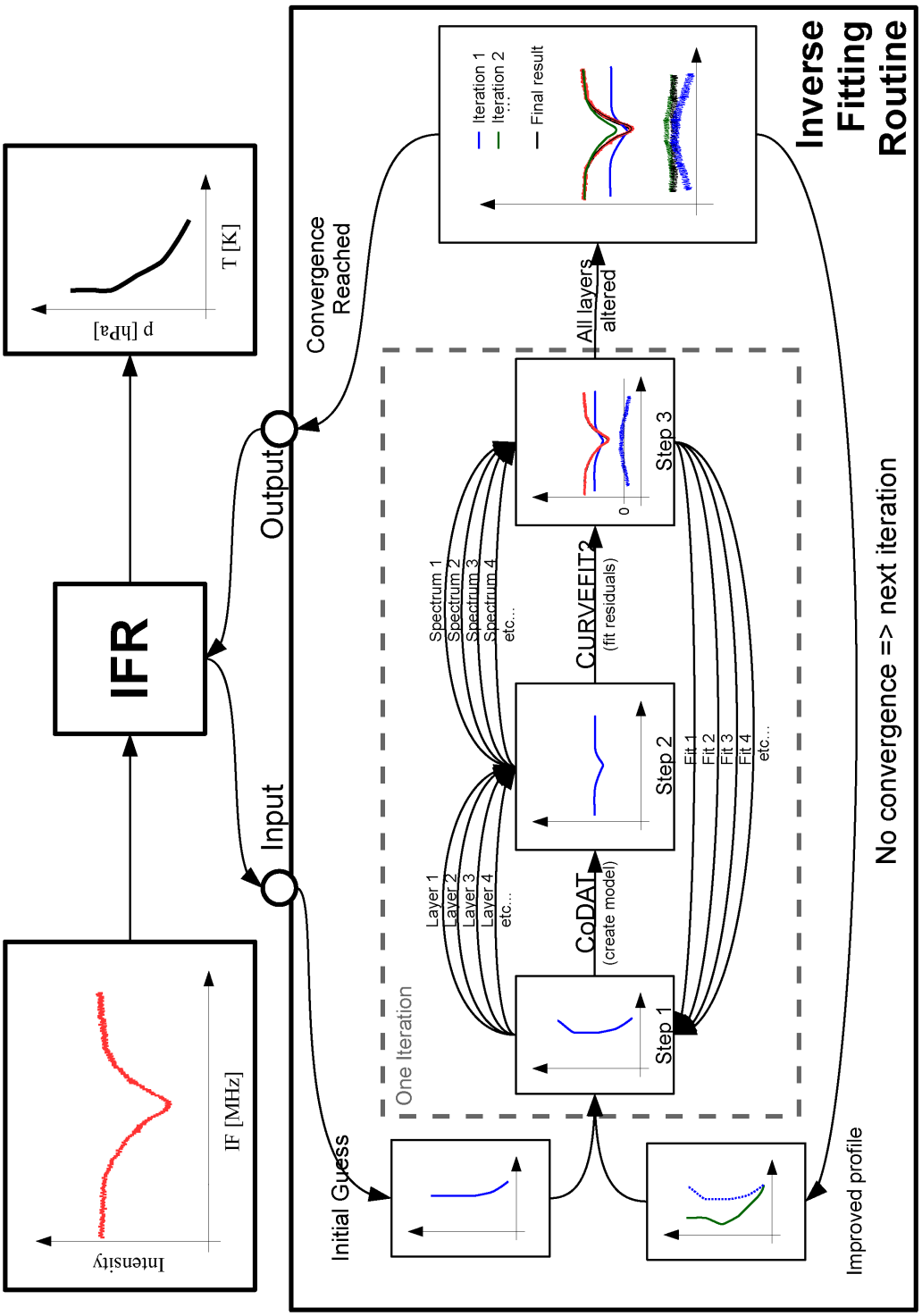

Figure 3.2: *Schematic view on the* IFR. *See Sec. 3.2 for details*

have previously been input parameters as described above in Sec. 3.1.3. For the work herein, emphasis was given to the retrieval of the predominant pressure-temperature gradient in the planet's nightside atmosphere. For convenience the thermal profile will be called pT-profile.

The initial approach was to write an inversion algorithm, that runs the radiative transfer engine for the given observing location on the planet and iteratively compares the model to the data. The scheme of the newly developed IFR is given in Fig. 3.2. In a first step, a sophisticated guess has to be assumed as the initial boundary condition. Starting of from this initial guess, CODAT creates a modeled spectrum based on the observationally constrained input parameters given in the code (step 2 in Fig. 3.2). In a third step, the residuals between the modeled spectrum and the data are calculated and a least square fit of the residuals is applied. The three steps are performed by consecutively altering the temperature layer by layer within one iteration. The iteration process itself is repeated, until the residuals between the model and the data are minimal and convergence is reached. By minimizing the residuals, the true value of the pT-profile can be retrieved. The fit to the residuals is performed by incorporating robust nonlinear Levenberg-Marquardt based model parameter optimization algorithms to constrain the derivation of model atmospheres consistent with observed spectra and to estimate statistical uncertainties for the model parameters. The profile thus retrieved represent the true atmospheric thermal structure, required to accurately simulate the radiative transfer so that the obtained model spectrum coincides to the observational one.

The IFR is written in the interactive data language (IDL) environment. The software contains various modules, e.g. for building the initial guess, calling the CODAT input and the data files. The program uses the IDL incorporated subroutine CURVEFIT2 for fitting. CURVEFIT2 provides such a least square fit to a nonlinear function of an arbitrary number of parameters. The thermal profiles are presented to the optimization algorithm in parametrized form. Additionally, upper and lower bounds have been imposed on these quantities. The complete IDL code for the inversion routine is given in Appendix B.

Under the assumption of a constant-with-altitude atmospheric CO_2 volume mixing ratio, the coupling between the abundance and thermal structure is relaxed [101]. The main task at hand reduces to the judicious selection of set of atmospheric pressure layers for which the parameters can be accurately extracted using the inversion technique.

3.3 Altitude Resolution

The gaseous atmosphere of a terrestrial planet is assumed to be an ideal gas. Since, according to the ideal gas equation, pressure and temperature are directly correlated, their simultaneous deduction is not possible with just one reference measurement. Thus, to retrieve a vertical pressure/temperature gradient, one parameter needs to be fixed. In our case, the pressure levels are fixed whereas the temperature is allowed to vary in order to fit the model to the data. To obtain a realistic assumption of the pressure levels, hydrostatic equilibrium through the atmosphere above 60 km is assumed. The barometric formula relates the pressure to the altitude as:

$$p(h) = p_0 \cdot e^{-\frac{h}{H}} \tag{3.1}$$

where, p_0 is the pressure at height h_0, $H = R\,T\,g^{-1}\,M^{-1}$ the scale height of the atmosphere containing a gas with the molar mass M at temperature T, g is the gravitational constant of the planet and $R = 8.315\,\mathrm{J\,mol^{-1}\,K^{-1}}$ the gas constant. The scale height H represents the altitude in atmosphere, where the pressure dropped to 1/e of the surface pressure. Here, H is used to estimate the first order altitude resolution of the pT-profile.

For Venus, atmospheric composition can be assumed to be almost purely CO_2 with a mixing ration of 0.965, with $M_{CO_2} = 44.01\,\mathrm{g\,mol^{-1}}$ and $g = 8.87\,\mathrm{m\,s^{-2}}$. Since the Venusian atmosphere becomes optically thick for IR radiation at an altitude of $\sim 63 \pm 3$ km [102] , the surface pressure of the opaque shell must be adapted for Eq. (3.1) to $p_0 = 100$ hPa. On a global scale, T is estimated to be between 200 K and 240 K, yielding H in the interval from 4.26 km to 5.11 km. This yields an uncertainty of the calculated pressure levels, which is taken into account by displaying error bars for the resulting pT-profile.

The altitude resolution is constrained by the data. Finer resolution grids for the altitude did not have solutions on which the fitting routine would converge. Another effect that appeared when using a finer altitude resolution is an oscillation of the retrieved pT-profile. This oscillation is caused by a cross correlation between adjacent pressure layers. The spectral information is not high enough to resolve smaller altitude bins and the retrieval algorithm can compensate an erroneous temperature by assuming an inversely wrong temperature in the next pressure layer. This leads to a propagating error through the whole pT-profile. The influence of the altitude resolution on the retrieval has been studied and investigated intensively for this work. Examples of such oscillating pT-profiles, where the altitude resolution was to high are shown in Fig. 3.3.

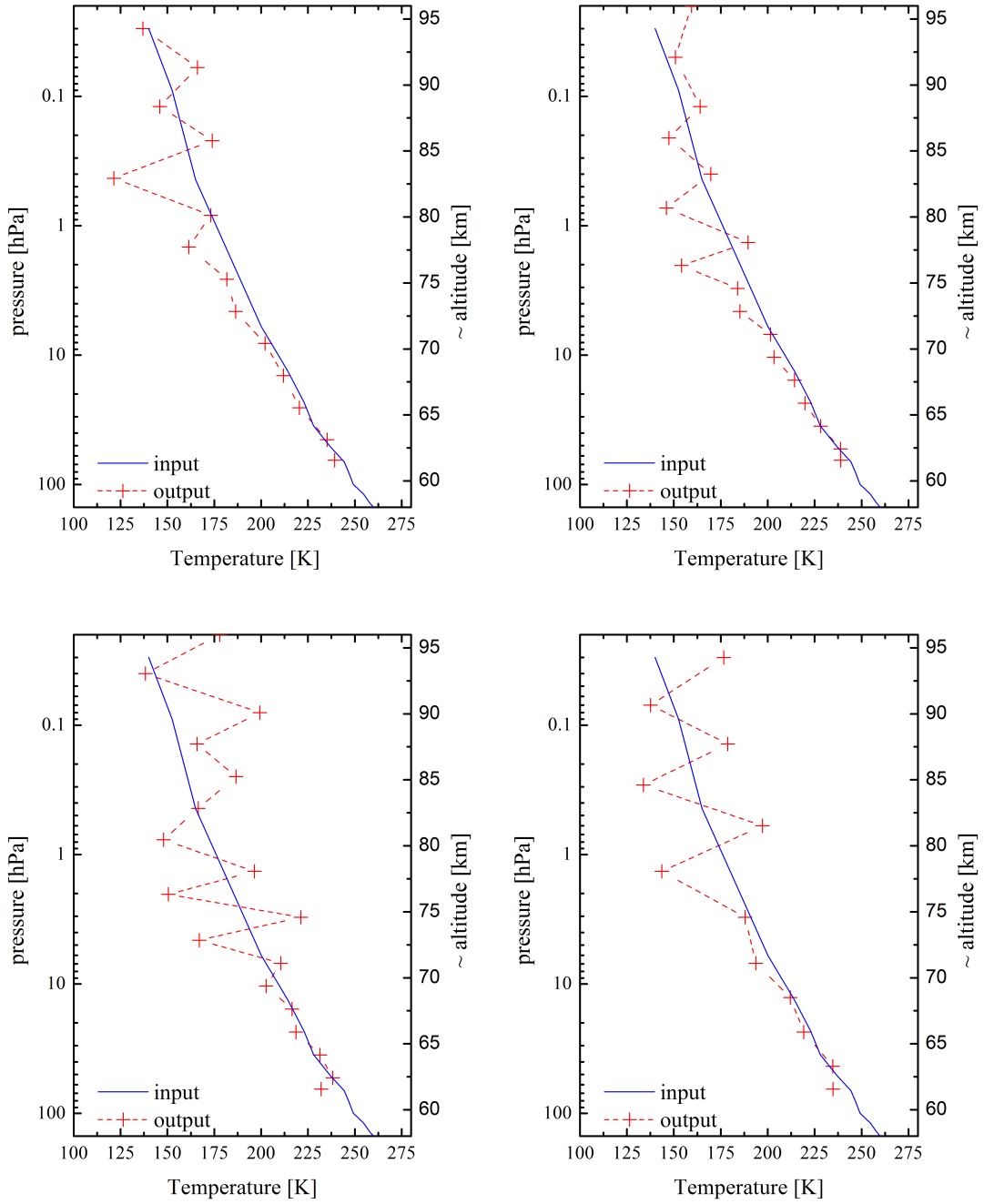

Figure 3.3: *Examples of retrieved oscillating pT-profiles were the altitude resolution was chosen to be too high. The profiles where deduced from the same synthetic spectrum.*

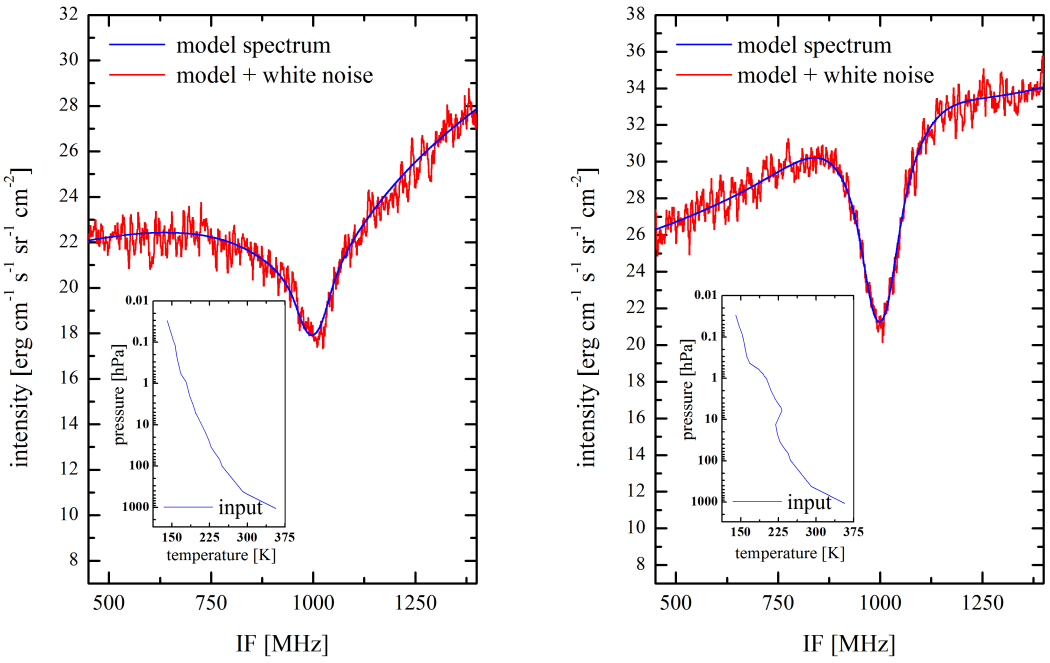

(a) *Synthetic spectrum based on a monotonic decreasing with altitude profile at the sub-observer point.*

(b) *Synthetic spectrum based on a perturbed pT-profile at the equator 65° W of the CML.*

Figure 3.4: *Synthetic spectra - Blue: Modeled radiative transfer through the atmosphere based on the temperature profile displayed in the insert graphic. Red: Model, superimposed with random white noise in order to simulate observed data. The data was smoothed over 5 MHz for display.*

3.4 Proof of Concept

To investigate the reliability of the described retrieval method, temperatures were reobtained from synthetic data, which were created using previously well-known profiles. In a first step, CoDAT was used to simulate the radiative transfer through the Venusian atmosphere at an arbitrary position on the planet using a given input pT-profile. Then, white noise was added to the model with a noise magnitude, adequate to simulate an observed heterodyne spectrum. As mentioned in Sec. 2.4.5, the measured data possess only white noise if the integration time for one cycle does not exceed the Allan-time. Hence, an investigation of the synthetic spectra with pure with noise is adequate. Two such spectra are displayed in Fig. 3.4(a) and Fig. 3.4(b) for one observing position at the sub-observer point on the planetary

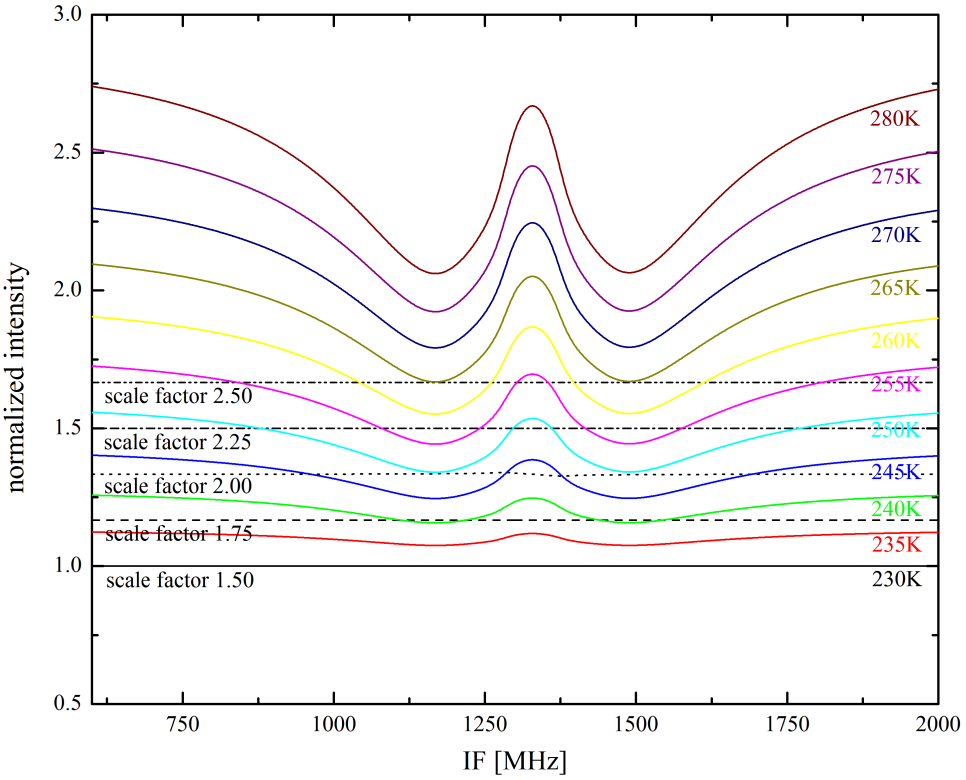

Figure 3.5: *Influence of the scale factor and the background radiation to the incident signal intensity. An increase of the background radiation in terms of the surface temperature has a non-linear effect on the spectral distribution (colored lines). The increase of the scale factor, results in a purely linear intensity scaling over the whole spectral range (dashed lines).*

disk and another at the equator and 65° W (EQ65W) of the CML. The insert graphics in Fig. 3.4 represents the initial pT-profile used as input parameter for the model. The blue line in the main graphic displays the modeled spectrum from CoDAT. The red spectra are the synthetic data sets with white noise. Data was smoothed over 5 MHz for display. It is sufficient to assume a pure white noise contribution.

3.4.1 The Scale Factor

As discussed before, the scale factor is one of the most crucial parameters for the retrieval algorithm. The scale factor is introduced into CoDAT to account for optical losses in the transmission line between the telescope primary mirror and the

detector. It can be understood as a linear intensity correction factor. In an ideal case of a perfect alignment to the telescope and lossless optical components the scale factor equals 1. However, in a real system, optical losses have a measurable effect on the intensity and cannot be neglected. Nevertheless, the losses in the instrument itself are not relevant, because the incident signal intensity on the detector is calibrated in relation to the different calibration loads. Thus, the scale factor varies with the quality of instruments telescope adaption. It is essential to investigate, whether a variation in the scale factor contributes to the thermal profile analog to a change of the background temperature, or only by resulting in a linear shift of the whole profile.

In order to investigate the influence on the retrieved profile the correlation between the scale factor and the background radiation emitted by the targets surface was investigated. Therefore, CoDAT was used to simulate spectra for different background radiations. In Fig. 3.5 the correlation between the scale factor and the targets background radiation is displayed. The pT-profile was given and only the bottom layer, representing the surface temperature of a blackbody radiator, was modified. The temperature has been increased in steps of 5 K from 230 K up to 280 K. The intensity of the background radiation is normalized to the spectral intensity distribution corresponding to a surface temperature of 230 K (comp. colored lines in Fig. 3.5).

In Fig. 3.5, it can be observed, that the increase of the background radiation has a non-linear influence on the spectral distribution of the incident signal intensity. This is within the expectation, since the background radiation originates from the bottom of the line forming region and must have a more complex effect on the shape of the absorption line, because the whole radiative transfer through the atmosphere is biased by the surface emissivity of the radiator. Hence, the scale factor can only produce a total shift of the retrieved profile, due to the purely linear intensity scaling of the signal (comp. dashed lines in Fig. 3.5). Local variations of the temperature gradient between the single pressure layers are not affected by the scale factor. The scale factor can thus be decoupled from the temperature retrieval.

Nevertheless, good knowledge of the scale factor is inevitable to avoid linear shifts of the whole profiles. In order to estimate the scale factor it is convenient to observe well characterized uniform filled sources such as the lunar disk or the sun. The scale factor usually varies within a range of 1.4 to 2.8 depending on the instrument and the telescope.

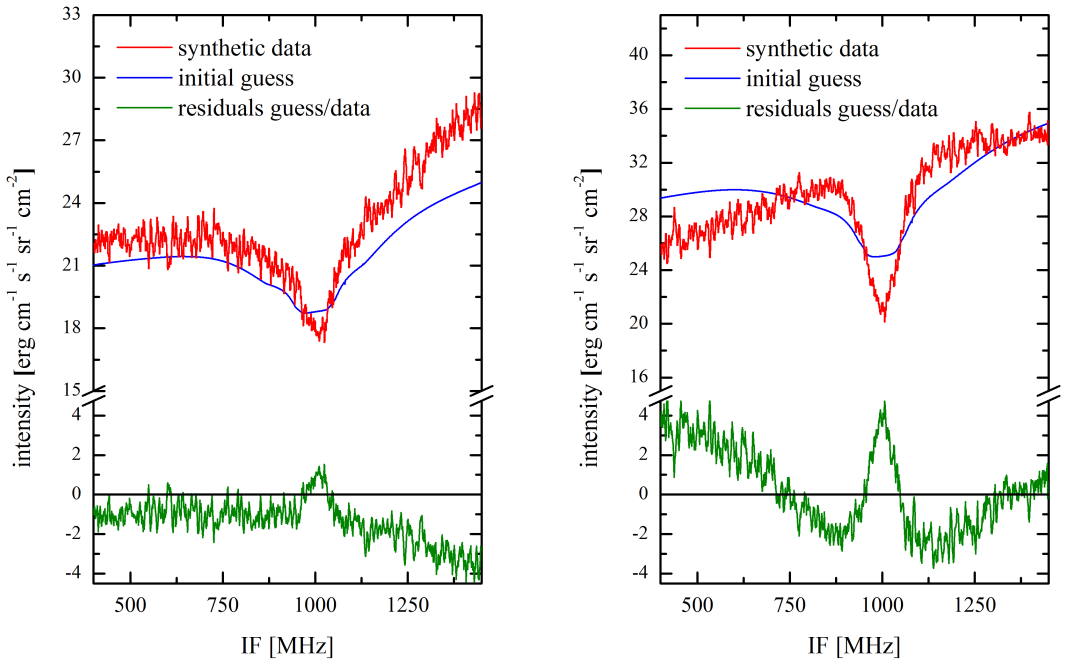

Figure 3.6: *Fit guess for synthetic spectra. Blue: Modeled radiative transfer through the atmosphere based on the initial guess temperature profile. Red: synthetic data as introduced on Fig. 3.4. Green: residuals between initial guess model and synthetic data.*

3.4.2 The Initial Guess

The analysis described herein does not employ an a-priori based optimal estimation. In order to define the inevitable initial boundary condition for the retrieval method, an initial guess is created. When starting the routine, the user has to enter the approximate absolute intensity of the absorption line tip and its center frequency. From these parameters and under the assumption of a pressure broadening of the line with a self broadening coefficient of $0.12\,\mathrm{cm}^{-1}$/atm, an initial DSB spectrum is created. From there on, the initial temperature profile, which is used for further analysis, contains two arrays of parameters, the pressure gradient and the temperatures in the corresponding layers. The pressure layers are fixed and calculated in advance (comp. to the following Sec. 3.3). The bottom pressure layer, from where the background radiation is emitted, can be retrieved and fitted by the routine. This retrieval is constrained by the self broadening of the line at the highest pressure. However, an initial pressure must be assumed in the input

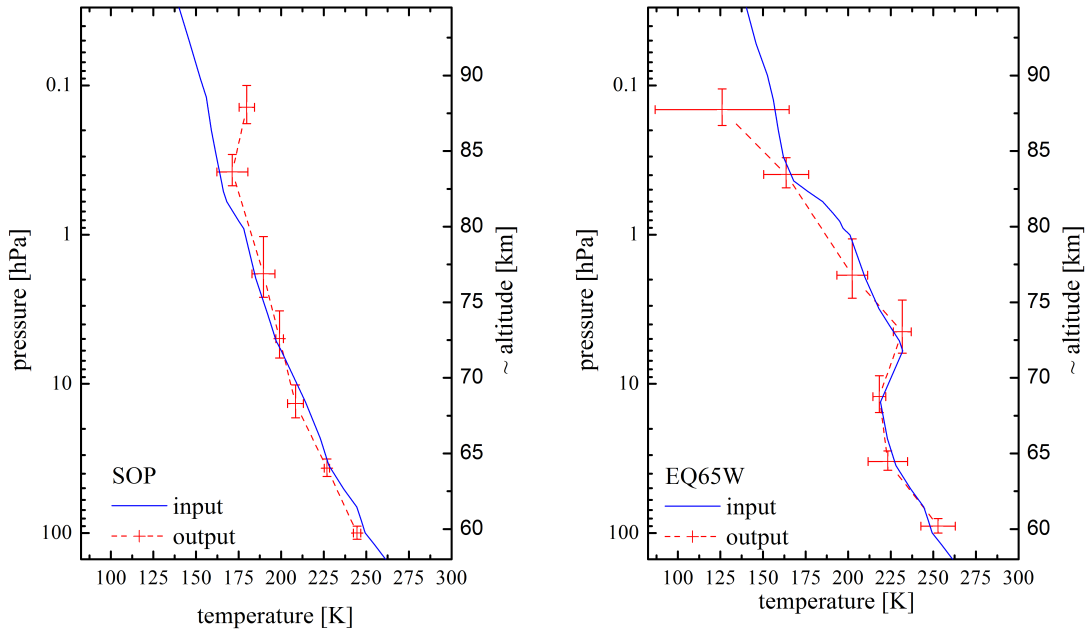

(a) *Retrieved pT-profile (red) for a monotonic increasing input profile (blue). Only the top point deviates significantly from the input file. This can be due to saturation of the line tip.*

(b) *Retrieved pT-profile (red) for a disturbed input profile (blue). All points are in good agreement within the error margins.*

Figure 3.7: *Retrieved pT-profiles (output, red) from synthetic data (comp. Fig. 3.4). In blue, the input profiles are displayed. Pressure errors account for the varying scale height in the atmosphere. For information on the temperature errors, please refer to the main text.*

file as a dummy character. The initial temperature array is calculated according to Planck's law for the radiation originating at the highest pressure level and the radiative transport through the atmosphere using CoDAT. Starting from this initial guess, the inversion routine can iteratively adapt the temperature profile, such that the residuals between the data set and the modeled spectrum are minimized. In Fig. 3.6 examples of a data set and the corresponding spectrum according to the respective initially guessed pT-profile are displayed.

3.4.3 Analysis of Synthetic Spectra

The output pT-profiles, which were deduced from the synthetic data are displayed in Fig. 3.7. The input (blue) and the retrieved profiles (red) agree within the

uncertainty margins. As mentioned, retrieved temperatures are influenced by two critical parameters: absolute calibration of radiance and spectral line position (affected by differential Doppler shift correction). The former is represented by the scale factor as discussed before in Subsec. 3.4.1. The line position can be calculated from the relative Doppler shift between target and observer. However, due to winds in the target's atmosphere, a small frequency variation is possible. To obtain the temperature uncertainty, the scale factor is varied by $\pm 10\,\%$ and the frequency position by $\pm 5\,\mathrm{MHz}$ around their expected values. In case any of these parameters possesses an unrealistic value, the fitting routine does not find a closed solution and crashes. Thus, at least 31 pT-profiles for each spectrum were deduced. Finally, all profiles are averaged. The uncertainties are represented by the deviation of the maximum and the minimum values to the median. For the analyzed profiles, deviations that exceed the uncertainties are only seen near the upper and lower boundaries of the profile in Fig. 3.7(a). However, the results are still compatible to the input values and the relative errors are less than 10%.

This can be understood when regarding the so-called normalized altitude weighting functions in Fig. 3.8. These functions describe the contribution of the single pressure layers to the spectrum at a certain frequency. The weighting functions are an approximation of the error analysis of the forward model in terms of the specific parameter. They give an idea on the information content of a set of measurements. However, the altitude resolution is, despite the well-defined peaks, not only correlated to the widths of the peaks, but also to their spacing, as it has been described by *Roger et al.* [103]. In Fig. 3.8, the normalized weighting functions are displayed for these frequencies, where the contribution from the single layers of the applied pressure grid for the retrieval of the temperature profiles in Fig. 3.7 is maximal. It can now be stated, that for the low pressure layers, no defined peak can be found. Hence, the contribution from the high altitudes to the pT-profile is minimal. Also, for the bottom layer at around 100 hPa in both profiles, the peak of the function is not found, since one, the contribution to the spectra extends beyond the detection bandwidth and two, the atmosphere gets opaque at these altitudes. Nevertheless, the weighting functions can proof, that the pressure grids, applied for deducing the thermal properties, are reasonable. Since there is no overlapping of the peaks, there are no cross-correlations between the pressure layers. Hence, the information content in the spectra is sufficient to resolve the proposed amount of atmospheric layers.

Further studies on the uncertainties of the retrieval algorithm were made by analyzing the deviation between the input and the output model. In Fig. 3.9 the synthetic data, which have been used for the proof of concept so far are plotted along with the output model. The best fit, as mentioned before, is found by itera-

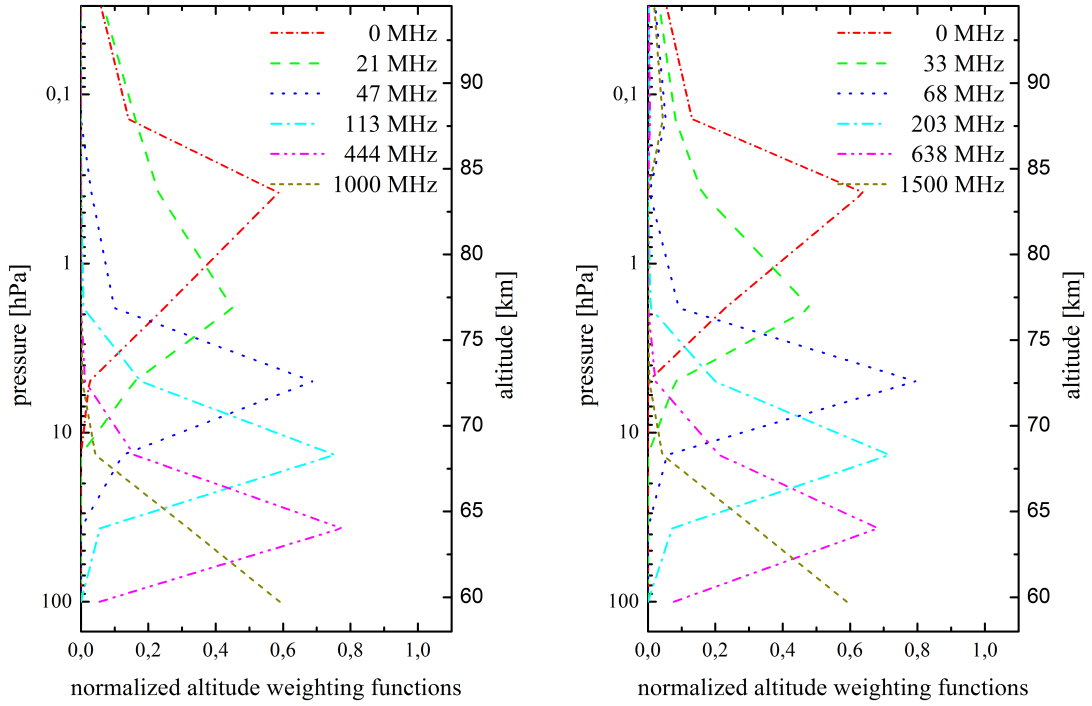

(a) *At the line center (0 MHz), the line forming occurs between 2 hPa and 0.2 hPa. Contributions at 1000 MHz offset of the center, are located at low altitudes < 61 km.*

(b) *The contribution maximum at 33 MHz for the pressure layer at ∼ 1.8 hPa is not as defined as for all other layers, nevertheless a clear local maximum can be identified and the layer can be resolved.*

Figure 3.8: *Normalized altitude weighting functions. Displayed is the contribution of the single pressure layers to the spectrum at 6 frequencies. The frequencies are those, where the contribution from one specific layer is maximal. The frequencies are given as an offset to the frequency of the line center.*

tively varying the pT-profile and thus adapting the model, calculated with CoDAT, to the synthetic data set. However, taken the uncertainties of the retrieval into account, as they have been discussed before, an output model was calculated. Hence, the final output models, shown in Fig. 3.9, are based on the deduced pT-profiles displayed in Fig. 3.7. In addition, the residuals between the input model and the synthetic data and the output model and the synthetic data are displayed. It can be observed, that the noise amplitudes of the residuals are commensurate to each other and linear through zero. For better understanding, the residuals between the input and the output model was calculated and is plotted in Fig. 3.9. It has to be noted, that these residuals (yellow line) are in both cases smaller than the

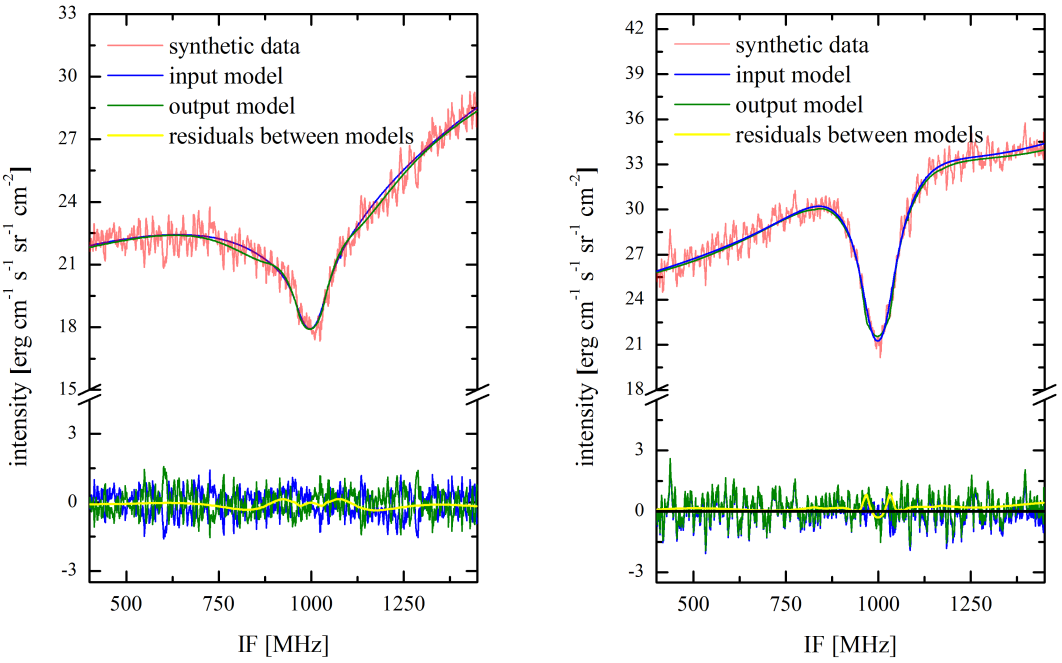

(a) *Synthetic data as displayed in Fig. 3.4(a). Best fit to the data yielding the retrieved pT-profile displayed in Fig. 3.7(a).*

(b) *Synthetic data as displayed in Fig. 3.4(b). Best fit to the data yielding the retrieved pT-profile displayed in Fig. 3.7(b).*

Figure 3.9: *Comparison between the input model and the best fit. The blue and red lines represent the input model and synthetic data. The green line represents the best fit to the synthetic data (output model). On the bottom of the figures, the residuals between the input model and the synthetic data (blue), between the output model and the synthetic data (green) and between the input and the output model (yellow) are displayed.*

SNR, which was initially superimposed to the input model. Thus, the convergence of the output model to the input model is depending on the SNR of the synthetic data. It has to be remarked, that the uncertainty of the output model, hence the best fit to the data, depends on the SNR. However, the global solution is still well described by the minimization of the residuals and the retrieved profiles in Fig. 3.7 are within the uncertainty margins.

From these studies, it can be shown, that the newly developed retrieval method delivers reliable results for the pT-profiles. In the next step, the method will be applied to actual measurements acquired on Venus.

Chapter 4

"Only at the end do you realize the power of the Dark Side."
(Star Wars)

The Atmosphere of Venus

4.1 State of the Art

Venus is besides the moon the brightest object in the sky without self-luminescences and it has been an object of interest for mankind since the antique days. The planet Venus is a solid body with an equatorial radius of 6051.8 km and is of similar size as Earth. Since Venus possesses a surrounding atmosphere it can be categorized as a terrestrial planet. Due to its Earth-like size it is often called Earth's sister planet, although there are some major differences between the two, e.g. the clockwise rotation direction of the solid body. This retrograde rotation is unique for a planet in our solar system. The rotation axis of Venus has almost no tilting angle against its orbital plane, yielding a lack of seasons during the Venusian year. Despite the very small inclination, the axis tilt is given as 177.36° in order to define a counterclockwise rotation. In Fig. 4.1, pictures of the planet can be found, taken with ultraviolet (Fig. 4.1(a)) and real color (Fig. 4.1(b)) imagery. Venus has no natural satellite and is the second planet from the sun. Its elliptical orbit's semi-major axis is ~ 0.72 AU and the sidereal orbiting period is ~ 224.7 Earth days. The very slow solid body rotation of the planet, with a period of ~ 243.0 hours, yields a divergence between the sidereal rotation period and the solar day. A solar day, the time between two sunrises on Venus, is only ~ 116.7 hours, thus by a fac-

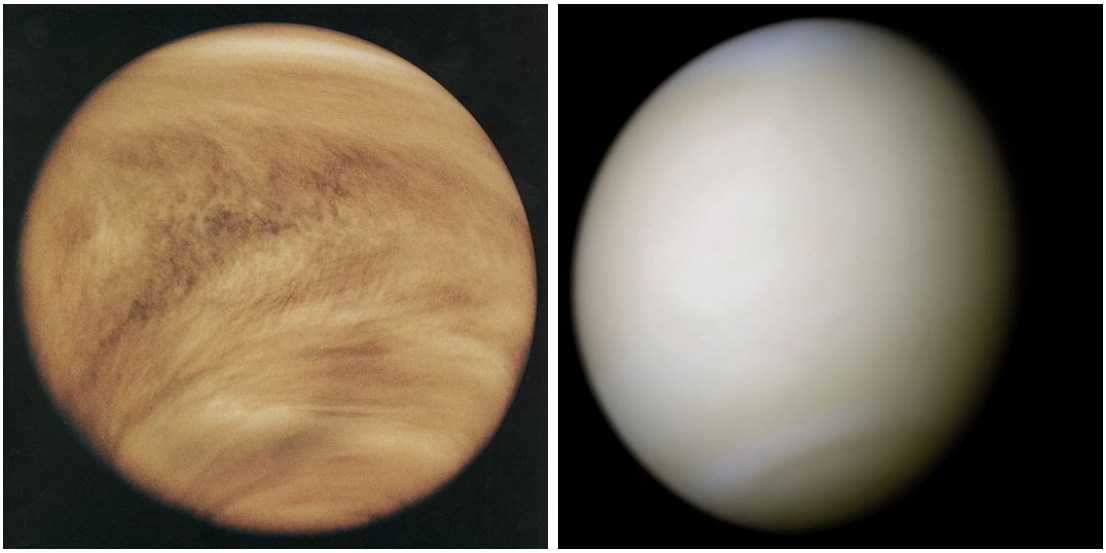

(a) *Ultraviolet image of Venus' clouds as seen by the* PVO *in 1979 [104].*

(b) *Venus in real colors, processed from clear and blue filtered Mariner 10 images. Image processing by R. Nunes [105].*

Figure 4.1: *Images of Venus*

tor of ~ 2.08 smaller. The most important bulk and orbital parameters of Venus and Earth are summarized in Tab. 4.1. Venus is globally covered by a thick, fast rotating, high-altitude, Y-shaped cloud layer (comp. Fig. 4.1(a)) and its surface pressure is with ~ 92.000 hPa almost one magnitude higher than on Earth.

4.1.1 Introduction

Ground-based observations of temperatures on Venus have been performed since the middle of the 20^{th} century using microwave and infrared spectroscopy [19, 107]. With the dawn of the space era, mesospheric temperatures were measured from space. Since then, a manifold of missions, including orbiter, landers, entry probes and flybys have been performed [20], shading light on the mysteries of Venus' atmosphere.

The recent space- and ground-based observing techniques and exemplary results are presented and discussed in the first part of this chapter (comp. Subsec. 4.1.3 and Subsec. 4.1.4). In addition, the most sophisticated circulation models for Venus' atmosphere which have been developed lately are introduced in Subsec. 4.1.5. The observations that were performed on Venus are presented in the second part,

Parameter	Venus	Earth	Ratio (Venus/Earth)
Radius at equator (km)	6051.8	6378.1	0.949
Surface gravity (km/s^2)	8.87	9.81	0.905
Natural satellites	0	1	-
Semimajor axis (10^6 km)	108.21	149.6	0.723
Sidereal orbit period (days)	224.701	365.256	0.615
Sidereal rotation period (days)	243.0	0.998	243.686
Solar day (days)	116.750	1	116.750
Obliquity to orbit (deg)	177.36	23.44	7.567
Distance from Earth (10^6 km)			
Minimum	38.2	-	-
Maximum	261.0	-	-
Apparent diameter (arcsec)			
Minimum	9.7	-	-
Maximum	66.0	-	-

Table 4.1: *Important orbital parameters of Venus and Earth from [106].*

Sec. 4.2. In the third part of this chapter, first measurements of CO_2 absorption lines from the Venusian nightside atmosphere, using IR heterodyne spectroscopy are analyzed and the resulting pT-profiles will be presented and discussed (comp. Subsec. 4.3.1). In the fourth part, a comparison to selected, well-established observing techniques will be given in more detail, in order to investigate the results in the context of other Venus temperature retrieval methods (comp. Sec. 4.4). Emphasis will be given especially to the coordinated observing campaign with the Vex Radio-science Experiment (VeRa) during observations in May 2012 (Sec. 4.3.3). Finally, in Sec. 4.5 a conclusion will be drawn for the analysis of Venus nightside temperature profiles, which were deduced from infrared heterodyne spectroscopy for the first time.

4.1.2 Structure, Composition & Thermal Properties

Venus' atmosphere can be divided into three main thermal regimes: the troposphere (0–60 km), the mesosphere (60–100 km) and the thermosphere (>100 km). In the dense and stable troposphere, temperature decreases monotonically by a lapse rate of $\approx$-10 K km^{-1}[108, 109]. The turbulent and thermally variable mesosphere contains either a temperature gradient and several inversions on the nightside [110–112] or isothermal behavior on the dayside [109]. The thermosphere

above 100 km is very cold, especially on the nightside and thus it is also often called cryosphere [113].

The troposphere extends into the main cloud layer. Recent observations show that the upper cloud top is located around 74 km altitude for low and mid latitudes and subsides to $\sim$65 km at the poles [114], assuming roughly 22 km cloud thickness. Above and below the main cloud layer variable hazes exist [115, 116]. Planck radiation originates from the top of the main clouds and the atmosphere becomes opaque to thermal infrared radiation in altitude regions around 60 km corresponding to the 100 hPa pressure level [102]. The troposphere holds the strong retrograde zonal superrotation. The four day period of the superrotation is a mean value for an altitude corresponding to the cloud top, where the RZS reaches its maximum with wind speeds of up to 100 ms^{-1}. The rotation period extends to five days at the equator, and decreases to three days for mid-latitudes and towards the poles. A meridional wind component is almost negligible at these altitudes (max. 10 ms^{-1} at 50° latitude and zero at the equator and the poles) [117]. Towards the poles though, the superrotation extends in spiral-like patterns and forms a fast rotating vortex on both hemispheres. The thermal properties of the vortices reveal a slightly warmer polar region compared to the surrounding latitudes, yielding a cold collar at $\sim$75° latitude.

The dynamics in the thermosphere are dominated by an axis-symmetric circulation, the so-called sub-solar to anti-solar (SS-AS) flow. This stable circulation cell is driven by solar insolation in the UV spectral range. Molecules are heated and rise at the SSP, they escape radial symmetrically and are accelerated along the pressure gradient field lines towards the day-night boundary, called the terminator. The pressure gradient evolves by the big temperature difference between the sunlit dayside and the dark nightside. Then, on the nightside the molecules decelerate and subside at the ASP. Due to some asymmetry, caused by rotational influences and shear effects from the mesospheric RZS contribution, the downwelling of the air masses appears not precisely at the ASP, but in its close vicinity [118]. The dynamics of Venus dayside thermosphere at $\sim$110 km have been extensively studied using IR-heterodyne observation techniques [30–32].

The mesosphere, located between the tropo- and the thermosphere is the turbulent transition region between the two most dominant wind regimes. Direct measurements of wind speeds in the mesosphere are rare due to the lack of valuable tracers in these altitudes. Only sub-mm observations of CO can provide information on the dynamical properties of the mesosphere by observing Doppler-shifted absorption lines. Altitude resolution, however, is thus depending on model constrains and SNR of the spectra.

The atmosphere of Venus contains mostly carbon dioxide and nitrogen. Minor gaseous species can be found with a concentration of few ppm. Aerosols and droplets of sulfuric acid occur in the clouds, which are mainly composed of sulfur oxide and these droplets. Trace amounts of sulfur, chloride and carbon indicate that Venus might have been volcanically active [118]. In Tab. 4.2 an overview of the atmospheric parameters and the composition of the major and minor species is given for Venus and Earth. The high amount of CO_2 in the Venusian atmosphere and its dense structure yields a strong greenhouse effect on Venus [116]. This greenhouse effect leads to the fact, that, despite its further solar distance compared to Mercury, the surface of Venus is the hottest in our solar system.

Parameter	Venus	Earth
Surface pressure (hPa)	92000	1014
Surface density (kg/m^3)	~ 65	1.217
Mass of atmosphere (kg)	4.8×10^{20}	5.1×10^{18}
Mean molecular weight (g/mole)	43.45	28.97
Composition		
Major	96.5% CO_2	78.08% N_2
	3.5% N_2	20.95% O_2
Minor	150 ppm SO_2	9340 ppm Ar
	70 ppm Ar	400 ppm CO_2
	20 ppm H_2O	18.18 ppm Ne
	17 ppm CO	5.24 ppm He
	12 ppm He	1.7 ppm CH_4
	7 ppm Ne	0.55 ppm H_2

Table 4.2: *Atmospheric parameters of Venus and Earth. Minor constituents are given in parts per million (ppm) [106].*

4.1.3 Space-based Observations

The era of space exploration of Venus has started about 50 years ago. The Soviet Union inaugurated the investigation of the planetary structure from space, badging the United States to pick up the race. Space-based observations of atmospheric temperatures is performed ever since, either remotely, by using various instruments on board of the Soviet Venus exploration spacecrafts, i.e. Venera 9, 10, 15–16 [120–124], the US Mariner 5 [125, 126], Pioneer Venus (PV) [127] and Magellan [128] or through in-situ measurements of their entry probes and landers [129].

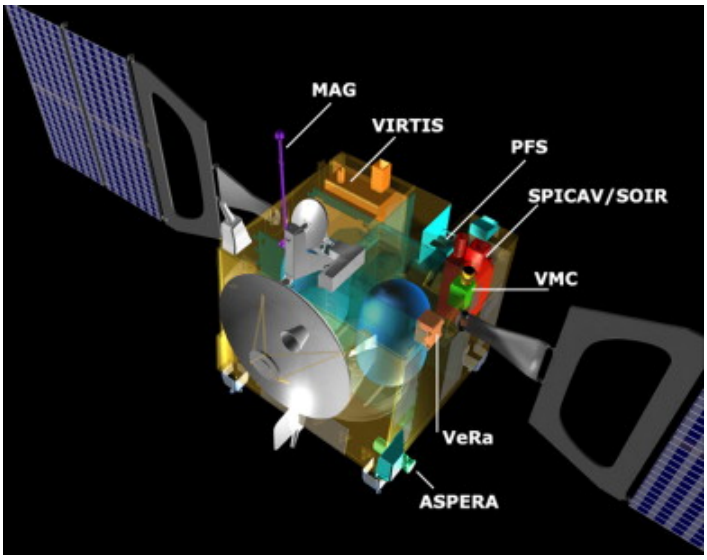

(a) *Drawing of the* Vex *spacecraft with the incorporated payloads, from Svedhem et al. [27]. Only the instruments* Virtis, Spicav/Soir *and VeRa will be presented herein.*

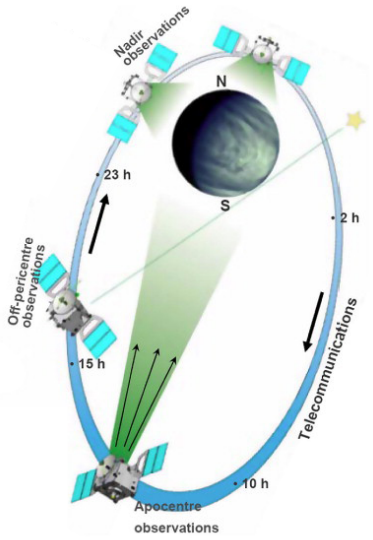

(b) *Sketch of the* Vex *orbit. Figures along the orbital time. From Titov et al. [119]*

Figure 4.2: *Venus Express spacecraft and orbit.*

More recently, the observations of Esa's Venus Express (Vex) [27] have greatly contributed to our understanding of Venus' atmosphere. Vex is the latest spacecraft that successfully reached the planet. A later attempt by the Japan Aerospace Exploration Agency (Jaxa) to install the orbiter Akatsuki around Venus in 2010 was not accomplished [130]. The satellite is currently orbiting the sun and another try to enter into a Venus orbit cannot be performed earlier than November 2015 [131, 132]. The recent Vex mission of Esa is presented in more detail in the following, given emphasis on the instruments which are applied to investigate Venus' thermal properties.

Venus Express - VeRa, VIRTIS & SOIR

Current space-based remote sensing of the Venusian mesospheric and thermospheric temperatures is successfully performed on board of Vex by the Visible and Infrared Thermal Imaging Spectrometer (Virtis) [133], the Solar Occultation in the InfraRed (Soir) spectrometer [134] and the Venus Express Radio Science Experiment (VeRa) [135]. Those instruments have provided multiple data sets during the last decade, but due to orbital constrains, the global coverage is limited.

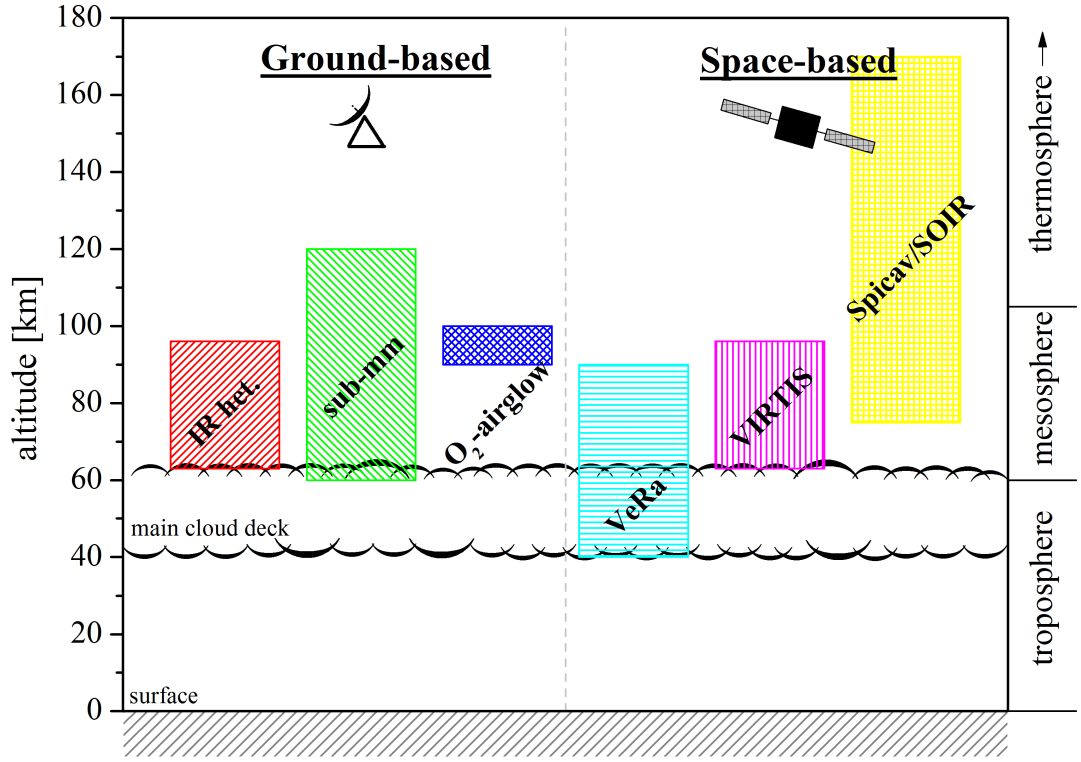

Figure 4.3: *Scheme of the probing altitudes in the Venusian nightside hemisphere of the space- and ground-based instruments and observing techniques, which are discussed and compared in this work.*

Venus Express is ESA's first satellite exploration mission to Venus. VEX was launched in November 2005 and injected into its assigned 24-hour elliptical quasi-polar orbit in April 2006. The mission was proposed to find a valuable reuse for the design of the spacecraft Mars Express [136]. The key scientific objectives include the comprehensive investigation of the atmospheric composition and chemistry, dynamics and structure, as well as observations of the cloud and haze layers and studies of the energy balance and global greenhouse effect.

The satellite bus is a cubic 3-axes stabilized platform with two telecommunication antennas, fixed to opposed sides of the cube. The main antenna, which is oriented towards Venus, is a 1.3 m dish (comp. Fig. 4.2). The payload includes seven instruments, from which five are inherited from the Mars Express mission. The locations of the instruments in the spacecraft are shown in Fig. 4.2(a). VEX spectroscopic observing bandwidth spans from the UV to the thermal IR wavelength. Various observation techniques are applied by the different instruments,

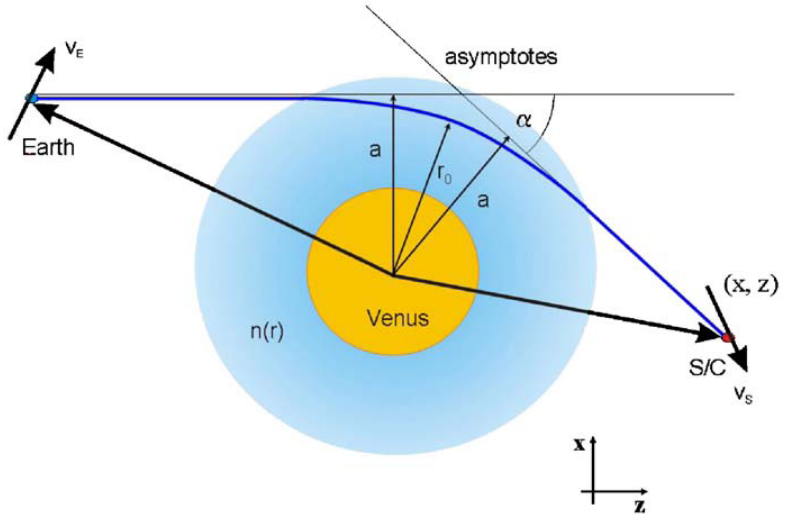

Figure 4.4: *Ray bending in Venus' atmosphere displayed in a planetocentric coordinate system from Häusler et al. [135]. Ray path closest approach distance r_0 and deflection angle α are related to the impact parameters and the refraction index $n(r)$.*

such as direct detection methods or solar, stellar or radio-occultation. The instruments probing the atmosphere in the altitude region between 60 km and 100 km, which is the relevant region for comparison to IR heterodyne observations, will be presented in the following. A schematic overview of the probing altitudes of the various instruments and techniques is given in Fig. 4.3.

Vex has passed its nominal phase mission. It is now operating at its fourth extension and it is difficult to foresee how long it can be operated, especially as far as fuel reserve is concerned. However, Esa has announced in June 2013 that funding will be terminated by the end of 2014 [137]. With the imminent shut down of Vex and the orbital insertion failure of Akatsuki, the importance of ground-based observations increases significantly.

VeRa

The Venus Express Radio Science Experiment sounds the atmosphere in the X- and S-band at 3.6 cm and 13 cm. The scientific aims of VeRa are manifold and the study of the thermal properties of the neutral atmosphere is just one of them. The VeRa experiment is a radio occultation measurement. An ultrastable oscillator (Uso), on board of Vex, serves as a reference radiation source [138]. The signal of the Uso is detected by ground-based receivers. VeRa probes the neutral atmosphere between $\sim$40 km and $\sim$90 km by analyzing the refracted ray emitted by the Uso. The highly refractive atmosphere of Venus makes the altitude region below 40 km inaccessible for radio occultation, however, above this boarder the instrument can

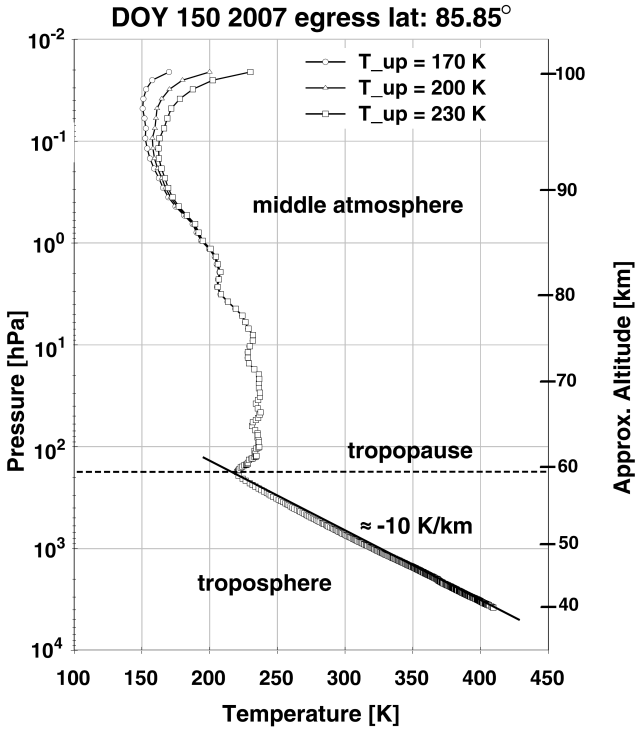

Figure 4.5: *Example of a pT-profile as seen by VeRa, from Tellmann et al. [109]. Three profiles are calculated for observations at 85°N and LT 15:50 with upper boundary conditions 170, 200 and 230 K. The profiles merge at an altitude of ∼ 90 km.*

characterize the thermal behavior as a function of altitude, latitude and local time (LT) [135]. During the Earth occultation of the spacecraft, the radio ray penetrates the atmosphere and is subject to a varying refraction angle as it emerges through the different altitudes. Hence, the ray bending is depending on the present atmospheric conditions. In Fig. 4.4 a scheme of the radio signal's trajectory in the Venusian atmosphere is shown. The utilization of two simultaneous one-way downlink frequencies enables observations during ingress and egress of one orbit [108].

To derive the temperature gradient in the atmosphere, hydrostatic equilibrium and the ideal gas law is assumed for data processing. The height profiles can be directly deduced from the neutral density number profile, which is simultaneously obtained by VeRa during one occultation, as it is described in detail by *Tellmann et al.* [109]. Thus, the temperature profile is calculated as

$$T(h) = \frac{\mu_{up}}{\mu(h)} \cdot T_{up} + \frac{\bar{m}}{k \cdot n(h)} \int_{h}^{h_{up}} n(h') \cdot g(h') dh' \tag{4.1}$$

where h is the altitude, $\mu(h)$ the refractive profile, $n(h)$ the neutral density profile, $\bar{m}$ the mean molecular mass of the mixed neutral atmospheric species, $g(h)$ the altitude-dependent acceleration of gravity. The integration requires an upper boundary condition, represented by the parameter T_{up}. This upper boundary condition is chosen to represent the temperature at an altitude of 100 km. For retrieval, three profiles with different upper boundary conditions are investigated. An example of the pT-profile derived from radio occultation observations is displayed in Fig. 4.5 with T_{up} = 170, 200 and 230. A large amount of these profiles have been collected up to now with a very high altitude resolution of a few hundred meters. The uncertainties of the retrieved temperatures vary with altitude, with the highest uncertainty at the upper boundary of 100 km (10%) and the lowest uncertainty of a fraction of a Kelvin at the lowest accessible altitudes. Comparison of VeRa measurements to IR heterodyne observations will be discussed in detail in Subsec. 4.3.3 and Subsec. 4.4.1.

VIRTIS

VIRTIS is the acronym of the Visible and Infrared Thermal Imaging Spectrometer. The spectrometer is directly inherited from the ESA ROSETTA mission. It combines imaging and spectrometry in a unique way. The dual instrument covers the visible and near-IR wavelengths from 0.3 µm to 5 µm, split into two imaging spectrometers, the VIRTIS-M-vis (0.3–1 µm) and VIRTIS-M-IR (1–5 µm) and one high resolution spectrometer VIRTIS-H (2–5 µm), with separate telescopes [133]. The FoV on Venus, corresponding to the slit aperture of the spectrometer is 0.25×64 mrad for the VIRTIS-M channels covering about one-third of the diameter of Venus apparent disk at the orbital apocenter. The single resolution cell of VIRTIS is 0.58×1.75 mrad, yielding a spatial resolution of ∼20 km on the Venusian disk. Besides the monitoring of trace gases in the lower atmosphere and total cloud opacity, as well as atmospheric dynamics in and above the main cloud deck, VIRTIS has been applied for investigations of the thermal properties of Venus' nightside mesosphere. The VIRTIS-M-IR channel was used to observe the CO_2 band at 4.3 µm. The spectral resolution was chosen in a way to be adequate to probe the altitude region between 63 km and 96 km [112]. On the dayside the signal is dominated by the 4.3 µm non-LTE emission and the model used for analysis cannot account for this contribution. Thus, only nighttime temperature maps are at hand from VIRTIS observations. Lately, also VIRTIS-H observations were analyzed for nightside temperature retrieval by *Migliorini et al.* [139]. The high spectral resolution observation of the mid-IR CO_2 band can additionally provide a large amount of global temperature maps. Therefore, space-based infrared spectroscopy can contribute a lot to the investigation of Venus' nightside hemisphere, despite its fairly poor vertical resolution.

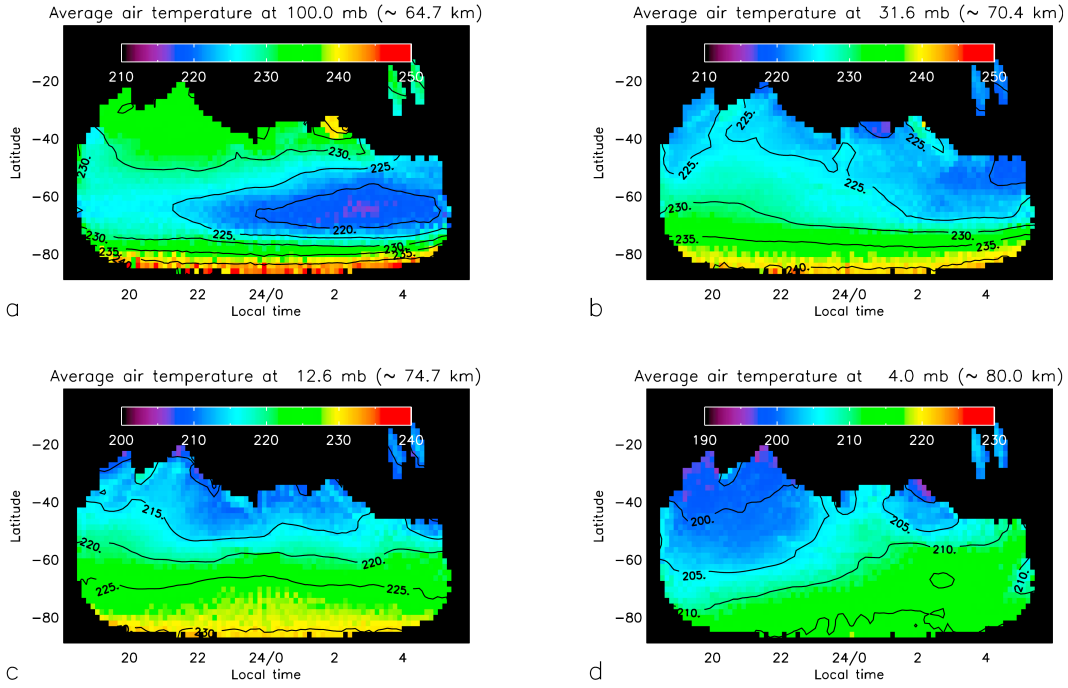

Figure 4.6: *Example of the mean temperature field as observed by* VIRTIS *from Grassi et al. [112]. Temperatures are mapped as a function of latitude and local time for four selected pressure levels: (a) 100 mbar, (b) 31.6 mbar, (c) 12.6 mbar (d) 4.0 mbar.*

Examples of the thermal distribution of Venus' southern hemisphere at four different altitudes are given in Fig. 4.6. The mean temperature field of the nightside, as seen by VIRTIS, from local time 18:00 to 6:00 is on display. A detailed comparison to the deduced profiles from IR-heterodyne observations at the corresponding observing location and local time will be presented later on. It can be observed in Fig. 4.6, that strong variability of the temperature is present at the high pressure level (100 mbar) in the middle latitudes between 45°S and 70°S. Whereas in the lower pressure levels at 12.5 mbar, the temperature increases towards the pole, but an isothermal behavior during the whole night is observed for each latitude.

A newly developed retrieval technique by *Haus et al.* [140] derives temperature profiles from VIRTIS measurements in a self-consistent way in dependence on the cloud parameters, i.e. the cloud top where the atmosphere gets opaque for IR radiation. Their technique underlines the possibility of cloud top altimetry by investigation of continuum radiation. They have found that the cloud top has a strong variability with latitude and local time [141].

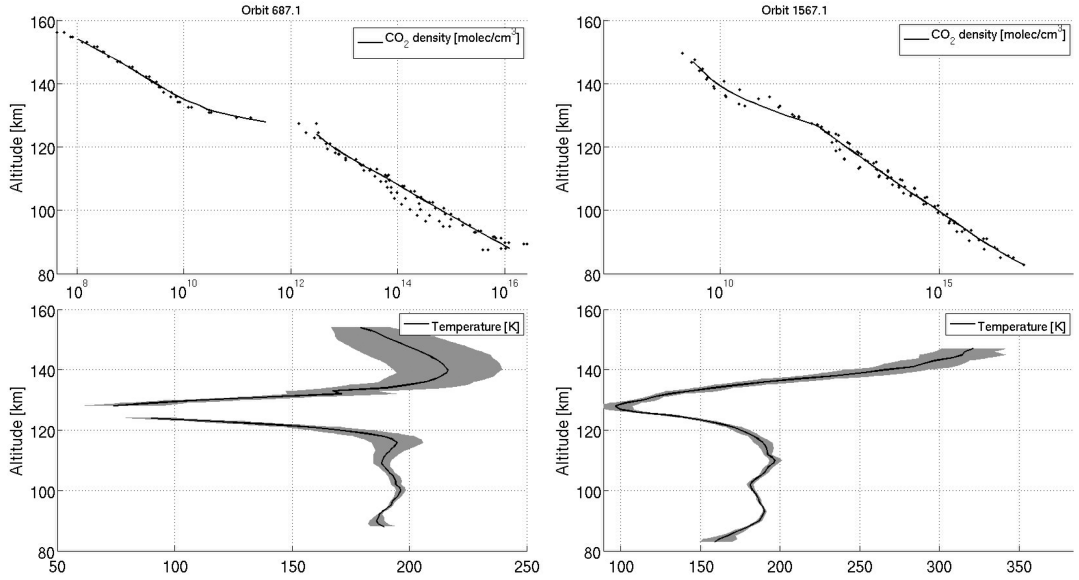

Figure 4.7: *Example of two sets of profiles: (left) a North polar measurement and (right) an equatorial measurement. [. . .] (top) In the CO_2 density panels, the points are the retrieved individual density values, and the black line is the averaged profile. The error ranges between 1 and 5%. (bottom) In the temperature panels, the gray envelope is the error on the temperature. Typical temperature error values are 1 to 20 K, from Mahieux et al. [142].*

SPICAV/SOIR

The Solar Occultation in the InfraRed instrument is one of three spectrometers which are accumulated into the French SPICAV (Spectrospcopy for the Investigation of the characteristics of the atmosphere of Venus) receiver. The SOIR spectrometer is a solar occultation IR spectrometer operating in the near-IR spectral region between 2.2–4.3 µm. The spectral resolution of the instrument is with $\frac{\nu}{\Delta\nu} \geq 1.5\times10^4$ the highest of any instrument on board of VEX. The main scientific objective was the determination of mixing ratios of water and deuterated water in the atmosphere [143]. Additionally, the thermal properties and composition of the neutral atmosphere can be derived iteratively from the rotational structure of the fully resolved CO_2 absorption bands [134]. With SOIR, the CO_2 density and temperature can be retrieved between 70 km and 170 km altitude. Since the receiver utilizes the solar occultation technique, observations can only be performed at the terminator. The slit of SOIR has a rectangular shape with a spatial viewing angle of 30 arcmin. The apparent size of the sun at Venus' orbit is $\sim$44 arcmin, so that the slit remains within the solar apparent dimension [142].

Temperature retrieval with SOIR requires good knowledge of the CO_2 density profile that is deduced simultaneously. To derive the CO_2 densities, however, a pT-profile has to be assumed as initial boundary condition. These steps are then repeated iteratively until convergence between the model and the data is reached [134, 142]. In addition, the profiles are grouped in five latitude zones, which are chosen to be statistically meaningful. The mean and standard values of the atmospheric parameters, i.e. temperature, are then computed. This way, zonally averaged, altitude dependent VAST (Venus Atmosphere from SOIR measurements at the Terminator) profiles are created [142]. An example of a retrieved VAST density and temperature profiles is given in Fig. 4.7.

4.1.4 Ground-based Observations

Ground-based measurements of temperatures in the Venus' mesosphere are most commonly conducted by observing carbon monoxide (CO) transitions in the sub-mm wavelength range [111, 144–146]. Also investigation of O_2 airglow can provide thermal information of Venus' nightside [147, 148]. The probing altitudes are displayed in Fig. 4.3, together with the space instruments on board of VEX. In the following, the two ground-based observing techniques are introduced.

Sub-mm Observations

An important tracer in Venus' atmosphere is carbon monoxide. The first CO transition in the microwave spectral range at 115 GHz has been detected in 1976 [149]. In recent years, ground-based observations of the rotational transition of the ^{12}CO and ^{13}CO isotopes have been conducted extensively by *Clancy et al.* [111, 146, 150] and *Rengel et al.* [144] [145]. Sub-mm observations are commonly performed using heterodyne receivers with a spectral bandwidth, sufficient to resolve the two transitions simultaneously. The thermal and structural properties of the mesosphere between 60 and 120 km altitude can be probed with this technique. For thermal, dynamical and compositional analysis, a spectral convolution between the spectra of two isotopes is analyzed. Since the observation of the ^{12}CO and ^{13}CO isotopes is performed simultaneously, the possibility to precisely model the radiative transfer through the atmosphere exists. This allows a self-consistent model-data spectral line comparison [146]. For fitting the model to the lines, an optimal estimation method is applied, similar to the algorithm for infrared heterodyne as described before in Chap. 3. An a-priori guess has to be introduced to the routine as initial boundary condition. The altitude resolution of sub-mm observations is approximately 2 km. The SNR is much higher, compared to IR heterodyne spectroscopy.

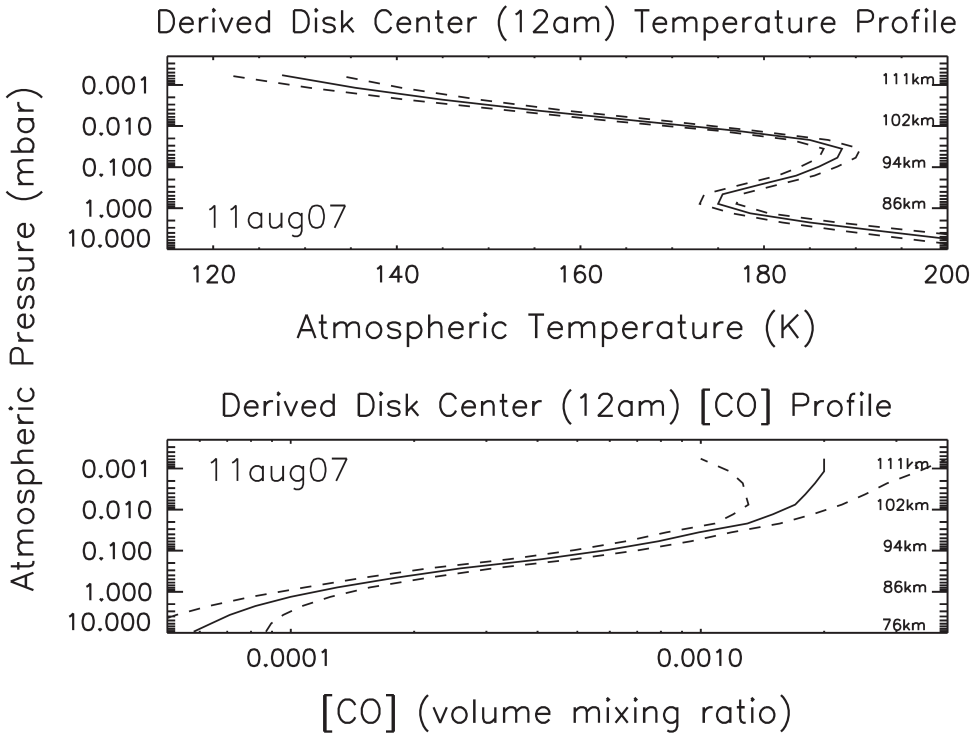

Figure 4.8: *Retrieved temperature (top panel) and CO volume mixing (lower panel) profiles, associated with the sub-mm radiative transfer analysis from observations on August 11, 2007 at the center of the apparent disk of ^{12}CO and ^{13}CO line absorptions. The dashed line envelopes indicate 2σ precision limits, from Clancy et al. [146].*

However, a major drawback of observations at few hundred GHz is the low spatial resolution. Since, the optics cannot be assumed as simple rays at these wavelengths, the Gaussian optic has to be taken into account. There, the divergence of the beam is anti-proportionally depending on the wavelength of the radiation. Besides, the FoV is depending on the dish size of the telescope and is approximately of one magnitude larger then the FoV for IR observations. Additionally, sub-mm, mm or radio heterodyne receivers are much more sensitive to the ambient weather conditions, i.e. humidity and vaporised water in the air. Of course, these receiver provide a coherent detection as well and scattered light is not affecting the noise contribution, but the temperature of the transition line, called antenna temperature in Eq. (2.6), contributes to the total performance of the receiver, the system temperature T_{sys}.

Clancy et al. have performed lots of observations since 2001 using the Mauna Kea based JCMT (James Clerk Maxwell Telescope). In particular, a global mapping of

the Venusian nightside disk has been conducted during each inferior conjunction between 2001 and 2007 [146]. The data was acquired using JCMT's sub-mm *B*-band receivers for detecting the $J = 3 \rightarrow 2$ transition of ^{12}CO at a frequency of ~ 345 GHz and of ^{12}CO at ~ 330 GHz. The system temperature, T_{sys}, was typically between ~ 200–1000 K with a quantum limit of $T_{ql} = 16.6$ K and the FoV at these frequencies was ~ 14 arcsec. Consequently, a global mapping consists of 4–5 beam elements along the equator or CML. As an example, the retrieved temperature and CO volume mixing ratio profiles from one sub-mm nightside observations at the JCMT is shown in Fig. 4.8. The pT-profile in the top graph is plotted for an altitude between~ 80–115 km. The retrieved temperatures are roughly between 200 K and 175 K for altitudes up to 86 km, before an inversion layer and rapid cooling appears above.

The German group from the Max-Planck Institute (MPI) for Solar System Research usually uses the Heinrich-Hertz Submillimeter Telescope (HHSMT) at the summit of Mount Graham, AZ, USA. The telescope's location is elevated 3178 m above sea-level and its primary dish is 10 m across. A detailed comparison between the data from *Rengel et al.* will be discussed later on in Subsec. 4.4.2. They observed, amongst others, the $J = 2 \rightarrow 1$ transition, at frequencies of ~ 230 GHz for ^{12}CO and ~ 220 GHz for ^{13}CO.

O_2-Airglow

Ground-based observations of airglow phenomena in the Venusian nightside atmosphere have been investigated for the O_2 near-IR emission at 1.27 µm since the mid 1970s. *Connes et al.* [151] have found, that the near-IR emission is roughly 1,000 times brighter than the previously discovered visible O_2-airglow. It is believed, that oxygen atoms are created by UV photolysis of CO_2 in the dayside atmosphere and then rapidly transported towards the ASP, where the atoms recombine to molecular oxygen under emission of radiation. The transmission path is in an altitude of ~ 120 km, driven by the SS-AS flow dominated circulation cell. Thus, the particles are accelerated on the sunlit and decelerated on the dark hemisphere. The recombination of the atomic particles does not happen exactly at the ASP, but is shifted slightly towards the dawn terminator [152]. The recombined molecules are excited and emit the excess energy via radiation in downwelling [153]. The altitude region where O_2-airglow occurs is assumed to be between 90–100 km. After nocturnal recombination, the molecules are forced on their way back to the sunlit side of the plant, where they combine with CO to CO_2, completing the cycle.

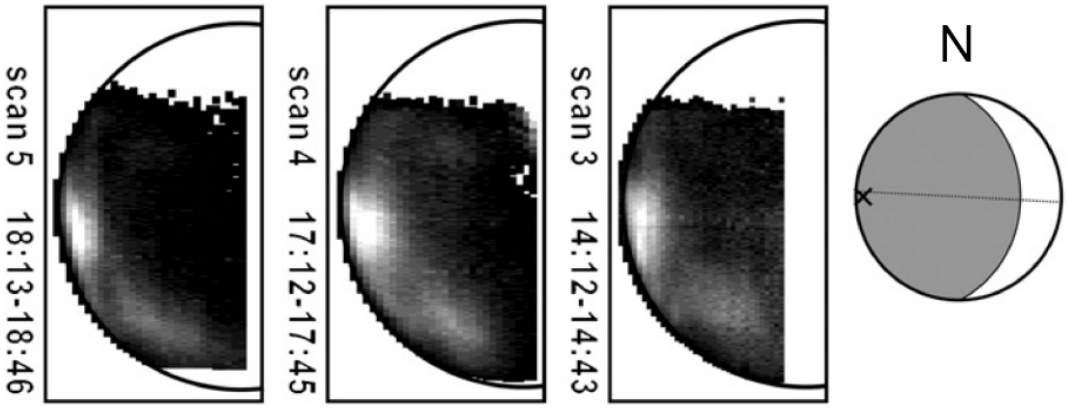

Figure 4.9: *Distribution of the airglow intensity on July 14, 2007 at* IRTF *for 3 different measurements with an integration time of* ~ 30 *min, from Ohtsuki et al. [154]. The orientation of Venus is indicate on the right hand side.*

Rotational temperatures can be recalculated from the observed intensity of the transitions in the emitting layer. Commonly, a spectral distinction between the P, Q and R-branch of the ro-vibrational band can be made with sufficiently high spectral resolution of $\frac{\nu}{\triangle\nu} \approx 1000$. However, a vertical resolution cannot be achieved with airglow observations. Typical O_2-airglow temperatures vary between 175–193 K, yielding a fitting uncertainty of 40–70 K. The emission in the corresponding altitude region for the equatorial latitudes shows a strong diurnal thermal and spatial variability within hours [152] but is strongly enhanced around the ASP [154]. The advantage of airglow measurements is the possibility of direct temperature retrieval from the line intensity. A global mapping and investigations of latitudinal or longitudinal variations performed by *Ohtsuki et al.* [154] can be found in Fig. 4.9. The figure shows the variability of the emission intensity on the Venusian nightside for three measurements in July 2007.

O_2-airglow measurements have also been performed from space, using the VEX VIRTIS-M channel. These observations are the most reliable source for the latitudinal morphology of the emission. In addition, further airglow measurements, especially for the NO recombination UV emission of nitrogen and oxygen in ~ 115 km altitude, have been performed and analyzed [155], but will not be further considered, since the altitude exceeds the probing region for IR heterodyne observations.

4.1.5 General Circulation Models

General circulation models (GCMs) for Venus' atmosphere are still rudimentary. The first model for Venus' thermal properties in the lower and middle atmosphere was developed in 1985 [110] as the Venus International Reference Atmosphere (VIRA) [156] and updated in 1997 [157]. The model is based on the in-situ measurements performed by the PV lander [158]. More recent models addressing the mesosphere were developed in the past years, laying stronger emphasis on simulating the dynamical behavior of clouds [159–161]. These models, however, assume heating rates which are inconsistent with observation [162]. The most realistic attempt to include the radiative transfer was achieved by an analytical approach by *Lebonnois et al.* [163].

Venus International Reference Atmosphere

The Venus International Reference Atmosphere was the first attempt to model Venus' lower and middle atmosphere with small uncertainties up to an altitude of $\sim 100\,\mathrm{km}$. The model accumulates various data sets from the early space missions to Venus, such as PVO and the Venera missions [110]. It relies on the data provided by the entry probes to predict the thermal structure of the deep atmosphere below 40 km. The measurements of the Venera probes showed a highly variable deep atmosphere with thermal fluctuations of 30 K, whereas the four PVO landers have detected deviations of only 10 K. These differences origin in the different latitudes and local times of the entry probes descents. However, a constant temperature lapse rate was found and implemented into the VIRA model, thus assuming static stability for the troposphere. For the middle atmosphere, data was also collected by using radio occultation technique. This augmentation of available data made it possible to investigate the latitudinal behavior of the thermal properties. The VIRA model can thus predict the pT-profile for the lower atmosphere for the day- and the nightside for 5 different latitudinal ranges 0–30°, 30–45°, 45–60°, 60–75° and 75–90°. However, the profiles are assumed to be equal on the norther and southern hemisphere and the spatial resolution is rather poor. The model was updated 12 years after its first publication, including the latest results of ground- and space-based observations. The most important contribution to update the thermal profiles was provided by the VEGA 2 entry probes, by IR sounding of Venera 15 and the Galileo mission and further radio occultation measurements (Venera 15, 16, PVO and Magellan) [157]. Nevertheless, despite the fact that the model is outdated and knowledge on the Venusian tropo- and mesosphere has

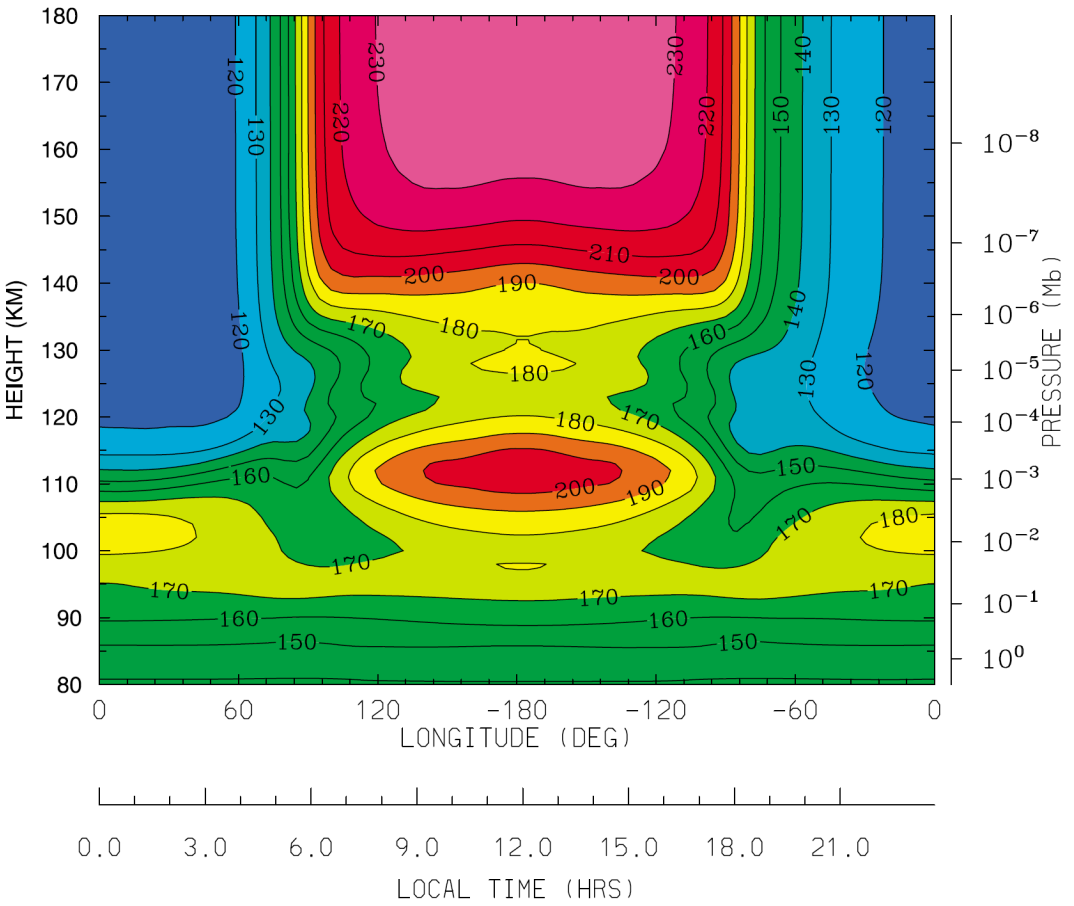

Figure 4.10: *Global temperature map from* VTGCM *simulations for the "mean"* VEX *case for observing geometry at 2.5°N, from Brecht et al. [164].*

increased significantly in the era of VEX, VIRA is still the most common model, utilized to compare observations and models to a global expectation value. It is helpful to both, observers and modelers, for a first order classification of their results.

NCAR VTGCM

The National Center for Atmospheric Research (NCAR) has developed one of the first 3-dimensional (3D) hydrodynamic models for the structure and circulation of the Venusian thermosphere in the late 1980s [165]. The Venus Thermosphere General Circulation Model (VTGCM) is based on a previously well established circulation model for Earth which has been modified and merged with their former

2D model for Venus. Since then, the VTGCM has been constantly modified and updated. The latest version is now capable of modeling both hemispheres, the northern and the southern, separately, instead of mirroring one to the other [164]. The model provides several important parameters for the neutral atmosphere between ∼70–200 km at the nightside and 70–300 km at the dayside. The VTGCM covers the important transition region between the two dominant circulation patterns, the RZS and the SS-AS flow. It was especially designed for modeling the dynamics in the upper mesosphere and thermosphere, but can also predict the thermodynamic behavior in these altitudes. Recent efforts have been made to successfully implement the O_2 and NO airglow effects and to sophisticatedly simulate the nightside temperature distributions as they are observed by the various VEX instruments.

In Fig. 4.10 a global map of the Venusian thermospheric temperatures from VTGCM calculations is displayed for an exemplary observing geometry at 2.5°N. The VTGCM was adapted such, that the boundary conditions of the model, i.e. solar irradiation, matched to the mean observing conditions during VEX orbits. On the nightside hemisphere, between LT ∼21:00 and 04:00, a constant, cold temperature of ∼120 K for altitudes above ∼120 km can be observed. It should be pointed out, that for lower altitudes, which are commensurate to IR heterodyne observations, the upper mesosphere is assumed to be isothermal along the isobars between 1–0.1 hPa (mbar). On the dayside, around noon, a hot spot is predicted at ∼112 km altitude, which must be understood as an inversion layer, since the temperatures cool down with altitude up to ∼140 km, before they increase again into the warm dayside upper thermosphere. The warm layer is created by near-IR (mostly 4.3 µm) heating.

LMD GCM

The GCM developed by the Laboratoire de Météorologie Dynamique (LMD) has been created to model the Venusian atmosphere from the surface to ∼100 km altitude. This three-dimensional model is based on a GCM for Earth, also developed at the LMD. The LMD-GCM includes topography, diurnal cycle, dependence on specific heat and temperature and a radiative transfer module for infrared radiation [163]. The model allows the computation of the temperature field, which is globally consistent to observations. However, recent analysis of the modeled temperature field show a deviation to space-based observations in high altitudes (∼65–100 km) of roughly 10–20 K [166].

Fig. 4.11 shows an example of a computed temperature profile through Venus' atmosphere, averaged over all latitudes and longitudes. The model is especially

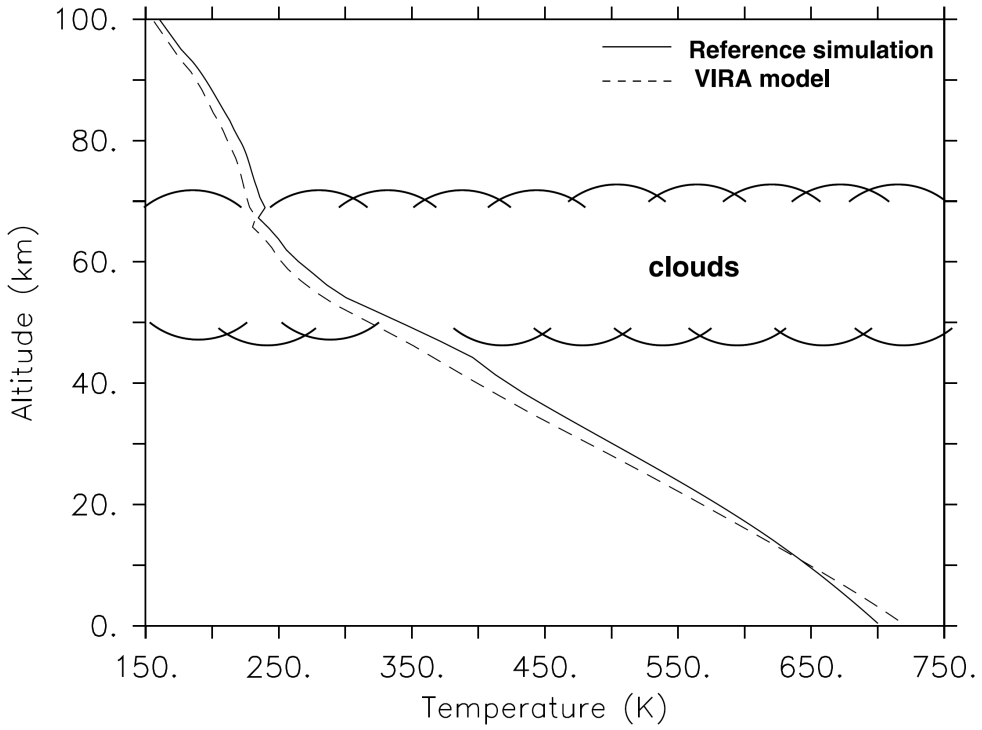

Figure 4.11: *Vertical temperature profile (solid line) computed with the* LMD-GCM. *The result is averaged over longitudes, latitudes and 2 Venus days of the simulation, from Lebonnois et al. [163]. It is compared to the reference* VIRA *profile.*

useful to predict the climatic and atmospheric conditions of Venus. A first simulation for a full radiative transfer scheme was run for 350 Venusian days (111 Earth years) and a convergence of all atmospheric parameters towards a steady state was achieved [163].

4.2 Observing Campaigns

The spectrometer THIS and HIPWAC were mounted on two different telescopes during two campaigns in 2012. THIS was installed at the McMath-Pierce Solar Telescope at Kitt Peak, Arizona, USA, whereas HIPWAC was used for observations at the NASA Infrared Telescope Facility on Mauna Kea, Hawaii, USA. An overview of the observing locations and conditions can be found in Tab. 4.3. Detailed information on the specific observational parameters during the observing days can be found in Tab. C.1 in Appendix C. For each campaign the $^{12}C^{16}O_2$ P(12) transition in the mid-IR N-band at $\bar{\nu} = 951.19226\,\mathrm{cm}^{-1}$ was probed. The relative Doppler shift between Earth and Venus during each run was sufficient to shift the observed line away from the core of the terrestrial CO_2 absorption (comp. Tab. 4.5).

Camp.	Instrument	Telescope & Location	FoV	Altitude	Date
A	THIS	McMath-Pierce, Kitt Peak, AZ	1.7”	2096 m	March 20 - 29 2012
B	HIPWAC	IRTF, Mauna Kea, HI	0.9”	4205 m	May 18 - 21 2012

Table 4.3: *Overview of the observing campaigns A and B.*

4.2.1 Campaign A - March 2012

Observing campaign A took place between March 20$^{\mathrm{th}}$–29$^{\mathrm{th}}$ 2012 UT. THIS was mounted to the McMath on Kitt Peak. The Kitt Peak Observatory is located at an altitude of 2096 m above sea level. Solar telescopes are highly feasible for ground-based observations of Venus, since they do not have any sun avoidance requirements. Heterodyne spectroscopy, as a coherent detection method, allows observations during the day, since no stray-light is collected within the field of view. The focusing mirror's diameter of the McMath is 1.57 m [167], which corresponds to a diffraction limited FoV of 1.7 arcsec.

Venus was at maximum western elongation with an increasing angular diameter from 21.1 arcsec to 24.6 arcsec. The illuminated fraction of the apparent disk decreased from 56% to 49%.

Two different locations along the nightside equator were targeted. One observing position at 30°W of the terminator (corresponding LT on Venus 20:00, from here

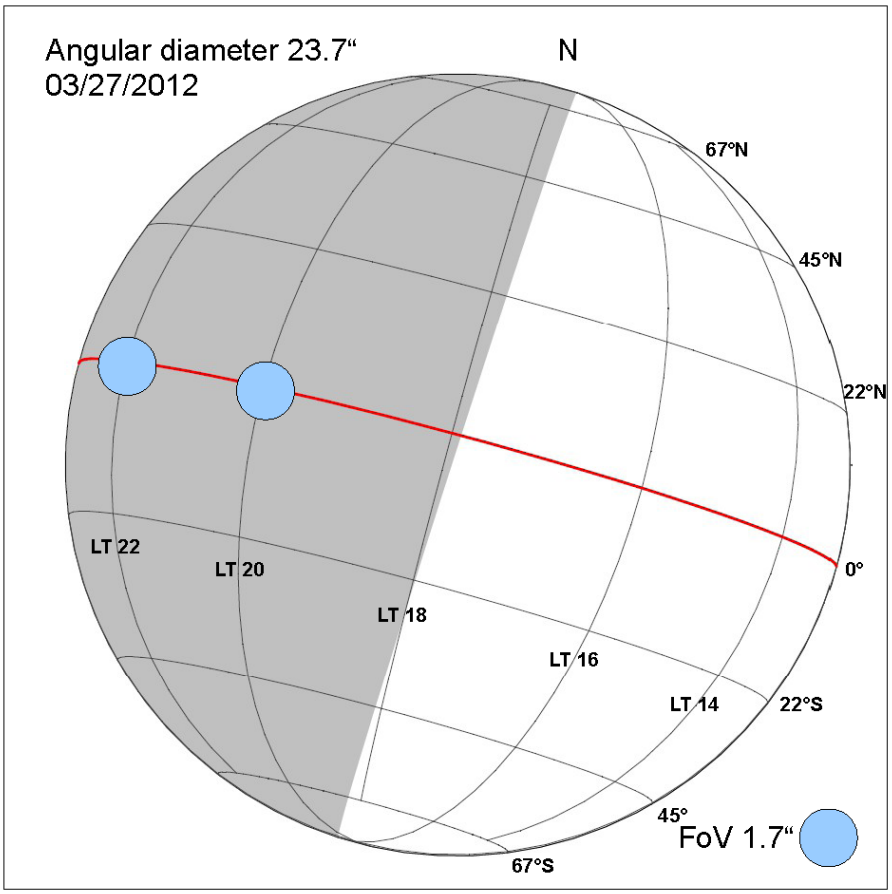

Figure 4.12: *Observing geometry of Venus for campaign A in March 2012 at the McMath on Kitt Peak. The blue circle represents the diffraction limited field of view true to scale with the angular diameter of the apparent disk. The angular diameter of the apparent disk varied between 21.1” and 24.6” and the illuminated fraction between 56% and 49% within the time of observation. For orientation, the LT and the latitudes are indicated for the geometry on March 27.*

on called EQLT20) and the other at 60°W of the terminator (LT 22:00, called EQNLT22). In Fig. 4.12 the observing geometry and the targeted locations, represented by the FoV, are displayed. The integration time was 154 min on source at EQLT20, acquired between March 20$^{\text{th}}$–23$^{\text{rd}}$ and 480 min at EQLT22 acquired between March 22$^{\text{nd}}$–29$^{\text{th}}$. In order to remain at a constant local time, the observing positions were tracked and the longitudinal positions in planet based coordinates varied from $\sim$158°W to $\sim$168°W for LT 20:00 and from $\sim$135°W to $\sim$187°W for LT 22:00, respectively.

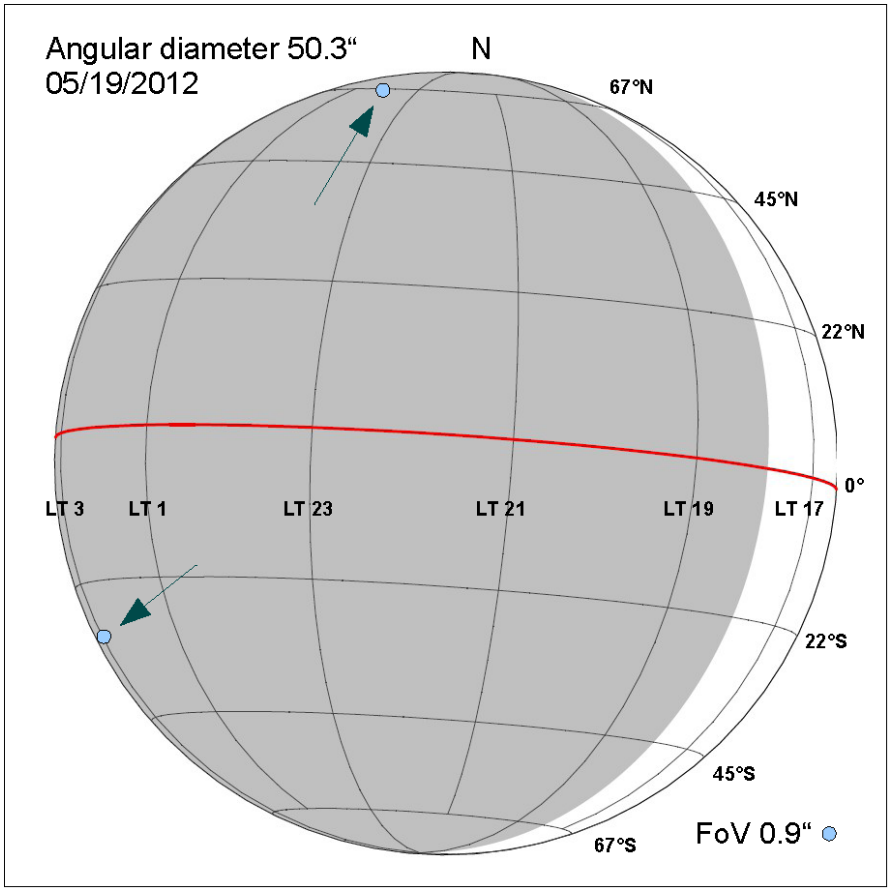

Figure 4.13: *Observing geometry of Venus for campaign B in May 2012 at the* IRTF *on Mauna Kea. The blue circle represents the diffraction limited field of view true to scale with the angular diameter of the apparent disk. The angular diameter of the apparent disk varied between 49.2” and 51.4” and the illuminated fraction between 11% and 7%. For orientation, the LT and the latitudes are indicated for the geometry on May 19.*

4.2.2 Campaign B - May 2012

Observing campaign B, between May 18$^{\text{th}}$ and May 22$^{\text{nd}}$ UT, was with HIPWAC mounted on the IRTF on Mauna Kea. The telescope is located at an altitude of 4205 m above sea level. The IRTF is a Cassegrain telescope with a 3 m primary mirror. The mirror size corresponds to a FoV of 0.9 arcsec.

With Venus approaching inferior conjunction, its angular diameter increased from $\sim$ 49 arcsec to $\sim$ 51 arcsec. The illuminated crescent of the apparent disk decreased from 11% to 7%.

Two different locations on the nightside were targeted. One observing position at 67°N and anti-solar point (ASP) longitude (67NLT0) and the other at 33°S at the dark limb (33SDL). In Fig. 4.13 the observing geometry and the targeted locations, represented by the FoV, are given in relative diameters. The integration time was 96 min at 67NLT0 acquired on May 18nd–21st UT and 160 min on source at 33SDL, acquired between May 19th–22nd UT. To remain at the dark limb, the observing position was kept constant at 33°S and 85°W of the sub-observer point, which corresponds to an only slightly varying longitude of $\sim 1.5°$ in planet based coordinates around $\sim 235.5°$W. For 33SDL, the planetary LT was not constant and changed from 03:20 to 03:26. For the ASP (LT0h) longitude, the observing position at 67°N was tracked and the longitudinal position in planet based coordinates varied from $\sim 279°$W to $\sim 291°$W.

Camp.	Ang. Diameter (% illuminated)	Position	Latitude	Longitude	Venus Local Time
A	21.1" - 24.6" (56% - 49%)	EQLT20	0°N	158°∼168°W	20:00
		EQLT22	0°N	135°∼187°W	22:00
B	49.2" - 51.4" (11% - 7%)	67NLT0	67°N	279°∼291°W	00:00
		33SDL	33°S	∼235.5°W	03:20 - 03:26

Table 4.4: *Overview of the observing geometry during the observing campaigns in 2012.*

4.3 IR Heterodyne: Data Analysis & Results

Ground-based observations of Venus' mesosphere were accomplished using infrared heterodyne spectroscopy. IR heterodyne instruments have proven to be powerful tools to investigate the dynamical and thermal properties of terrestrial planet atmospheres for many years [29–31, 40, 49, 70, 168]. The ultra high resolving power of $\frac{\nu}{\Delta\nu} \geq 10^7$ allows the analysis of single molecular transition features in the mid-IR wavelength range. Measurements of temperatures in the thermosphere can be derived from the widths of narrow CO_2 non-LTE emission lines originating near the 1 µbar pressure level [33, 35]. However, these solar induced non-LTE emission lines occur only on the sunlit side of the planet and cannot provide altitude resolved profiling of temperatures down to the cloud tops. Nightside profiles down to the cloud tops can only be achieved by analyzing the CO_2 absorption lines in the mid-IR N-band. Such absorption features, without superimposed emission lines, are present on the Venusian nightside. Ground-based observations can also provide long term coverage of an arbitrary position on the visible disk of the planet.

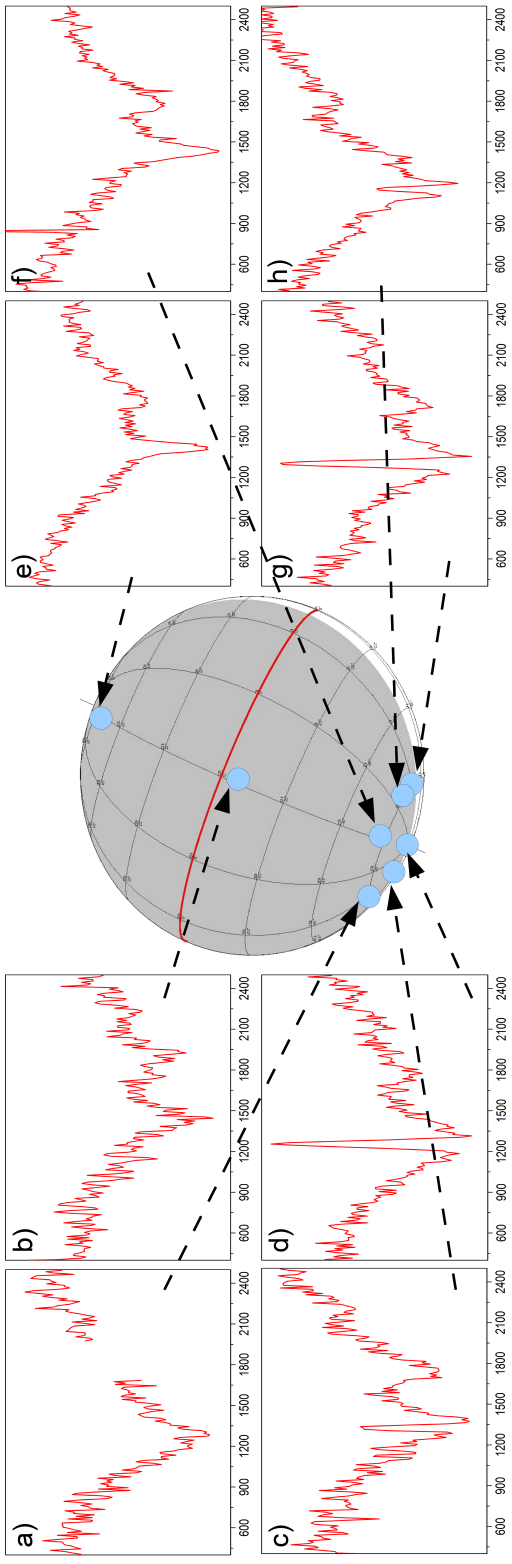

Figure 4.14: *Spectra obtained during several observing campaigns in 2009. Plotted is the intensity in a.u. vs the IF in MHz. The blue circles indicate the FoV during observations. The spectra are not used for further analysis and temperature retrieval. The feature at ∼ 1700 MHz in all spectra is due to an impedance mismatch on the detector. It can be observed, that the non-LTE emission feature immediately occurs when the beam slices the sunlit crescent. The non-LTE emission line can be observed in all four spectra at the bottom [c), d), g), h)].*

In Fig. 4.14, a variety of observed spectra are shown. These data sets were obtained during various observing runs in 2009 using THIS. Some of the spectra are very noisy. All spectra show a feature at around 1700 MHz. This is due to an impedance mismatching on the detector during observations. Therefore, these data sets are useless for analysis of the broadening and the temperature retrieval. However, the set of spectra can demonstrate how rapidly the non-LTE emission feature evolves as soon as the beam slices the sunlit crescent and may serve as an preliminary indication of the global variability of the CO_2 absorption features in the Venusian nightside hemisphere. For deduction of thermal profiles, a careful investigation of the full line shape has to be performed. Hence, the new spectra, acquired during the observing campaigns presented in Sec. 4.2, are used to reveal the thermal properties of Venus. In the following, the measurements are presented in detail.

4.3.1 Measured Spectra

Due to the ultra high frequency resolution, the observed CO_2 ro-vibrational line shape on Venus is well sampled, as is the wing of the corresponding telluric component. In our bandpass B only a single line is noted. The neighboring CO_2 transitions are beyond a spectral distance of $\sim 16 \cdot B$ and line mixing effects are minimal.

In Fig. 4.15–4.18, the measured data (red) is displayed along with the output model of the IFR (blue) and their residuals (green). Each spectrum was rescaled to 10 MHz resolution for display. The original spectra with the full resolution of 1 MHz can be found in Appendix C. The results of the newly developed inverse fitting procedure will be presented in the following section. The data was acquired during several observing days and co-added to increase the SNR. Prior to co-addition, the individual IF spectra were frequency corrected, taking the varying relative Doppler shift between Venus and Earth into account. Thus, the IF center frequency $\nu_{\mathrm{IF,c}}$ of the absorption line in the final heterodyne spectrum corresponds to the frequency of the first day of observation.

To model the spectrum, the terrestrial transmittance has to be taken into account as described earlier in Subsec. 3.1.2. Thus, for campaign A, the mid-latitude winter atmospheric model [169] and for campaign B the tropical standard model was introduced into the GENLN2 code. The resulting IR heterodyne model spectra were calculated with CODAT, using the retrieved pT-profile as input profile. For comparison, it is plotted along with the data in Fig. 4.15–Fig. 4.18. Also the residuals between the data and the model spectra are provided. The RMS is an

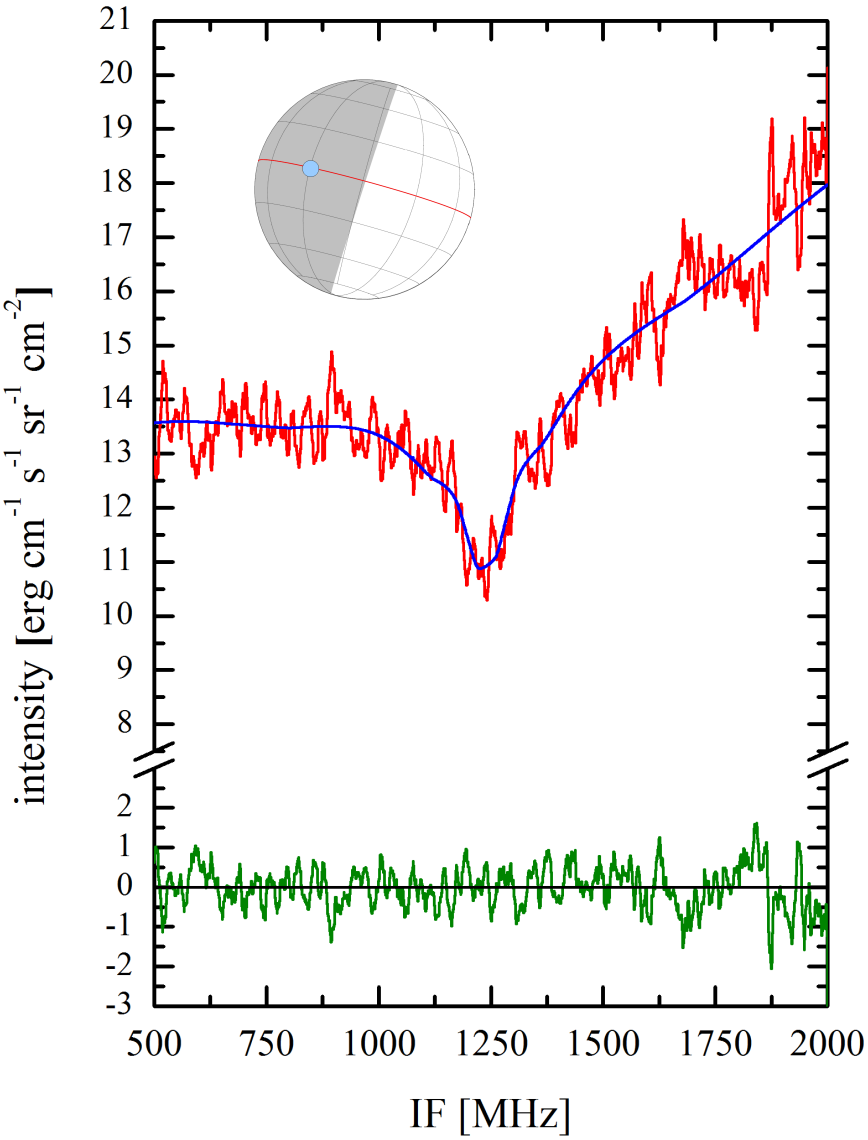

Figure 4.15: *Measured Spectrum from campaign A at EQLT20: The observing geometry is displayed in the insert graphic. The data is displayed in red with a SNR of 4.3 ± 0.5, the best fit in blue and the residuals in green. The center frequency of the line is at 1245 MHz. The normalized RMS of the residuals indicates the noise amplitude. See Sec. 4.3.2 for details. The normalized RMS is 1.10 for an integration time of 154 min on source. The spectrum was rescaled to 10 MHz resolution for display. For the full resolution spectrum see Fig. C.1.*

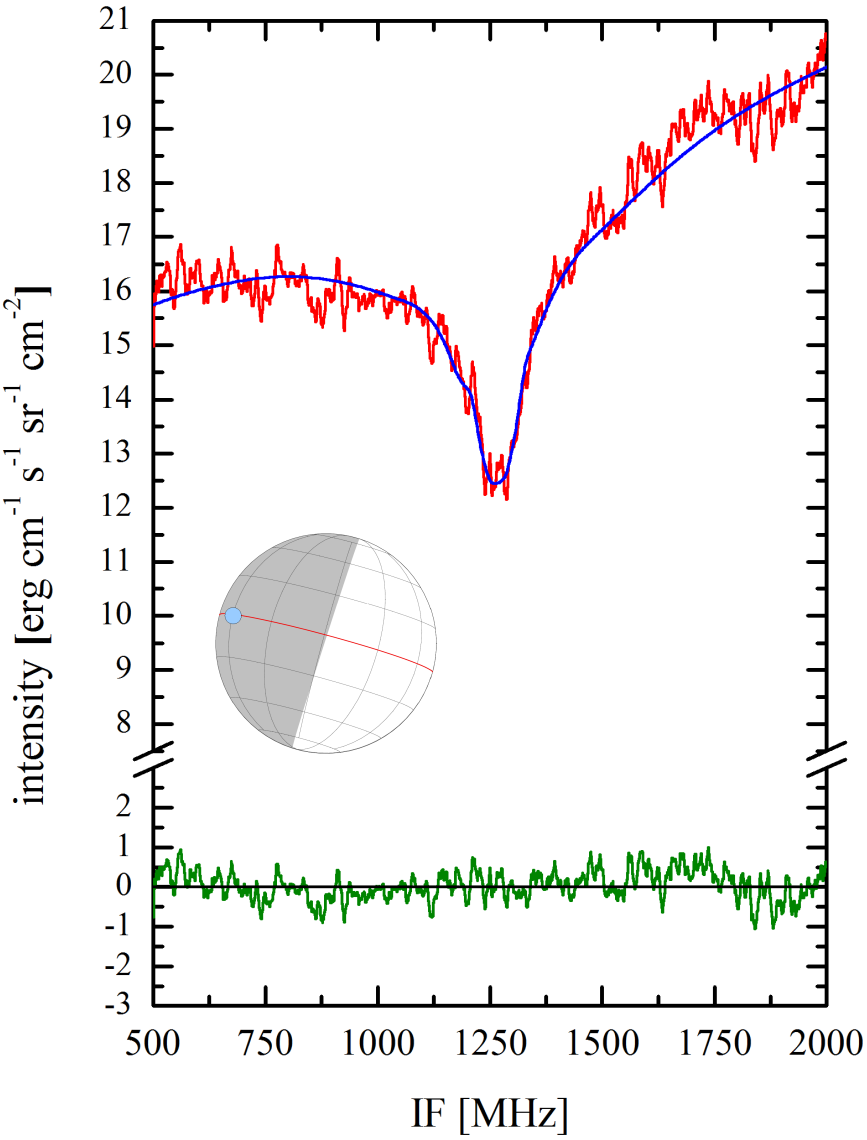

Figure 4.16: *Measured Spectrum from campaign A at EQLT22: The observing geometry is displayed in the insert graphic. The data is displayed in red with a SNR of 6.6 ± 0.5, the best fit in blue and the residuals in green. The center frequency of the line is at 1265 MHz. The normalized RMS of the residuals indicates the noise amplitude. See Sec. 4.3.2 for details. The normalized RMS is 0.79 for an integration time of 480 min on source. The spectrum was rescaled to 10 MHz resolution for display. For the full resolution spectrum see Fig. C.2.*

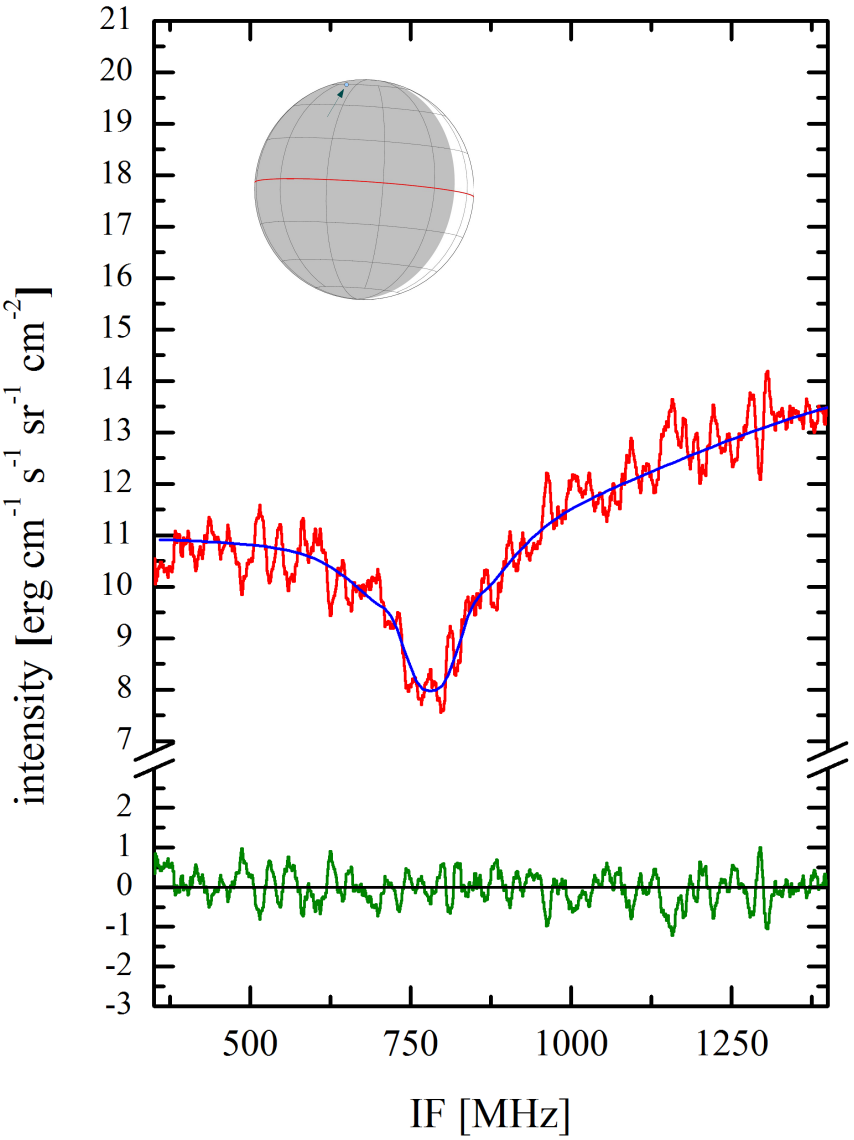

Figure 4.17: *Measured Spectrum from campaign B at 67NLT0: The observing geometry is displayed in the insert graphic. The data is displayed in red with a SNR of 4.8 ± 0.3, the best fit in blue and the residuals in green. The center frequency of the line is at 777 MHz. The normalized RMS of the residuals indicates the noise amplitude. See Sec. 4.3.2 for details. The normalized RMS is 0.79 for an integration time of 96 min on source. The spectrum was rescaled to 10 MHz resolution for display. For the full resolution spectrum see Fig. C.3.*

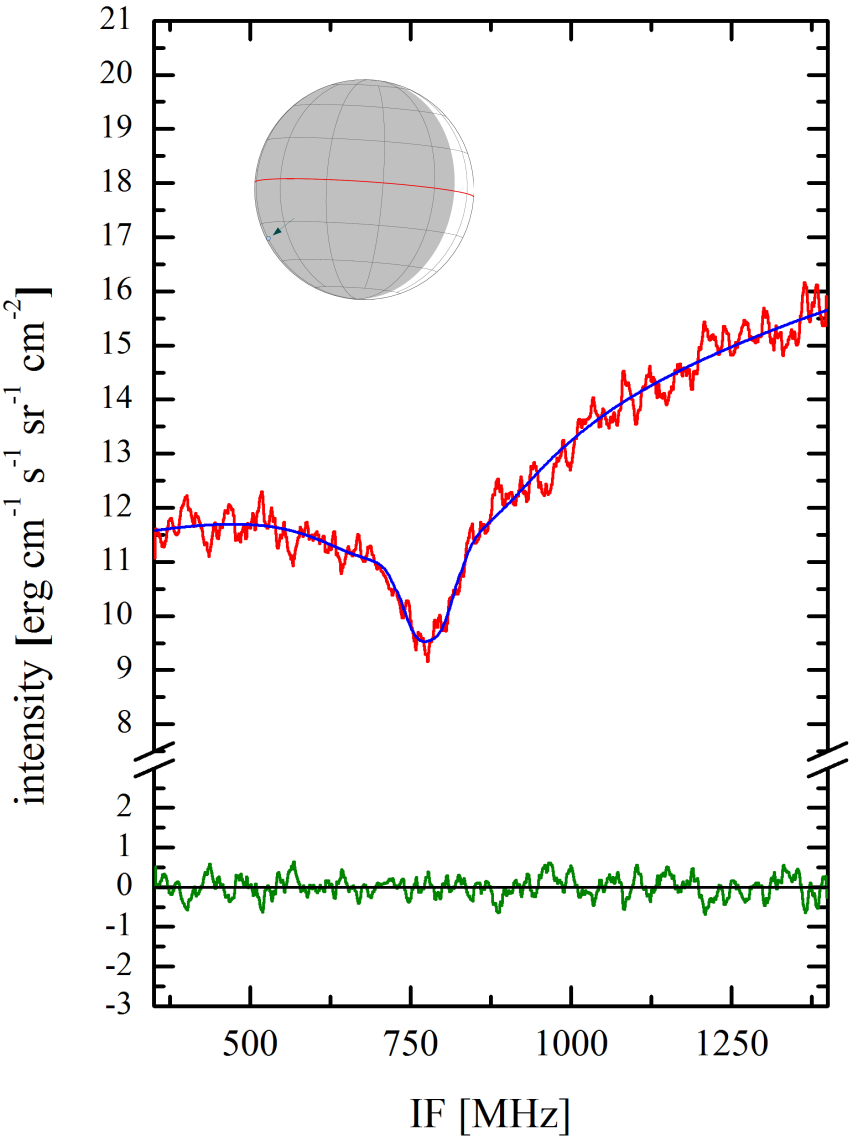

Figure 4.18: *Measured Spectrum from campaign B at 33SDL: The observing geometry is displayed in the insert graphic. The data is displayed in red with a SNR of 6.4 ± 0.2, the best fit in blue and the residuals in green. The normalized RMS of the residuals indicates the noise amplitude. See Sec. 4.3.2 for details. The center frequency of the line is at 777 MHz. The normalized RMS is 0.59 for an integration time of 160 min on source. The spectrum was rescaled to 10 MHz resolution for display. For the full resolution spectrum see Fig. C.4.*

indicator for the noise amplitude of each measurement. In the following, the RMS is normalized to $1\,\mathrm{erg\,cm^{-1}\,s^{-1}\,sr^{-1}\,cm^{-2}}$ for convenience.

During campaign A, whilst observing on position EQLT20 (Fig. 4.15), the radial velocity v_r between the approaching target and the observer changed from $13.22\,\mathrm{km\,s^{-1}}$ to $13.30\,\mathrm{km\,s^{-1}}$. This results in a variation of the relative Doppler shift of 7.61 MHz. The individual spectra were corrected to obtain a resulting line IF center frequency of 1245 MHz. The total on-source integration time was 154 min. The corresponding SNR is calculated as the ratio between the depth of the absorption line and the noise amplitude and is found to be (4.3 ± 0.5). Further analysis of the noise amplitude and the RMS will be discussed later. An overview of the spectral properties of the single measurements can be found in Tab. 4.7. On position EQLT22 (Fig. 4.16), v_r changed from $13.26\,\mathrm{km\,s^{-1}}$ to $13.40\,\mathrm{km\,s^{-1}}$ during the total on-source integration time of 480 min. The SNR of the spectrum is (6.6 ± 0.5). The corresponding relative Doppler variation is 13.32 MHz. Here, the individual spectra were corrected to a resulting line IF center frequency of 1265 MHz.

During campaign B, for 67NLT0 (Fig. 4.17) and 33SDL (Fig. 4.18), v_r decreased from $8.11\,\mathrm{km\,s^{-1}}$ to $6.83\,\mathrm{km\,s^{-1}}$, yielding a shift of the relative Doppler shift of 121.75 MHz. Individual measurements were corrected to an IF center frequency of 777 MHz. The SNR for 67NLT0 was found to be (4.8 ± 0.3) for a corresponding integration time of 96 min and (6.4 ± 0.2) for 160 min of on-source integration at 33SDL. All spectral properties are summarized in Tab. 4.5

Camp.	Position	v_r [$\mathrm{km\,s^{-1}}$]	$\nu_{\mathrm{IF,c}}$ [MHz]	τ [min]	SNR
A	EQLT20	(13.26 ± 0.04)	1245	154	(4.3 ± 0.5)
	EQLT22	(13.33 ± 0.07)	1265	480	(6.6 ± 0.5)
B	67NLT0	(7.47 ± 0.64)	777	96	(4.8 ± 0.3)
	33SDL	(7.47 ± 0.64)	777	160	(6.4 ± 0.2)

Table 4.5: *Overview of the spectral properties from the observations, including the relative velocity between Venus and Earth v_r, the IF center position of the absorption line $\nu_{\mathrm{IF,c}}$, the total on-source integration time τ and the SNR of the data.*

EQLT20			
p (hPa)	$\triangle p$ (hPa)	T (K)	$\triangle T$ (K)
0.38	0.09	174.72	6.00
1.83	0.80	189.95	6.00
4.98	1.74	198.16	7.56
13.53	3.36	206.29	9.82
36.79	4.90	226.38	10.58
107.68	10.77	240.87	9.26

EQLT22			
p (hPa)	$\triangle p$ (hPa)	T (K)	$\triangle T$ (K)
0.20	0.05	174.10	15.66
0.55	0.11	186.88	11.65
1.99	0.46	198.18	13.47
5.41	0.94	208.33	15.75
14.72	1.34	217.87	16.06
41.37	4.14	226.19	14.78

67NLT0			
p (hPa)	$\triangle p$ (hPa)	T (K)	$\triangle T$ (K)
-	-	-	-
0.20	0.05	166.19	15.48
0.55	0.11	184.62	17.34
1.99	0.46	198.58	22.80
5.41	0.94	205.90	17.46
14.72	1.34	225.39	24.63
44.77	4.47	224.72	13.96

33SDL			
p (hPa)	$\triangle p$ (hPa)	T (K)	$\triangle T$ (K)
0.07	0.03	177.34	2.45
0.25	0.06	191.23	3.24
0.69	0.13	192.24	2.24
2.49	0.62	197.62	3.28
6.77	1.17	206.07	2.93
18.39	1.67	212.39	3.51
52.48	5.25	225.37	1.49

Table 4.6: *Retrieved temperature at given pressure layers for IR-heterodyne observations on Venus.*

4.3.2 Temperature Profiles

The retrieved pT-profiles from IR heterodyne observations are shown in Fig. 4.19–4.22 for each observing position. An approximation of the corresponding altitude according to the barometric formula (comp. Eq. (3.1)) in the Venusian atmosphere is provided at the right hand y-axis of each figure. The numerical profiles are given in Tab. 4.6 for each observing position. The assumption of a range of possible background temperatures in the calculation of the pressure layers, yields a varying scale height in Eq. (3.1), leading to the uncertainties in y-direction, as it has been discussed before (comp. Sec. 3.3). The temperature uncertainties are found by deriving multiple profiles for varying initial boundary conditions for the line center position and the scale factor. The error bars represent the deviation between the minimum and maximum value that was found. For details on the uncertainty retrieval of the temperatures please refer to Sec. 3.4. Note that the profiles acquired on the equator during campaign A are smooth and monotonically decreasing with altitude, whereas the profiles derived from observations at mid- and high-latitudes during campaign B show more variations. A summary on the most important results from the retrieved profiles, such as lapse rate and high pressure boundary for each observing position is given in Tab. 4.7.

Camp.	Position	τ [min]	RMS	lapse rate [$\mathrm{K\,km^{-1}}$]	p_0 [hPa]
A	EQLT20	154	1.10	(-3.4 ± 1.3)	107.7
	EQLT22	480	0.79	(-2.2 ± 0.7)	41.4
B	67NLT0	96	0.79	(-3.0 ± 1.4)	44.8
	33SDL	160	0.59	(-1.6 ± 0.1)	52.5

Table 4.7: *Overview of the properties of the retrieved thermal profiles from the observations, including the total on-source integration time τ, the normalized RMS of the residuals between model fit and data, the retrieved maximum temperature lapse rate and the high pressure boundary p_0.*

EQLT20

The RMS for EQLT20 is 1.1. At EQLT20 (Fig. 4.19), the slope changes at around 72 km altitude. Due to the logarithmic scale, and for better comparability, the temperature lapse rate will be given in respect to the altitude in km instead of the pressure in hPa. Altitude and pressure are correlated according to the barometric formula given in Eq. (3.1). Applying a linear fit through the data, the lapse rate at EQLT20 is found to be (-3.4 ± 1.3) $\mathrm{K\,km^{-1}}$ at lower altitudes and drops to (-2.2 ± 0.7) $\mathrm{K\,km^{-1}}$ at higher altitudes. Beneath the highest pressure that could be

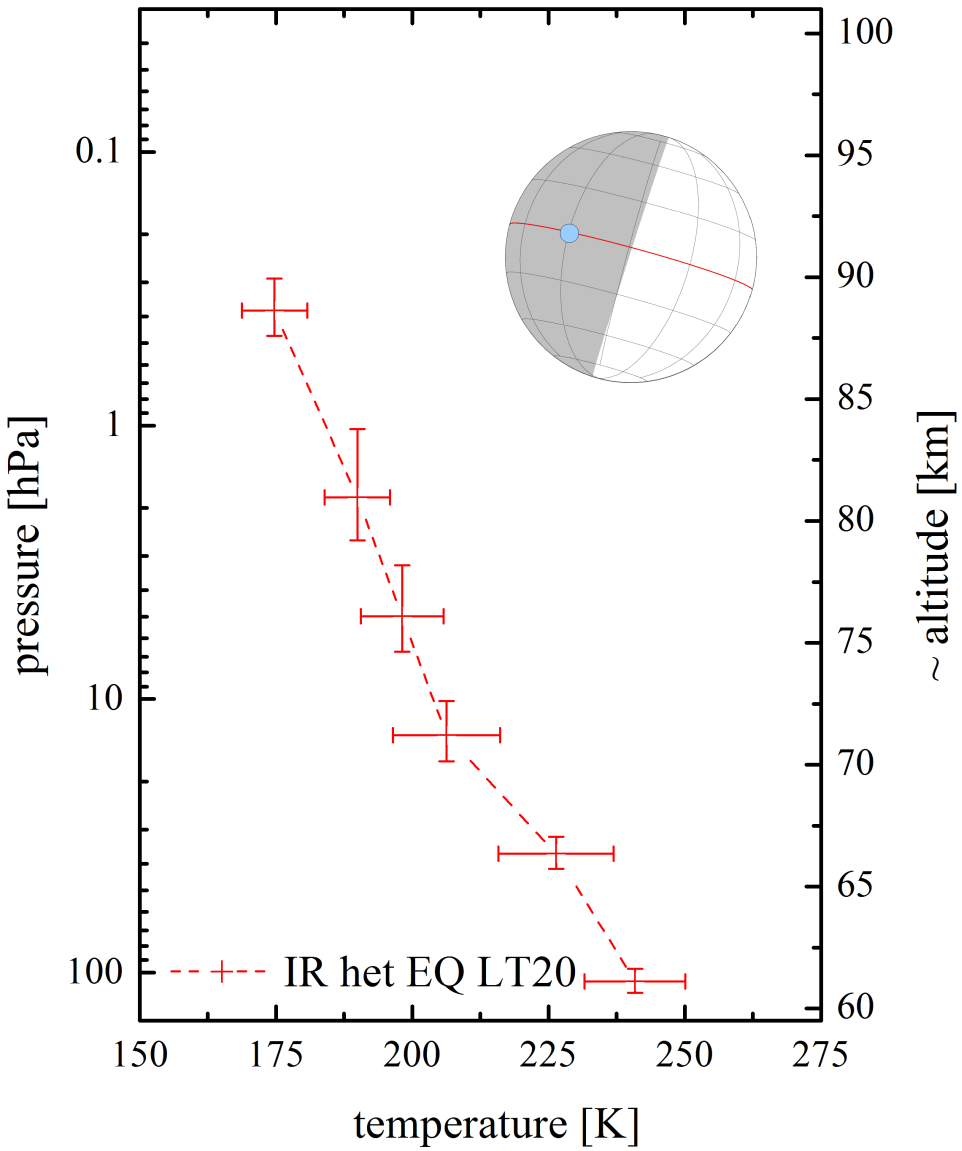

Figure 4.19: *pT-profile from campaign A at EQLT20: The observing geometry is displayed in the insert graphic. The derived temperatures (with corresponding uncertainties) in the Venusian atmosphere are displayed in red. The temperature lapse rate can be divided into two major segments. Between the highest pressure level at 107.7 hPa, where the atmosphere becomes optically thick, and 13.5 hPa it is found to be (-3.4 ± 1.3) K km^{-1}, whereas from 13.5 hPa up to 1.8 hPa is (-2.2 ± 0.7) K km^{-1}.*

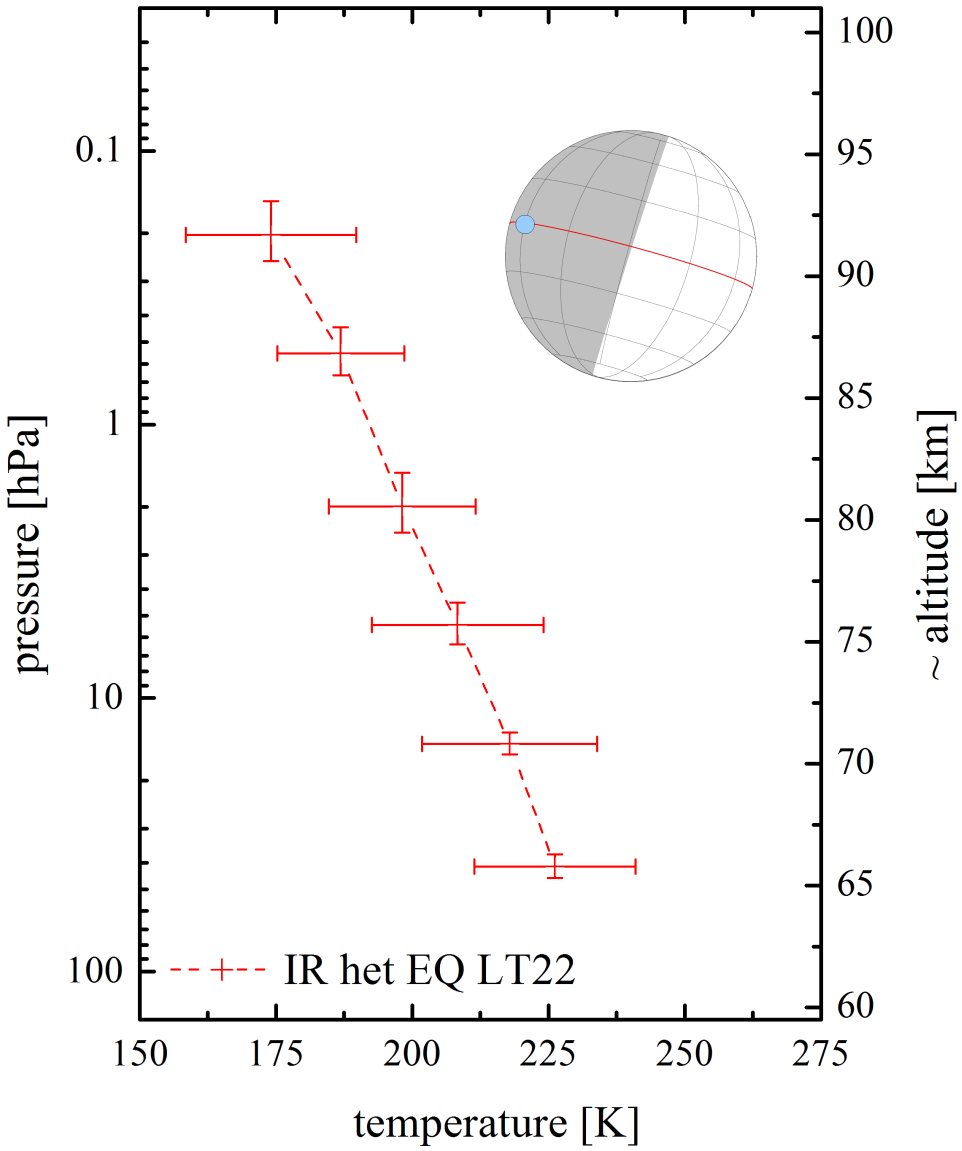

Figure 4.20: *pT-profile from campaign A at EQLT22: The observing geometry is displayed in the insert graphic. The derived temperatures (with corresponding uncertainties) in the Venusian atmosphere are displayed in red. The temperature lapse rate is almost constant with (-2.2 ± 0.7) K km^{-1}. At around 40 hPa the atmosphere gets opaque.*

probed (p_0) of 107.7 hPa, the atmosphere becomes opaque and no further information can be extracted from the data.

EQLT22

At EQLT22 (Fig. 4.20), there is a lapse rate of (-2.2 ± 0.7) K km^{-1} monotonically decreasing throughout the mesosphere. Again, the mid-latitude atmosphere model was used to simulate the terrestrial transmittance. The high pressure boundary p_0 was found to be at 41.4 hPa. For observations close to the limb, the longer ray path along the LoS through the atmosphere provokes a higher opacity contribution from the higher altitudes than for observations close to disk center. Hence, the atmosphere becomes optically thick before the cloud top is reached. Unfortunately, this cannot be avoided, because the model does not account for the curvature of the planet. The pressure layering was adapted, according to the retrieved value for p_0. The normalized RMS is 0.79 and thus, significantly smaller due to the longer integration time.

67NLT0

For the only observation at higher latitudes at 67NLT0 (Fig. 4.21), the temperature profile differs from those found at low latitudes. p_0 was found to be at 44.8 hPa, here again, due to the curvature of the planet. At the lower altitudes ($\sim$65 km to $\sim$73 km) the profile is almost isothermal, before the temperature decreases in altitude with a lapse rate of (-3.0 ± 1.4) K km^{-1}. The normalized RMS of the residuals is 0.79. The high uncertainties correspond to the broad line tip, as it can be observed in Fig. 4.17, yielding a variation of the center frequency of $> \pm 25$ MHz. The broadening can be caused by an isothermal profile at the high altitudes. However, the SNR is not high enough to extract further information.

33SDL

The temperature lapse rate at 33SDL in Fig. 4.22 is (-1.6 ± 0.1) K km^{-1} up to an altitude of $\sim$92 km. Then, a sudden decrease at high altitudes is indicated. The high pressure boundary p_0 is 52.5 hPa. The error bars are comparably small, caused by the high SNR (normalized RMS=0.56), yielding the possibility to more precisely estimate the input parameters. Also, the high SNR enables the resolution of the high altitude temperature at $\sim$97 km. However, as it was shown by the analysis of the synthetic data in Sec. 3.4.3 the top layer temperature retrieval might be offset to the true value, due to the low amount of spectral information in the line tip.

In Fig. 4.23, all four profiles which were retrieved during the two observing campaigns are plotted for comparison.

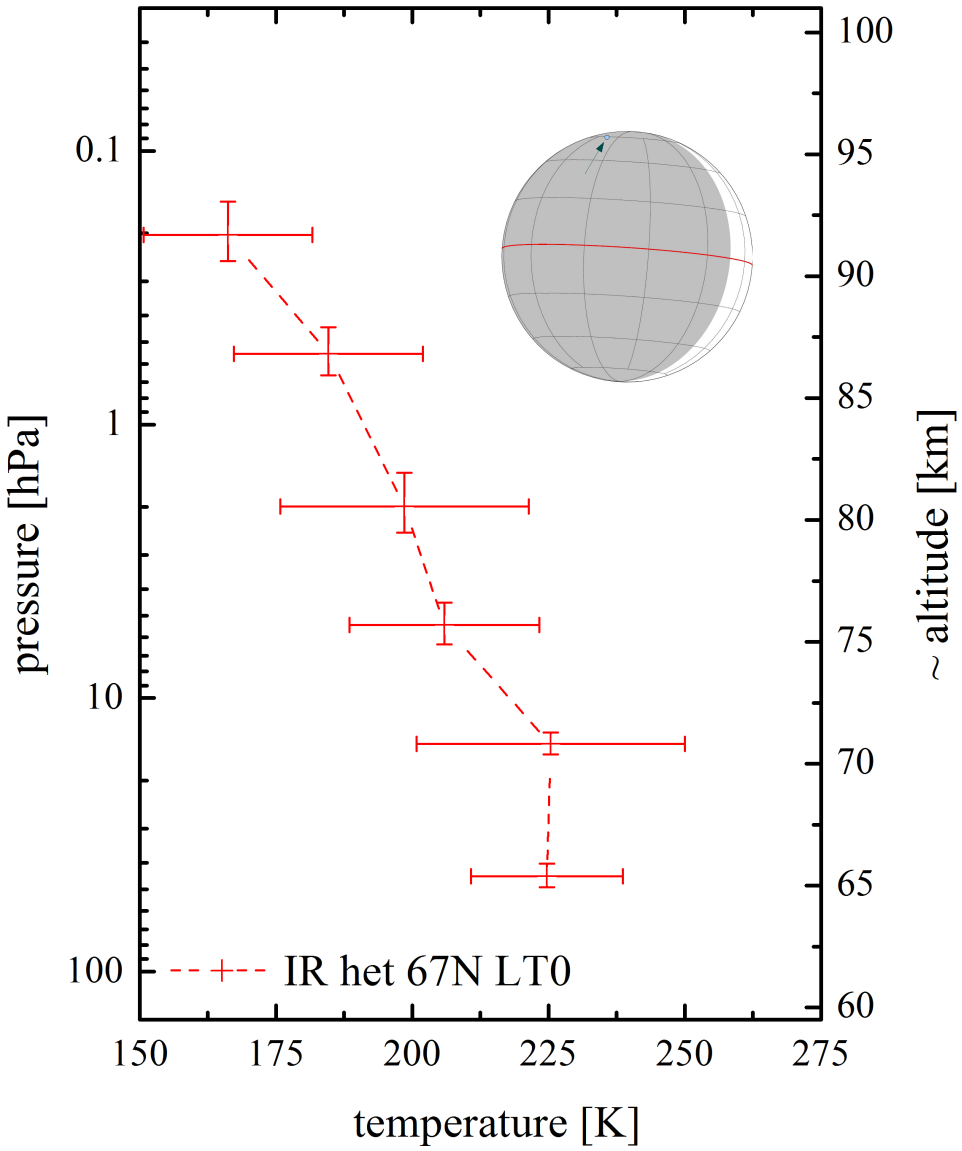

Figure 4.21: *pT-profile from campaign B at 67NLT0: The observing geometry is displayed in the insert graphic. The derived temperatures (with corresponding uncertainties) in the Venusian atmosphere are displayed in red. The profile is almost isothermal at lower altitudes and decreases with a lapse rate of (-3.0 ± 1.4) K km^{-1} in higher layers. The highest pressure, where the atmosphere gets opaque is at around 44 hPa.*

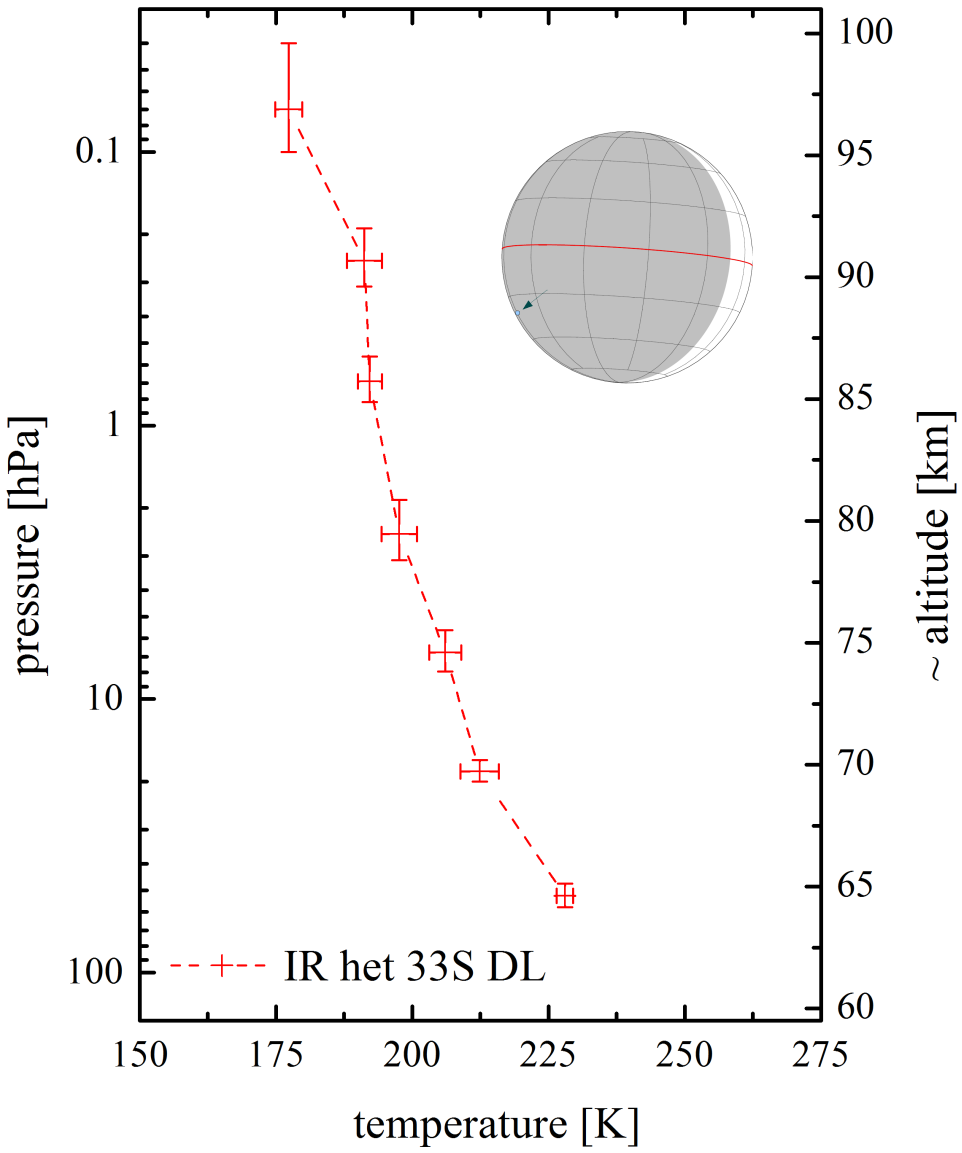

Figure 4.22: *pT-profile from campaign B at 33SDL: The observing geometry is displayed in the insert graphic. The derived temperatures (with corresponding uncertainties) in the Venusian atmosphere are displayed in red. The lapse rate in lower altitudes is (-1.6 ± 0.1) K km^{-1}. Due to the good SNR of the data (comp. Fig. 4.18), an additional pressure layer at ∼ 0.07 hPa could be resolved. There, the temperature suddenly drops at high altitudes. The atmosphere gets opaque at the highest pressure at ∼ 52 hPa.*

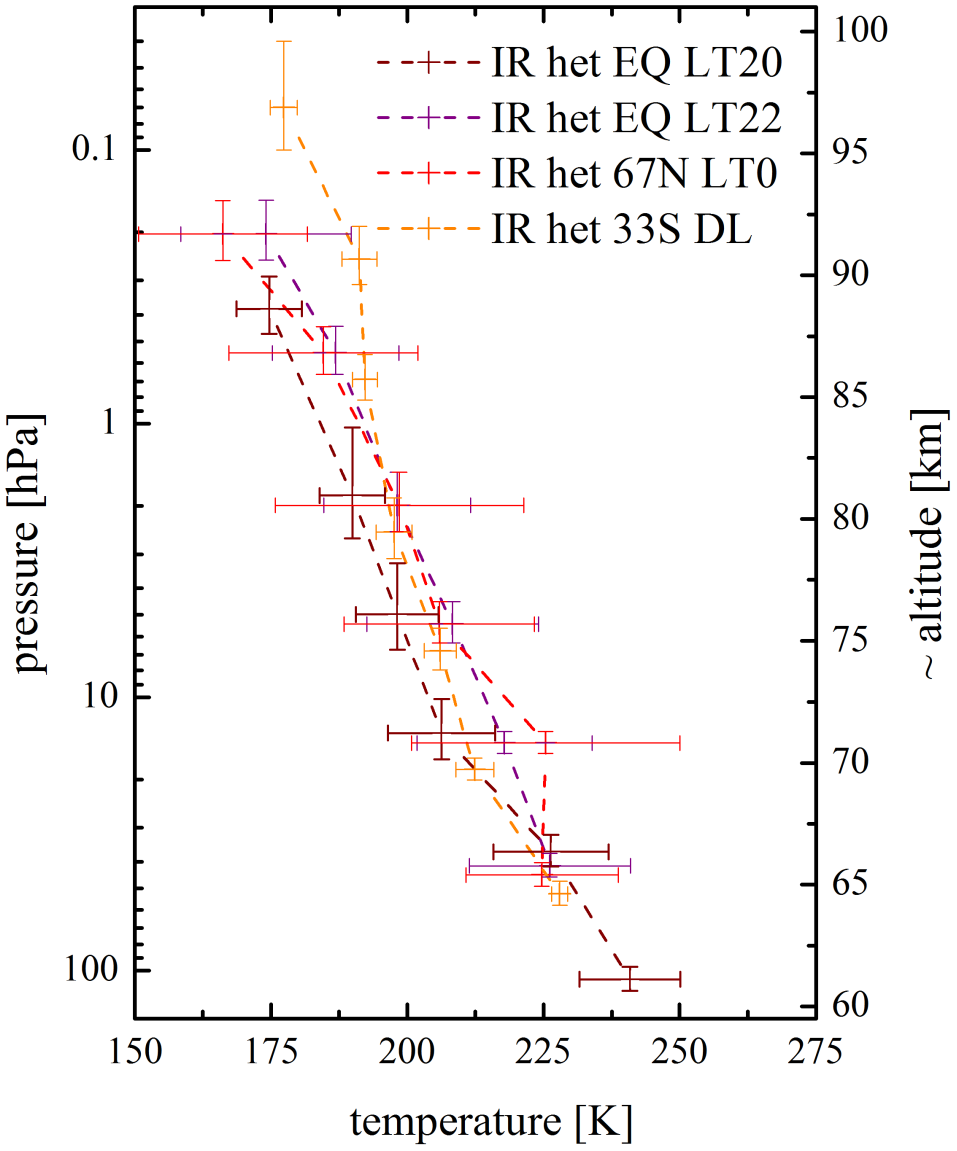

Figure 4.23: *All pT-profiles from both campaigns: The derived temperatures (with corresponding uncertainties) for the various observing positions in the Venusian atmosphere are displayed.*

4.3.3 Coordinated Campaign with Venus Express

During campaign B, coordinated observations between the VEX VeRa team and IR heterodyne ground-based spectroscopy group took place. The VeRa instrument is presented in detail in Sec. 4.1.3. VeRa has observed during six orbits the very position on Venus as it was observed by IR heterodyne using HIPWAC at the IRTF. VEX was in its 24-hour orbits 2218–2223 on May 17th–22nd. An overview of the orbital parameters from VEX and the exact observing positions from VeRa can be found in Tab. 4.8. Due to the ray bending in the atmosphere, VeRa probes a range of latitudes and longitudes while observing. The latitudes for the bottom point of the profile ($\sim$40 km altitude) and the top point at 100 km are given for reference in Tab. 4.8. The longitudes are not relevant for comparison, and the true LT on Venus is given instead. In the following, the VeRa profiles will be assigned according to a mean latitude and LT value. As discussed before, the retrieval technique for RO data requires the assumption of upper boundary conditions. Hence, each profile is represented by a set of three with varying upper boundary conditions. The upper boundary condition, however, becomes irrelevant for lower altitudes, since the profiles converge at $\sim$1 hPa. There, the uncertainty of the method is given as $\sim$1 K. Since the errors are small, they will be neglected for display. The radio signal was detected at the ESA ground stations in New Norcia, Australia, yielding a similar viewing angle to the limb of Venus compared to the observing location at the IRTF on Mauna Kea, Hawaii. The resulting profiles from each VeRa measurement, all obtained during ingress, are plotted in Fig. 4.24. The retrieved profile from the IR heterodyne observation is plotted too, for comparison, although, simultaneous observations at the dark limb and 33°S were performed only during orbit 2220, 2221 and 2222. Nevertheless, profiles from

Orbit	UT Date	Latitude			Local Time		
#	(mm/dd)	$\sim$40 km	100 km	mean	$\sim$40 km	100 km	mean
2218	05/17	31.15°S	37.39°S	34.3°S	03:34	03:39	03:36
2219	05/18	31.75°S	37.15°S	34.5°S	03:31	03:41	03:36
2220*	05/19	30.58°S	36.80°S	33.7°S	03:36	03:46	03:39
2221*	05/20	31.16°S	36.35°S	33.8°S	03:45	03:53	03:49
2222*	05/21	29.29°S	35.80°S	32.5°S	03:49	03:59	03:54
2223	05/22	28.62°S	35.15°S	31.9°S	04:06	04:11	04:08

Table 4.8: *Observing geometry of VeRa during the coordinated campaign in 2012. The latitude and LT for each orbit is given for the lowest and highest sampling point in $\sim$32 km and 150 km altitude, as well as the the mean value. Orbits with an asterisk correspond to the days with simultaneous IR heterodyne observation.*

Figure 4.24: *Pressure-temperature profiles measured with* VEX *VeRa for different orbits during the coordinated campaign in May 2012. High diurnal variability of the temperature profile can be seen from the VeRa data. The IR heterodyne profile is compared to each VeRa profile for convenience, although, the IR heterodyne profile was retrieved only from data acquired between May 19$^{\text{th}}$–21$^{\text{st}}$ UT, corresponding to orbit 2220–2222.*

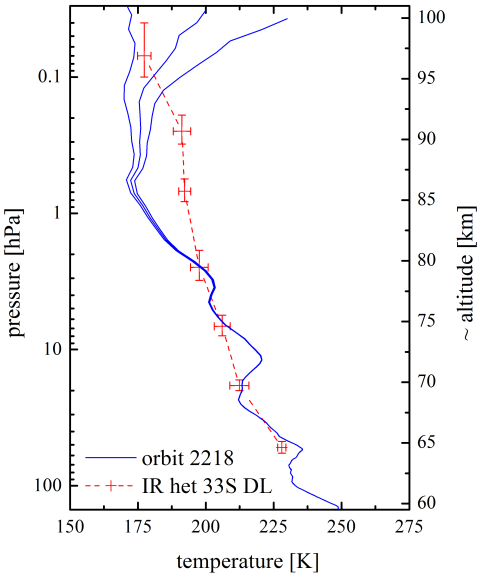

(a) *Orbit 2218 on May 17$^{\text{th}}$ at 34.3°S LT 03:36. Small scale temperature fluctuations in altitudes between 60–80 km. VeRa data was acquired two days before IR heterodyne observations.*

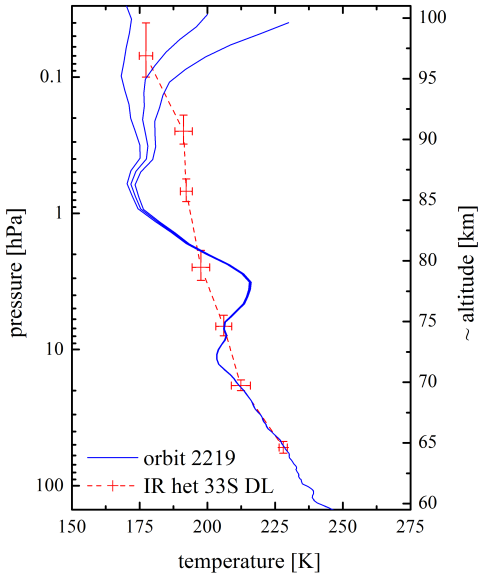

(b) *Orbit 2219 on May 18$^{\text{th}}$ at 34.5°S LT 03:36. Strong temperature inversion appeared within less than 24 hours (comp. to orbit 2218) at ∼ 78 km altitude. VeRa data was acquired one day before IR heterodyne observations.*

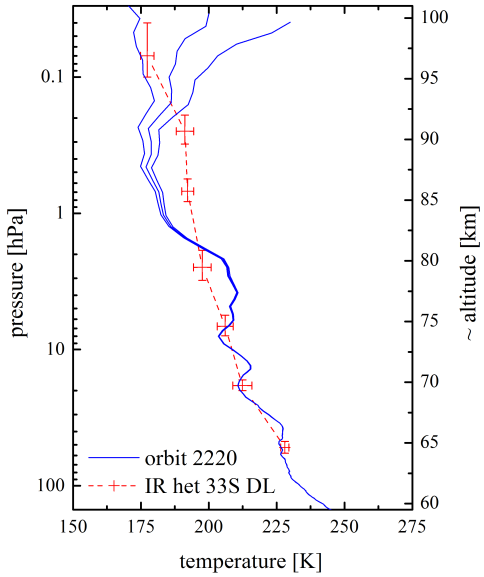

(c) *Orbit 2220 on May 19$^{\text{th}}$ at 33.7°S LT 03:39. Temperature inversion weakened and fluctuations in lower altitudes are more pronounced. VeRa data was acquired on the first day of IR heterodyne observations.*

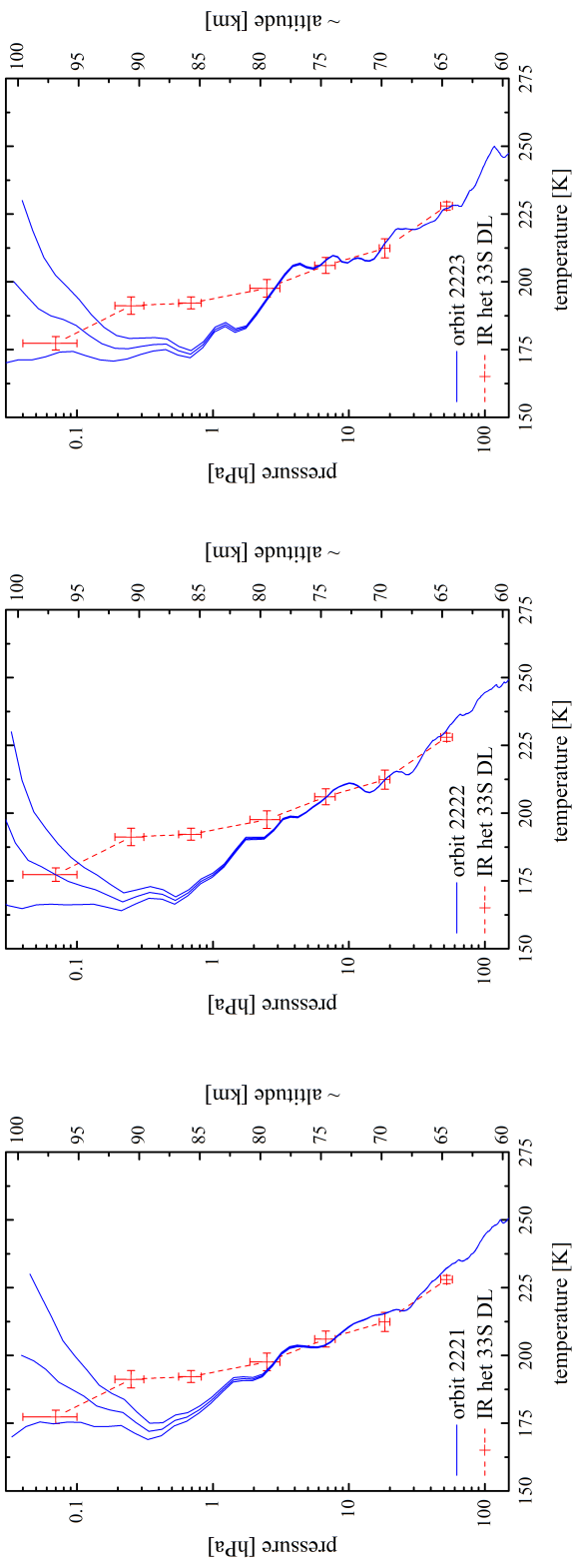

(d) *Orbit 2221 on May 20th at 33.8°S LT 03:49. Temperature is decreasing monotonically with altitude with low variability. VeRa data was acquired on the second day of IR heterodyne observations.*

(e) *Orbit 2222 on May 21st at 32.5°S LT 03:54. Temperature is decreasing monotonically with altitude and getting colder than on previous days. VeRa data was acquired on the third day of IR heterodyne observations.*

(f) *Orbit 2223 on May 22st at 31.9°S LT 04:08. Small scale variations and smaller gradient up to ∼ 80 km altitude. Lower altitudes are even colder. VeRa data was acquired on the first day after IR heterodyne observations.*

one day before and after the observations, and the retrieval from orbit 2218 is also shown, to demonstrate the highly diurnal variability of the temperatures in the Venusian mesosphere. In the profile from orbit 2219 a warm layer at ~ 3 hPa can be observed. This thermal inversion tends to rapidly disappear within a few hours, since no indication of the inversion is present in the profile from orbit 2218 and only a light warming is observed one day later, during orbit 2220. Hence, short term thermal fluctuations in the Venus mesosphere are possible. Also, as it can be seen in Fig. 4.24(c), small scale temperature changes, including inversions or isothermal parts, exist in the VeRa profiles. These fluctuation can be caused i.a. by locally constrained short time scale phenomena, like gravity waves [170]. Hence, such fluctuations, cannot be detected with ground-based IR heterodyne spectroscopy because of the longer integration time of the former and the lower altitude resolution of the latter. The longer integration time, yields a time average within the stacked data set. For a better comparison of IR heterodyne retrieval to the radio occultation measurements, the VeRa profiles are also averaged over the observing period. The mean profile from orbits 2220–2222 is then compared to the retrieved IR heterodyne profile in Fig. 4.25. The agreement between the two profiles is remarkable. For lower altitudes, between the cloud top at ~ 64 km (52.48 hPa) and 80 km (2.49 hPa), the retrieved temperatures agree within the uncertainty range. At 18.38 hPa, 6.77 hPa and 2.49 hPa, the obtained values are even identical for both techniques. Above this altitude region, the VeRa profiles begin to diverge, yielding a higher uncertainty. Comparison in this altitude region is thus more complex. The high altitude resolution of radio occultation, of less than 1 km, yields the possibility to reveal a lot more structure in the thermal profile. In order to make the techniques comparable, the profile of one of the methods has to be rescaled. Since an upscaling of the IR heterodyne profile is not possible, the VeRa profiles were downscaled to an altitude resolution commensurate with IR heterodyne spectroscopy. The rescaled pT-profiles for VeRa observations during the Vex orbits 2220–2222 are shown in Fig. 4.26. Again, the IR heterodyne profile is displayed along for comparison. Additionally, the mean VeRa profile is rescaled. This final profile yields the best representation of the radio occultation measurements for comparison to the retrieval with the newly developed IR heterodyne method. The results are displayed in Fig. 4.27. It has to be noted that almost all retrieved temperatures agree within the uncertainty margin. Only the layer at 0.69 hPa is slightly warmer in the IR heterodyne profile. This is most probably due to the slightly different LT of the observing position. As it can be seen in the diurnal variation of the VeRa profiles in Fig. 4.26, a cooling of ~ 10 K for a later LT of ~ 15 min is possible (comp. Fig. 4.26(a) and Fig. 4.26(c)). The LT deviation of the observing position between IR heterodyne and the RO observations is even ~ 30 min for the last observing day on May 21st.

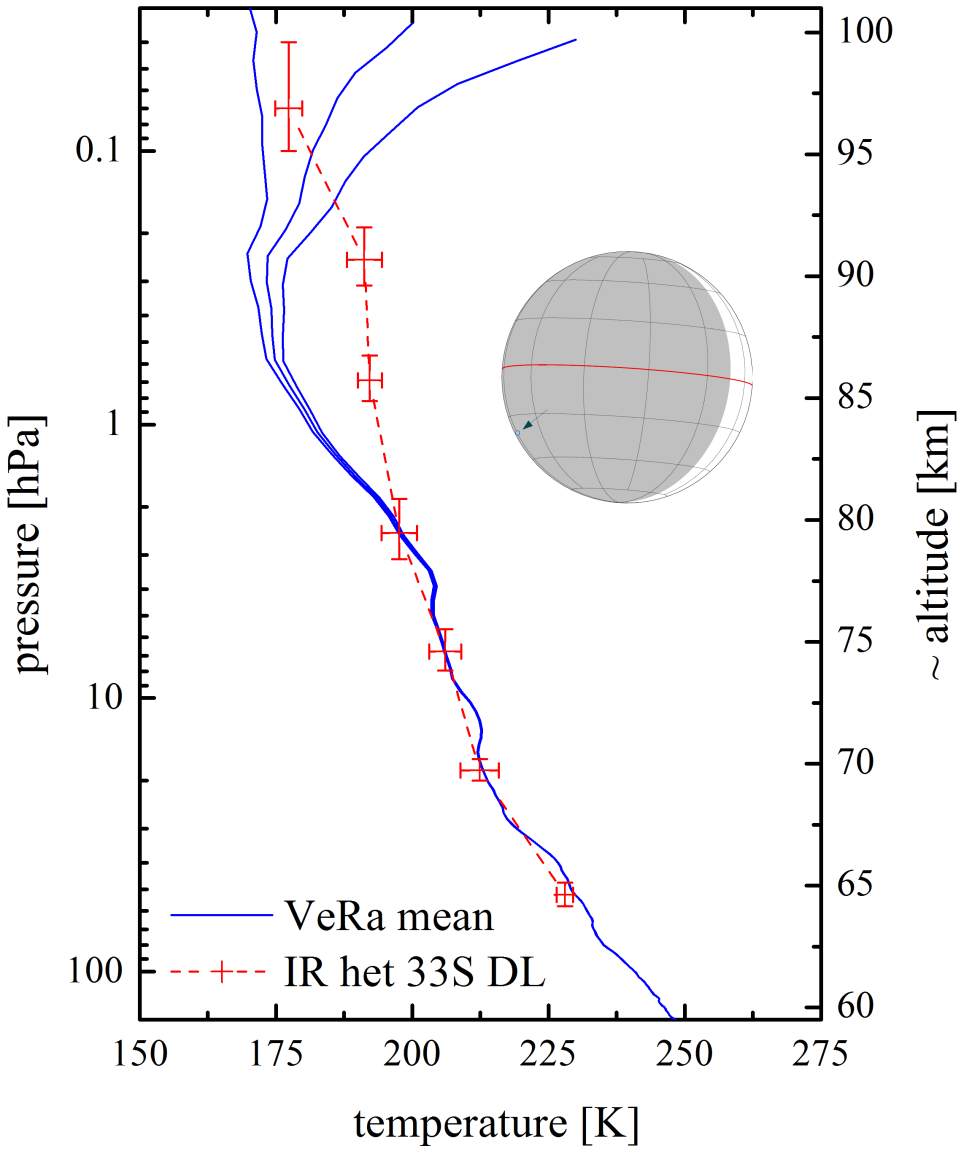

Figure 4.25: *pT-profiles from coordinated observations in May 2012. The (blue) VeRa profile represents the average of the temperature profiles obtained during radio occultation observations during* Vex *orbits 2220–2222, observing between 32.5°S and 33.7°S and LT 03:39 and 03:54. The (red) IR heterodyne profile was retrieved from data obtained during simultaneous observations. The latitude was constant at 33°S, the LT varied between 03:20 and 03:26. Radio occultation probed a slightly different LT, with an approximately 15 minutes offset. The observing position is indicated in the inset graphic.*

Figure 4.26: *Temperature profiles measured with* VEX *VeRa during the coordinated campaign. The altitude resolution of the VeRa profiles was rescaled to be commensurate with the IR heterodyne observation. The small scale fluctuations cannot be seen any more. Only a general cooling of the atmosphere can be observed. The IR heterodyne profile was retrieved from data taken on May 19$^{\text{th}}$–21$^{\text{st}}$ UT corresponding to orbit 2220–2222.*

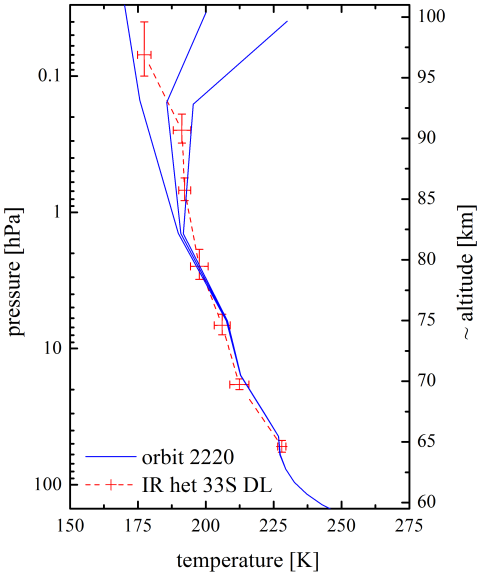

(a) *Rescaled pT-profile from orbit 2220. For high altitude resolution profile see Fig. 4.25(c). The weak temperature inversion, that was seen before has vanished.*

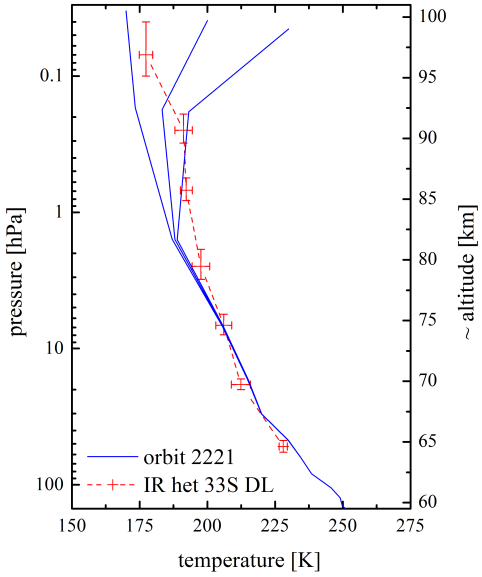

(b) *Rescaled pT-profile from orbit 2221. For high altitude resolution profile see Fig. 4.25(d). The temperatures decrease monotonically with altitude. At high altitudes a cooling took place.*

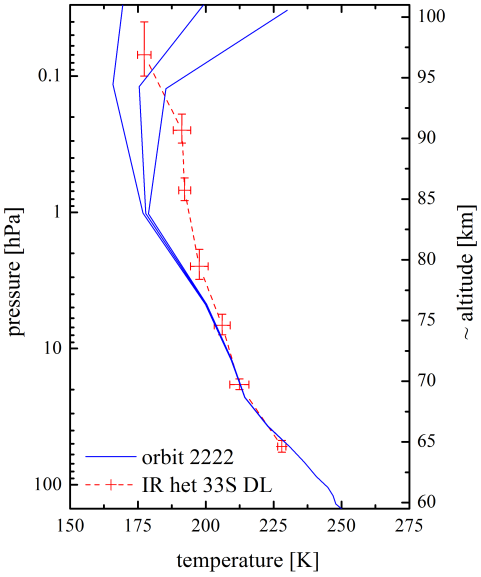

(c) *Rescaled pT-profile from orbit 2222. For high altitude resolution profile see Fig. 4.25(e). The cooling of the higher altitudes is even more pronounced.*

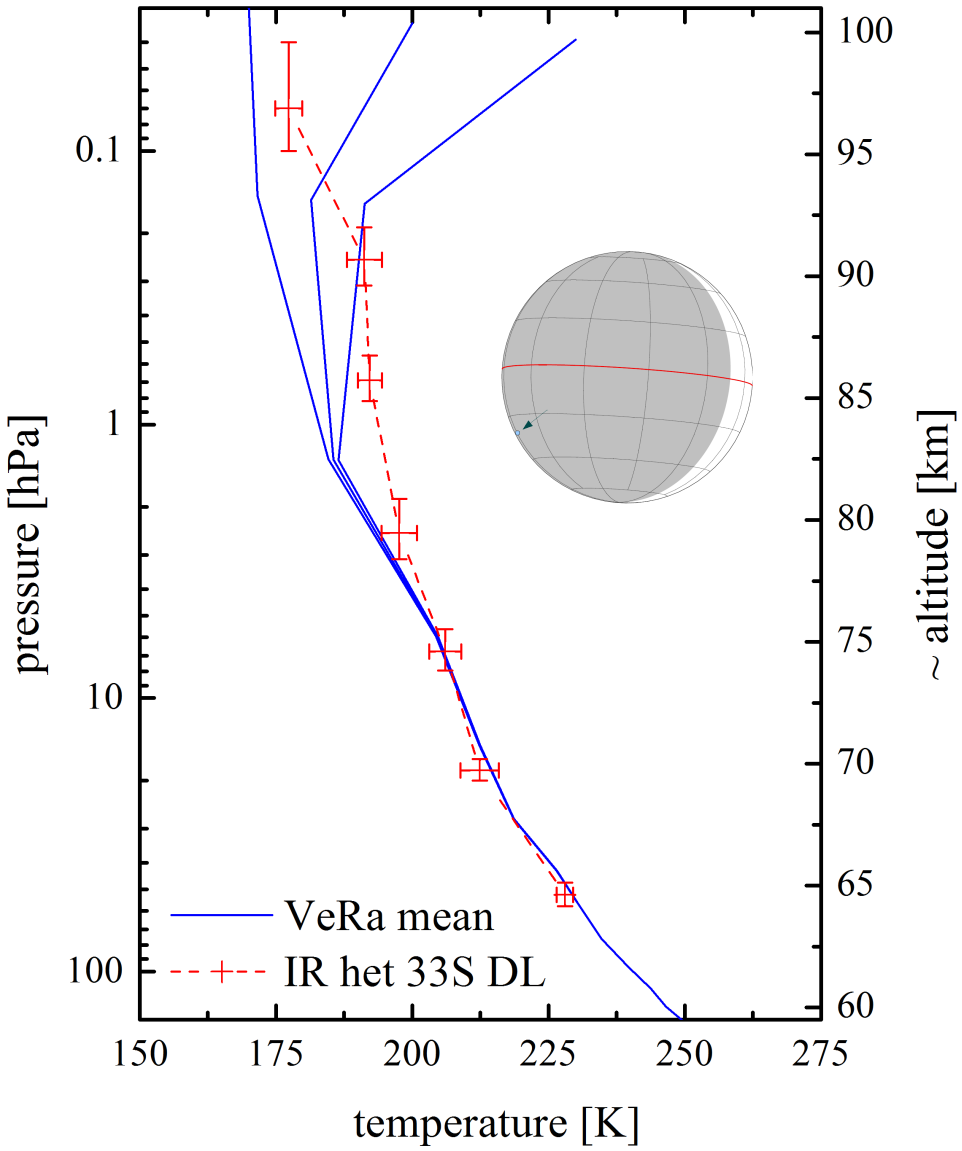

Figure 4.27: *pT-profiles from coordinated observations in May 2012. The (blue) VeRa profile represents the average from the temperature profiles obtained during radio occultation observations during* Vex *orbits 2220–2222, observing between 32.5°S and 33.7°S and LT 03:39 and 03:54. The (red) IR heterodyne profile was retrieved from data obtained during simultaneous observations. The latitude was constant at 33°S, the LT varied between 03:20 and 03:26. Radio occultation probed a slightly different LT, with an approximately 15 minutes offset. The observing position is indicated in the inset graphic.*

4.4 Comparison

In this section, the retrieved data will be compared to existing Venus temperature observations and the reference atmosphere, as they have been previously introduced in Sec. 4.1.3, Sec. 4.1.4 and Sec. 4.1.5. The results are discussed in terms of comparison to space- and ground-based observations. Emphasis will be placed on the radio occultation measurements from Vex with VeRa. Also the Virtis and the Spicav/Soir team has provided data sets for comparison. Ground-based observations of CO in the Venusian atmosphere will be investigated in relation to the IR heterodyne profiles. Additionally, a comparative study would be incomplete without taking the Venus International Reference Atmosphere into account.

4.4.1 Comparison to Space-based Observations

VeRa

The retrieved temperature profiles derived from the measurements that have not been subject of the coordination, are compared to existing VeRa data sets, too. The data were provided by the VeRa team from *Silvia Tellmann* [171]. The extensive amount of VeRa profiles enables a detailed comparison of the IR heterodyne profiles to space-based observations for the specific observing positions. However, despite the numerous observations with VeRa, there is no guarantee of a total agreement between both, the observed latitude and LT. Hence, the temperature profile, closest to the observed position will be provided for comparison. Also, the much higher altitude resolution of the radio science experiment yields more variability of the profiles. For better comparison, the VeRa profiles are rescaled to a low altitude resolution commensurate, with infrared sounding, as it has been discussed in the previous section. Therefore, the temperatures within one scale height of $\sim 5\,\mathrm{km}$ are averaged, representing a mean temperature in the single layers. However, both profiles are provided for completeness.

In Fig. 4.28, the comparison between the IR heterodyne profiles from campaign A at EQLT20 and EQLT22 to VeRa profiles at corresponding observing positions is shown. The latitudes observed with VeRa are not identical to the IR heterodyne observations, but the agreement is sufficient, since the FoV of IR heterodyne observations covers a range of latitudes within the telescope beam. The LT of the VeRa profile is later than for the IR heterodyne observations for the LT 20:00 measurement, and the atmosphere is warmer at lower altitudes. The profiles from the second observing position differ in LT, too. There, the VeRa profile was obtained for an earlier LT and the temperatures are colder than those measured with This.

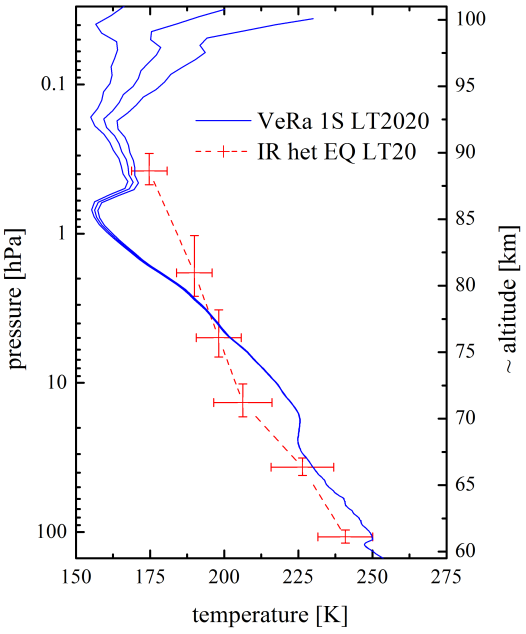

(a) *VeRa profile with high altitude resolution,* $\sim 0.5\,km$.

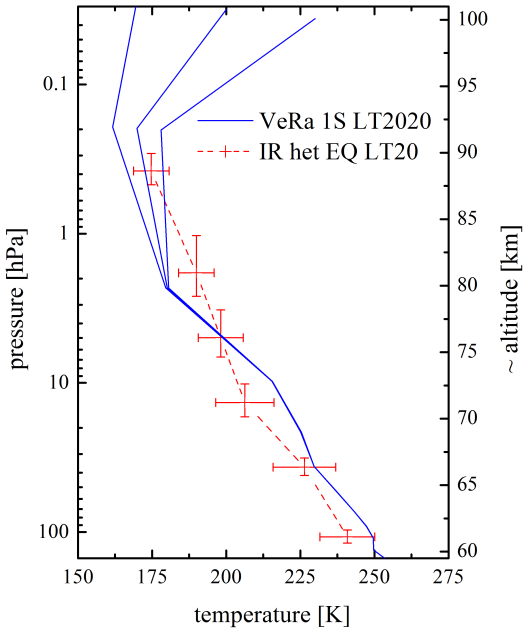

(b) *VeRa profile with low altitude resolution,* $\sim 4.2\,km$.

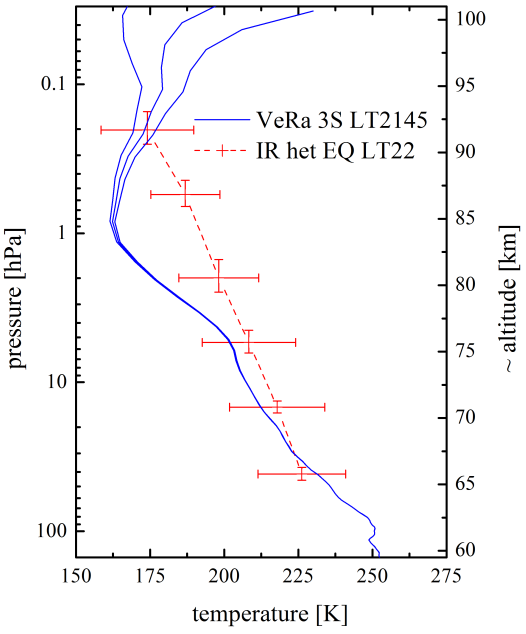

(c) *VeRa profile with high altitude resolution,* $\sim 0.5\,km$.

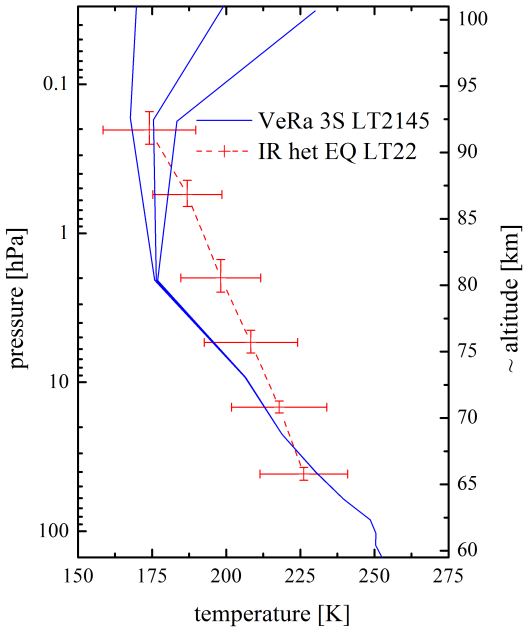

(d) *VeRa profile with low altitude resolution,* $\sim 4.2\,km$.

Figure 4.28: *pT-profiles from IR heterodyne observations (red) and VeRa (blue) at corresponding observing locations. (a) and (b): EQLT20 and 1°S and LT 20:20 The two profiles are in agreement within the error margins except for the 13.5 hPa and 1.83 hPa layer. (c) and (d) for EQLT22 and 3°S (3S)) and LT 21:45. The profiles agree within the error margins for the low altitudes and the top layer.*

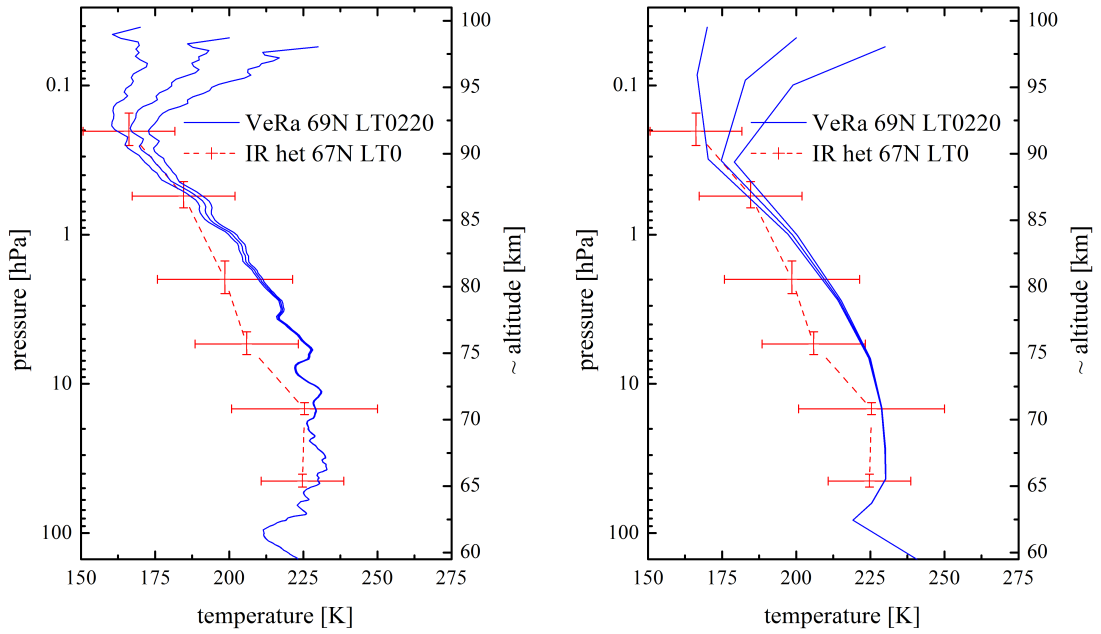

(a) *VeRa profile with high altitude resolution, ~ 0.5 km.*

(b) *VeRa profile with low altitude resolution, ~ 4.2 km.*

Figure 4.29: *pT-profiles from IR heterodyne observations (red) and VeRa (blue) at corresponding observing locations (67°N (67N) and 69°N (69N)) and local time (00:00h and 02:20h). The profiles are in agreement within the error margins for the low altitudes and the top layer.*

At the lower altitudes, between ~65.5 km and ~76 km, the profiles are in good agreement for EQLT22. For the higher altitudes though, the VeRa profile shows a much cooler atmosphere. The better spatial and altitude resolution of VeRa enables the investigation of the thermal behavior in more detail. Additionally, it has to be considered that the integration time for observations at EQLT22 was extensive, leading to an averaging over several days.

In Fig. 4.29 the retrieved profile from campaign B at 67NLT0 is compared to a radio occultation measurement at 69°N at LT 02:20. Since the FoV on campaign B was smaller than it was on A, and the apparent disk of Venus was much bigger, the latitudinal deviation might not be neglected this time. However, due to the curvature of the planet, observations towards the limb cover an even larger latitude or LT region. Thus, the geometry can, here again, be assumed as equal. The local time, though, deviates a lot between the two observations. The profile with high altitude resolution in Fig. 4.29(a) shows a lot of small scale inversions in the lower altitude region between ~63 km and ~72 km. Nevertheless, the global structure

of this region can be understood as isothermal, since the temperature gradient is almost zero. This isothermal behavior can also be found in the IR heterodyne profile. When regarding the comparison to the VeRa profile with a rescaled low altitude resolution of $\sim 4.2\,\mathrm{km}$, the measurements agree within the error margins for each single pressure layer.

VIRTIS

VIRTIS temperature retrieval is quiet similar to the inversion method used for data analysis for IR-heterodyne spectroscopy. The instrument and its applications are presented in Sec. 4.1.3. The VIRTIS method, developed by *Grassi et al.* [172], applies a numerical inversion to the input radiance acquired by observing the CO_2 $4.3\,\mu\mathrm{m}$ band. The pressure grid is fixed and atmospheric opacity at $4.3\,\mu\mathrm{m}$ can be assumed as equal to the optical depth at $10.5\,\mu\mathrm{m}$. Thus, the real altitude resolution for the VIRTIS temperatures is directly comparable to observations in the mid-IR. The four IR-heterodyne pT-profiles will now be compared to VIRTIS profiles. Two profiles were acquired with the VIRTIS-M [112] and the other two with the VIRTIS-H [139] channels. The data were provided to me by the VIRTIS team from *Alessandra Migliorini* [173]. It must be noted, that the observed positions are not identical, neither timely nor spatially. Hence, comparison is always limited.

The retrieved pT-profile from IR-heterodyne observations during campaign A are compared to a VIRTIS-M and a VIRTIS-H profile from the corresponding LT and similar latitudes in Fig. 4.30. The two IR heterodyne profiles agree within the uncertainty range for each single pressure layer with the VIRTIS observations. Only the high pressure level at $\sim 100\,\mathrm{hPa}$ deviates for the EQLT20 (Fig. 4.30(a)) measurement. The agreement of the pT-profiles for EQLT22 (Fig. 4.30(b)) is remarkable. The temperature gradient is very similar and the values are almost identical. The VIRTIS-H profile probes the atmosphere deeper than the IR heterodyne profile does. This is caused by the observing geometry and the curvature of the planet. The pressure grid for IR-heterodyne is chosen to be adequate for observations at the limb. The error of the VIRTIS-H profile is taken from *Migliorini et al.* [139] and assumed to be 4 K.

Both VIRTIS profiles do not show the cold bulge that is seen by VeRa for the low latitudes at around 1 hPa in the previous comparison. The altitude resolution of the IR receiver VIRTIS is identical to the IR heterodyne instrument. This gives either an additional proof, that the cold layer can not be resolved, or as a second possibility, is time dependent and is simply not seen during these observations. Possibility one can be proven, following the arguments used in Sec. 4.3.3. The lower altitude resolution yields an averaging over one scale height and small scale

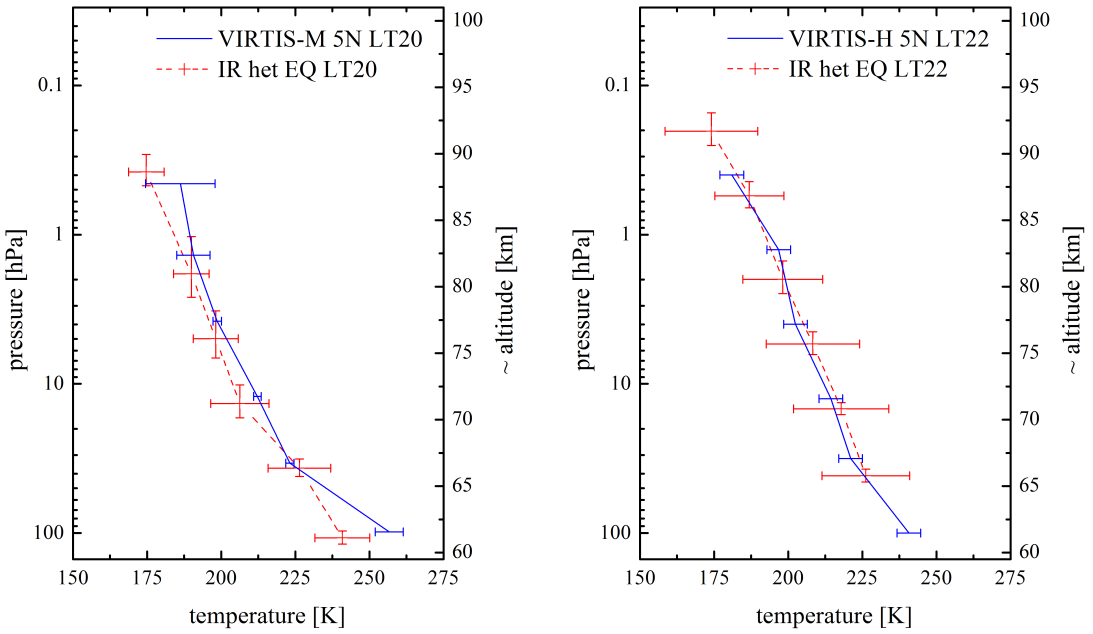

(a) *The* Virtis *data was acquired using the* Virtis*-M channel at 5°N LT 20:00. The two profiles are in agreement within the error margins except for the high pressure layer.*

(b) *The* Virtis *data was acquired using the* Virtis*-H channel at 5°N LT 22:00. The two profiles are in very good agreement within the error margins.*

Figure 4.30: *pT-profiles from IR heterodyne observations (red) during campaign A and* Virtis *(blue) at corresponding observing positions (equator (EQ) and 5°N (5N)) and local time.*

fluctuations can not be observed. A positive argument for possibility two is that the cold layer, was present during the coordinated campaign, but it was strongly varying within three days (comp. Fig. 4.26), yielding a time dependency.

The profiles from campaign B are displayed in Fig. 4.31. The measurement at 67NLT0 (Fig. 4.31(a)) is compared to a corresponding Virtis-H profile from 65°N. The Virtis profile does not show an isothermal behavior at lower altitudes as it can be observed in the IR heterodyne profile. Therefore, no change in the temperature lapse rate can be seen in Virtis data for an altitude between ∼75–85 km. However, despite the higher temperatures in the IR heterodyne profile at ∼14.7 hPa, the two profiles agree within the error margins. The 33SDL (Fig. 4.31(b)) profile agrees to the Virtis-M profile within the uncertainty range for each single pressure layer, except at the pressure level at ∼33 hPa. Also, the higher SNR of the data set enables the resolution of the temperature at the low pressure at ∼0.7 hPa.

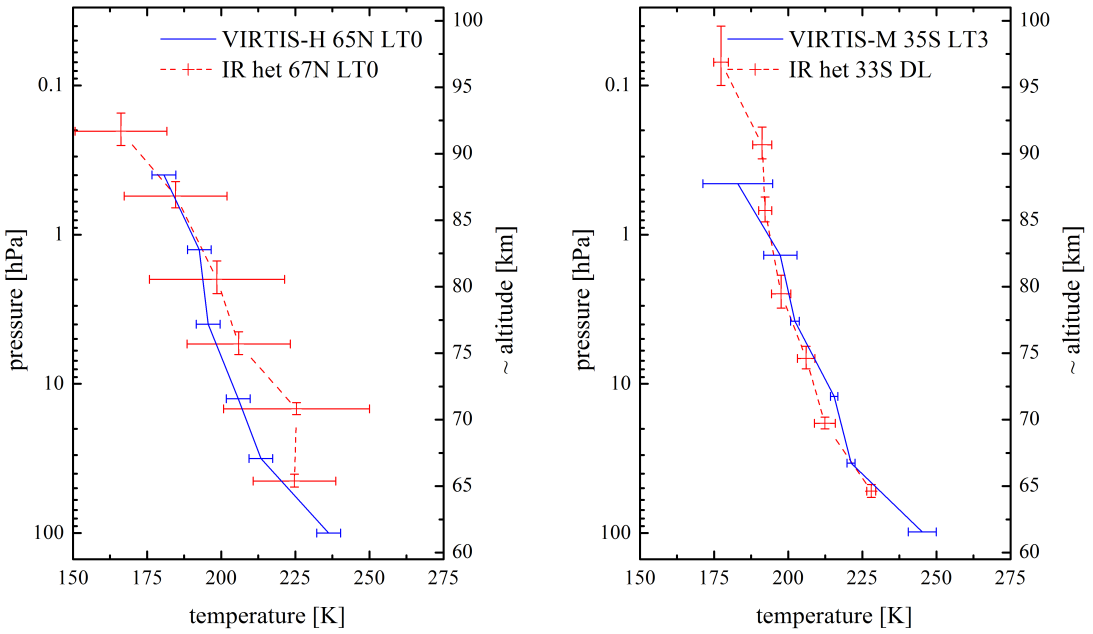

(a) *The* Virtis *data was acquired using the* Virtis*-H channel at 65°N LT 0:00. The two profiles are in agreement within the error margins. The* Virtis *profile does not show the isothermal behavior at lower altitudes. This property is shifted to higher altitudes between ∼ 75–85 km.*

(b) *The* Virtis *data was acquired using the* Virtis*-M channel at 35°S LT 03:00. The two profiles are in agreement within the error margins except for the pressure layer at ∼ 33 hPa. Due to the observing geometry and longer integration time for this special data set, the IR-heterodyne retrieval is sensitive to lower pressures than* Virtis*.*

Figure 4.31: *pT-profiles from IR heterodyne observations (red) during campaign B and* Virtis *(blue) at corresponding observing positions and local time.*

SPICAV/SOIR

Comparison to Spicav/Soir data is a bit less sophisticated, since the solar occultation data can only be acquired at the terminator. Also, the Spicav/Soir team provided only weighted averaged profiles for various latitude bins over the morning and the evening terminator. The receiver and the retrieval technique are explained in Sec. 4.1.3. The data were provided by the Virtis team from *Arnauld Mahieux* [174]. There is no distinction between the northern and southern hemisphere in the following Spicav/Soir data. The Spicav/Soir profiles will be compared to the retrieved pT-profiles form IR heterodyne observations. Plotted are the profiles for the morning and evening terminator as well as a mean profile between the two. The uncertainty of the profiles given in all plots, is the standard deviation between

Figure 4.32: *pT-profiles from IR heterodyne observations (red) and* SPICAV/SOIR *(blue) at corresponding observing locations (equator and 0–30° latitudinal average) at LT 20:00 and 22:00 and the terminator (evening, morning and mean), respectively. The uncertainties of the* SOIR *measurements are represented by the standard deviation between the morning and the evening profile. The profiles are in good agreement within the uncertainty range for all data points, except for the highest altitude at EQLT20 in (b).*

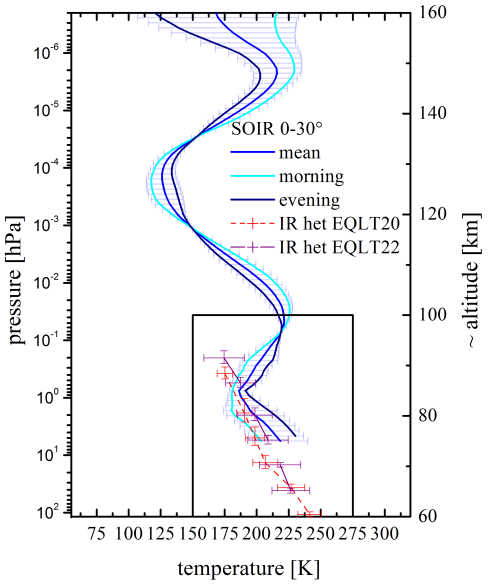

(a) *Comparison between the IR heterodyne profiles (red, purple) and the complete* SOIR *profiles from the morning terminator (light blue), the evening terminator (dark blue) and the mean profile (blue).*

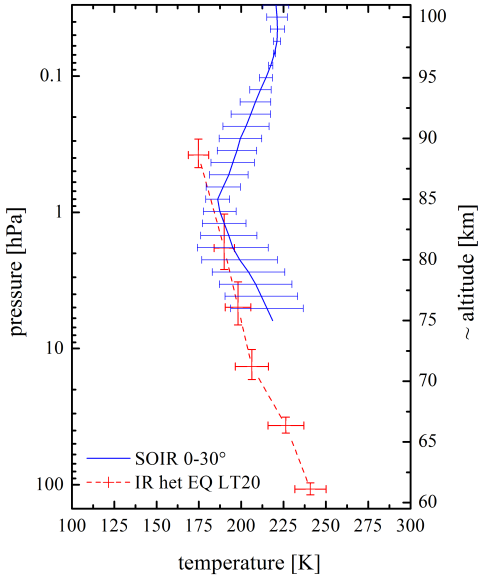

(b) *Comparison of the IR heterodyne profile (red) to the mean* SOIR *profile for low latitudes (blue) between 0–30°. The black box in Fig. (a) indicates the zoom factor on the two profiles.*

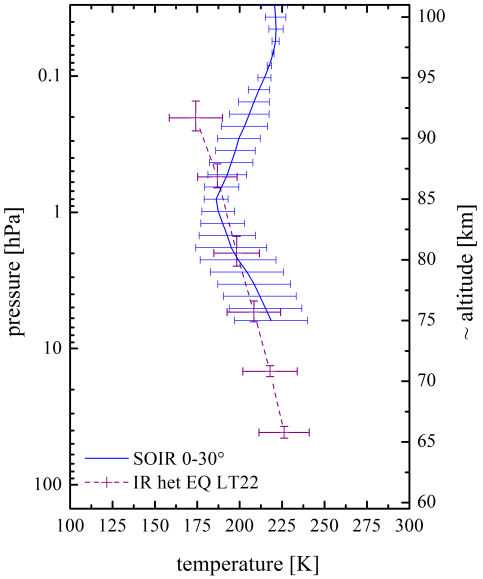

(c) *Comparison of the IR heterodyne profile (purple) to the mean* SOIR *profile for low latitudes (blue) between 0–30°. The black box in Fig. (a) indicates the zoom factor on the two profiles.*

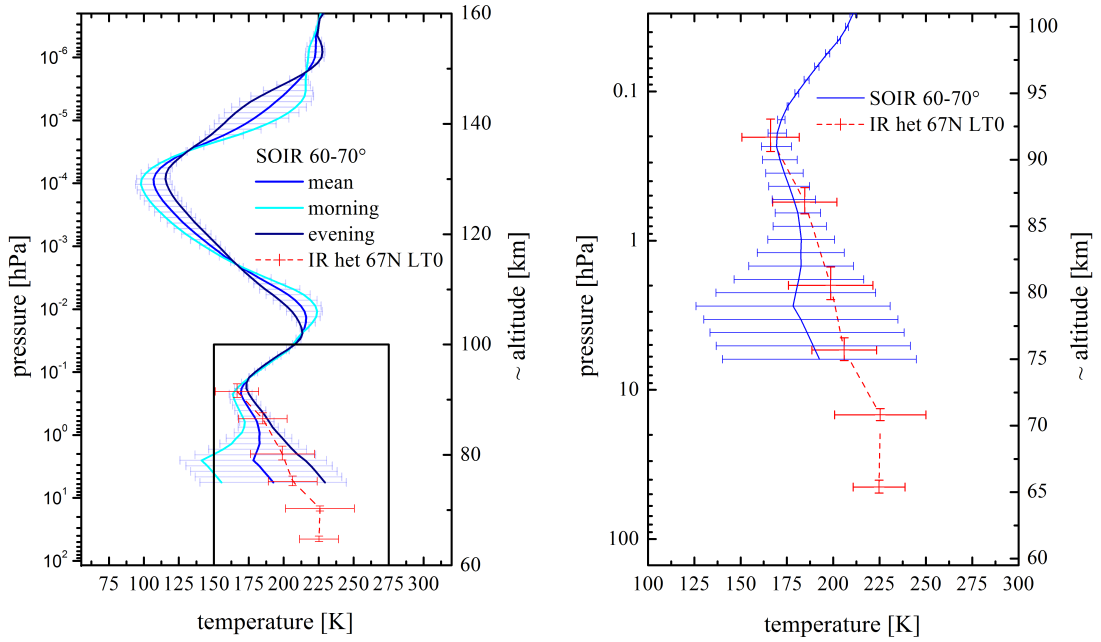

(a) *Comparison between the IR heterodyne profile (red) and the complete* Soir *profiles from the morning terminator (light blue), the evening terminator (dark blue) and the mean profile (blue).*

(b) *Comparison of the IR heterodyne profile (red) to the mean* Soir *profile for high latitudes (blue) between 60–70°. The black box in Fig. (a) indicates the zoom factor on the two profiles.*

Figure 4.33: *pT-profiles from IR heterodyne observations (red) and* Spicav/Soir *(blue) at corresponding observing locations (67N and 60–70° latitudinal average) at local time 22:00 and the terminator (evening, morning and mean), respectively. The uncertainties of the* Soir *measurements are represented by the standard deviation between the morning and the evening profile. The profiles are in good agreement within the uncertainty range for all data points.*

the morning and the evening pT-profile.

In Fig. 4.32 the pT-profile, deduced from observation during campaign A at EQLT20 (Fig. 4.32(b)) and EQLT22 (Fig. 4.32(c)) are compared to the Spicav/Soir data for the low latitudes from 0–30°. In Fig. 4.32(a), the Spicav/Soir profile for the whole probing altitude is displayed. The atmosphere seen by IR heterodyne tends to be cooler at LT 20:00 than suggested by the Spicav/Soir data. However, the Spicav/Soir profile represents the weighted average of all measurements and comparability is limited, since the standard deviation of the single profiles for each, the morning and the evening measurements, are much larger in reality ($\triangle T_{m/e}$ $\sim$65 K), but have been omitted in the graphic. In Fig. 4.32(a), a zoom into the

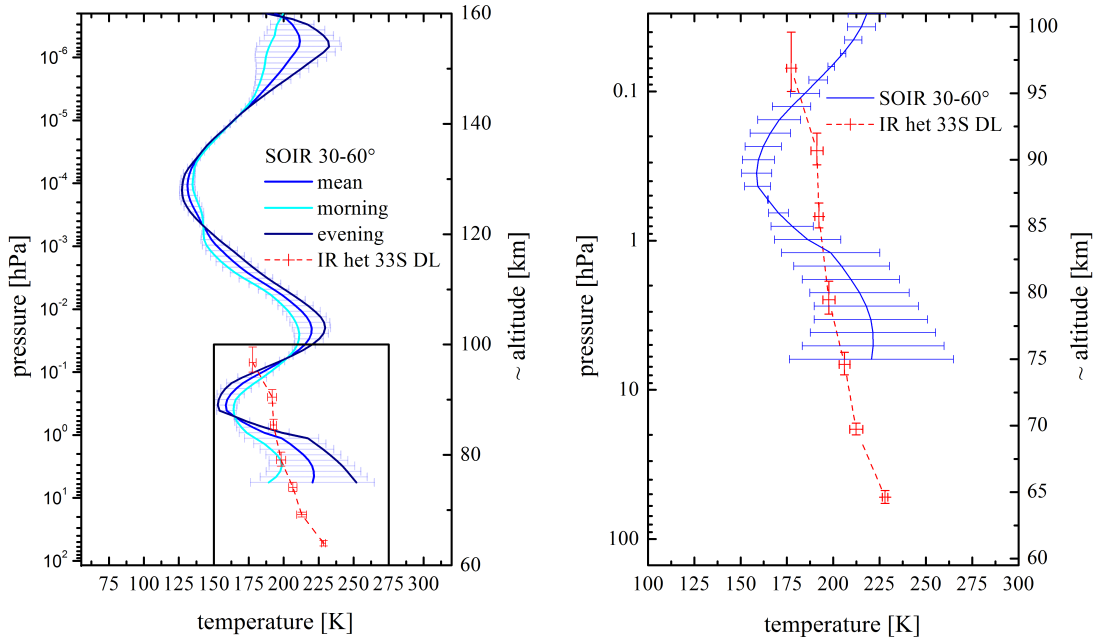

(a) *Comparison between the IR heterodyne profile (red) and the complete* Soir *profiles from the morning terminator (light blue), the evening terminator (dark blue) and the mean profile (blue).*

(b) *Comparison of the IR heterodyne profile (red) to the mean* Soir *profile for mid-latitudes (blue) between 30–60°. The black box in Fig. (a) indicates the zoom factor on the two profiles.*

Figure 4.34: *pT-profiles from IR heterodyne observations (red) and* Spicav/Soir *(blue) at corresponding observing locations (33S and 30–60° latitudinal average) at the dark limb (DL) and the terminator (evening, morning and mean), respectively. The uncertainties of the* Soir *measurements are represented by the standard deviation between the morning and the evening profile. The profiles are in good agreement within the uncertainty range for all data points, except the 0.2.*

altitude region commensurate to IR heterodyne detection is given. Comparison is performed to the mean profile from Soir. The profiles are in good agreement and only the top altitude data point exceeds the uncertainty margin for both profiles. The standard deviation of the mean profile is $\sim$21 K for altitude between $\sim$60 and $\sim$80 km.

For campaign B, the comparison between the high latitude measurement at 67°N and the corresponding Vast bin from 60–70° from Spicav/Soir can be found in Fig. 4.33. The solar occultation data show a much larger variability in the altitudes between 75 and 90 km, compared to the previously discussed low latitude profiles. The standard deviation between the morning and the evening terminator

measurements exceeds 50 K. Thus, the two profiles are in agreement within the uncertainty. Anyhow, the profiles even agree for all pressure layers taking only the uncertainty margin of the IR heterodyne profile into account. The other profile from campaign B at 33SDL is compared to the SPICAV/SOIR profiles for the mid-latitudes between 0–30° in Fig. 4.34. The solar occultation instrument detected a large amount of variation in the mesosphere, yielding proportionally large uncertainties due to the increased standard deviation of the mean profile compared to the other latitudes. The uncertainty at the lower altitudes from 60–72 km is $\triangle$T $\sim$70 K. Despite this vast variability, the two data points at $\sim$2.5 hPa and $\sim$6.7 hPa of the IR heterodyne profile agree within their error margins with the SPICAV/SOIR profile. Above, the errors decrease, but the two profiles are still in good agreement, except for the 0.25 hPa pressure layer. There, a deviation of $\sim$30 K was measured.

4.4.2 Comparison to Ground-based Observations

Sub-Millimeter

Sub-millimeter observations have been performed in 2007 by *Rengel et al.* [144]. During their observations, Venus was close to maximum eastern elongation, yielding an approximately half illuminated apparent disk. In Fig. 4.35 the observing geometry and beam positions are displayed. The FoV (circle, dashed) was 32 arcsec across, exceeding the size of the Venusian disk, which was $\sim$24 arcsec. The cross (line, solid), originating in the center of Venus (circle, solid), indicates the orientation in respect to the equatorial plane. The illuminated fraction of Venus is located on the right hand side of the cross, hence, opposed is the nightside. Observations from June 14 and 15 2007 will be compared to the IR heterodyne profiles, in particular, these sub-mm observations, which have been performed for four different geometrical positions on the nightside of Venus. The data were provided by the MPI team from *Miriam Rengel* [175]. Measurements including the nightside were performed at beam positions 5, 9, 11 and 14. Positions 10, 12, 13 and 15 are pure dayside data and will not be considered for comparison. An overview of the conditions and the geometry for sub-mm observations is given in Tab. 4.9. The derived profiles are displayed in Fig. 4.36. All profiles from the four different positions are plotted. Besides, the averaged profile is given, which will be used for comparison to the IR heterodyne measurements. All profiles show a more or less pronounced bulge in an altitude of $\sim$80 km. This inversion layer is highly variable as it can be seen in Fig. 4.36(a) considering the profiles from position 5. The profile 06/15/07-#2 has a strong inversion, whereas the profiles 06/15/07-#1

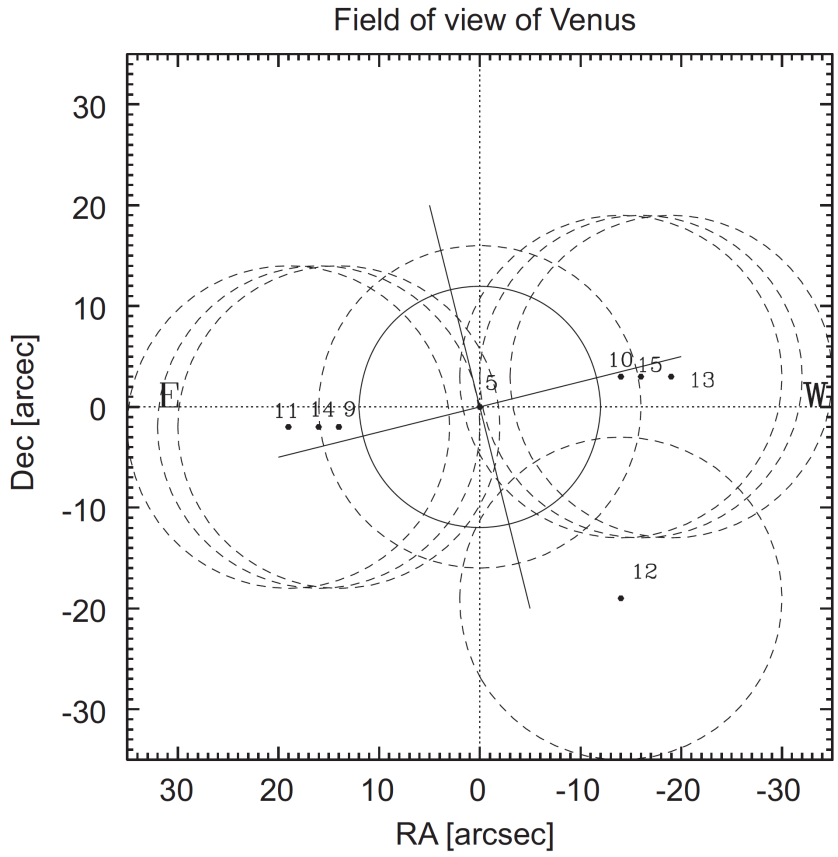

Figure 4.35: *Schematic of the beam positions on Venus during sub-mm observations in June 2007. The cross (solid line) indicates the orientation of the equator and CML in respect to the equatorial plane. The circles indicate the FoV (dashed) and the Venusian apparent disk (solid), respectively. Observing geometry at point 5, 9, 11 and 14 include measurements of the nightside. Beam position 10, 12, 13 and 15 will be omitted in the following. From Rengel et al. [144].*

Beam position Fig. 4.35	Date (2007)	δα [arcsec]	δβ [arcsec]	profiles quantity
5	06/14	0	0	4
9	06/14	14	-2	3
11	06/14	19	-2	2
5	06/15	0	0	3
14	06/15	16	-2	1

Table 4.9: *Geometrical parameters for sub-mm observations on Venus nightside. δα and δβ (right ascension and declination) are the astronomical coordinates of a point on the celestial sphere when using the equatorial coordinate system [144]. The last column gives the amount of profiles obtained on the specific observing day and geometry.*

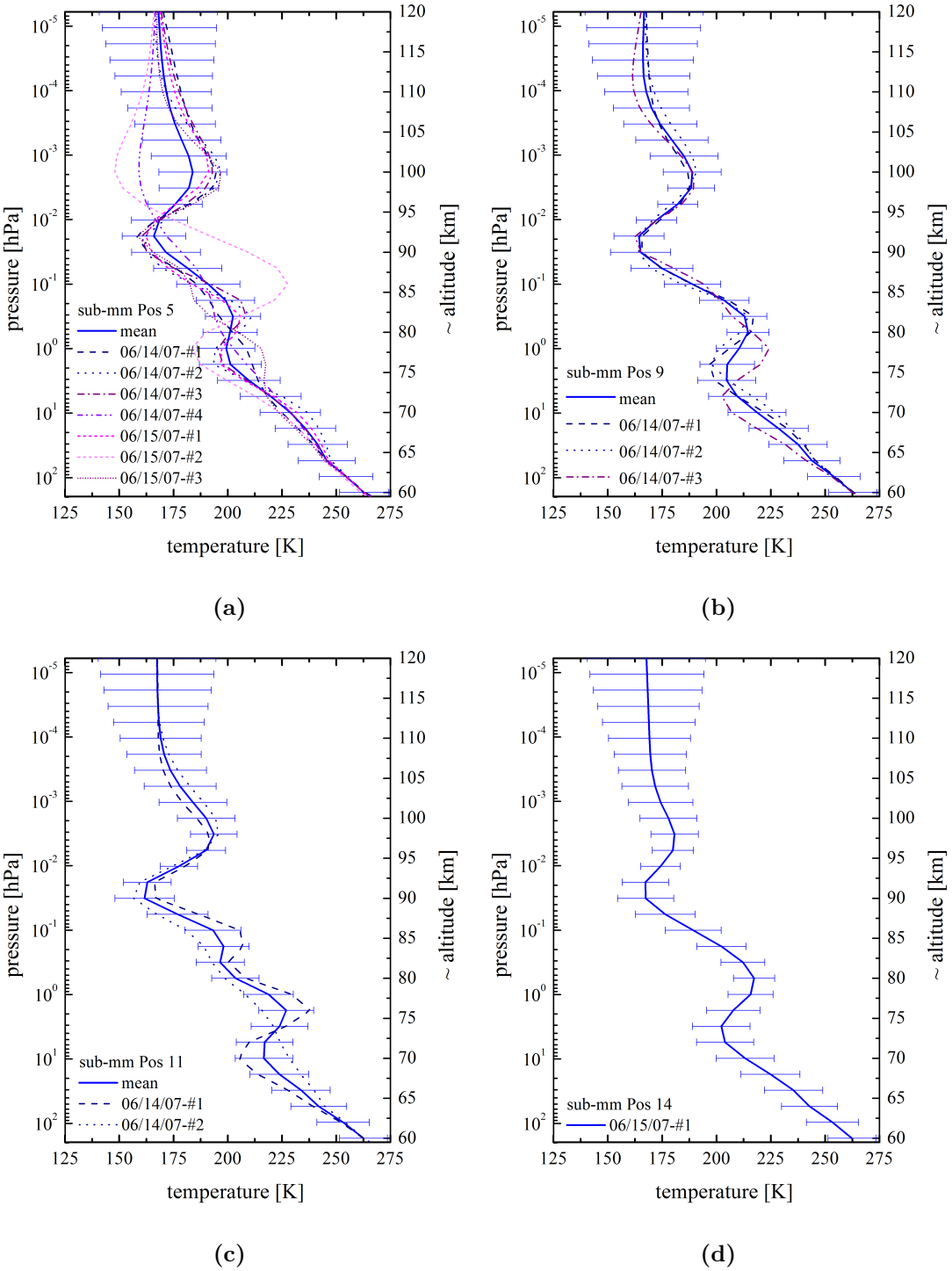

Figure 4.36: *Pressure-temperature profiles from sub-mm observations on June 14 and 15 2007. The dashed lines represent the single measurements at the corresponding position in Fig. 4.35. The solid lines display the average of all profiles from one position. The uncertainties of the mean profile are the averaged uncertainties from all measurements. At position 14, only one profile is available.*

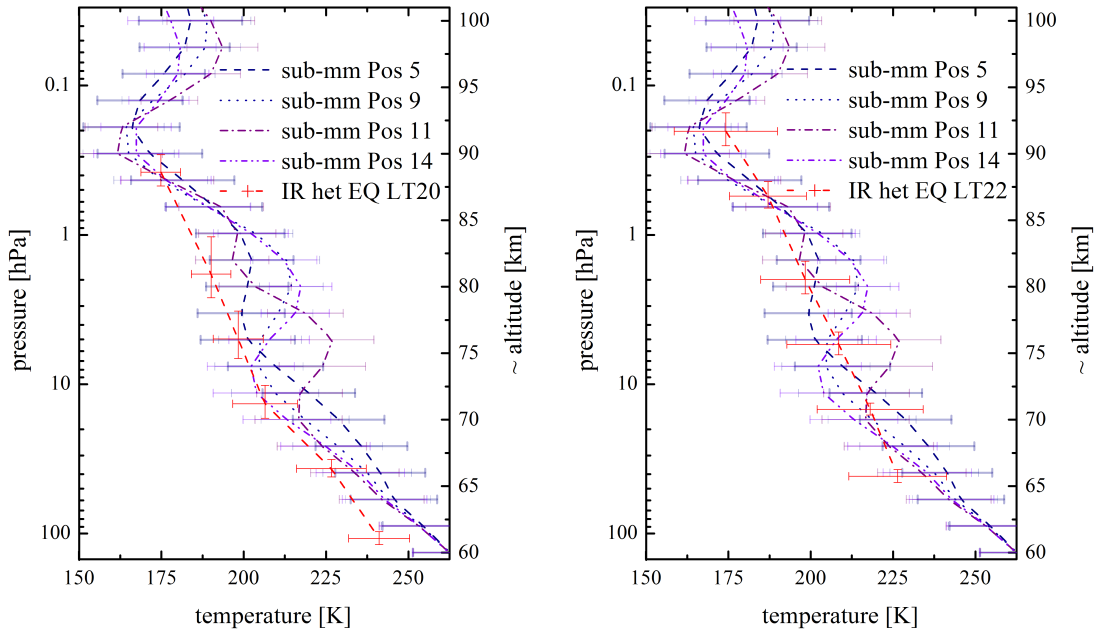

(a) *IR heterodyne observations at the equator and local time 20:00.*

(b) *IR heterodyne observations at the equator and local time 22:00.*

Figure 4.37: *pT-profiles from IR heterodyne observations (red) during campaign A and sub-mm observations (bluish) for all sub-mm observing positions on the Venusian nightside disk in June 2007. The sub-mm profiles are the mean values of the profiles in Fig. 4.35 in the respective altitude region. The IR heterodyne profiles agree within the uncertainty range with the sub-mm observations.*

and -#3 are a lot colder at the respective altitude. However, these temporal variations cannot be observed with IR heterodyne spectroscopy, especially due to the much longer integration time. It is therefore useful to compare only the averaged profiles to the IR heterodyne measurements. Also, the lower spatial resolution of sub-mm observations has to be pointed out again. The FoV does not even resolve the Venusian disk during these observations. Thus, comparison of single profiles to the spatially variable IR data is limited and an analysis of each single IR heterodyne measurement in respect to all averaged sub-mm profiles will be discussed in the following.

In Fig. 4.37 the comparison of the retrieved profiles from campaign A to the averaged sub-mm observations from observing position 5, 9, 11 and 14 are presented. The temperatures of both retrieval techniques agree within the uncertainty margin. Although, the sub-mm profiles show more variability, it has to be pointed out, that the sub-mm profiles represent an weighted average over a broad range

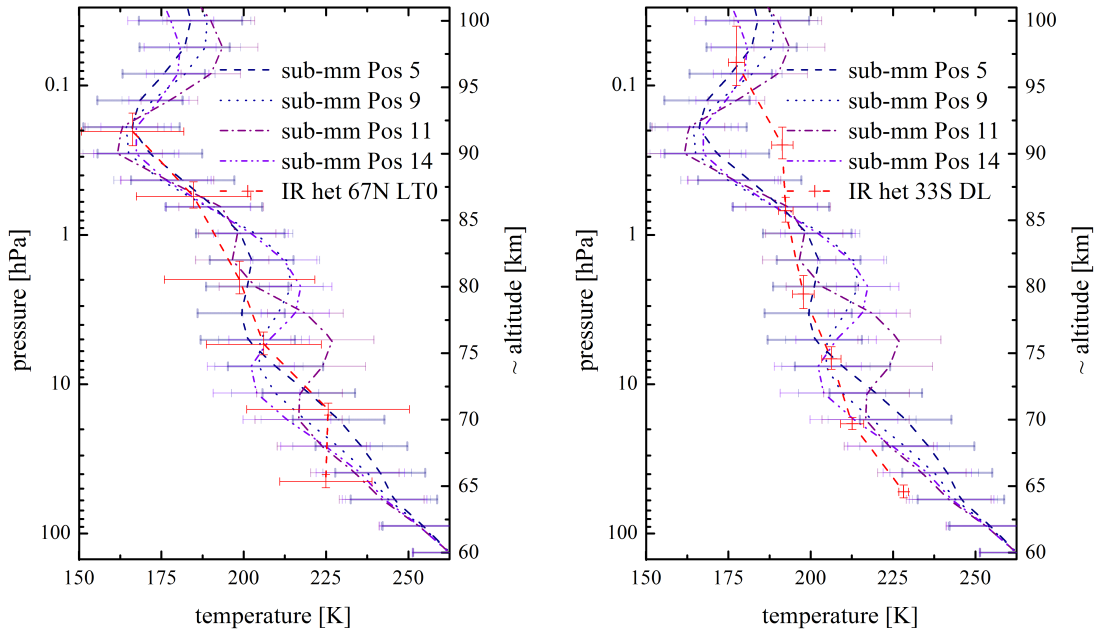

(a) *IR heterodyne observations at 67°N and local time 0:00.*

(b) *IR heterodyne observations at 33°S and the dark limb.*

Figure 4.38: *pT-profiles from IR heterodyne observations (red) during campaign B and sub-mm observations (bluish) for all sub-mm observing positions 5 (disk center) on the Venusian disk in June 2007. The sub-mm profiles are the mean values of the profiles in Fig. 4.35 in the respective altitude region. The IR heterodyne profiles agree within the uncertainty range with the sub-mm observations.*

of LT, since the beam covers almost all of the nightside disk. Taken this into account, the IR heterodyne profile at EQLT20 (Fig. 4.37(a)) is shifted to colder temperatures compared for instance to the profile from observing position 5, which was acquired with a beam centered on the Venus' apparent disk, yielding contribution also from the sunlit side of the planet. The other profile, obtained during campaign A, EQLT22 (Fig. 4.37(b)) agrees within the uncertainty range with all sub-mm profiles at each pressure layer. The IR heterodyne profile shows a much more stable temperature decrease with altitude, again caused by the long integration of 480 min whilst the seven days of observations, but also due to the higher altitude resolution of the sub-mm profiles.

For campaign B, the high latitude measurement at 67NLT0 (Fig. 4.38(a)), is difficult to compare. The sub-mm profiles were all obtained at, or close to, the equator. The wide FoV does include the high latitudes too, but the characteristics of the circumpolar region cannot be defined well enough by sub-mm measurements to make

a sophisticated analysis of these latitudes. Still, the average profiles are compared to the IR heterodyne data for the sake of completeness. The sub-mm profiles, unsurprisingly, do not show the isothermal part in the lower altitude. Nevertheless, the variability of the temperatures retrieved with sub-mm heterodyning enables at least a global comparison and it is to observe, that the profiles coincide. Concerning the observing position at 33SDL (Fig. 4.38(b)) comparison is very limited due to geometrical constrains. Sub-millimeter measurements were carried out close to Venus orbit's maximum eastern elongation. Thus, the nightside of Venus, which was half illuminated, covered only local times roughly from noon to midnight. The profile obtained with IR heterodyne, in contrast, covers a local time from 3:20 till 3:26 in the morning, hence a position on Venus, not approachable from the ground in June 2007. The profiles plotted in the graph nevertheless agree within in the uncertainty range. The bottom layer at ~ 65 km altitude is remarkably cooler for the IR profile, whereas at higher altitudes, especially at ~ 91 km it is substantially warmer. This might be most probably due to the vast divergence of the observed local times.

4.4.3 Comparison to the Reference Atmosphere

As mentioned before in the introductory part of this chapter, the Venus International Reference Atmosphere provides the most commonly used model profiles for representation of the thermal properties of Venus. Although the model is only based on five profiles each on the day- and the nightside, and the outdated state of the art, it is still the model for temperature comparison. Talking about Venus' thermal properties, the VIRA profiles have to be taken into account, at least for completeness.

In Fig. 4.39 the five VIRA pT-profiles at hand for the Venusian nightside are displayed. The profiles were taken from *Seiff et al.* [110]. The model predicts a cooling of the lower altitudes within the cloud deck (40–60 km) towards the poles, whereas the upper altitudes above the clouds tend to develop a warmer isothermal part or even transform into an inversion layer. All profiles converge into the same course at an altitude of ~ 100 km. The model does not distinguish between the northern and the southern hemisphere and assumes a symmetric behavior. The temperatures in the altitude region commensurate to IR heterodyne observations will be compared to the retrieved profiles in the following.

The profile derived from the first observing position on campaign A at EQLT20 is plotted together with the VIRA prediction for the low latitudes between 0–30° in Fig. 4.40(a). The measurement agrees within its uncertainty range to the model

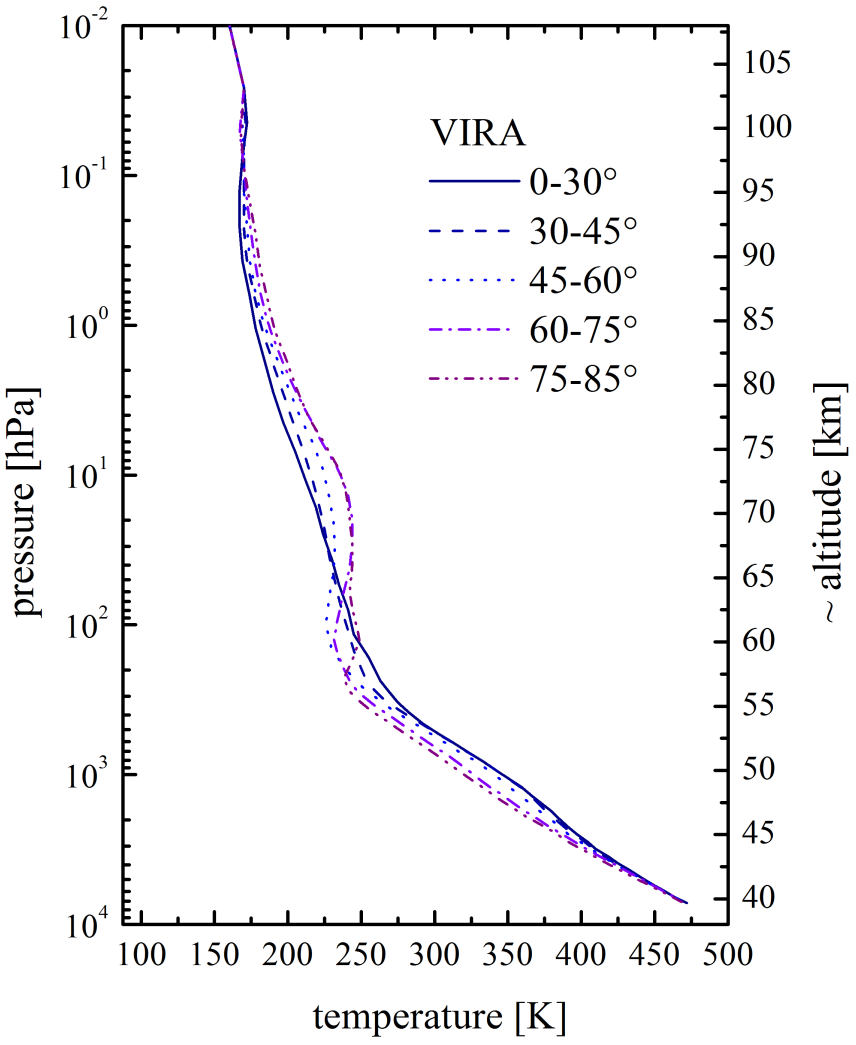

Figure 4.39: *Model predictions from* VIRA *for pT-profiles for the Venusian nightside. The latitudinal variation represents the northern and southern hemisphere, assuming a symmetric behavior. Towards higher latitudes, the low altitude temperature (40–60 km) decreases. At the cloud top, a change in the temperature profile is predicted for all latitudes. In the low latitudes, a steep lapse rate for a monotonically decreasing with altitude profile is observed, transforming into an isothermal layer with a tendency of an inversion towards the poles. The profiles merge for the upper boundary at 100 km altitude.*

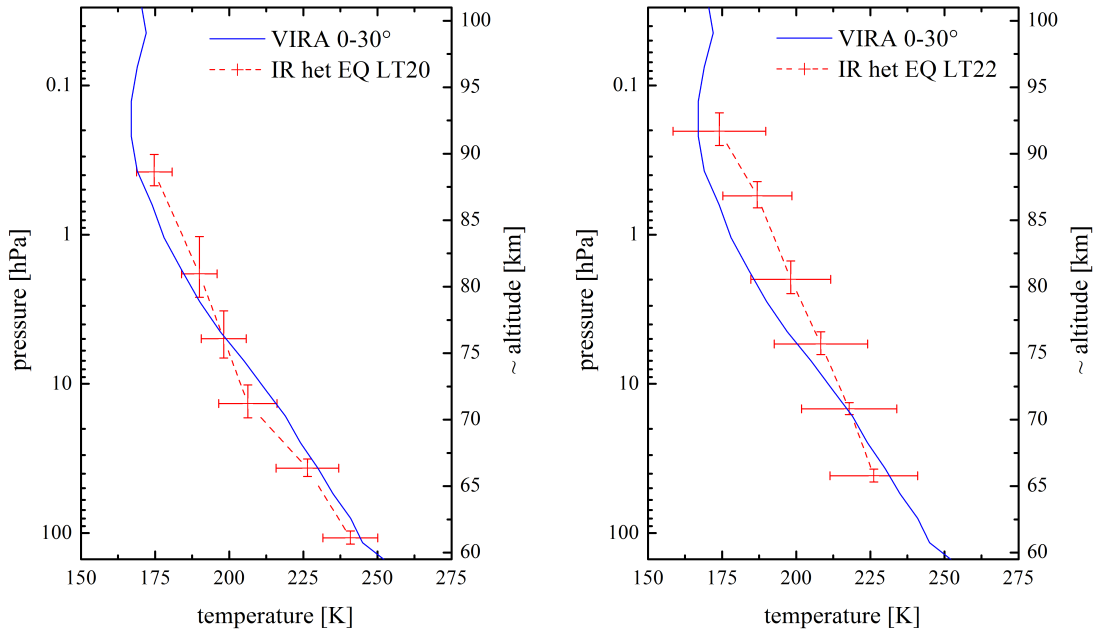

(a) *IR heterodyne observations at the equator and local time 20:00. The profiles coincide within the uncertainties of the IR heterodyne profile.*

(b) *IR heterodyne observations at the equator and local time 22:00. The two profiles coincide except for the pressure layer at 0.55 hPa.*

Figure 4.40: *pT-profiles from IR heterodyne observations (red) during campaign A and* Vira *model predictions (blue) for the corresponding low-latitudes between 0–30°, averaged over the Venusian nightside.*

for each single pressure layer. The small deviation to higher temperatures in the region between 60–75.5 km and the crossing point at 75 km, predicting colder air above, can be due to the low latitudinal resolution of the model. Also the Vira profiles is averaged for the whole nightside, neglecting all thermal variations from the evening to the morning terminator. In Fig. 4.40(b), the same Vira model for low-latitudes is displayed along with the IR heterodyne profile at EQLT22. The two profiles coincide within the error margins, except for the pressure layer at 0.55 hPa, $\sim$87 km altitude. The large deviation in this layer is part of the global behavior of the IR heterodyne profile, which tends to measure slightly warmer temperatures than predicted by Vira in the higher altitudes. Only the high pressure layer (lowest altitude) is colder than the Vira model claims. However, again, it has to be pointed out, that the model is only an average over a manifold of parameters and thus, cannot be regarded as representative for the selected observing geometry.

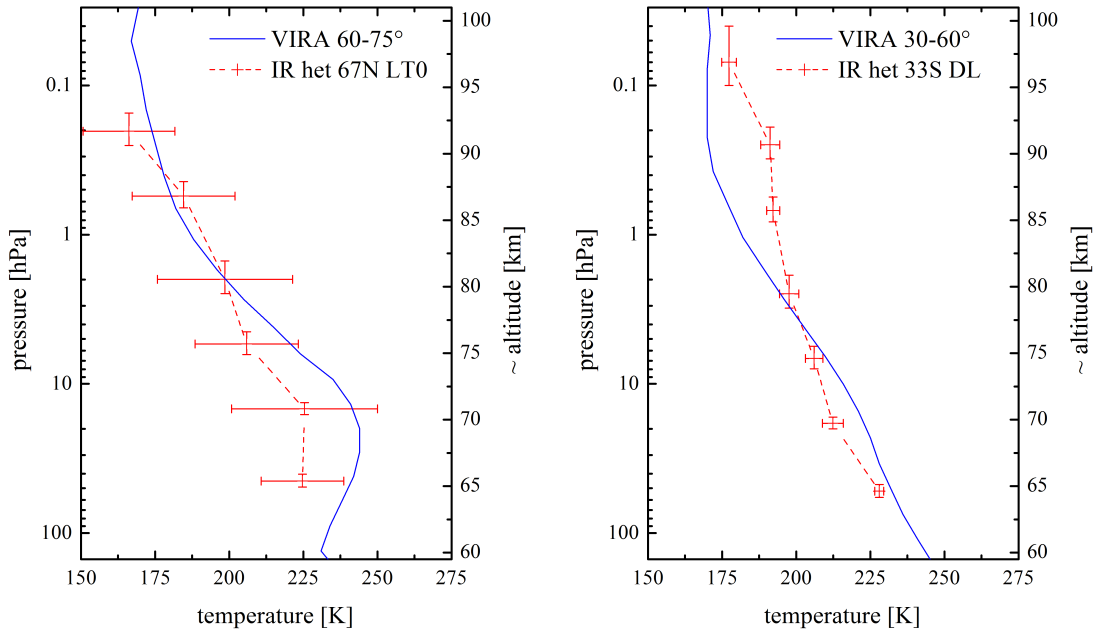

(a) *IR heterodyne observations at 67° N and local time 0:00. The two profiles coincide within the uncertainties of the IR heterodyne profile.*

(b) *IR heterodyne observations at 33° S and the dark limb. The two profiles do not agree within the uncertainties, except for the middle layers.*

Figure 4.41: *pT-profiles from IR heterodyne observations (red) during campaign B and* Vira *model predictions (blue) for the corresponding latitudes between 60–75° (Fig. 4.41(a)) and 30–60° (Fig. 4.41(b)), averaged over the Venusian nightside.*

The comparison between the Vira model for for the campaign B measurements is provided in Fig. 4.41. For higher latitudes between 60–75° at observing position 67NLT0 (Fig. 4.41(a)) the model shows a small temperature inversion at altitudes around 69 km. The IR heterodyne profile is almost isothermal for the corresponding region just above the cloud layer. Except for the high pressure layer at 44.77 hPa, all temperatures are in agreement with the Vira prediction. Above the inversion layer, the model, as well as the observations, show a decrease with altitude and the profiles are, despite the bad spatial resolution of the model, compatible. The profile measured at the 33SDL is displayed along with the mid-latitude Vira profile in Fig. 4.41(b). The Vira model predicts a constant decrease with altitude of the temperature in the Venusian nightside mid-latitudes. A small bulge towards a higher temperature can be observed in the profile at an altitude around 70 km. For higher altitudes, above $\sim$ 87 km, the model gets isothermal. The two profiles show the most significant deviation of all profiles. Only the temperatures in the middle pressure layers at 6.77 hPa and 2.49 hPa are in agreement with

the VIRA prediction within their uncertainties. However, the previous comparisons to space- and ground-based observations have proven, that the observations are a sophisticated representation of the mesospheric thermal structure. The large deviation of the two profiles might be due to the lack of data and, as mentioned before, the poor spatial resolution. Especially the high diurnal variability in the mesospheric mid-latitudes can explain the bad compliance of the observation and the model.

4.5 Conclusion Venus

The new inversion routine, especially developed to deduce vertical pressure- temperature profiles by analyzing the shape of CO_2 absorption lines, has been applied to four different spectra, obtained on the nightside hemisphere of Venus. The data sets were retrieved during two observing campaigns in 2012. Retrieval of thermal profiles from ground-based observations in the mid-IR has never been accomplished before. The results represent vertical temperature profiles, which are obtained from ground-based IR heterodyne spectroscopy for the first time ever. The new technique enlarges the possibility of investigation of the Venusian atmosphere from Earth. It is found, that an integration time of at least 90 min on the source is needed to receive a SNR, which is sufficient for the retrieval method. The uncertainties of the temperatures are depending on the SNR and are found to be in the range between 1.5–25 K. The altitude resolution of the new IFR for Venus profiles is one full scale height of ~ 4.5 km throughout the probing region. The corresponding pressure grid is calculated according to the barometric formula in Eq. (3.1) and is adapted to the specific conditions of each observing position. The required integration time imposes constrains on the possibility to observe short time fluctuations, i.e. to investigate the static stability of the mesosphere. However, the new technique has proven to be applicable to extraterrestrial observations and thus widens the field of application for remote sensing in the mid-IR wavelength range.

The results are discussed in the context of existing measurements from space and ground. An overview of each observing position, compared to all other considered profiles is given in Fig. 4.42. It is found, that the profiles retrieved with IR heterodyne observations coincide in any way to the previously well-established observing techniques. Variability of the IR heterodyne profiles with latitude and local time is observed. Especially towards the pole, an isothermal behavior of the lower altitude, just above the clouds, is seen. This is conform to other observations.

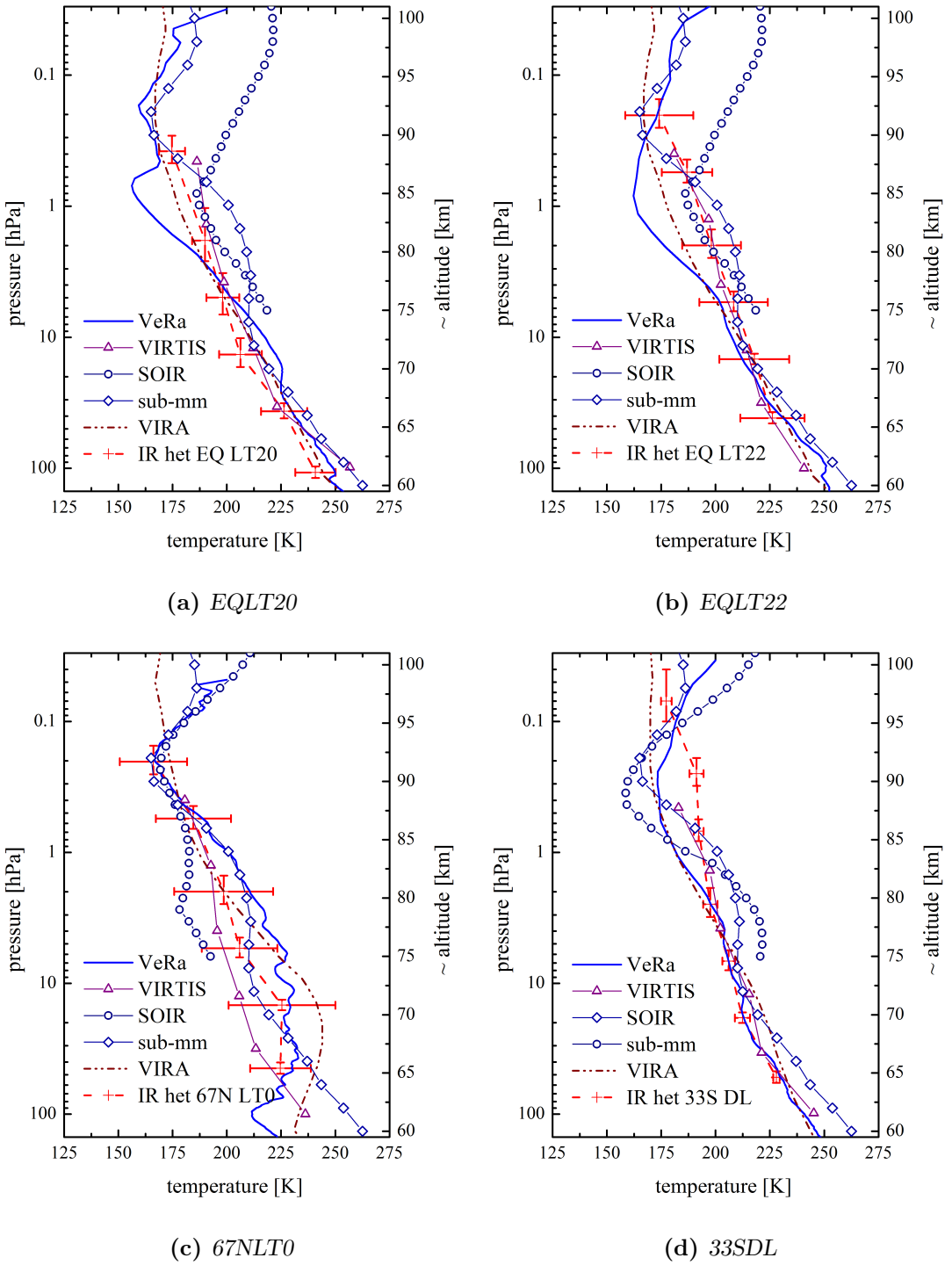

(a) *EQLT20* **(b)** *EQLT22*

(c) *67NLT0* **(d)** *33SDL*

Figure 4.42: *pT-profiles from IR heterodyne observations (red) at the four different observing positions plotted with all profiles from the different observing techniques and model predictions described in the previous comparison section.*

Ground-based observations is not compatible to space exploration in respect to spatial resolution or integration time, but it stands out by its financial budget and flexible application possibilities. The results found in the work herein are proven to be reliable and a high potential for future measurements is given. Comparison to models, however, is still limited, but IR heterodyne observation can contribute to improve existing GCMs by providing observed data. The new ground-based observing possibility can contribute a lot to the exploration of Venus, especially in the post-VEX era. Despite the lower altitude resolution for IR observations compared, i.e. to heterodyning at sub-mm wavelengths, infrared measurements can provide a much more detailed mapping of the planet, due to its higher spatial resolution.

Besides the thermal properties in the Venusian atmosphere, the new inversion routine could also be able to contribute altimetry data. As mentioned, the Venusian atmosphere becomes opaque to IR radiation at the cloud top. Hence, the highest pressure value that is found, can be allocated to the cloud top altitude. However, this would need a revision of the applied radiative transfer code. Up to date, CODAT does not account for the curvature of the planet, since it was designed as a 2D model. To assign a defined cloud top altitude at locations more than 30° apart from the disk center, a 3D model is mandatory.

Chapter 5

"Mars is there, waiting to be reached."
(Buzz Aldrin)

The Atmosphere of Mars

5.1 Introduction

Mars is the second closest planet to Earth and the fourth in the heliocentric row. The planet possesses a surrounding atmosphere and a solid core. Besides Mercury, Mars is the smallest planet in our solar system with an equatorial radius of 3396.2 km. Its red surface is caused by oxidized iron, which globally covers the planet. Despite its smaller size, Mars is presumably the most Earth-like planet in our solar system in terms of climate condition and habitability. The orbit is elliptical with a semi-major axis of ~ 1.52 AU and a sidereal orbiting period of ~ 686 Earth days. The sidereal rotation period is just a little longer than on Earth, yielding a 24.6 h Mars-day. Mars is the only other terrestrial planet, besides Earth, with an atmosphere that shows a distinct seasonal behavior due to an axis tilt of 25.19°. The Martian seasons are commonly characterized in terms of the solar longitude L_S. A solar longitude of 0° corresponds to the northern hemisphere spring equinox. During the winter season, large ice caps form in the polar regions as it can be seen in Fig. 5.1(a). The most important bulk and orbital parameters of Mars are summarized in comparison to Earth in Tab. 5.1. The Martian topography is versatile, but basically it has to be distinguished between the so called lowlands in the northern hemisphere and the highlands in the south-

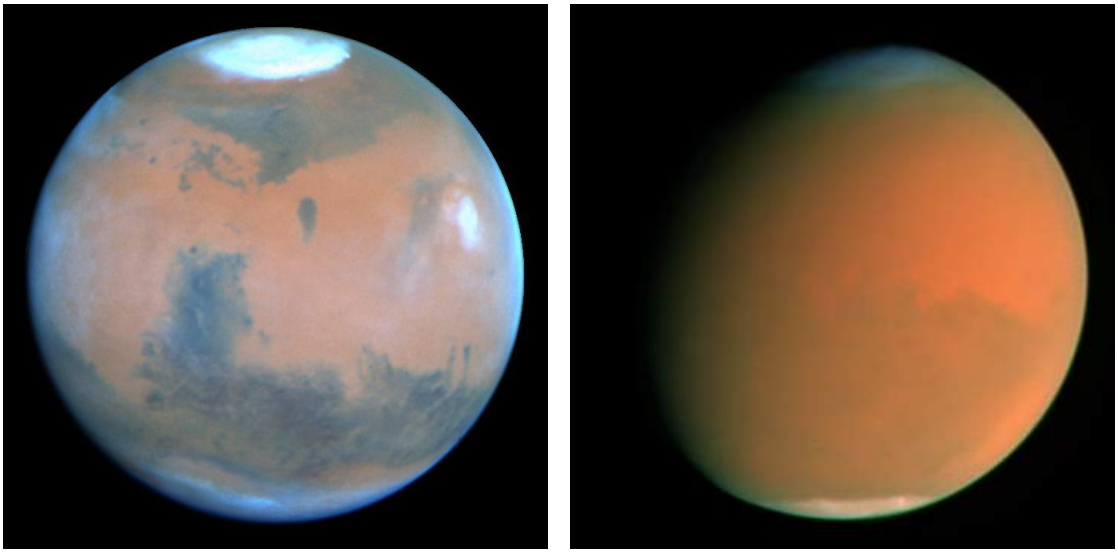

(a) *Martian surface features. The Syrtis Major region can be found at ∼ 270° longitude [176].*

(b) *Mars observed during a global dust storm in September 2001*

Figure 5.1: *Global images of Mars, taken by the Wide-Field Planetary Camera 2 on the Hubble Space Telescope*

ern hemisphere. The Martian equivalent of the telluric sea-level, or geoid, is called areoid, defined at the pressure level of the triple-point of water, at 6.105 hPa.

The atmosphere of Mars can be divided into three main thermal regimes. The lower atmosphere, the troposphere, extends up to an altitude of ∼ 45 km. The mesosphere is located between ∼ 45 km and ∼ 110 km. On top, the exosphere, or thermosphere is located up to ∼ 200 km altitude. The hottest temperatures in the troposphere can be found around the SSP during summer, when solar insulation is at its maximum. The coldest temperatures, on the other hand, are found to be at the winter poles. Hence, the temperatures are subject to a high latitudinal variability over seasons. The thin Martian atmosphere can supply only a small greenhouse effect. Therefore, a high temperature gradient exists between the day- and the nightside atmosphere, forcing zonal wind fields around the planet [7].

Besides the gaseous component of the atmosphere, the Martian dust plays an important role for the radiative balance of the planet. During global dust storms, i.e. the dust is lifted into the lower troposphere, covering the planet in an opaque shell. See Fig. 5.1(b) for a reference picture on this effect. The dust absorbs solar light at visible and mid-IR wavelengths around 9 µm [178]. Lofted dust can contribute to a strengthening of the Martian meridional circulation cells and thus leads to a stronger pressure gradient [7]. The airborne dust can contribute on one

Parameter	Mars	Earth	Ratio (Mars/Earth)
Radius at equator (km)	3396.2	6378.1	0.532
Surface gravity (km/s^2)	3.71	9.81	0.379
Natural satellites	2	1	-
Semimajor axis (10^6 km)	227.92	149.6	1.524
Sidereal orbit period (days)	686.980	365.256	1.881
Sidereal rotation period (days)	1.027	0.998	1.029
Solar day (hours)	24.660	24.000	1.027
Obliquity to orbit (deg)	25.19	23.44	1.075
Distance from Earth (10^6 km)			
Minimum	55.7	-	-
Maximum	401.3	-	-
Apparent diameter (arcsec)			
Minimum	3.5	-	-
Maximum	25.1	-	-

Table 5.1: *Important orbital parameters of Mars and Earth from [177].*

Parameter	Mars	Earth
Surface pressure (hPa)	6.105	1014
Surface density (kg/m^3)	~ 0.020	1.217
Mass of atmosphere (kg)	2.5×10^{16}	5.1×10^{18}
Mean molecular weight (g/mole)	43.34	28.97
Composition		
Major	95.3% CO_2	78.08% N_2
	2.7% N_2	20.95% O_2
	1.6% Ar	-
	0.13% O_2	-
	0.07% CO	-
Minor	210 ppm H_2O	9340 ppm Ar
	100 ppm NO	400 ppm CO_2
	2.5 ppm Ne	18.18 ppm Ne
	0.85 ppm HDO	5.24 ppm He
	0.3 ppm Kr	1.7 ppm CH_4
	0.08 ppm Xe	0.55 ppm H_2

Table 5.2: *Atmospheric parameters of Mars and Earth. Minor constituents are given in parts per million (ppm) [177].*

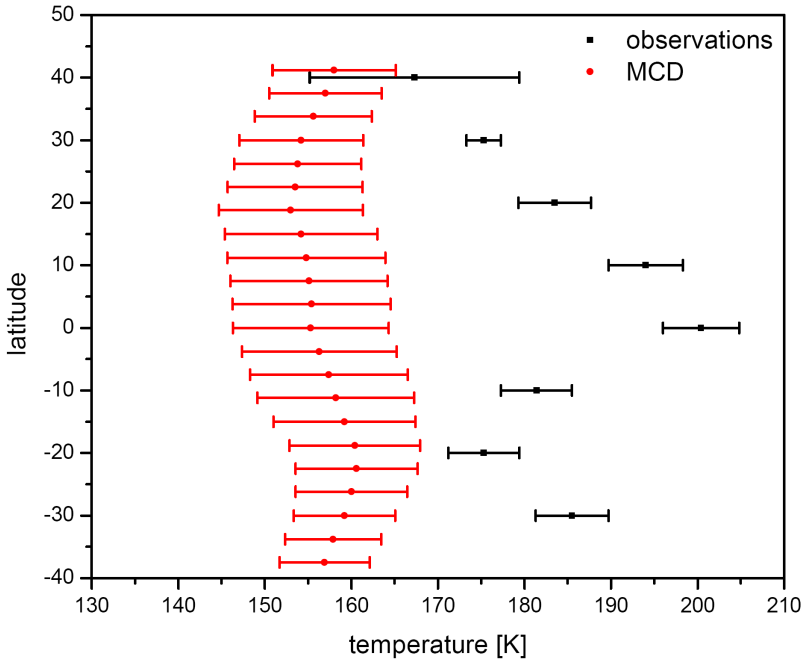

Figure 5.2: *Kinetic temperatures in the 0.001 hPa pressure level retrieved from IR heterodyne observations of CO_2 non-LTE emission features in 2007 (black), compared to* MCD *model predictions. The error bars represent the fitting uncertainty (black) and monthly average from the* MCD *(red). From Stupar [41].*

hand to the greenhouse effect, by back-scattering emitted light from the Martian surface, but on the other hand, weaken the solar insulation, producing local regions of high static stability [179].

5.1.1 Temperatures from IR Heterodyne on Mars

In recent years IR heterodyne spectroscopy has been utilized to study the thermal properties of the Martian mesosphere. For this purpose, spectra taken on the dayside of the planet were analyzed. The Martian dayside spectra are composed of two different features: a broad absorption feature from lower, pressure-broadening dominated altitudes and a narrow non-LTE emission core. For the investigation of the purely Doppler-broadened non-LTE features, the broad CO_2 absorption line, originating from lower altitudes needs to be removed. Temperatures on the sunlit side of the planet can be directly deduced from the width of the non-LTE emission feature. Non-LTE emission occurs at a pressure level around 1 µbar (0.001 hPa). CO_2 molecules in the atmosphere are pumped by solar irradiation to

higher energy states at 4.3 µm and de-excite by spontaneous emission at 10.3 µm. The probability for spontaneous emission increases that for collisional de-excitation at this low pressure level [53]. A careful analysis of the thermal properties at the 0.001 hPa level has been conducted by *Stupar* [41]. He used CoDAT as a forward model in order to diminish the effect of the absorption feature to the non-LTE. Hence, a good knowledge on the underlaying thermal profile is inevitable. Therefore, model predictions from the Mars Climate Database (MCD [180]) were used as input pT-profiles, carefully chosen for the specific observing position. A latitudinal variability of the kinetic temperatures between $\sim$170 and $\sim$200 K for observations performed in 2007 was found. Fig. 5.2 shows a comparison between the IR non-LTE temperatures and model predictions from the MCD. With the newly developed IFR, the temperature profiles can be additionally deduced from the absorption line, widening the probing altitude to the lower troposphere. Hence, the impact of IR heterodyne observations can be increased significantly for the Martian atmosphere.

5.2 Retrieval of Thermal Profiles

First attempts to deduce vertical temperature profiles from observations on the Martian dayside have been performed recently. Up to date, only preliminary results for one observing geometry can be provided. The approach of the IFR suffers some issues when applied to Mars observations which will be discussed in the following. Further studies need to be made in the future, in order to establish the IFR for Mars. A proof of concept that, performed to show the reliability of the IFR for Martian data, did not yet provide the unambiguous results as it was the case for Venus. Hence, predications on the thermal properties of the Martian atmosphere at lower altitudes are still limited. In addition the analyzed data seem to be contaminated by a standing wave pattern in the back-end radiometer. In the following, the proof of concept is presented in detail and the results from first analysis of Martian spectra using the IFR are discussed.

5.2.1 Altitude Resolution

The biggest constraint when dealing with Martian data is the altitude resolution in the lower troposphere. Following the approach described in Sec. 3.3 by using the barometric formula for a first order assumption of the pressure layering, the scale height on Mars is estimated to be around 10.5 km. A CO_2 volume mixing ratio of 0.935 is assumed. The gravitational constant on Mars required in Eq. (3.1)

is $g = 3.71\,\mathrm{m\,s^{-2}}$ and the pressure at the surface is chosen to be 6.1 hPa, which corresponds to the 0 km altitude at the areoid. Since the Martian surface holds more topographic variability than the Venusian cloud decks, the surface pressure may vary by ± 4.0 hPa. The average temperature at - and within the first atmospheric layer above - the surface on Mars is highly variable in latitudes and local time and T is estimated to be between 190 K and 230 K, yielding a scale height between 9.67 km and 11.71 km. This leads to an uncertainty in the determined pressure, which is accounted for by providing error bars in the plots.

5.2.2 Proof of Concept

Similar to the Venus proof of concept in Sec. 3.4, a variety of synthetic spectra was created to simulate observed IR heterodyne data. To create the spectra, pressure-temperature profiles were extracted from the MCD as input profiles and white noise was added to the modeled spectra.

One major impact on the retrieval of thermal profiles from data obtained at the Martian dayside is the presence of the non-LTE emission line in the core of the absorption feature. In order to investigate the influence of the emission feature on the retrieval method, two spectra with different non-LTE emission intensities were created based on the same pT-profile. The pressure grid for the retrieval was determined according to an altitude resolution of a full scale height. The results are summarized in Fig. 5.3. In the top figures (Fig. 5.3(a) and Fig. 5.3(b)), the synthetic spectra are displayed along with the input model and the output model. The spectrum displayed by the blue line was obtained using the blue pT-profile in Fig. 5.3(c) in both cases. The green lines represent the computed spectra, using the retrieved output pT-profiles - also displayed in Fig. 5.3(c). During the retrieval, the non-LTE emission was simulated by CODAT by superimposing a Gaussian function with given input parameters to the absorption line at the specific frequency position. Only the intensity of the non-LTE emission line was varied. The FWHM was kept constant. It can be observed, that the output model deviates strongly from the data sets. The residuals, plotted at the bottom of Fig. 5.3(a) and Fig. 5.3(b) show a wavy pattern. The wings of the line cannot be accurately fitted when applying the chosen pressure grid. However, the normalized altitude weighting functions displayed in Fig. 5.3(d) show well-defined and isolated peaks, yielding the capability to resolve each specific pressure layer individually. Only the top layers contribute equally to the line formation and the layer at the lowest pressure of ~ 0.15 hPa must be neglected. The intensity of the non-LTE emission core influences the quality of the fit only at the line core. Nevertheless, the derived temperature profiles in Fig. 5.3(c) agree within the uncertainties to each other and

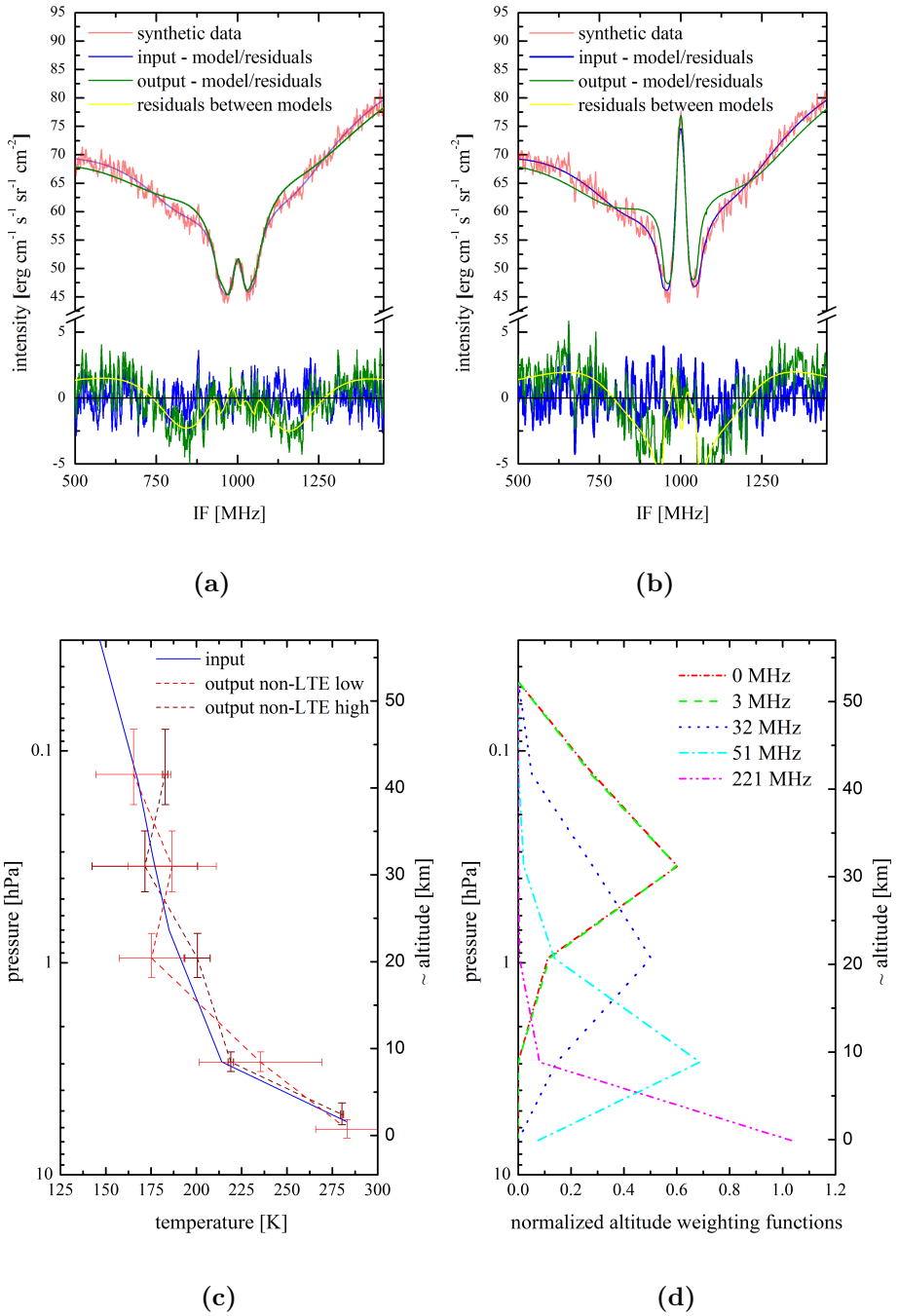

Figure 5.3: *Synthetic spectra to simulate observed IR heterodyne data from Mars. Top: (a) and (b) - Synthetic data with white noise (red), modeled radiative transfer through the atmosphere, 1) (blue) based on the blue input-profile displayed graphic (c) and 2) (green) based on the retrieved pT-profiles in graphic (c) for the respective spectrum, each with the corresponding residuals to the data. 4) The residuals between the input and the output model (yellow). The data sets were smoothed over 5 MHz for display. Bottom: (c) - Input (blue) and retrieved (redish) pT-profiles from the synthetic spectra. (d) - Normalized altitude weighting functions to display the contribution of the single pressure layers to the spectra at 5 different frequencies. The frequencies are those, where the contribution of one specific layer is maximum. The frequencies are given as an offset to the frequency of the line center.*

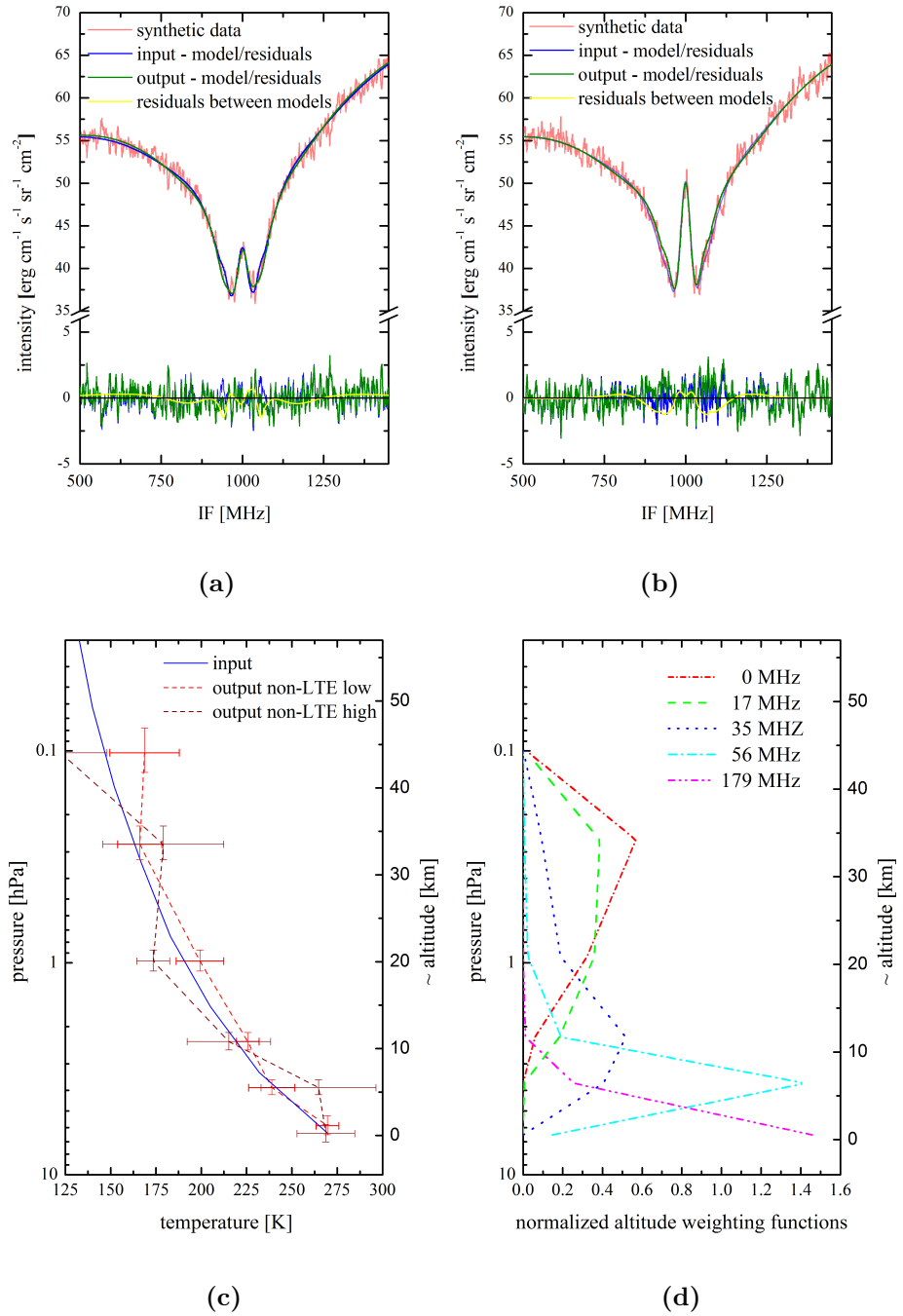

Figure 5.4: *Synthetic spectra to simulate observed IR heterodyne data from Mars. Top: (a) and (b) - Synthetic data with white noise (red), modeled radiative transfer through the atmosphere, 1) (blue) based on the blue input-profile displayed graphic (c) and 2) (green) based on the retrieved pT-profiles in graphic (c) for the respective spectrum, each with the corresponding residuals to the data. 4) The residuals between the input and the output model (yellow). The data sets were smoothed over 5 MHz for display. Bottom: (c) - Input (blue) and retrieved (redish) pT-profiles from the synthetic spectra. (d) - Normalized altitude weighting functions to display the contribution of the single pressure layers to the spectra at 5 different frequencies. The frequencies are those, where the contribution of one specific layer is maximum. The frequencies are given as an offset to the frequency of the line center.*

to the input profile, although variations in the profiles exist. These variations are due to cross-correlations between the low-pressure layers, which cannot be individually resolved.

Further synthetic spectra were created, taking a different temperature input profile as a basis (comp. Fig. 5.4(a) and Fig. 5.4(b)). With the gained knowledge about the altitude resolution, these spectra were analyzed and the pT-profiles were regained. This time, the pressure layers were calculated assuming an altitude resolution of half a scale height in the high pressure levels ($< 1\,\mathrm{hPa}$) and one full scale height above. This approach was performed in order to increase the fit quality at the wings of the absorption line. The resulting temperature profiles for two such spectra, with a low and a high non-LTE emission intensity are plotted at the bottom left in Fig. 5.4. The two profiles agree within the uncertainties except for the value at $\sim 1\,\mathrm{hPa}$. However, the profiles are still not in exact compliance, which would have been expected. This can be due to the influence of the non-LTE emission peak. At the top of Fig. 5.4 the input and the output model are compared. The models are based on the thermal profiles plotted in Fig. 5.4(c). The output models fit very well to the data and the residuals are even and without any noticeable variation that exceeds the noise. The deviation between the input and the output model is reasonable small - less than the noise amplitude. Hence, in order to obtain a better fit between the in- and the output model, the SNR has to be increased.

Another issue could still be the altitude resolution, which might have been chosen to high with a value of half a scale height. The normalized altitude weighting functions for the applied pressure grid are plotted in Fig. 5.4(d). It can be observed, that only the two bottom layers can be resolved. The contribution to the line forming in the third layer is already smeared and the contribution from the $\sim 3.7\,\mathrm{hPa}$ and the $\sim 2.2\,\mathrm{hPa}$ layer at a frequency $\pm 35\,\mathrm{MHz}$ offset to the line center is almost identical. Hence, a cross-correlation between the two layers cannot be avoided anymore. The high altitude layers, in contrast, contribute mostly to the line tip. Since the non-LTE emission is superimposed at these frequencies, the retrieved temperatures are of limited significance. It can be assumed, that the line wings form in the pressure layers between the surface and $\sim 1\,\mathrm{hPa}$ ($\sim 20\,\mathrm{km}$ altitude). Nevertheless, the top layers cannot be neglected, since they contribute to the line formation even down to the lower layers. Only the top layer at $0.1\,\mathrm{hPa}$ has no influence on the line forming and must be omitted for future retrieval.

With these synthetic data sets it can be shown, that the basic idea of the IFR can be applied to heterodyne spectra obtained in the Martian dayside atmosphere. The influence of the non-LTE emission core is marginal and vanishes within the retrieval uncertainty. Nevertheless, the first attempts to retrieve sophisticated and reliable temperature profiles from these spectra suffered some issues which cannot

be neglected. A careful investigation of the altitude resolution has to be performed when dealing with Martian spectra, since is neither the spectra can be accurately modeled (for a low altitude resolution of a full scale height) nor cross-correlation between the adjacent layers can be avoided (for a high altitude resolution of half a scale height). Hence, the truth is somewhere in between, yielding the possibility of a non-linear pressure binning. This has to be taken into account for the analysis of observed spectra.

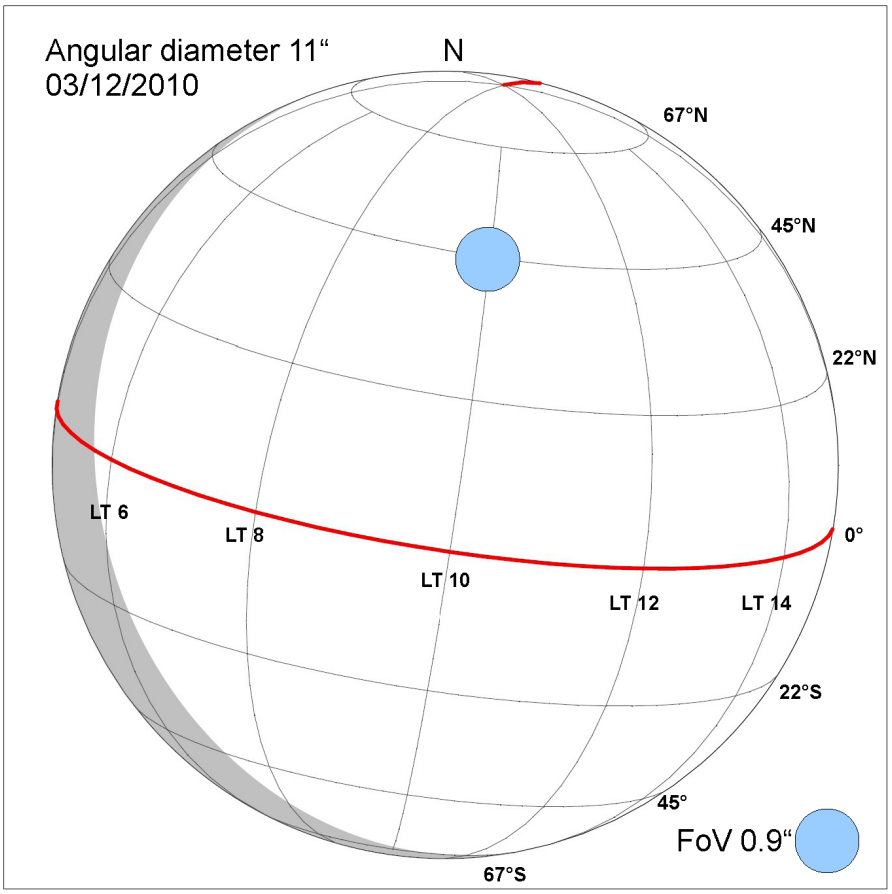

Figure 5.5: *Observing geometry of Mars for campaign C in March 2010 at the* IRTF *on Mauna Kea. The blue circle represents the diffraction limited field of view true to scale with the angular diameter of the apparent disk. The angular diameter of the apparent disk was ∼11” and the illuminated fraction 94% . For orientation, the LT and the latitudes are indicated for the geometry on March 12.*

5.3 Data Analysis and Results

To investigate the behavior of the IFR when applied to measured data, a spectrum obtained with with IR heterodyne observations is analyzed. In the following, relevant information on the spectral properties is given and preliminary results are presented.

5.3.1 Observing Campaign C

Observation of absorption lines on the Martian dayside were carried out, amongst others, using the spectrometer THIS at the IRTF in March 2010. Mars was at solar longitude $L_s = 62.8$, which corresponds to the northern summer, in Martian year 30. Mars' angular diameter was 11" with an illuminated fraction of 96%. One observing position was approached, which possesses a SNR feasible for temperature retrieval. The observing geometry and the positions are shown in Fig. 5.5. The blue circle indicates the FoV at the targeted position, true to scale to the apparent disk of Mars. The observed position is located at 45°N latitude and 151°W in planetary coordinates, corresponding to an LT on Mars of $\sim$10:00 (45NLT10). The total on-source integration time was $\sim$17 min and any possible changes in the observing geometry due to the motion of Mars will be neglected for this short period.

Camp.	Instrument	Telescope & Location	FoV	Altitude	Date
C	THIS	IRTF, Mauna Kea, HI	0.9"	4205 m	March 12 2010

Table 5.3: *Overview of the observing campaign C.*

L_s	Ang. Diameter (% illuminated)	Position	Latitude	Longitude	Mars Local Time
62.8	11" (96%)	45NLT10	45°N	151°W	10:00

Table 5.4: *Overview of the observing geometry for campaign C.*

5.3.2 Measured Spectrum at 45NLT10

The measured spectrum from observations at position 45NLT10 is shown in Fig. 5.6. The corresponding SNR, here again calculated as the ratio between the depth of

the absorption line and the noise amplitude, was found to be (5.8 ± 1.5). The data (red) is plotted along with the output model of the IFR (blue) and their residuals (green). The spectrum was rescaled to 10 MHz resolution for display. The original spectrum with the full resolution of 1 MHz can be found in Appendix D. The model is based on the retrieved thermal profile displayed in Fig. 5.7 and discussed in the next section. To obtain the temperature profile from the data, a pressure grid was calculated assuming a layering which corresponds to three fourth of a scale height for the high-pressure layers (< 1.5 hPa) and a full scale height above. This was intended to improve the fit quality and to simultaneously avoid cross-correlation between adjacent pressure layers. However, the fit of the IFR does still not match the data very well. A sine fit was applied to the residuals, revealing a standing wave pattern that contaminates the data. The standing wave has a frequency of ~ 830 MHz and was interspersed to the IF processing while observing. In the gray shaded area, the non-LTE emission core resides. It can be observed, that despite the sinusoidal behavior, the residuals are minimal at those frequencies. For analyzing the spectrum, the non-LTE emission was modeled by CODAT by superimposing a Gaussian fit to the absorption line. The analysis of the width of the non-LTE emission would thus require a removal of the standing wave pattern in the data. The retrieved kinetic temperatures from the Gaussian width would therefore be erroneous.

5.3.3 Results and Comparison

The retrieved pT-profile is plotted in Fig. 5.7. Additionally, the MCD profile for the corresponding observing position is provided for comparison. Despite the bad fit to the spectrum, caused by the standing wave in the data, the retrieved profile agrees to the MCD profile within the uncertainties at three pressure layers. The lowest pressure layer is of low significance, since 1) the non-LTE emission is superimposed

45NLT10			
p (hPa)	$\triangle p$ (hPa)	T (K)	$\triangle T$ (K)
0.13	0.03	198.4	2.8
0.35	0.07	175.9	23.8
0.95	0.15	187.7	16.9
2.94	0.41	205.0	6.6
7.80	0.80	220.4	3.3

Table 5.5: *Retrieved temperature at given pressure layers for IR-heterodyne observations on Mars*

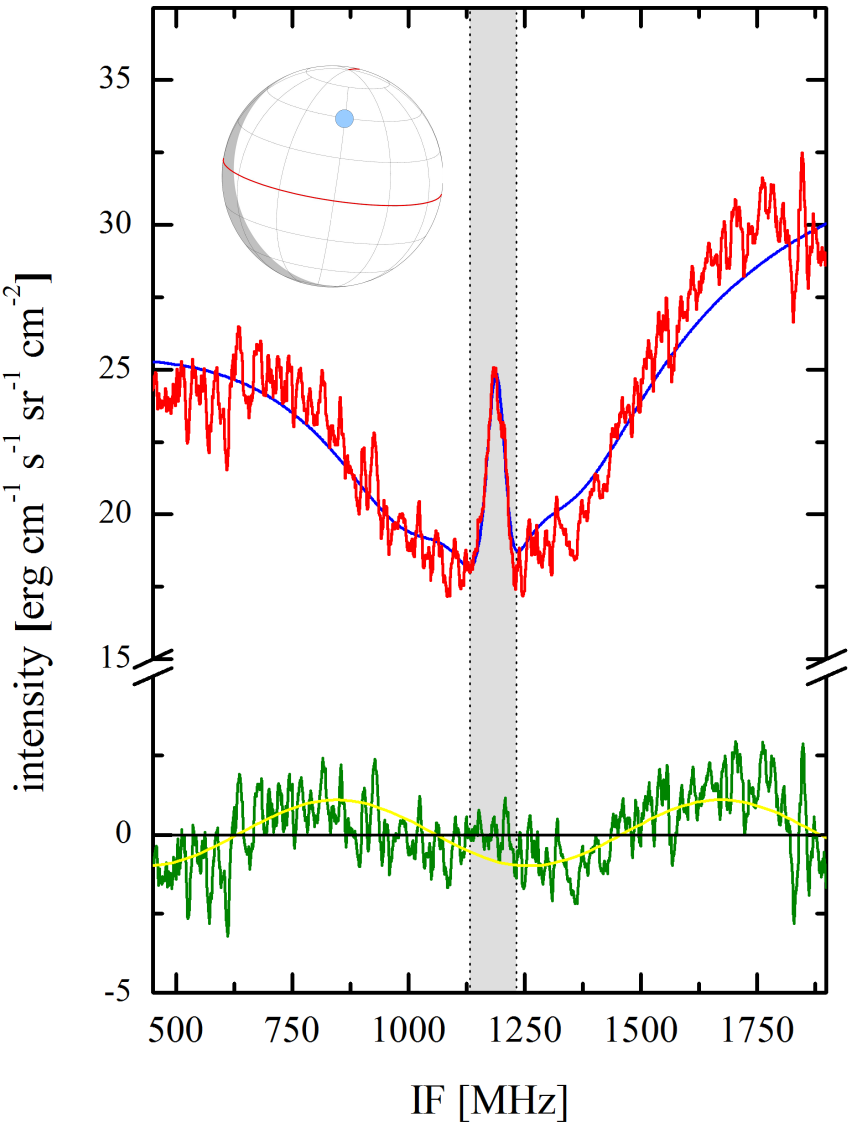

Figure 5.6: *Measured Spectrum from Campaign C at 45NLT10: The observing geometry is displayed in the insert graphic. The data is displayed in red with a SNR of* 5.8 ± 1.5*, the best fit in blue and the residuals in green. The center frequency of the line is at 1148 MHz. The normalized RMS of the residuals indicates the noise amplitude. The normalized RMS is 1.59 for an integration time of 17 min on source. The spectrum was rescaled to 10 MHz resolution for display. For the fully resolved spectrum see Fig. D.5. The gray shaded area marks the frequency position of the line center, where the non-LTE emission resides. It can be seen, that due to the fit of the emission, the residuals in this area are minimal, despite the sinusoidal standing wave pattern.*

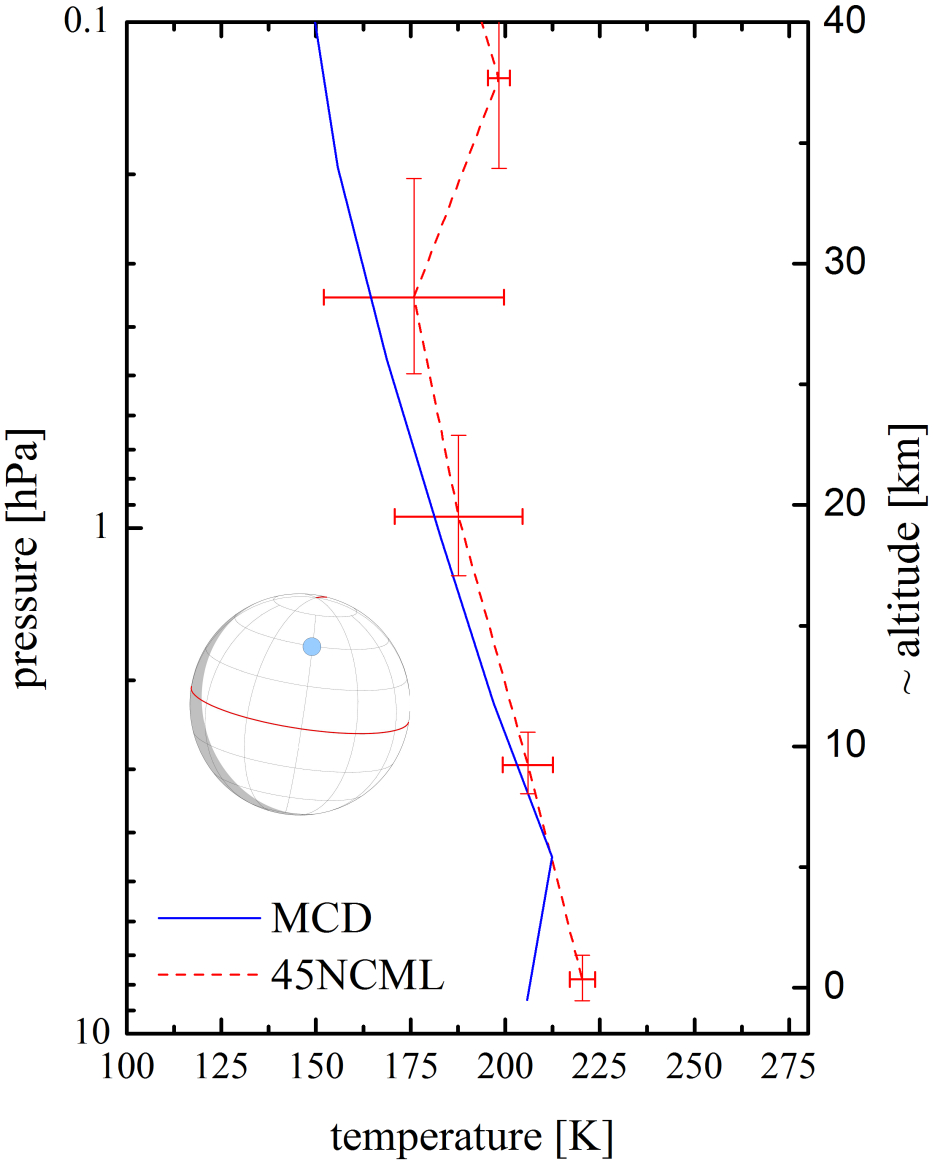

Figure 5.7: *Temperature profile from Campaign C at 45NLT10: The derived temperatures (with corresponding uncertainties) in the Martian atmosphere are displayed in red. The observing geometry is displayed in the insert graphic. The blue profile represents the pT-profile predicted by the* MCD *for the corresponding observing position. The two profiles agree within the uncertainties, except for the lowest and the highest pressure layer.*

to the data and 2) the contribution to the line formation from this layer is not high enough (comp. Fig. 5.3(d)). The highest pressure layer deviates from the MCD prediction towards higher temperatures. That can be due to the altitude resolution, which is not high enough to resolve small-scale variations like this temperature inversion close to the surface. Hence, the IFR retrieves an averaged temperature for the high-pressure layer.

5.4 Conclusion Mars

With the presented analysis, first statements about the possible application of the newly developed IFR can be given. The analysis of the Martian synthetic spectra yields a variety a complications that must be accounted for. The most crucial point is the altitude resolution of the retrieval. A careful analysis of the spectra has to be performed and different pressure grids need to be applied to avoid cross-correlations between adjacent layers and to uniquely resolve and retrieve the dominant temperature in each layer. In addition, the non-LTE emission feature that is present on the Martian dayside pollutes the spectra. Since the low pressure layer contributes also to the line formation offset to the line center position, a temperature can still be retrieved. However, the low pressure temperatures are not as reliable as those in the high-pressure layers and further studies on the influence of this emission feature needs to be performed.

The analysis of one measured spectrum shows a surprisingly good agreement to the prediction from the MCD, despite the very low fit quality. A standing wave pattern, polluting the spectrum, that was never seen before, was revealed from the data. A sine fit to the residuals yields a frequency of $\sim 830\,\mathrm{MHz}$ of the wave, which was picked up during observations. The results are yet only preliminary and still of low significance.

Chapter 6

"There are more things in heaven and earth, Horatio,
Than are dreamt of in your philosophy. ."
(William Shakespeare's Hamlet)

Outlook and Summary

Besides Venus and Mars, more terrestrial planets exist in our solar system. Especially the study of Titan's atmosphere by investigating the dynamical and thermal structure and composition has been emphasized by IR heterodyne spectroscopy in the past [49]. In addition, atmospheric studies of the most terrestrial planet - the Earth - by using IR heterodyne spectroscopy has been initiated recently. The possibility of the retrieval of thermal and dynamical properties of the telluric stratosphere is of high interest in the future.

In the following sections, an outlook on further applications on Mars and Venus for the newly developed IFR is given (see Sec. 6.1.1). In Sec. 6.1.2, the potential application to Titan measurements and in Sec. 6.1.3, the possible analysis of telluric ozone is discussed briefly.

6.1 Outlook

6.1.1 Retrieval of Kinetic Temperatures

Mars

The analysis of the Martian dayside spectra requires further investigation, however, the principal application of the IFR to Mars data has been shown in Chap. 5. Besides the analysis of the absorption line and the coherent deduction of thermal profiles, the kinetic temperature of the CO_2 molecules at the low pressure layer of 0.001 hPa can be performed by fitting the non-LTE emission line. An implication of CODAT as forward model into the IFR would enlarge the potential of the routine by simultaneously deriving the thermal profile and the kinetic temperature. A manifold of data from a variety of observing campaigns since 2005 has not yet been processed. Especially the data sets obtained during an observing campaign in 2007, shortly after a global duststorm was present on Mars, are of interest. An approach to derive the kinetic temperatures using the MCD profiles as basis has failed in the past, due to the erroneous temperature/pressure profiles which did not account accurately for the lofted dust.

Venus

On Venus, the non-LTE emission core can be observed together with a broad absorption feature for observations at the terminator. As it has been displayed in Fig. 4.14 in Chap. 4, a strong emission feature exists as soon as the FoV covers only small fractions of the sunlit side of Venus. Hence, a simultaneous deduction of the thermal profile and the kinetic temperature in the 0.001 hPa pressure layer would also be possible for Venus observations. This approach would strengthen the impact of IFR since the altitude probing region could be increased up to an altitude of ~ 110 km.

Another future plan should be the global mapping of the Venusian nightside by using IR heterodyne spectroscopy. The high spatial resolution of infrared observations would allow a sophisticated investigation of a broad variety of observing position on the apparent planetary disk. In addition, continuous ground-based observations of the thermal properties of Venus' nightside can be performed and significantly contribute to the understanding of the atmospheric properties. With the imminent shut-down of VEX, the space exploration of Venus suffers a great loss and ground-based observations need to be intensified.

It was shown, that the IFR has the potential to retrieve the high pressure boundary, where Venus atmosphere becomes opaque for infrared radiation. This pressure layer corresponds to the top of the main cloud deck. Hence, cloud top altimetry could be a further application of the IFR. For a reliable retrieval of the altitude of the opaque shell around Venus, either a 3-dimensional model needs to be applied, which can account for the curvature of the planet towards the limb, or the approach has to be restricted to an observing area spanning between about $\pm 30°$ away from the sub observer point. Within this area, the curvature of the planet has no noticeable effect.

6.1.2 Titan

The Saturnian moon Titan is the most Earth-like body in the outer planetary system. Its atmosphere consists mainly of molecular nitrogen (N_2) and methane (CH_4) whereas only trace amounts of CO_2 and other hydrocarbons like ethane (C_2H_6) can be found [182]. The thermal structure of the atmosphere would allow only the detection of emission features, since the temperature profile shows a strong inversion in the higher altitudes (comp. Fig. 6.1). Observations of ethane

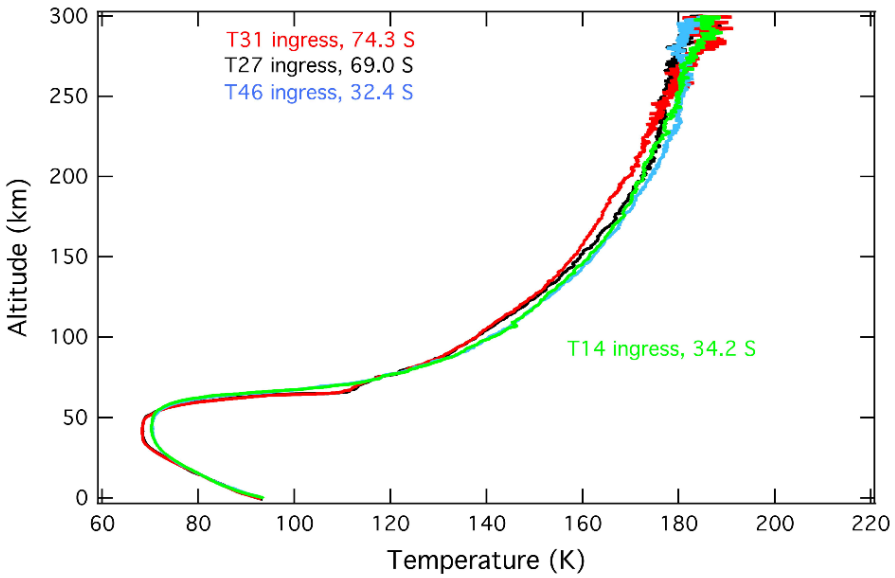

Figure 6.1: *Temperature vs. altitude profile in Titan's atmosphere from the surface to 300 km (0.1 hPa) altitude. Profiles were acquired with the RO experiment aboard of the Cassini spacecraft at four different orbits probing various latitudes (Schinder et al. [181]).*

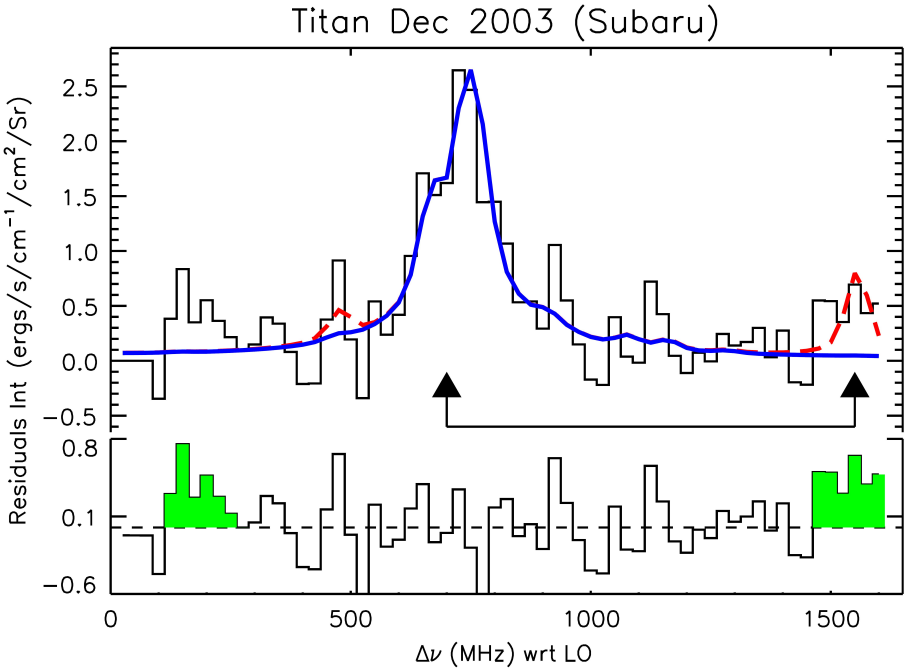

Figure 6.2: *Measurements of ethane emission lines from Titan taken with HIPWAC at the Subaru telescope in 2003.* CoDAT *was used to fit the data for a uniformly mixed C2H6 mole fraction profile. From Kostiuk et al. [49].*

emission lines have been performed in Titan's atmosphere using ground-based infrared heterodyne spectroscopy by *Kostiuk et al.* [49]. They used the full radiative transfer code CoDAT presented in the Chap. 3 as a forward model with a known input temperature profile to find the best fit to the line. They have found that varying the thermal profile leads to a better fit result and were therefore able to judge on the thermal behavior in certain altitude regions. This approach requires a reliable profile as input parameter. The line broadening is also affected by the vertical volume-mixing-ratio of the molecule. For a self-consistent derivation of the true vertical temperature profile a good SNR and a precise knowledge on the abundance profile is needed. The former requires a very long integration time, similar to observations on Venus. The latter is reasonably well mixed [183] in the line forming region between 10 hPa and 0.1 hPa [49].

A retrieval of the vertical temperature profile from IR heterodyne observations could be accomplished under certain conditions. The apparent size of Titan from Earth is considerably small and large telescopes, like the Subaru telescope on Mauna Kea, are needed to spatially resolve the planetary disk. One issue that then needs to be considered is that the line shape contains information on the

global average of the temperature profile, which is highly variable [181]. However, this would be comparable to the spatial resolution of sub-mm observations at Mars and Venus. Mapping of temperatures cannot be accomplished using ground-based IR heterodyne techniques and in the era of space-based remote sensing of Titan's atmosphere the scientific contribution of ground-based observations of Titan is only of low significance.

6.1.3 Earth

In recent years the IR heterodyne instruments THIS and iCHIPS have been used to observe stratospheric ozone (O_3) in the telluric atmosphere. The atmospheric ozone layer peaks at an altitude of around 30 km, which makes it highly feasible for analysis of stratospheric dynamics and temperatures. In Fig. 6.3 a spectrum of a telluric O_3 absorption line is shown. the spectrum was obtained in solar occultation mode in February 2010. The line forming region is assumed to be around the O_3 peak density, but a full analysis of the line shape, using a radiative transfer model has not yet been performed. The main issue concerning the analysis of solar occultation measurements, is that the radiative transfer code at hand, CODAT, can only calculate the bottom to top transfer (comp. Chap. 3). The radiation detected on Earth is emerging through the atmosphere from the top to the bottom. Two possible scenarios can thus lead to a sophisticated full analysis of the O_3 line shape. One, CODAT has to be revised and updated such that a transfer calculation for radiation penetrating the atmosphere from space to the surface is possible, or two, the more likely scenario, that CODAT will be replaced in the IFR by a radiative transfer code, that already possesses the required capabilities.

Two important parameters can be retrieved from the line shape of the O_3 absorption feature. The pressure-broadening of the line, yields the thermal profile in the atmosphere, comparable to analysis of the CO_2 absorption lines presented in this work. The second parameter, not detectable in measurements of absorption features of extraterrestrial atmospheres, is the line of sight wind velocity. Solar occultation measurements of atmospheric trace gases on Earth yield the big advantage of a very high SNR (comp. Fig. 6.3(a)), commonly one to two magnitudes higher than on Venus or Mars, even for short integration times. This high SNR enables the revelation of the dynamical profile in the atmospheric layers. Up to now, only one LoS wind velocity was retrieved from the ozone line by fitting a Voigt profile to the center of the line. The line core is formed in higher altitudes region than the broader wings. The fit yields the center frequency and the Doppler shift of the line away from its rest frequency is thus due to a stratospheric wind. The retrieval of the LoS wind velocities in Fig. 6.3 is summarized in *Stangier et al.* [51].

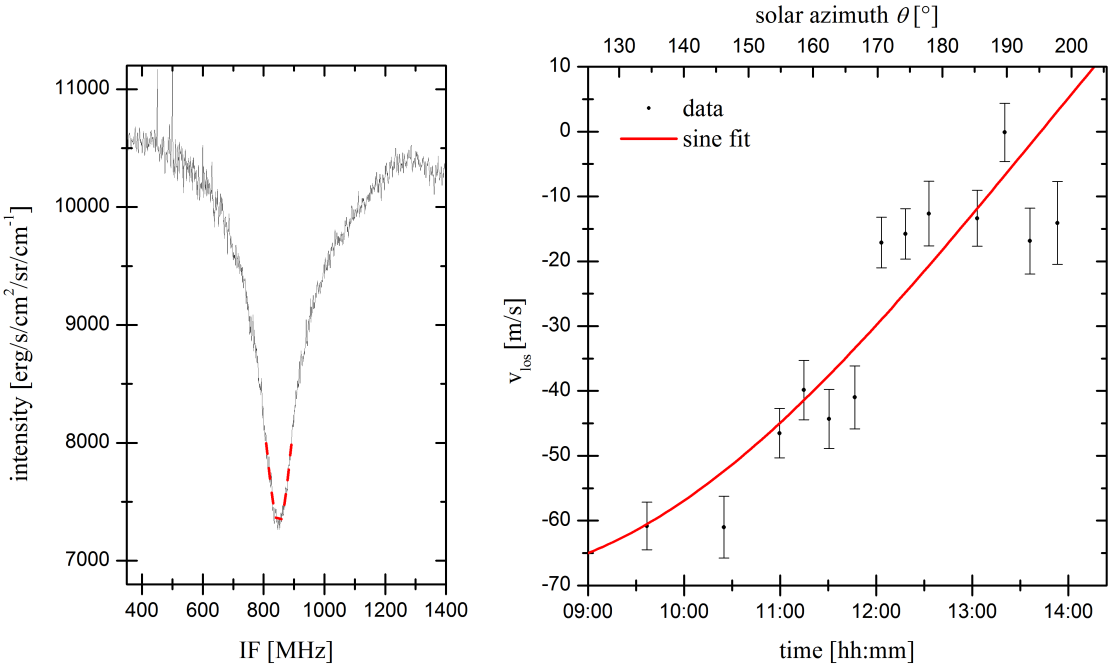

(a) *One example of a measured O_3 absorption line and a Voigt fit to the line peak (red). The SNR for an integration time of ~ 5 min is ~ 65 and thus more than 15 times higher than on Venus or Mars.*

(b) *Resulting line of sight wind velocities from the Doppler shifted peak positions of the absorption line plotted vs. the observing time. The fit error is represented by the error bars. A sine function with a period of 24 h was fitted to the data.*

Figure 6.3: *Measured stratospheric O_3 absorption line and LoS wind velocities. From Stangier et al. [51].*

A vertical wind shear, or even different wind velocities, in the stratosphere lead to a deformation of the line shape due to varying Doppler shifts. The idea is to fit 4–5 absorption features to different spectral regions. Each fit yields a Doppler shifted center frequency. From these fits, an analysis of the vertical wind profile can be provided. This technique has been successfully applied on stratospheric ozone emission features using microwave detection techniques [184].

One issue still to solve is the accuracy of the ozone rest line. The uncertainty of the O_3 line in the mid-IR is unreported in the HITRAN database. Hence, spectroscopic laboratory measurements of the precise center frequency of the detected O_3 transition must be performed in advance to give a reliable statement on the real stratospheric winds.

6.2 Summary

In this thesis, the retrieval of atmospheric temperatures from pressure-broadened CO_2 absorption lines, observed with infrared heterodyne spectroscopy was performed for the first time.

In the introductory chapter the possibilities of planetary science in general and heterodyne spectroscopy in particular were discussed. The new approach of investigating the broad absorption features widens the probing altitudes for IR heterodyning in the planetary atmospheres of Venus and Mars. In addition, a brief overview of the content of this thesis was provided in Chap. 1.

In the second chapter, the principles of infrared heterodyne spectroscopy were presented and the sensitivity and noise properties were discussed briefly. Also an introduction on the different line broadening effects was given in Chap. 2, concluding that a radiative transfer model is necessary to fully describe the absorption behavior of planetary atmospheres. The third part of this chapter was focused on the characteristics of the heterodyne receivers THIS and HIPWAC, which have been used for observations.

The newly developed IFR was presented in detail in Chap. 3, along with a proof of concept of the retrieval for the Venusian nightside. The model, used for calculating the radiative transfer through the atmospheres (CODAT), was discussed and an investigation of the altitude resolution applicable for Venus' mesospheric nightside spectra was provided. It was found, that the retrieval of thermal profiles with an altitude resolution of approximately one full scale height (on Venus $\sim 4.5\,\mathrm{km}$) has been possible. It could be shown, that a lower resolution leads to unwanted oscillations in the retrieved profiles in higher altitudes, due to cross-correlations between adjacent atmospheric layers. The proof of concept showed the reliability of the IFR, under the assumption of these previously found preconditions.

The thermal properties of Venus were discussed extensively in Chap. 4. After some introductory sections on the specific atmospheric characteristics and the state of art in remote sensing and in-situ measuring techniques and circulation models, the observing campaigns in 2012, especially performed to obtain Venusian nightside spectra, were presented. The analysis of the measured spectra was described and the first thermal profiles retrieved from IR heterodyne observations were presented. During the second campaign in 2012, a coordinated measurement was conducted together with the VEX VeRa experiments. The results of this campaign were elaborated and a very good agreement between the profiles of the two techniques was found. In the last part of the chapter, further thorough comparison of the newly retrieved temperatures to other space- and ground-based observations as

well as to the Venus International Reference Atmosphere was accomplished.

In contrast to Venus, Mars shows a strong CO_2 absorption features on its dayside. The thermal properties of Mars were discussed in Chap. 5 and a further, diligent proof of concept was performed, accounting for the changed preconditions for Martian dayside spectra. Especially the contribution of the solar induced non-LTE emission feature was emphasized, but also the influence of the altitude resolution on the retrieval was investigated. It could be shown, that the retrieval of Martian temperatures in the lower altitudes is much more sensitive to the applied pressure layering than on Venus. An altitude resolution of approximately three quarter of a full scale height for the lower layers was adequate to model the spectrum and to concurrently retrieve a profile without cross-correlations. With this knowledge, a measured spectrum from observations in 2010 was analyzed. A contamination of the data by a standing wave, which interspersed during the measurement, was found. Despite the contaminated data set, the found temperatures coincide with predictions from the Mars Climate Database.

The last chapter (Chap. 6) of this thesis, including this summary, gave an outlook on the potential future applications of the IFR. The retrieval of thermal properties from Venus' dayside and the simultaneous deduction of the kinetic temperatures from the non-LTE emission was discussed. Additionally, possible observations of temperatures on the terrestrial Saturn moon Titan and solar occultation measurements of stratospheric ozone on Earth were exposed.

Appendix

A Optimization of Integration Times

According to the error propagation law, the error of the spectrum calculated in Eq. (2.11) is

$$\Delta F \cdot (H - C) = \sqrt{\Delta S^2 + \Delta R^2 + F^2 \cdot (\Delta H^2 + \Delta C^2)} \tag{A.1}$$

Assuming radiometric behavior for each source $\Delta i^2 = \frac{i}{\sqrt{\delta \tau_i}}$, $i = \mathrm{S, R, C, H}$ and introducing Eq. (2.8) it is

$$\Delta F \cdot (H - C) = \frac{1}{\sqrt{\delta_{fl}}} \cdot \sqrt{\frac{S^2}{\tau_S} + \frac{R^2}{\tau_R} + F^2 \cdot \left(\frac{H^2}{\tau_H} + \frac{C^2}{\tau_C} \right)} \tag{A.2}$$

In order to find the minimum value for the noise amplitude of the measured spectrum F, as described in Eq. (2.11), it is necessary to minimize the expression underneath the square root in Eq. (A.2). To take the side condition

$$\tau - \Sigma_i \tau_i = 0 \,\mathrm{with}\, i = \mathrm{S, R, C, H} \tag{A.3}$$

into account, neglecting potential dead times τ_d, the Lagrange formalism is used.

$$\begin{gathered} \chi = \frac{S^2}{\tau_S} + \frac{R^2}{\tau_R} + F^2 \cdot \left(\frac{H^2}{\tau_H} + \frac{C^2}{\tau_C} \right) - \lambda \left(\tau - \Sigma_i \tau_i \right) \\ \frac{\partial \chi}{\partial \tau_S} \doteq \frac{\partial \chi}{\partial \tau_R} \doteq \frac{\partial \chi}{\partial \tau_C} \doteq \frac{\partial \chi}{\partial \tau_H} \doteq \frac{\partial \chi}{\partial \lambda} \doteq 0 \end{gathered} \tag{A.4}$$

which obviously states that

$$\tau_H = \tau_C \cdot \frac{H}{C} \text{ and } \tau_S = \tau_R \cdot \frac{S}{R} \text{ and } \tau_S = \tau_H \cdot \frac{S}{FH} \tag{A.5}$$

Introduction of those expressions into Eq. (A.3) results in

$$\frac{S}{\tau_S} = \frac{1}{\tau}\left(S + R + F\left(H + C\right)\right) \tag{A.6}$$

and substitution of τ_H and τ_C in Eq. (A.2) with the terms found in Eq. (A.5) yields

$$\Delta F \cdot (H - C) = \frac{1}{\sqrt{\delta_{fl}}} \cdot \sqrt{\frac{S}{\tau_S} \cdot \left(S + R + F\left(H + C\right)\right)} \tag{A.7}$$

By introducing Eq. (2.8) and Eq. (A.6), the resulting noise amplitude in K in dependence on the total integration time τ can be written as

$$\sigma^2\left(\tau, F\right) \cdot \left(T_H - T_C\right) = \Delta F \cdot \left(T_H - T_C\right) = \frac{T_{rec}}{\sqrt{\delta_{fl}\tau}} \cdot \left(T_S + T_R + F\left(T_H + T_C\right)\right) \tag{A.8}$$

With those calculations the total integration τ time can be divided into accurate exposure times τ_i on each source to achieve optimal noise reduction performance of the instrument.

B The IDL Inversion Routine

Status: April 2014:

```
1  ; atm_temp_inver test
2  ; Version 4.0
3
4  ; ===================================================
5  pro atanh_init, n1, hw, x_val4tanh, tanh_func
6
7  n2 = n1 * 1.0d0
8
9  x_val4tanh = dindgen( n1 ) / n2 * ( 2.0*hw ) - hw
10
11 tanh_func = tanh( x_val4tanh )
12
13 end
14
15 ; ===================================================
16 function atanh, x_int_val
17
18 common atanh_inits, x_val4tanh, tanh_func
19
20 ;ind = where( x_int_val gt 1 or x_int_val lt -1 )
21 ;if ( ind[0] ne -1 ) then begin
22 ;   print, "Out of bounds value when calculating inverse-tanh [-1,1]
       in: ", x_int_val
23 ;   print, "   for elements ", ind
24 ;   STOP
25 ;endif
26
27 ; Interpolate the fine grid to determine the inverse-tanh.
28 return, ( interpol( x_val4tanh, tanh_func, x_int_val )  )
29
30 end
31
32 ; ===================================================
33 pro atm_temp_invert_params_packing, params, action=action
34
35 common parameters, t_base, t_baseMin, dt_base, p0_base, dp_base,
       inpts, tin, pin, tsurf
36
37 common controllers, vary, lo_bound, up_bound
38
39 common data_ObsConfigFile, dind, obsConfigFile, dataFile
40
41 ; Constraining the pressure of the lowest layer (surface pressure)
42 ; to a positive range is achieved using a mapping to the hyperbolic
```

```
43  ; tan function.
44  ; Tanh(x) is bounded by -1 (for x -> -inf) and +1 (for x -> +inf).
45  ; The function z(x) = 1+tanh(x) has the bounds   0 < z(x) < 2, with
46  ; the symmetry point being z(x) = +1 at x=0. However, we offset this
47  ; point to x = 1 for enhanced stablity in the optimization.
48  ; In the optimization, we guide the algorithm to a solution for the
49  ; pressure constrained by specific bounds. These bounds are centred
      on
50  ; a new variable x2 = x - 1 and z(x2) = z(x-1) = +1 for x2 = 0
51  ; (i.e., tanh(x2) = 0 at x2=0 and x=1). This also guarentees that
52  ; 1+tanh(x2) results in a positive value P > 0 mapping for P.
53  ;   Pressure minimum: P0 (= press of layer above layer close to
54  ;        surface) -- lower bound.
55  ;   Pressure diffrence dP = P1 - P0    ; where P1 is the maximum in
      the
56  ;      lowest layer pressure range -- P1 is the upper bound.
57  ;   Pressure at surface layer: P = P0+dP*(1+tanh(x2))/2
58  ; By design, for x2 -> -inf, we have P = P0
59  ;            for x2 -> +inf, we have P = P0 + dP = P1
60  ;            for x2 = 1, we have P = P0 + dP/2
61  ; We map the pressure parameter to x2.
62  ;    x2 = atanh( 2*( P - P0 ) / dP - 1 )
63  ;
64  ; For the temperature, we have
65  ;    T = T_baseMin + dT*(1+tanh(x))/2     where T_baseMin is small
66  ; positive real value.
67  ;    x = atanh( 2*( T-T_baseMin )/dT - 1 )
68  ;
69
70  case action of
71
72  ; Pack the parameters vector.
73    0: begin
74  ; Map the pressure in the lowest layer (closest to surface) to a
75  ; variable guarenteed to be positive (see above discussion).
76      var_p_surf = 1.0d0 + atanh( ( pin[inpts-1] - p0_base ) / $
77                                  dp_base * 2.0d0 - 1.0d0 )
78  ; Map the temperature values so it is positive.
79      var_tinx   = 1.0d0 + atanh( ( tin - T_baseMin ) / dT_base * 2.0 -
            1.0 )
80      var_tsurfx = 1.0d0 + atanh( ( tsurf - T_baseMin ) / dT_base * 2.0
            - 1.0 )
81
82  ; Construct the vector contain all parameters -- both fixed and
83  ; variable.
84      p_all = [ var_tinx, var_tsurfx, var_p_surf ]
85
86      params[ * ] = p_all[ where(vary) ]
87
```

```
 end

; Unpack the paraemters vector and populate the real variables.
  1: begin

; The parameters with variable (vary) set for active fitting.
    ind0 = where( vary eq 1 )
; The layers where the temperature is set to vary.
    ind1 = where( ind0 le (inpts-1) )
; Fill the layers where the temperature is set to vary.
    tin[ind0[ind1]] = T_baseMin + dT_base * 0.5d0 * ( 1.0d0 + $
                      tanh( params[ 0:( total(vary[ind0[ind1]]) -1 )
                         ] - 1.0d0 ) )

; If requested, reset the surface temperature.
    if ( where( ind0 eq inpts )  ne -1 ) then $
        tsurf = T_baseMin + dT_base * 0.5d0 * ( 1.0d0 + $
                            tanh( params[ total(vary[ind0[ind1]]) ] -
                               1.0d0 ) )

; If requested, reset the surface pressure.
    if ( where( ind0 eq inpts+1 )  ne -1 ) then begin
       psurfx = params[ total(vary[ind0[ind1]]) + 1 ]
       pin[ inpts - 1 ] = p0_base + dp_base * 0.5d0 * $
      ( 1.0d0 + tanh( psurfx - 1.0d0 ) )
    endif

  end
  else: begin
    print, "Illegal value for action (only 0,1 permitted):", action
  endelse

endcase

end

; ===================================================================
pro atm_temp_invert_funct, x, params, fvec, isave=isave, iter=iter,
    flambda=flambda

common parameters, t_base, t_baseMin, dt_base, p0_base, dp_base,
    inpts, tin, pin, tsurf

common controllers, vary, lo_bound, up_bound

common data_ObsConfigFile, dind, obsConfigFile, dataFile

common atm_vals, ngases, ixgas, iqv, xqv, self, qvmix, $
             z0, radius, grav, theta, ground, pmix, $
```

```
133             molwt, bckgrd, nems, wems, ems
134
135 if ( n_elements(isave) ne 1 ) then isave = 0
136 if ( n_elements(iter)  ne 1 ) then iter  = 0
137 if ( n_elements(flam)  ne 1 ) then flam  = 0
138
139 ; Unpack the parameters and populate the variables associated with
      the
140 ; physical properties.
141 atm_temp_invert_params_packing, params, action=1
142
143 if ( isave eq 1 ) then begin
144 ;  sav_file = 'Iter-' + strcomress( iter, /remove ) + '.sav'
145   savFile = 'Iter-' + strcompress( iter, /remove ) + '.sav'
146   print, " **** Saving parameters for iter #:" + strcompress( iter )
        + " **** "
147   save, file=savFile, params, inpts, tin, pin, tsurf
148 endif
149
150 if ( tsurf le 0.0 ) then begin
151   print, "  Illegal value for surface temperature (K): ", tsurf
152   stop
153 endif
154 if ( min(tin) le 0.0 ) then begin
155   print, "  Illegal value for temperature in layers (K): ", min( tin
        )
156   stop
157 endif
158 if ( pin[0] le 0.0 ) then begin
159   print, "  Illegal value for surface pressure (mb): ", pin[0]
160   stop
161 endif
162
163 irhs_atm, file='fort.91', read=0, write=1, $
164             inpts, pin, tin, $
165             ngases, ixgas, iqv, xqv, self, $
166             qvmix, $
167             z0, radius, grav, theta, $
168             ground, $
169             pmix, molwt, tsurf, bckgrd, $
170             nems, wems, ems
171
172 comm = 'sed -e s/T_surf/' + strmid( strcompress( tsurf, /remove ), 0,
      7 ) + $
173        '/' + ' -e s/DATAFILENAME/' + file_basename( dataFile ) + '/'
             + $
174        ' <' + obsConfigFile + ' >fort.94'
175
176 spawn, comm, exit_status=status
```

```
177
178 if ( status ne 0 ) then begin
179   print, "  Error modifying observer configuration file: ",
        obsConfigFile
180   print, "  Reported status error: ", status
181   stop
182 endif
183
184 if ( total( finite(tin) ) ne n_elements(tin) ) then stop
185
186 spawn, '/usr/local/codat/bin/beamwrap1', exit_status=status
187
188 if ( status ne 0 ) then begin
189   print, "  Error in CoDAT execution; reported error: ", status
190   stop
191 endif
192
193 read_results, file='fit_results.dat', freq=freq0, model=m0
194
195 ; fvec = m0[ dind ]
196
197 p_vec = [ tin, tsurf, pin[inpts-1] ]
198
199 ; Upper-limit peg
200 up_peg = abs( total( ( p_vec - up_bound )>0 ) )
201
202 ; Lower-limit peg
203 lo_peg = abs( ( total( lo_bound - p_vec )>0 ) )
204
205 ; Perturb the spectral model if any subset of parameters exceed the
206 ; bounds.
207 fz   = interpol( m0, freq0, x )
208 fvec = fz + ( up_peg + lo_peg )
209
210 if ( isave eq 1 ) then oplot, x, fz, col=3
211
212 ; if ( up_peg gt 0 or lo_peg gt 0 ) then STOP
213
214 end
215
216 ; ===================================================
217 pro atm_temp_invert_report_results_subpro, lun, chisq, flambda,
      params, psig, $
218       tsurf, pin, tin, tin_guess, psurf_guess, tsurf_guess
219
220 np   = n_elements( params )
221 inpts = n_elements( pin )
222
223 printf, lun, " ========================================="
```

```
224 printf, lun, "    ** Finaly reduced chisq:      ", chisq
225 printf, lun, "    ** Marquardt parameter:       ", flambda
226 printf, lun, ""
227
228 printf, lun, "    ** Parameter values (normalized) follow"
229 for i=0,np-1 do $
230   printf, lun, strcompress( i, /remove ) + "    " + strcompress(
        params[i], /remove ) + $
231     "    " + strcompress( psig[i], /remove )
232
233 printf, lun, ""
234 printf, lun, "    ** Solutions"
235 printf, lun, "  Tsurf (solution&guess): ", tsurf, tsurf_guess, $
236         format='(a28,1x,f7.3)'
237 printf, lun, "  Psurf (solution&guess): ", pin[inpts-1], psurf_guess,
      $
238         format='(a28,1x,f7.3)'
239 printf, lun, ""
240 printf, lun, " P (mb)        T (K)     T_Guess (K)"
241 for i=0,inpts-1 do $
242   printf, lun, pin[i], tin[i], tin_guess[i], format='(f7.3,4x,f8.3,4x
        ,a11)'
243 printf, lun, ""
244 printf, lun, " ================================================="
245
246 end
247
248 ; ============================================================
249 pro atm_temp_invert_report_results, chisq, flambda, params, psig, $
250       tsurf, pin, tin, tin_guess, psurf_guess, tsurf_guess, file=
          saveFile
251
252 ; Print to screen
253 atm_temp_invert_report_results_subpro, -1, chisq, flambda, params,
      psig, $
254       tsurf, pin, tin, tin_guess, psurf_guess, tsurf_guess
255
256 ; Write to a text file.
257 openw, lun, /get, saveFile+'.txt'
258 atm_temp_invert_report_results_subpro, lun, chisq, flambda, params,
      psig, $
259       tsurf, pin, tin, tin_guess, psurf_guess, tsurf_guess
260 close, lun   &   free_lun, lun
261
262 end
263
264 ; ============================================================
265 pro atm_temp_invert_iter_show
266
```

```
267 n = 0
268
269 files = file_search( 'tmp/', 'Iter-*.sav', count=n )
270
271 if ( n ge 1 ) then begin
272
273    restore, files[0]
274
275    m = size( params, /dimen )
276    m = m[0]
277
278    p = dblarr( m, n )
279
280    for i=0,(n-1) do begin
281      restore, files[i]
282      p[*,i] = 1.0d0 + tanh( params - 1.0d0 )
283    endfor
284
285   set_plot, 'ps'
286   epsFile = 'ParamChanges'
287   device, file=epsFile+'.eps', xsiz=5, ysiz=4, /inch, /encaps, /color
288   make_ct, ncol=m
289   plot, indgen(n)+1, p[0,*], yran=[(min(p)-0.01)>(-1.01),(max(p)
          +0.01)<2.01], $
290         ysty=1, xsty=1, backg=1, col=0, xtit='Iteration number', $
291         ytit='Parameter value (normalized)'
292   for i=1,(m-1) do oplot, indgen(n)+1, p[i,*], col=1+i
293   device, /close
294   set_plot, 'x'
295
296   spawn, 'epstopdf ' + epsFile + '.eps'
297   if ( file_test( epsFile+'.pdf' ) eq 1 ) then begin
298      spawn, 'rm -f ' + epsFile+'.eps'
299      case !version.os of
300         'darwin': spawn, 'open ' +   epsFile+'.pdf'
301         'linux':  spawn, 'evince ' + epsFile+'.pdf'
302      endcase
303   endif
304
305 endif
306
307 end
308
309 ; ===================================================
310 pro atm_temp_invert_parse_guessFile, pin, tin, tsurf, vary, lo_bound,
       up_bound, $
311                                      option=iopt, file=file
312
313 if ( n_elements(iopt) ne 1 ) then begin
```

```
314     print, 'Syntax:'
315     print, '    atm_temp_invert_parse_guessFile, pin, tin, tsurf, $'
316     print, '              vary, lo_bound, up_bound, $'
317     print, '              option=0, file="FitGuess.txt"'
318     print, '    atm_temp_invert_parse_guessFile, pin, tin, tsurf, $'
319     print, '              vary, lo_bound, up_bound, $ '
320     print, '              option=1, file="FitGuess.txt"'
321     retall
322 endif
323
324 case iopt of
325
326     0: begin
327        openr, lun, /get, file
328        skipcomments, lun
329        readf, lun, inpts
330        x = dblarr( 6, inpts )
331
332        vary = intarr( inpts+2 )
333        lo_bound = intarr( inpts+2 )
334        up_bound = intarr( inpts+2 )
335        skipcomments, lun
336        readf, lun, x
337        pin = reform( x[1,*] )
338        tin = reform( x[2,*] )
339        vary[0:(inpts-1)] = reform( x[3,*] )
340        lo_bound[0:(inpts-1)] = reform( x[4,*] )
341        up_bound[0:(inpts-1)] = reform( x[5,*] )
342
343        skipcomments, lun
344        y = dblarr( 4 )
345        readf, lun, y
346        tsurf = y[0]
347        vary[inpts] = reform( y[1] )
348        lo_bound[inpts] = reform( y[2] )
349        up_bound[inpts] = reform( y[3] )
350
351        skipcomments, lun
352        y = dblarr( 4 )
353        readf, lun, y
354        pin[(inpts-1)] = y[0]
355        vary[inpts+1] = reform( y[1] )
356        lo_bound[inpts+1] = reform( y[2] )
357        up_bound[inpts+1] = reform( y[3] )
358
359        close, lun   &   free_lun, lun
360     end
361
362     1: begin
```

```
363         inpts = n_elements( pin )
364         openw, lun, /get, file
365         printf, lun, "# Thermal profile guess"
366         printf, lun, "# Number of layers"
367         printf, lun, inpts
368         printf, lun, "# Layer      P (mb)     T (K) Fix/Vary LowerB
                UpperB"
369         for i=0,inpts-1 do begin
370            printf, lun, i+1, pin[i], tin[i], 1, tin[i]-50.0, tin[i
                ]+50.0, $
371               format='(i,4x,f8.4,4x,f6.2,4x,i2,4x,f6.2,4x,f6.2)'
372         endfor
373
374         printf, lun, "# Surface temperature (may be different than in
                above profile)"
375         printf, lun, tsurf, 1, tsurf-25, tsurf+25, $
376            format='(f6.2,4x,i2,4x,f6.2,4x,f6.2)'
377
378         printf, lun, "# Pressure of layer closest to surface (same as
                in above profile)"
379         printf, lun, max(pin), 1, max(pin)-10, max(pin)+10, $
380            format='(f6.2,4x,i2,4x,f6.2,4x,f6.2)'
381
382
383         close, lun   &   free_lun, lun
384      end
385
386      else: begin
387         print, "   Illegal value for iopt:", iopt, " ..... Quiting!"
388         retall
389      end
390
391   endcase
392
393   end
394
395   ; ===================================================================
396   pro atm_temp_invert_plot_results, pin, tin, origAtmFile
397
398   set_plot, 'ps'
399   epsFile = 'FitSummary'
400   device, file=epsFile+'.eps', xsiz=5, ysiz=8, /inch, /encaps, /color
401   make_ct, ncol=3
402
403   th = 4
404   !p.multi = [ 0, 1, 2 ]
405
406   irhs_atm, file=origAtmFile, read=1, write=0, zn, zpin, ztin
407
```

```
408 plot, tin, pin, yran=[max([pin,zpin])+1,(min([pin,zpin]))], $
409   /nodata, /ylog, backg=1, col=0, charthick=th, charsiz=1.1, $
410   xran=[min([tin,ztin])-2,max([tin,ztin])+2], xsty=1, ysty=1, $
411   tit='User specified (black), Recovered (red)', xtit='T (K)', $
412   ytit='P (mb)', thick=th, xthick=th, ythick=th, xmargin=[10,4]
413 oplot, tin, pin, col=2, thick=th
414 oplot, ztin, zpin, col=0, thick=th
415
416 read_results, file='tmp/fit_results.dat', freq=f, model=m, data=d
417 d_m = d - m
418 xran = [ min(f)-1, max(f)+1 ]
419
420 plot, f, d, xsty=1, ysty=1, tit='Data & Fit', yran=[min([d,d_m])-1,
      max([d,d_m])+1], $
421   xran=xran, xtit='!4Dm!3 (MHz wrt LO)', ytit='Intensity (erg/s/cm!u
        -1!n/cm!u2!n/Sr)', $
422   thick=th, xthick=th, ythick=th, col=0, backg=0, charthick=th,
        charsiz=1.2
423 oplot, f, m, thick=th, col=2
424 oplot, f, d_m, col=4
425 oplot, [xran[0],xran[1]], [0,0], thick=th, col=0, lin=2
426
427 device, /close
428 set_plot, 'x'
429 !p.multi = 0
430
431 spawn, 'epstopdf ' + epsFile + '.eps'
432 if ( file_test( epsFile+'.pdf' ) eq 1 ) then begin
433       spawn, 'rm -f ' + epsFile+'.eps'
434       case !version.os of
435          'darwin': spawn, 'open ' +   epsFile+'.pdf'
436          'linux':  spawn, 'evince ' + epsFile+'.pdf'
437       endcase
438 endif
439
440 end
441
442 ; ===================================================================
443 pro atm_temp_invert
444
445 common atanh_inits, x_val4tanh, tanh_func
446
447 common parameters, t_base, t_baseMin, dt_base, p0_base, dp_base,
      inpts, tin, pin, tsurf
448
449 common controllers, vary, lo_bound, up_bound
450
451 common data_ObsConfigFile, dind, obsConfigFile, dataFile
452
```

```
453 common atm_vals, ngases, ixgas, iqv, xqv, self, qvmix, $
454              z0, radius, grav, theta, ground, pmix, $
455              molwt, bckgrd, nems, wems, ems
456
457 ; Delete all old windows
458 WHILE !D.WINDOW ne -1 do wdelete
459
460 ; The observer configuration file.
461 obsConfigFile = '../Base/fort.94-Base-sim-0N0W'
462
463 ; The data file.
464 dataFile = '../data/034.dat'
465
466 ; The atmospheric thermal profile.
467 atmFile ='../Base/fort.91_venus_100mbar'
468
469 ; Enter the corresponding index
470 index = 001
471
472 ; Scale factor
473 scale_fac = 1.5
474
475 ; LO frequency [cm-1]
476 lo_freq = 951.19226
477
478 pushd, 'tmp'
479
480 ; Remove existing save files that store intermediate parameter values
481 spawn, 'rm -f Iter-*.sav'
482
483 ; Parse the atmospheres file.
484 irhs_atm, file=atmFile, read=1, write=0, $
485              inpts, pin0, tin0, $
486              ngases, ixgas, iqv, xqv, self, $
487              qvmix, $
488              z0, radius, grav, theta, $
489              ground, $
490              pmix, molwt, tsurf0, bckgrd, $
491              nems, wems, ems
492
493 ; Extract the data
494 read_data, infile=dataFile, freq=freq0, spec=data0, wt=w0, switchwt=
    c0
495
496 plot, freq0, data0
497 ;Ask for center frequency of absorption line
498
499 print, "Please mark the bottom of the absorption line (ignore any
    emission):"
```

```
500 cursor, f_min, a
501 print, f_min, a
502 userValue1 =f_min
503 ;a = 12.5
504 ;a = 32.6
505 ;Print, ""
506 ;Print, "Please enter center frequency of absorption line: "
507 ;read, userValue1
508 ;userValue1 = 1079
509 ;f_min = userValue1
510 Print, ""
511 Print, "Value entered: "
512 Print, f_min
513 Print, ""
514 ;Print, "If correct, please enter '1'"
515 ;read, userValue2
516 ;        if ( userValue2 ne 1 ) then begin
517 ;        print, "OK, quitting.....aborted by user!"
518 ;        retall
519 ;        endif
520 ;a = 9.0
521 ;print, "Please mark the bottom of the absorption line (ignore any
        emission):"
522 ;cursor, f_min, a
523
524 ; The pressure broadening coefficient (self: 0.12 cm-1/atm) converted
525 ; to MHz/mb.
526 p_coef = 0.3 * 3.0d4 / 1013.0
527
528 fitGuessFile = 'FitGuess'
529
530 if ( file_test(FitGuessFile) eq 1 ) then begin
531
532 ; A Guess File does exist. Assume user wants this to be used.
533    print, ""
534    print, "    *** Guess file found in tmp. Will use this *** "
535    print, "        Waiting for 2 sec"
536    wait, 2.0
537    print, ""
538    atm_temp_invert_parse_guessFile, pin0, tin0, tsurf0, vary,
          lo_bound, up_bound, $
539                                     option=0, file=fitGuessFile
540 endif else begin
541
542    freq_sh0 = ( f_min + ( pin0 * p_coef ) ) < max( freq0 )
543    freq_sh1 = freq_sh0 / 3.0d4 + lo_freq
544
545    data0x = smooth( data0, 10 )
546
```

```
547     DSB = interpol( data0x, freq0, freq_sh0 );  * 2.0 / scale_fac
548     int = ( DSB - 0.5*median( DSB ) ) * scale_fac
549
550  ; Construct initial guesses.
551     tin_guess   = multi_bb( freq=freq_sh1, int=int, /i2t )
552     tsurf_guess = multi_bb( freq=[mean(freq_sh1)], int=[max(int)], /
           i2t )
553     atm_temp_invert_parse_guessFile, pin0, tin_guess, tsurf_guess,
           vary, $
554                             lo_bound, up_bound, option=1, file=fitGuessFile
555     print, "  ****** Guess file created. If needed please revise and "
            + $
556              "enter 1 to continue. *****"
557     read, userValue0
558     if ( userValue0 ne 1 ) then begin
559        print, "  OK, quiting.....  User entered: ", userValue0
560        file_delete, 'FitGuess/'
561        cd, '/home/this/taa/temp-invert-v5/'
562        retall
563     endif
564     atm_temp_invert_parse_guessFile, pin0, tin0, tsurf0, vary,
           lo_bound, up_bound, $
565                                        option=0, file=fitGuessFile
566  endelse
567
568  tin_guess   = tin0
569  psurf_guess = reform( pin0[inpts-1] )
570  tsurf_guess = tsurf0
571
572  ; Store initial values.
573  pin = pin0
574  tin = tin_guess
575  tsurf = tsurf_guess
576
577  t_base    = max( [ tin, tsurf ] )
578  t_baseMin = 050.0
579  dT_base   = 2.0 * t_base
580
581  ; Clamp the near surface pressure to a value higher than the layer
582  ; above so variations do not intrude into lower pressures causing a
583  ; pressure inversion during an optimization iteration.
584  p0_base = pin[ inpts - 2 ] + 0.2      ; max( pin ) + 5.0
585
586  ; Ensure that the active fit boundaries of the lowest layer pressure
587  ; does not extend to very high values -- clamp upper bound to 20%
588  ; above the guess value.
589  dp_base = 1.2 * pin[ inpts - 1 ] - p0_base
590
591  ; Initialize parameters.
```

```
592 params = dblarr( total( vary ) )
593
594 ; The total number of parameters.
595 np = n_elements( params )
596
597 ; Initialize the common block variables used in the tanh/atanh
598 ; calculation.
599 atanh_init, 20000L, 5.0, x_val4tanh, tanh_func
600
601 ; Pack the parameter variable.
602 atm_temp_invert_params_packing, params, action=0
603
604 ; Crop masked regions.
605 dind = where( c0 ne 0 )
606 c    = c0[ dind ]
607 wts  = w0[ dind ]
608 data = data0[ dind ]
609 freq = freq0[ dind ]
610
611 make_ct, ncol=3
612 ymax = max( data0, min=ymin )
613 ydel = ymax - ymin
614 yran = [ ymin - 0.05*ydel, ymax + 0.2*ydel ]
615
616 plot, freq, data, psym=3, backg=1, col=0, xsty=1, yran=yran, ysty=1,
      $
617   xtit='!4m!3 (MHz, wrt LO)', ytit='Radiance', tit='AOS data file: '
        + dataFile, $
618   /nodata
619 oplot, freq0, data0, psym=3, col=3
620 oplot, freq, data, psym=3, col=0
621
622 ; Show initial guess.
623 atm_temp_invert_funct, freq, params, y_init
624 oplot, freq, y_init, col=4
625
626 ; Set maximum number of iterations and tolerance level for
      convergence.
627 itmax = 50
628 tol   = 1.0d-3
629
630 p_init = params
631
632 yfit = curvefit2( freq, data, wts, params, psig, function='
      atm_temp_invert_funct', $
633   itmax=itmax, iter=iter, tol=tol, chisq=chisq, /noderiv, /double,
        status=status, $
634   yerr=yerr, mininc=0.01, flambda=flambda )
635
```

```
636 oplot, freq, yfit, col=2
637
638 popd
639
640 case status of
641   0: begin
642     print, "  Convergence reached. Iterations: ", iter
643   end
644   1: begin
645     print, "  LM failed to converge. Chisq increasing without bounds"
646     print, chisq
647   end
648   2: begin
649     print, "  LM failed to converge. Iterations: ", iter
650     print, "  Truncated by maximum number of iterations: ", itmax
651   end
652   else: begin
653     print, "Unknown error signal: ", status
654   end
655 endcase
656
657 ; Create a subdirectory for storing results.
658 saveDir  = 'T-invFits'
659 file_mkdir, saveDir
660
661 ; The base filename for saving results.
662 saveFile = saveDir + '/AtmFit'
663 saveFile = saveDir + '/Venus/sim/pT_' + STRCOMPRESS(index, /
      remove_all) + '_' + STRCOMPRESS(userValue1, /remove_all)
664
665 ; Store fit results as TEXT and IDL/SAVE formats.
666 atm_temp_invert_report_results, chisq, flambda, params, psig, $
667       tsurf, pin, tin, tin_guess, psurf_guess, tsurf_guess, file=
          saveFile
668 save, file=saveFile+'.sav', p_init, params, psig, yfit, freq, data, $
669   y_init, chisq, flambda, pin, tin, tsurf
670
671
672 ; Show iterations
673 ;atm_temp_invert_iter_show
674
675 window, /free
676 th = 2
677 ang = findgen(20)/19*2*!pi
678 usersym, cos(ang), sin(ang), /fill
679
680 plot,  tin_guess, pin0, yran=[max([pin0+3,pin]),min([pin0,pin])], /
      ylog, backg=1, col=0, $
```

```
681     xran=[min([tin,tin0,tsurf])-5,max([tin,tin0,tsurf])+5], xsty=1,
            ysty=1, $
682     thick=th, tit='Guess (black), recovered (red), init (green)', $
683     xtit='T (K)', ytit='P (mb)'
684  oplot, [tsurf_guess], [psurf_guess], psym=8, col=0, symsiz=2
685  oplot, tin,  pin, col=2, thick=th
686  oplot, [tsurf], [max(pin)], psym=8, col=2, symsiz=2
687
688  ; Overplot Initial profile (only for simulated data sets)
689  OpenR, lun, 'tmp/init_prof/fort.91_init_0N_non-iso_high-res', /
         Get_lun
690
691  headerInit = StrArr(1)
692  dataInit = FltArr(4,20)
693
694  ReadF, lun, headerInit, dataInit
695
696  pinit = dataInit[1,*]
697  Tinit = dataInit[2,*]
698
699  oplot, Tinit, pinit, col=4, symsize=2
700
701  ; Compare to simulation case.
702  ; atm_temp_invert_plot_results, pin, tin, 'Base/fort.91-ThermProf4'
703
704  FILE_DELETE, 'tmp/FitGuess'
705
706  ;PARSE_FORT91_TO_FITGUESS
707  Print, "FitGuess updated for line position @" +STRCOMPRESS(userValue1
         )+"MHz"
708
709  end
```

C Venus Observation: Spectra & Geometry

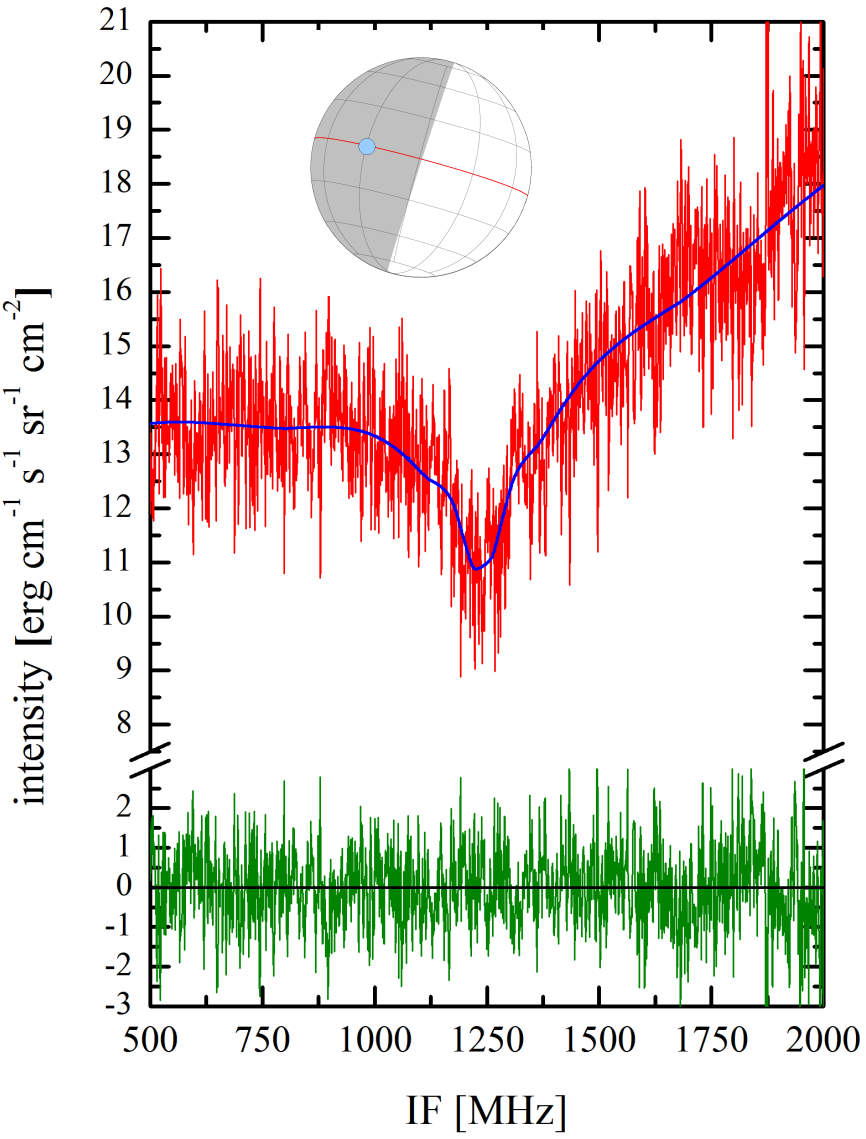

Figure C.1: *Measured spectra from campaign A at EQLT20 in high resolution (comp. Fig. 4.15). The data is displayed in red with a SNR of 4.3 ± 0.5, the best fit in blue and the residuals in green. The center frequency of the line is at 1245 MHz. The normalized RMS of the residuals indicates the noise amplitude. See Chap. 4 for details. The normalized RMS is 1.10 for an integration time of 154 min on source.*

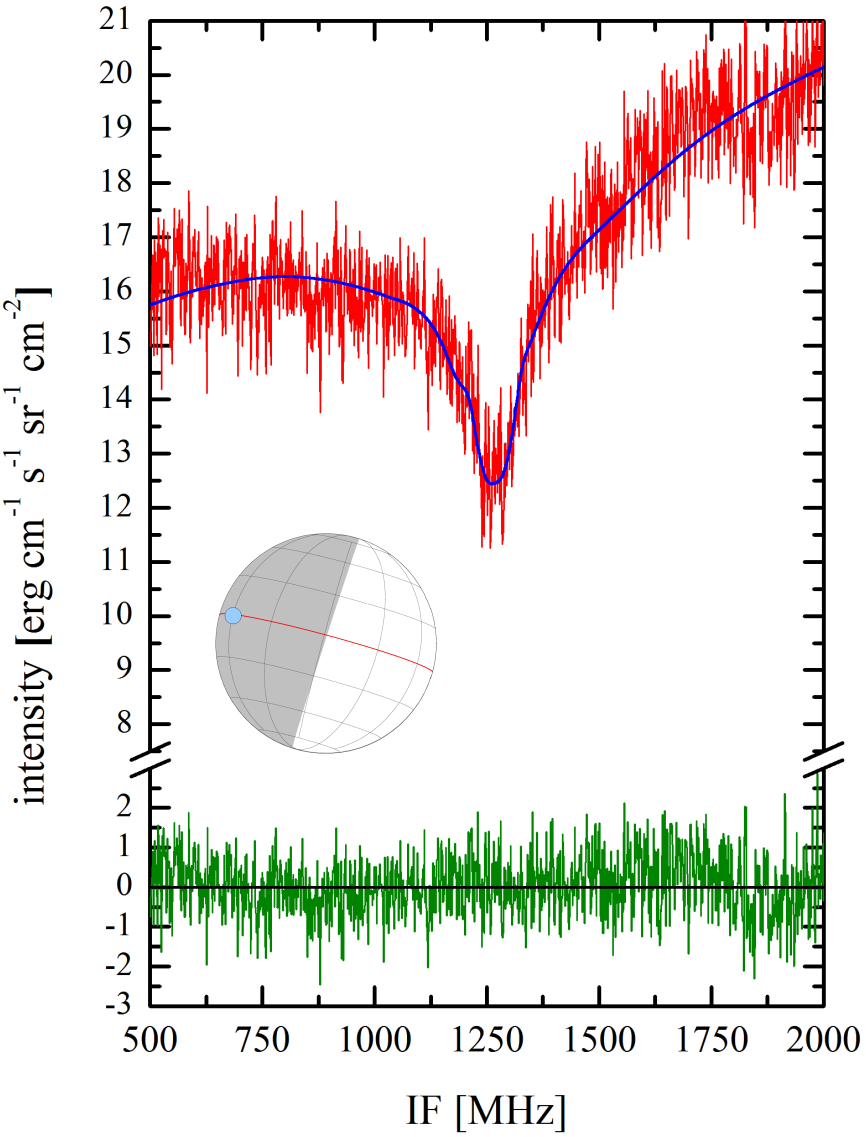

Figure C.2: *Measured spectra from campaign A at EQLT22 in high resolution (comp. Fig. 4.16). The data is displayed in red with a SNR of 6.6 ± 0.5, the best fit in blue and the residuals in green. The center frequency of the line is at 1265 MHz. The normalized RMS of the residuals indicates the noise amplitude. See Chap. 4 for details. The normalized RMS is 0.79 for an integration time of 480 min on source.*

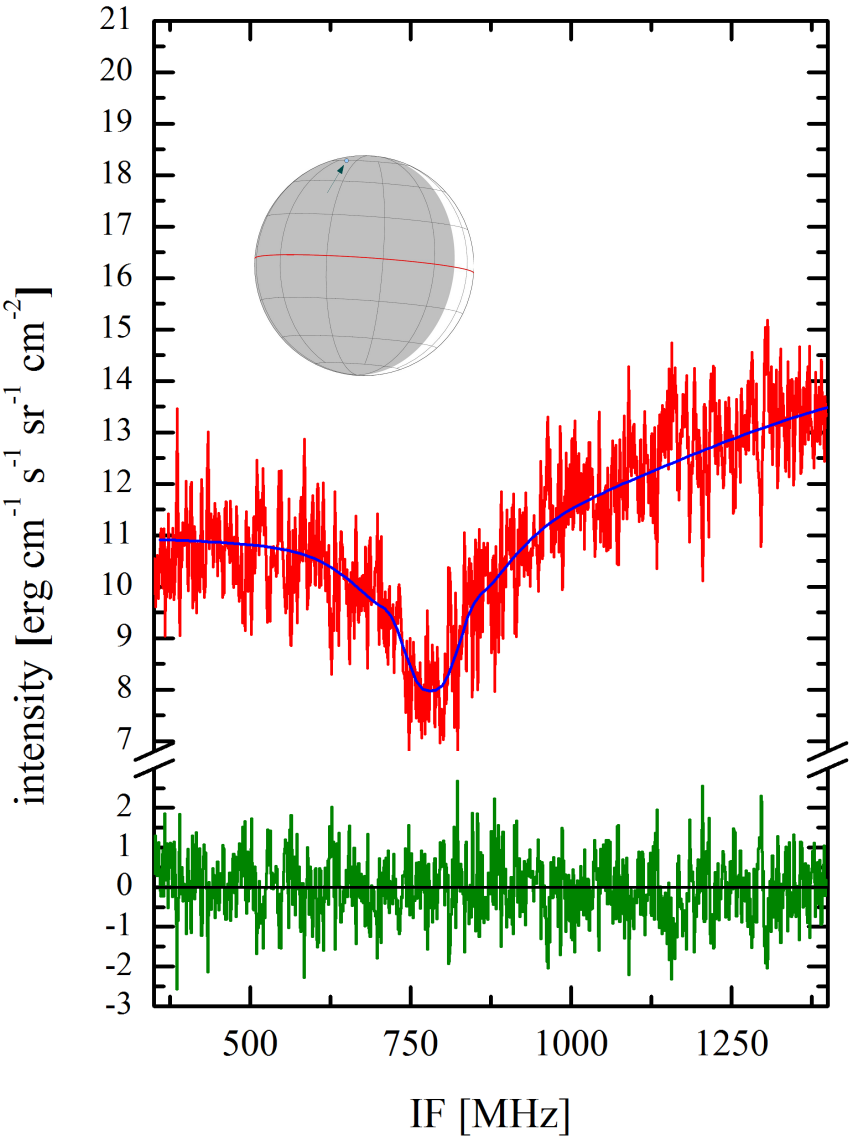

Figure C.3: *Measured spectrum from campaign B at 67NLT0 in high resolution (comp. Fig. 4.17). The data is displayed in red with a SNR of 4.8 ± 0.5, the best fit in blue and the residuals in green. The center frequency of the line is at 777 MHz. The normalized RMS of the residuals indicates the noise amplitude. See Chap. 4 for details. The normalized RMS is 0.79 for an integration time of 96 min on source.*

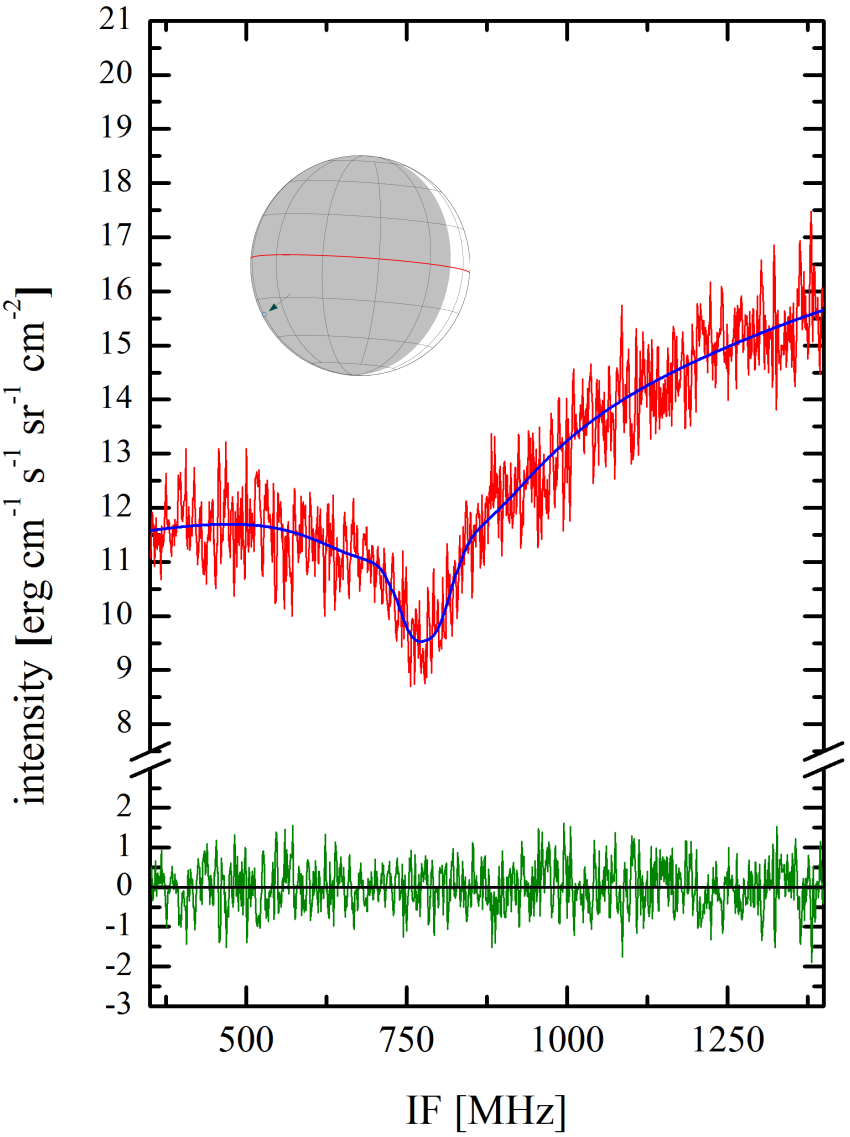

Figure C.4: *Measured spectrum from campaign B at 33SDL in high resolution (comp. Fig. 4.18). The data is displayed in red with a SNR of 6.4 ± 0.2. The best fit in blue and the residuals in green. The center frequency of the line is at 777 MHz. The normalized RMS of the residuals indicates the noise amplitude. See Chap. 4 for details. The normalized RMS is 0.59 for an integration time of 160 min on source.*

D Mars Observation: Spectrum

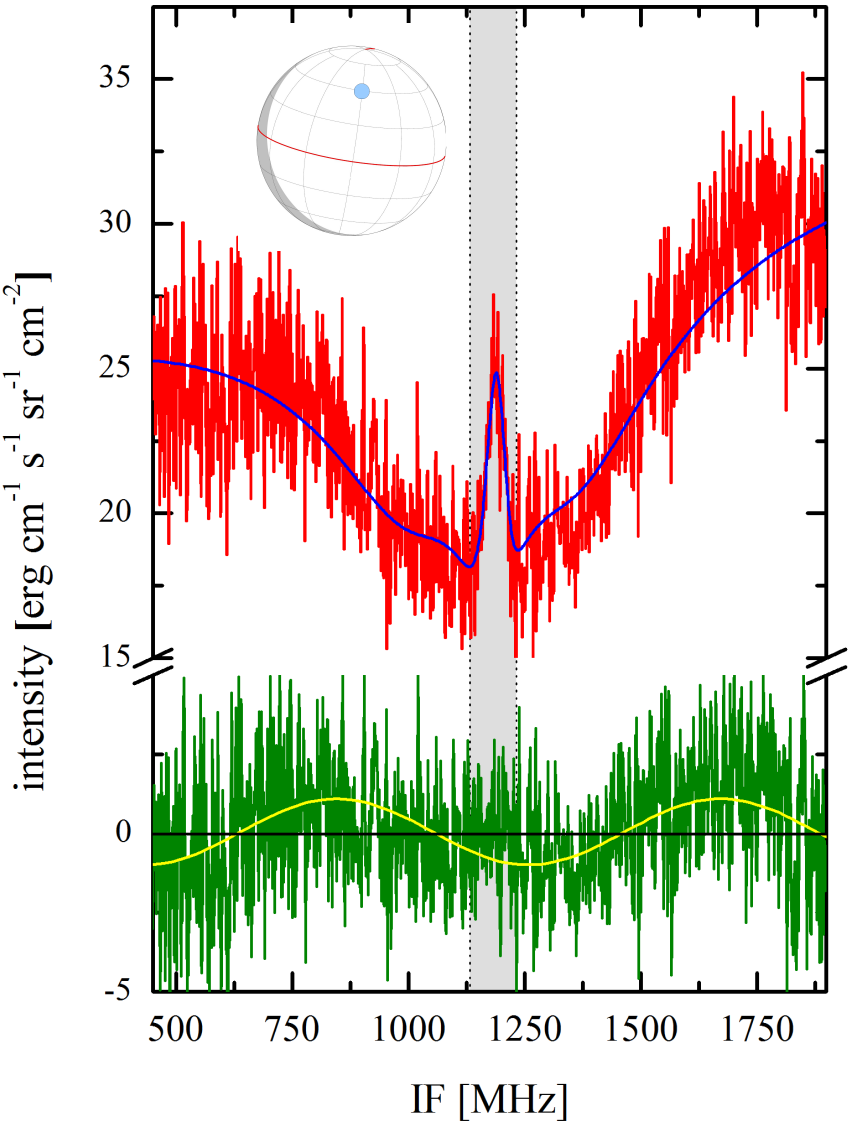

Figure D.5: *Measured Spectrum from Mars at 45NLT10 in high resolution (comp. Fig. 5.6). The data is displayed in red with a SNR of 5.8 ± 1.5, the best fit in blue and the residuals in green. The center frequency of the line is at 1148 MHz. The normalized RMS of the residuals indicates the noise amplitude. See Chap. 5 for details. The normalized RMS is 1.59 for an integration time of 17 min on source.*

Camp.	Date, UT (MM/DD)	Ang. Diameter (% illuminated)	Position	Lat.	Long. sky	Long. planet	Venus LT	τ (mm:ss)	airmass
A	03/20	22.01” (54.5%)	EQLT20	0°N	35.0°E	158.87–159.03°W	20:00	51:26	1.06 –1.02*
2012	03/21	22.24” (54.0%)	EQLT20	0°N	34.5°E	162.07–162.28°W	20:00	34:17	1.08*–1.04*
	03/22	22.47” (53.5%)	EQLT20	0°N	33.8°E	165.11–165.33°W	20:00	51:26	1.15*–1.03*
			EQLT22	0°N	63.8°E	135.37–135.69°W	22:00	77:09	1.02 –1.21
	03/23	22.70” (53.0%)	EQLT22	0°N	63.3°E	137.98–138.39°W	22:00	120:00	1.60 –1.03
			EQLT20	0°N	33.2°E	168.39–168.54°W	20:00	51:26	1.03*–1.03
	03/24	22.94” (52.4%)	EQLT22	0°N	62.6°E	141.73–141.95°W	22:00	51:26	1.12 –1.30
	03/27	23.70” (50.8%)	EQLT22	0°N	60.7°E	150.71–150.86°W	22:00	51:26	1.07*–1.02*
	03/28	23.96” (50.2%)	EQLT22	0°N	60.0°E	154.10–154.23°W	22:00	51:26	1.03 –1.11
	03/29	24.23” (49.7%)	EQLT22	0°N	59.4°E	157.12–157.31°W	22:00	51:26	1.02 –1.08
B	05/19	49.80” (10.1%)	67NLT0	67°N	35.0°E	282.37–282.59°W	0:00	48:00	1.17 –1.44
2012	05/20	50.42” (9.3%)	33SDL	33°S	85.0°E	235.21–235.35°W	3:20	112:00	1.02*–1.11
	05/21	51.17” (8.3%)	33SDL	33°S	85.0°E	236.58–236.63°W	3:27	48:00	1.05*–1.12
	05/23	52.50” (6.6%)	67NLT0	67°N	29.5°E	294.42–294.54°W	0:00	48:00	1.01 –1.06

Table C.1: *Detailed overview of the observing geometry during the observing campaigns in 2012. The angular diameter and illuminated fraction is given for the transit time of Venus on the respective observing day. The observing geometry is given for the center of the FoV. The longitudes are given in sky and planet based coordinates. The sky based coordinates are given in relation to the CML. The planet based longitudes represent the variation between the first and the last measurement. The on-source integration time is split into each observing day and position (τ). The airmass is a measure for the ray path through the terrestrial atmosphere, normalized to the shortest way for a zenith position (* observations performed before transit). Ephemeris were taken from the* HORIZONS *data base [185].*

Bibliography

[1] V. Formisano, S. Atreya, T. Encrenaz, N. Ignatiev, M. Giuranna, Detection of Methane in the Atmosphere of Mars, Science 306 (2004) 1758–1761. doi:10.1126/science.1101732.

[2] M. J. Mumma, G. L. Villanueva, R. E. Novak, T. Hewagama, B. P. Bonev, M. A. DiSanti, A. M. Mandell, M. D. Smith, Strong Release of Methane on Mars in Northern Summer 2003, Science 323 (2009) 1041–. doi:10.1126/science.1165243.

[3] V. A. Krasnopolsky, J. P. Maillard, T. C. Owen, Detection of methane in the martian atmosphere: evidence for life?, Icarus172 (2004) 537–547. doi:10.1016/j.icarus.2004.07.004.

[4] G. Sonnabend, D. Stupar, M. Sornig, T. Stangier, T. Kostiuk, T. A. Livengood, A search for methane in the atmosphere of Mars using ground-based mid infrared heterodyne spectroscopy, Journal of Molecular Spectroscopy 291 (2013) 98–101. doi:10.1016/j.jms.2013.05.009.

[5] G. L. Villanueva, M. J. Mumma, R. E. Novak, Y. L. Radeva, H. U. Käufl, A. Smette, A. Tokunaga, A. Khayat, T. Encrenaz, P. Hartogh, A sensitive search for organics (CH_4, CH_3OH, H_2CO, C_2H_6, C_2H_2, C_2H_4), hydroperoxyl (HO_2), nitrogen compounds (N_2O, NH_3, HCN) and chlorine species (HCl, CH_3Cl) on Mars using ground-based high-resolution infrared spectroscopy, Icarus223 (2013) 11–27. doi:10.1016/j.icarus.2012.11.013.

[6] A. Blanco, V. Orofino, M. D'Elia, S. Fonti, A. Mastandrea, A. Guido, F. Russo, Infrared spectroscopy of microbially induced carbonates and past life on Mars, Icarus226 (2013) 119–126. doi:10.1016/j.icarus.2013.05.016.

[7] S. C. R. Rafkin, J. L. Hollingsworth, M. A. Mischna, C. E. Newman, M. I. Richardson, Comparative Climatology of Terrestrial Planets, The University of Arizona Press, 2013, Ch. Mars: Atmosphere and Climate Overview, pp. 55–89. doi:10.2458/azu_uapress_9780816530595-ch003.

[8] S. Seager, Exoplanet Habitability, Science 340 (2013) 577–581. doi:10.1126/science.1232226.

[9] A. Wolszczan, D. A. Frail, A planetary system around the millisecond pulsar PSR1257 + 12, Nature355 (1992) 145–147. doi:10.1038/355145a0.

[10] J. Schneider. The extrasolar planets encyclopedia [online] (29.07.2014).

[11] W. J. Borucki, E. Agol, F. Fressin, L. Kaltenegger, J. Rowe, H. Isaacson, D. Fischer, N. Batalha, J. J. Lissauer, G. W. Marcy, D. Fabrycky, J.-M. Désert, S. T. Bryson, T. Barclay, F. Bastien, A. Boss, E. Brugamyer, L. A. Buchhave, C. Burke, D. A. Caldwell, J. Carter, D. Charbonneau, J. R. Crepp, J. Christensen-Dalsgaard, J. L. Christiansen, D. Ciardi, W. D. Cochran, E. DeVore, L. Doyle, A. K. Dupree, M. Endl, M. E. Everett, E. B. Ford, J. Fortney, T. N. Gautier, J. C. Geary, A. Gould, M. Haas, C. Henze, A. W. Howard, S. B. Howell, D. Huber, J. M. Jenkins, H. Kjeldsen, R. Kolbl, J. Kolodziejczak, D. W. Latham, B. L. Lee, E. Lopez, F. Mullally, J. A. Orosz, A. Prsa, E. V. Quintana, R. Sanchis-Ojeda, D. Sasselov, S. Seader, A. Shporer, J. H. Steffen, M. Still, P. Tenenbaum, S. E. Thompson, G. Torres, J. D. Twicken, W. F. Welsh, J. N. Winn, Kepler-62: A Five-Planet System with Planets of 1.4 and 1.6 Earth Radii in the Habitable Zone, Science 340 (2013) 587–590. arXiv:1304.7387, doi:10.1126/science.1234702.

[12] E. V. Quintana, T. Barclay, S. N. Raymond, J. F. Rowe, E. Bolmont, D. A. Caldwell, S. B. Howell, S. R. Kane, D. Huber, J. R. Crepp, J. J. Lissauer, D. R. Ciardi, J. L. Coughlin, M. E. Everett, C. E. Henze, E. Horch, H. Isaacson, E. B. Ford, F. C. Adams, M. Still, R. C. Hunter, B. Quarles, F. Selsis, An Earth-Sized Planet in the Habitable Zone of a Cool Star, Science 344 (2014) 277–280. arXiv:1404.5667, doi:10.1126/science.1249403.

[13] Y. Bhattacharjee, Almost-Earth Tantalizes Astronomers With Promise of Worlds to Come, Science 344 (2014) 249–249.

[14] T. M. Donahue, R. R. Hodges, Jr., Past and present water budget of Venus, J. Geophys. Res.97 (1992) 6083–6091. doi:10.1029/92JE00343.

[15] S. J. Mackwell, A. A. Simon-Miller, J. W. Harder, M. A. Bullock, Comparative Climatology of Terrestrial Planets, The University of Arizona Press, 2013. doi:10.2458/azu_uapress_9780816530595.

[16] A. T. Basilevsky, J. W. Head, The surface of Venus, Reports on Progress in Physics 66 (2003) 1699–1734. doi:10.1088/0034-4885/66/10/R04.

[17] S. M. Clifford, T. J. Parker, The Evolution of the Martian Hydrosphere: Implications for the Fate of a Primordial Ocean and the Current State of the Northern Plains, Icarus154 (2001) 40–79. doi:10.1006/icar.2001.6671.

[18] E. Pettit, S. B. Nicholson, Radiation Measures on the Planet Mars, PASP36 (1924) 269–272.

[19] E. Pettit, S. B. Nicholson, Temperatures on the Bright and Dark Sides of Venus, Publications of the ASP 67 (1955) 293. doi:10.1086/126823.

[20] D. Williams, Planetary Space Missions (2013).
URL http://nssdc.gsfc.nasa.gov/planetary/projects.html

[21] A. L. Albee, F. D. Palluconi, R. E. Arvidson, Mars Global Surveyor Mission: Overview and Status, Science 279 (1998) 1671. doi:10.1126/science.279.5357.1671.

[22] M. C. Malin, W. Calvin, R. T. Clancy, R. M. Haberle, P. B. James, S. W. Lee, P. C. Thomas, M. A. Caplinger, The Mars Color Imager (MARCI) on the Mars Climate Orbiter, J. Geophys. Res.106 (2001) 17651–17672. doi:10.1029/1999JE001145.

[23] R. S. Saunders, R. E. Arvidson, G. D. Badhwar, W. V. Boynton, P. R. Christensen, F. A. Cucinotta, W. C. Feldman, R. G. Gibbs, C. Kloss, Jr., M. R. Landano, R. A. Mase, G. W. McSmith, M. A. Meyer, I. G. Mitrofanov, G. D. Pace, J. J. Plaut, W. P. Sidney, D. A. Spencer, T. W. Thompson, C. J. Zeitlin, 2001 Mars Odyssey Mission Summary, Space Sci. Rev.110 (2004) 1–36. doi:10.1023/B:SPAC.0000021006.84299.18.

[24] J. E. Graf, R. W. Zurek, H. J. Eisen, B. Jai, M. D. Johnston, R. Depaula, The Mars Reconnaissance Orbiter Mission, Acta Astronautica 57 (2005) 566–578. doi:10.1016/j.actaastro.2005.03.043.

[25] M. Golombek, J. Grant, D. Kipp, A. Vasavada, R. Kirk, R. Fergason, P. Bellutta, F. Calef, K. Larsen, Y. Katayama, A. Huertas, R. Beyer, A. Chen, T. Parker, B. Pollard, S. Lee, Y. Sun, R. Hoover, H. Sladek, J. Grotzinger, R. Welch, E. Noe Dobrea, J. Michalski, M. Watkins, Selection of the Mars Science Laboratory Landing Site, Space Sci. Rev.170 (2012) 641–737. doi:10.1007/s11214-012-9916-y.

[26] R. Schmidt, Mars Express-ESA's first mission to planet Mars, Acta Astronautica 52 (2003) 197–202.

[27] H. Svedhem, D. V. Titov, D. McCoy, J.-P. Lebreton, S. Barabash, J.-L. Bertaux, P. Drossart, V. Formisano, B. Häusler, O. Korablev, W. J. Markiewicz, D. Nevejans, M. Pätzold, G. Piccioni, T. L. Zhang, F. W. Taylor, E. Lellouch, D. Koschny, O. Witasse, H. Eggel, M. Warhaut, A. Accomazzo, J. Rodriguez-Canabal, J. Fabrega, T. Schirmann, A. Clochet, M. Coradini, Venus Express – The first European mission to Venus, Planetary & Space Science 55 (2007) 1636–1652. doi:10.1016/j.pss.2007.01.013.

[28] G. Sonnabend, D. Wirtz, R. Schieder, P. F. Bernath, High-Resolution Infrared Measurements of H_2O and SiO in Sunspots, Sol. Phys.233 (2006) 205–213. doi:10.1007/s11207-006-2488-9.

[29] F. Schmuelling, J. Goldstein, T. Kostiuk, T. Hewagama, D. Zipoy, High precision Wind measurements in the upper Venus atmosphere, in: AAS/Division for Planetary Sciences Meeting Abstracts #32, Vol. 32 of Bulletin of the American Astronomical Society, 2000, p. 1121.

[30] M. Sornig, T. Livengood, G. Sonnabend, P. Kroetz, D. Stupar, T. Kostiuk, R. Schieder, Venus upper atmosphere winds from ground-based heterodyne spectroscopy of CO $_2$ at 10μm wavelength, Planetary & Space Science 56 (2008) 1399–1406. doi:10.1016/j.pss.2008.05.006.

[31] M. Sornig, T. A. Livengood, G. Sonnabend, D. Stupar, P. Kroetz, Direct wind measurements from November 2007 in Venus' upper atmosphere using ground-based heterodyne spectroscopy of CO $_2$ at 10 μm wavelength, Icarus217 (2012) 863–874. doi:10.1016/j.icarus.2011.03.019.

[32] M. Sornig, G. Sonnabend, D. Stupar, P. Kroetz, H. Nakagawa, I. Mueller-Wodarg, Venus' upper atmospheric dynamical structure from ground-based observations shortly before and after Venus' inferior conjunction 2009, Icarus225 (2013) 828–839. doi:10.1016/j.icarus.2012.12.005.

[33] G. Sonnabend, M. Sornig, R. Schieder, T. Kostiuk, J. Delgado, Temperatures in Venus upper atmosphere from mid-infrared heterodyne spectroscopy of CO $_2$ around 10μm wavelength, Planet. Space Sci.56 (2008) 1407–1413. doi:10.1016/j.pss.2008.05.008.

[34] P. Krötz, Observations of Upper Mesophere Temperatures on Venus and Evaluation of Mid-Infrared Detetctors for the Tuenable Heterodyne Infrared Spectrometer (THIS), Ph.D. thesis, University of Cologne (2010).

[35] G. Sonnabend, P. Krötz, F. Schmülling, T. Kostiuk, J. Goldstein, M. Sornig, D. Stupar, T. Livengood, T. Hewagama, K. Fast, A. Mahieux, Thermospheric/mesospheric temperatures on Venus: Results from ground-based high-resolution spectroscopy of CO $_2$ in 1990/1991 and comparison to results from 2009 and between other techniques, Icarus 217 (2012) 856–862. doi:10.1016/j.icarus.2011.07.015.

[36] G. Sonnabend, D. Wirtz, V. Vetterle, R. Schieder, High-resolution observations of Martian non-thermal CO_2 emission near 10 μm with a new tuneable heterodyne receiver, A&A435 (2005) 1181–1184. doi:10.1051/0004-6361:20042393.

[37] G. Sonnabend, M. Sornig, P. J. Krötz, R. T. Schieder, K. E. Fast, High spatial resolution mapping of Mars mesospheric zonal winds by infrared heterodyne spectroscopy of CO_2, Geophys. Res. Lett.33 (2006) 18201. doi:10.1029/2006GL026900.

[38] G. Sonnabend, M. Sornig, P. J. Kroetz, D. Stupar, L. Montabone, K. Fast, R. Schieder, Mars Mesospheric Winds Around Northern Spring Equinox from High Resolution Infrared Spectroscopy, LPI Contributions 1447 (2008) 9055–+.

[39] G. Sonnabend, P. Kroetz, M. Sornig, D. Stupar, Direct observations of Venus upper mesospheric temperatures from ground based spectroscopy of CO_2, Geophys. Res. Lett.37 (2010) 11102. doi:10.1029/2010GL043335.

[40] G. Sonnabend, M. Sornig, P. Kroetz, D. Stupar, Mars mesospheric zonal wind around northern spring equinox from infrared heterodyne observations of CO $_2$, Icarus217 (2012) 315–321. doi:10.1016/j.icarus.2011.11.009.

[41] D. Stupar, Observations of the Atmosphere of Mars using Mid-Infrared Heterodyne Spectroscopy and Investigation of Fabry-Pérot Quantum Cascade Lasers as Radiation Sources for Spectroscopy, Ph.D. thesis, University of Cologne (2012).

[42] K. Fast, T. Kostiuk, F. Espenak, J. Annen, D. Buhl, T. Hewagama, M. F. A'Hearn, D. Zipoy, T. A. Livengood, G. Sonnabend, F. Schmülling, Ozone abundance on Mars from infrared heterodyne spectra. I. Acquisition, retrieval, and anticorrelation with water vapor, Icarus 181 (2006) 419–431. doi:10.1016/j.icarus.2005.12.001.

[43] K. Fast, T. Kostiuk, T. Hewagama, M. F. A'Hearn, T. A. Livengood, S. Lebonnois, F. Lefèvre, Ozone abundance on Mars from infrared heterodyne spectra. II. Validating photochemical models, Icarus 183 (2006) 396–402. doi:10.1016/j.icarus.2006.03.012.

[44] K. E. Fast, T. Kostiuk, F. Lefèvre, T. Hewagama, T. A. Livengood, J. D. Delgado, J. Annen, G. Sonnabend, Comparison of HIPWAC and Mars Express SPICAM observations of ozone on Mars 2006-2008 and variation from 1993 IRHS observations, Icarus203 (2009) 20–27. doi:10.1016/j.icarus.2009.05.005.

[45] T. A. Livengood, T. Hewagama, T. Kostiuk, K. E. Fast, J. J. Goldstein, NOTE: Improved Determination of Ethane (C_2H_6) Abundance in Titan's Stratosphere, Icarus 157 (2002) 249–253. doi:10.1006/icar.2002.6823.

[46] T. A. Livengood, T. Kostiuk, G. Sonnabend, J. N. Annen, K. E. Fast, A. Tokunaga, K. Murakawa, T. Hewagama, F. Schmülling, R. Schieder, High-resolution infrared spectroscopy of ethane in Titan's stratosphere in the Huygens epoch, Journal of Geophysical Research (Planets) 111 (E10) (2006) 11. doi:10.1029/2005JE002669.

[47] T. Kostiuk, T. A. Livengood, G. Sonnabend, K. E. Fast, T. Hewagama, K. Murakawa, A. T. Tokunaga, J. Annen, D. Buhl, F. Schmülling, D. Luz, O. Witasse, Stratospheric global winds on Titan at the time of Huygens descent, Journal of Geophysical Research (Planets) 111 (2006) 7. doi:10.1029/2005JE002630.

[48] T. Kostiuk, T. A. Livengood, T. Hewagama, G. Sonnabend, K. E. Fast, K. Murakawa, A. T. Tokunaga, J. Annen, D. Buhl, F. Schmülling, Titan's stratospheric zonal wind, temperature, and ethane abundance a year prior to Huygens insertion, Geophysics Research Letters 32 (2005) 22205. doi:10.1029/2005GL023897.

[49] T. Kostiuk, T. Hewagama, K. E. Fast, T. A. Livengood, J. Annen, D. Buhl, G. Sonnabend, F. Schmülling, J. D. Delgado, R. Achterberg, High spectral resolution infrared studies of Titan: Winds, temperature, and composition, Planet. Space Sci.58 (2010) 1715–1723. doi:10.1016/j.pss.2010.08.004.

[50] T. A. Livengood, T. Kostiuk, F. Espenak, Temperature and abundances in the Jovian auroral stratosphere. 1: Ethane as a probe of the millibar region, Journal of Geophysical Research 98 (1993) 18813. doi:10.1029/93JE01043.

[51] T. Stangier, G. Sonnabend, M. Sornig, Compact Setup of a Tunable Heterodyne Spectrometer for Infrared Observations of Atmospheric Trace-Gases, Remote Sensing 5 (2013) 3397–3414. doi:10.3390/rs5073397.

[52] T. Stangier, *personally illustrated* (2014).

[53] M. A. López-Valverde, G. Sonnabend, M. Sornig, P. Kroetz, Modelling the atmospheric CO $_2$ 10-μm non-thermal emission in Mars and Venus at high spectral resolution, Planet. Space Sci.59 (2011) 999–1009. doi:10.1016/j.pss.2010.11.011.

[54] T. Stangier, T. Hewagama, M. Sornig, G. Sonnabend, T. Kostiuk, M. Herrmann, T. A. Livengood, Thermal Structure of Venus' Nightside Mesosphere as Observed by Infrared Heterodyne Spectroscopy at 10μm, *submitted to Planet. Space Sci.* (2014).

[55] G. Sonnabend, M. Sornig, P. Krötz, D. Stupar, R. Schieder, Ultra high spectral resolution observations of planetary atmospheres using the Cologne tuneable heterodyne infrared spectrometer, J. Quant. Spec. Radiat. Transf.109 (2008) 1016–1029. doi:10.1016/j.jqsrt.2007.12.003.

[56] P. Krause, Development and Characterization of New Components for a Miniaturized Heterodyne Infrared Spectrometer, Master's thesis, University of Cologne (2013).

[57] R. Schieder, V. Tolls, G. Winnewisser, The Cologne acousto optical spectrometers, Experimental Astronomy 1 (1989) 101–121. doi:10.1007/BF00457985.

[58] O. Hachenberg, B. Vowinkel, Technical foundations of radio astronomy, NASA STI/Recon Technical Report A 84 (1982) 28749.

[59] D. Wirtz, Erste Beobachtungen mit dem abstimmbaren Infrarot-Heterodynsystem THIS, Ph.D. thesis, University of Cologne (2005).

[60] M. M. Abbas, M. J. Mumma, T. Kostiuk, D. Buhl, Sensitivity limits of an infrared heterodyne spectrometer for astrophysical applications, Appl. Opt.15 (1976) 427–436. doi:10.1364/AO.15.000427.

[61] F. Schmülling, Entwicklung eines hochauflösenden Infrarot–Heterodynspektrometers mit einem Bleisalz–Diodenlaser als Lokaloszillator, Ph.D. thesis, University of Cologne (1997).

[62] Bernath, Peter F, Spectra of Atoms and Molecules, Oxford University Press, 1995.

[63] R. L. Abrams, Broadening coefficients for the P(20) CO2 laser transition, Applied Physics Letters 25 (1974) 609. doi:10.1063/1.1655330.

[64] D. W. Peterson, M. A. Johnson, A. L. Betz, Infrared heterodyne spectroscopy of CO_2 on Mars, Nature250 (1974) 128–130. doi:10.1038/250128a0.

[65] A. L. Betz, M. A. Johnson, R. A. McLaren, E. C. Sutton, Heterodyne detection of CO2 emission lines and wind velocities in the atmosphere of Venus, ApJ208 (1976) L141–L144. doi:10.1086/182251.

[66] M. A. Johnson, A. L. Betz, R. A. McLaren, C. H. Townes, E. C. Sutton, Nonthermal 10 micron CO2 emission lines in the atmospheres of Mars and Venus, ApJ208 (1976) L145–L148. doi:10.1086/182252.

[67] A. L. Betz, R. A. McLaren, M. A. Johnson, E. C. Sutton, Infrared heterodyne spectroscopy of CO2 in the atmosphere of Mars, Icarus30 (1977) 650–662. doi:10.1016/0019-1035(77)90087-2.

[68] M. A. Johnson, A. L. Betz, C. H. Townes, 10-micron heterodyne stellar interferometer, Physical Review Letters 33 (1974) 1617–1620. doi:10.1103/PhysRevLett.33.1617.

[69] D. D. S. Hale, M. Bester, W. C. Danchi, W. Fitelson, S. Hoss, E. A. Lipman, J. D. Monnier, P. G. Tuthill, C. H. Townes, The Berkeley Infrared Spatial Interferometer: A Heterodyne Stellar Interferometer for the Mid-Infrared, ApJ537 (2000) 998–1012. doi:10.1086/309049.

[70] T. Kostiuk, M. J. Mumma, Remote sensing by IR heterodyne spectroscopy, Applied Optics 22 (1983) 2644–2654. doi:10.1364/AO.22.002644.

[71] J. J. Goldstein, M. J. Mumma, T. Kostiuk, D. Deming, F. Espenak, D. Zipoy, Absolute Wind Velocities in The Lower Thermosphere of Venus Using Infrared Heterodyne Spectroscopy, Icarus 94 (1991) 45–63. doi:10.1016/0019-1035(91)90140-O.

[72] F. Schmülling, T. Kostiuk, D. Buhl, P. Rozmarynowski, K. Segal, T. Livengood, T. Hewagama, A new Infrared Heterodyne Instrument for measurements of Planetary Wind and Composition, in: AAS/Division for Planetary Sciences Meeting Abstracts, Vol. 31, 1999, p. 08.03.

[73] G. Sonnabend, Aufbau und Charakterisierung des Infrarot-Heterodyn-Spektrometers THIS, Ph.D. thesis, University of Cologne (2002).

[74] G. Sonnabend, D. Wirtz, F. Schmulling, R. Schieder, Tuneable Heterodyne Infrared Spectrometer for atmospheric and astronomical studies, Appl. Opt.41 (2002) 2978–2984. doi:10.1364/AO.41.002978.

[75] H. Nakagawa, S. Aoki, M. Kuroda, Y. Kasaba, I. Murata, S. Okano, Mid-infrared Heterodyne Spectroscopy Dedicated to Observation of Planet at Haleakala, Hawaii, in: EPSC-DPS Joint Meeting 2011, 2011, p. 357.

[76] D. Weidmann, G. Wysocki, High-resolution broadband (>100 cm^{-1}) infrared heterodyne spectro-radiometry using an external cavity quantum cascade laser, Optics Express 17 (2009) 248. doi:10.1364/OE.17.000248.

[77] A. Y. Klimchuk, A. I. Nadezhdinskii, Y. Y. Ponurovskii, Y. P. Shapovalov, A. V. Rodin, On the possibility of designing a high-resolution heterodyne spectrometer for near-IR range on the basis of a tunable diode laser, Quantum Electronics 42 (2012) 244–249. doi:10.1070/QE2012v042n03ABEH014759.

[78] J. Faist, F. Capasso, D. L. Sivco, C. Sirtori, A. L. Hutchinson, A. Y. Cho, Quantum Cascade Laser, Science 264 (1994) 553–556. doi:10.1126/science.264.5158.553.

[79] M. Beck, D. Hofstetter, T. Aellen, J. Faist, U. Oesterle, M. Ilegems, E. Gini, H. Melchior, Continuous Wave Operation of a Mid-Infrared Semiconductor Laser at Room Temperature, Science 295 (2002) 301–305. doi:10.1126/science.295.5553.301.

[80] Y. Yao, A. J. Hoffman, C. F. Gmachl, Mid-infrared quantum cascade lasers, Nature Photonics 6 (2012) 432–439. doi:10.1038/nphoton.2012.143.

[81] J. Faist, C. Gmachl, F. Capasso, C. Sirtori, D. L. Sivco, J. N. Baillargeon, A. Y. Cho, Distributed feedback quantum cascade lasers, Applied Physics Letters 70 (1997) 2670–2672. doi:10.1063/1.119208.

[82] T. Aellen, S. Blaser, M. Beck, D. Hofstetter, J. Faist, E. Gini, Continuous-wave distributed-feedback quantum-cascade lasers on a Peltier cooler, Applied Physics Letters 83 (2003) 1929. doi:10.1063/1.1609044.

[83] D. Wirtz, Die Frequenzkontrolle im Infrarot-Heterodyn-Spektrometers THIS. Diplomarbeit am I. Physikalischen Institut der Universität zu Köln, Master's thesis, Universität zu Köln (2000).

[84] M. Sornig, Investigations of Upper Atmosphere Dynamics on Mars and Venus by High Resolution Infrared Heterodyne Spectroscopy of CO_2, Ph.D. thesis, University of Cologne (2009).

[85] F. J. Duarte, Tunable lasers handbook, Academic Press, 1996.

[86] Raytheon Vision Systems, Operating Procedures and Test Reports for Wideband HgCdTe Photomixer Detectors (2005).

[87] T. de Graauw, F. P. Helmich, T. G. Phillips, J. Stutzki, E. Caux, N. D. Whyborn, P. Dieleman, P. R. Roelfsema, H. Aarts, R. Assendorp, R. Bachiller, W. Baechtold, A. Barcia, D. A. Beintema, V. Belitsky, A. O. Benz, R. Bieber, A. Boogert, C. Borys, B. Bumble, P. Caïs, M. Caris, P. Cerulli-Irelli, G. Chattopadhyay, S. Cherednichenko, M. Ciechanowicz, O. Coeur-Joly, C. Comito, A. Cros, A. de Jonge, G. de Lange, B. Delforges, Y. Delorme, T. den Boggende, J.-M. Desbat, C. Diez-González, A. M. di Giorgio, L. Dubbeldam, K. Edwards, M. Eggens, N. Erickson, J. Evers, M. Fich, T. Finn, B. Franke, T. Gaier, C. Gal, J. R. Gao, J.-D. Gallego, S. Gauffre, J. J. Gill, S. Glenz, H. Golstein, H. Goulooze, T. Gunsing, R. Güsten, P. Hartogh, W. A. Hatch, R. Higgins, E. C. Honingh, R. Huisman, B. D. Jackson, H. Jacobs, K. Jacobs, C. Jarchow, H. Javadi, W. Jellema, M. Justen, A. Karpov, C. Kasemann, J. Kawamura, G. Keizer, D. Kester, T. M. Klapwijk, T. Klein, E. Kollberg, J. Kooi, P.-P. Kooiman, B. Kopf, M. Krause, J.-M. Krieg, C. Kramer, B. Kruizenga, T. Kuhn, W. Laauwen, R. Lai, B. Larsson, H. G. Leduc, C. Leinz, R. H. Lin, R. Liseau, G. S. Liu, A. Loose, I. López-Fernandez, S. Lord, W. Luinge, A. Marston, J. Martín-Pintado, A. Maestrini, F. W. Maiwald, C. McCoey, I. Mehdi, A. Megej, M. Melchior, L. Meinsma, H. Merkel, M. Michalska, C. Monstein, D. Moratschke, P. Morris, H. Muller, J. A. Murphy, A. Naber, E. Natale, W. Nowosielski, F. Nuzzolo, M. Olberg, M. Olbrich, R. Orfei, P. Orleanski, V. Ossenkopf, T. Peacock, J. C. Pearson, I. Peron, S. Phillip-May, L. Piazzo, P. Planesas, M. Rataj, L. Ravera, C. Risacher, M. Salez, L. A. Samoska, P. Saraceno, R. Schieder, E. Schlecht, F. Schlöder, F. Schmülling, M. Schultz, K. Schuster, O. Siebertz, H. Smit, R. Szczerba, R. Shipman, E. Steinmetz, J. A. Stern, M. Stokroos, R. Teipen, D. Teyssier, T. Tils, N. Trappe, C. van Baaren, B.-J. van Leeuwen, H. van de Stadt, H. Visser, K. J. Wildeman, C. K. Wafelbakker, J. S. Ward, P. Wesselius, W. Wild, S. Wulff, H.-J. Wunsch, X. Tielens, P. Zaal, H. Zirath, J. Zmuidzinas, F. Zwart, The Herschel-Heterodyne Instrument for the Far-Infrared (HIFI), A&A518 (2010) L6. doi:10.1051/0004-6361/201014698.

[88] S. Heyminck, U. U. Graf, R. Güsten, J. Stutzki, H. W. Hübers, P. Hartogh, GREAT: the SOFIA high-frequency heterodyne instrument, A&A542 (2012) L1. arXiv:1203.2845, doi:10.1051/0004-6361/201218811.

[89] O. Siebertz, Akusto-optisches Spektrometer mit variabler Auflsung, Ph.D. thesis, University of Cologne (1998).

[90] M. Olbrich, A 3 GHz instantaneous bandwidth Acousto-Optical spectrometer with 1 MHz resolution, Ph.D. thesis, University of Cologne (2007).

[91] M. A. Janssen (Ed.), Atmospheric Remote Sensing By Microwave Radiometry, 1993.

[92] D. W. Allan, Precision Measurement and Calibration, NBS Special Publication, 1972, Ch. Statistics of atomic frequency standards, p. 466.

[93] R. Schieder, C. Kramer, Optimization of heterodyne observations using Allan variance measurements, A&A373 (2001) 746–756. arXiv:astro-ph/0105071, doi:10.1051/0004-6361:20010611.

[94] D. Deming, F. Espenak, D. Jennings, T. Kostiuk, M. Mumma, Evidence for high-altitude haze thickening on the dark side of Venus from 10-micron heterodyne spectroscopy of CO2, Icarus 49 (1982) 35–48. doi:10.1016/0019-1035(82)90055-0.

[95] T. Hewagama, J. Goldstein, T. A. Livengood, D. Buhl, F. Espenak, K. Fast, T. Kostiuk, F. Schmülling, Beam integrated high-resolution infrared spectra: Accurate modeling of thermal emission from extended clear atmospheres, Journal of Quantitiative Spectroscopy and Radiative Transfer 109 (2008) 1081–1097. doi:10.1016/j.jqsrt.2007.12.022.

[96] J. Goldstein, Absolute wind measurements in the lower thermosphere of venus using infrared heterodyne spectoscopy., Ph.D. thesis, University of Pennsylvania (1990).

[97] L. S. Rothman, I. E. Gordon, A. Barbe, D. C. Benner, P. F. Bernath, M. Birk, V. Boudon, L. R. Brown, A. Campargue, J.-P. Champion, K. Chance, L. H. Coudert, V. Dana, V. M. Devi, S. Fally, J.-M. Flaud, R. R. Gamache, A. Goldman, D. Jacquemart, I. Kleiner, N. Lacome, W. J. Lafferty, J.-Y. Mandin, S. T. Massie, S. N. Mikhailenko, C. E. Miller, N. Moazzen-Ahmadi, O. V. Naumenko, A. V. Nikitin, J. Orphal, V. I. Perevalov, A. Perrin, A. Predoi-Cross, C. P. Rinsland, M. Rotger, M. Šimečková, M. A. H. Smith, K. Sung, S. A. Tashkun, J. Tennyson, R. A. Toth, A. C. Vandaele, J. Vander Auwera, The HITRAN 2008 molecular spectroscopic database, J. Quant. Spec. Radiat. Transf.110 (2009) 533–572. doi:10.1016/j.jqsrt.2009.02.013.

[98] N. Jacquinet-Husson, L. Crepeau, R. Armante, C. Boutammine, A. Chédin, N. A. Scott, C. Crevoisier, V. Capelle, C. Boone, N. Poulet-Crovisier, A. Barbe, A. Campargue, D. C. Benner, Y. Benilan, B. Bézard, V. Boudon, L. R. Brown, L. H. Coudert, A. Coustenis, V. Dana, V. M. Devi, S. Fally, A. Fayt, J.-M. Flaud, A. Goldman, M. Herman, G. J. Harris, D. Jacquemart, A. Jolly, I. Kleiner, A. Kleinböhl, F. Kwabia-Tchana, N. Lavrentieva, N. Lacome, L.-H. Xu, O. M. Lyulin, J.-Y. Mandin, A. Maki, S. Mikhailenko, C. E. Miller, T. Mishina, N. Moazzen-Ahmadi, H. S. P. Müller, A. Nikitin, J. Orphal, V. Perevalov, A. Perrin, D. T. Petkie, A. Predoi-Cross, C. P. Rinsland, J. J. Remedios, M. Rotger, M. A. H. Smith, K. Sung, S. Tashkun, J. Tennyson, R. A. Toth, A.-C. Vandaele, J. Vander Auwera, The 2009 edition of the GEISA spectroscopic database, J. Quant. Spec. Radiat. Transf.112 (2011) 2395–2445. doi:10.1016/j.jqsrt.2011.06.004.

[99] D. P. Edwards, L. L. Strow, Spectral line shape considerations for limb temperature sounders, Journal of Geophysical Research 96 (1991) 20859. doi:10.1029/91JD02293.

[100] D. P. Edwards, GENLN2: A general line-by-line atmospheric transmittance and radiance model. Version 3.0: Description and users guide, Tech. rep., National Center for Atmospheric Research, Boulder, CO (jan 1992).

[101] T. Hewagama, T. Stangier, T. Kostiuk, T. Livengood, G. Sonnabend, M. Sornig, Thermal Profiles of Venus Atmosphere Above the Cloud Deck: Constrained Optimization Retrievals from Sub-Doppler Resolution Heterodyne Observations, in preparation.

[102] L. V. Zasova, N. Ignatiev, I. Khatuntsev, V. Linkin, Structure of the Venus atmosphere, Planetary & Space Science 55 (2007) 1712–1728. doi:10.1016/j.pss.2007.01.011.

[103] C. D. Rodgers, Characterization and error analysis of profiles retrieved from remote sounding measurements, J. Geophys. Res.95 (1990) 5587–5595. doi:10.1029/JD095iD05p05587.

[104] E. Bell, Photo Gallery Venus (2012).
URL http://nssdc.gsfc.nasa.gov/photo_gallery/photogallery-venus.html

[105] R. Nunes, Mariner 10 - 1973/75 - "Mission to Mercury and Venus" (2010).
URL http://www.astrosurf.com/nunes/explor/explor_m10.htm

[106] D. Williams, Venus Fact Sheet (2013).
URL http://nssdc.gsfc.nasa.gov/planetary/factsheet/venusfact.html

[107] C. H. Mayer, T. P. McCullough, R. M. Sloanaker, Observations of Venus at 3.15-CM Wave Length., Astrophysical Journal 127 (1958) 1. doi:10.1086/146433.

[108] M. Pätzold, B. Häusler, M. K. Bird, S. Tellmann, R. Mattei, S. W. Asmar, V. Dehant, W. Eidel, T. Imamura, R. A. Simpson, G. L. Tyler, The structure of Venus' middle atmosphere and ionosphere, Nature 450 (2007) 657–660. doi:10.1038/nature06239.

[109] S. Tellmann, M. Pätzold, B. Häusler, M. K. Bird, G. L. Tyler, Structure of the Venus neutral atmosphere as observed by the Radio Science experiment VeRa on Venus Express, Journal of Geophysical Research (Planets) 114 (2009) 0. doi:10.1029/2008JE003204.

[110] A. Seiff, J. T. Schofield, A. J. Kliore, F. W. Taylor, S. S. Limaye, Models of the structure of the atmosphere of Venus from the surface to 100 kilometers altitude, Advances in Space Research 5 (1985) 3–58. doi:10.1016/0273-1177(85)90197-8.

[111] R. T. Clancy, B. J. Sandor, G. H. Moriarty-Schieven, Venus upper atmospheric CO, temperature, and winds across the afternoon/evening terminator from June 2007 JCMT sub-millimeter line observations, Planetary & Space Science 56 (2008) 1344–1354. doi:10.1016/j.pss.2008.05.007.

[112] D. Grassi, A. Migliorini, L. Montabone, S. Lebonnois, A. Cardesìn-Moinelo, G. Piccioni, P. Drossart, L. V. Zasova, Thermal structure of Venusian nighttime mesosphere as observed by VIRTIS-Venus Express, Journal of Geophysical Research (Planets) 115 (2010) 9007. doi:10.1029/2009JE003553.

[113] J. L. Fox, S. W. Bougher, Structure, luminosity, and dynamics of the Venus thermosphere, Space Science Reviews 55 (1991) 357–489. doi:10.1007/BF00177141.

[114] N. I. Ignatiev, D. V. Titov, G. Piccioni, P. Drossart, W. J. Markiewicz, V. Cottini, T. Roatsch, M. Almeida, N. Manoel, Altimetry of the Venus cloud tops from the Venus Express observations, Journal of Geophysical Research (Planets) 114 (2009) 0. doi:10.1029/2008JE003320.

[115] V. Wilquet, A. Fedorova, F. Montmessin, R. Drummond, A. Mahieux, A. C. Vandaele, E. Villard, O. Korablev, J.-L. Bertaux, Preliminary characterization of the upper haze by SPICAV/SOIR solar occultation in UV to mid-IR onboard Venus Express, Journal of Geophysical Research (Planets) 114 (2009) 0. doi:10.1029/2008JE003186.

[116] M. A. Bullock, D. H. Grinspoon, Comparative Climatology of Terrestrial Planets, University of Arizona Press, 2013, Ch. The Atmosphere and Climate of Venus, pp. 19–54. doi:10.2458/azu_uapress_9780816530595-ch002.

[117] I. V. Khatuntsev, M. V. Patsaeva, D. V. Titov, N. I. Ignatiev, A. V. Turin, S. S. Limaye, W. J. Markiewicz, M. Almeida, T. Roatsch, R. Moissl, Cloud level winds from the Venus Express Monitoring Camera imaging, Icarus226 (2013) 140–158. doi:10.1016/j.icarus.2013.05.018.

[118] S. W. Bougher, D. M. Hunten, R. J. Phillips, Venus II–geology, geophysics, atmosphere, and solar wind environment, Vol. 1, University of Arizona Press, 1997.

[119] D. V. Titov, H. Svedhem, F. W. Taylor, S. Barabash, J.-L. Bertaux, P. Drossart, V. Formisano, B. Häusler, O. Korablev, W. J. Markiewicz, D. Nevejans, M. Pätzold, G. Piccioni, J.-A. Sauvaud, T. L. Zhang, O. Witasse, J.-C. Gerard, A. Fedorov, A. Sanchez-Lavega, J. Helbert, R. Hoofs, Venus express: Highlights of the nominal mission, Solar System Research 43 (2009) 185–209. doi:10.1134/S0038094609030010.

[120] O. I. Iakovlev, A. I. Efimov, S. S. Matiugov, T. S. Timofeeva, E. V. Chub, G. D. Iakovleva, Nighttime atmosphere of Venus from the results of radio occultation carried out by Venera 9 and Venera 10, Kosmicheskie Issledovaniia 16 (1978) 113–119.

[121] L. V. Ksanfomaliti, Venera 9 and 10 - Thermal radiometry, Icarus41 (1980) 36–64. doi:10.1016/0019-1035(80)90158-X.

[122] M. A. Kolosov, O. I. Yakovlev, A. I. Efimov, S. S. Matyugov, T. S. Timofeeva, E. V. Chub, A. G. Pavelyev, A. I. Kucheryavenkov, I. E. Kalashnikov, O. E. Milekhin, Investigation of the Venus Atmosphere and Surface by the Method of Radiosounding Using VENERA-9 and 10 Satellites, Acta Astronautica 7 (1980) 219–234. doi:10.1016/0094-5765(80)90062-4.

[123] D. Spänkuch, I. A. Matsygorin, R. Dubois, L. V. Zasova, Venus middle-atmosphere temperatures from Venera 15, Advances in Space Research 10 (1990) 67–75. doi:10.1016/0273-1177(90)90167-X.

[124] L. V. Zasova, The structure of the Venusian atmosphere at high latitudes, Advances in Space Research 16 (1995) 89–. doi:10.1016/0273-1177(95)00254-C.

[125] C. W. Snyder, Mariner V Flight Past Venus, Science 158 (1967) 1665–1669. doi:10.1126/science.158.3809.1665.

[126] C. Sagan, J. B. Pollack, On the Structure of the Venus Atmosphere, Icarus10 (1969) 274–289. doi:10.1016/0019-1035(69)90029-3.

[127] A. J. Kliore, I. R. Patel, Vertical structure of the atmosphere of Venus from Pioneer Venus orbiter radio occultations, Journal of Geophysical Research 85 (1980) 7957–7962. doi:10.1029/JA085iA13p07957.

[128] J. M. Jenkins, P. G. Steffes, D. P. Hinson, J. D. Twicken, G. L. Tyler, Radio occultation studies of the Venus atmosphere with the Magellan spacecraft. 2: Results from the October 1991 experiments, Icarus 110 (1994) 79–94. doi:10.1006/icar.1994.1108.

[129] L. Colin, The Pioneer Venus Program, Journal of Geophysical Research 85 (1980) 7575–7598. doi:10.1029/JA085iA13p07575.

[130] M. Nakamura, T. Imamura, N. Ishii, T. Abe, T. Satoh, M. Suzuki, M. Ueno, A. Yamazaki, N. Iwagami, S. Watanabe, M. Taguchi, T. Fukuhara, Y. Takahashi, M. Yamada, N. Hoshino, S. Ohtsuki, K. Uemizu, G. L. Hashimoto, M. Takagi, Y. Matsuda, K. Ogohara, N. Sato, Y. Kasaba, T. Kouyama, N. Hirata, R. Nakamura, Y. Yamamoto, N. Okada, T. Horinouchi, M. Yamamoto, Y. Hayashi, Overview of Venus orbiter, Akatsuki, Earth, Planets, and Space 63 (2011) 443–457. doi:10.5047/eps.2011.02.009.

[131] Y. Kawakatsu, S. Campagnola, C. Hirose, N. Ishii, An orbit plan toward AKATSUKI Venus reencounter and orbit injection, Tech. rep., Pasadena, CA: Jet Propulsion Laboratory, National Aeronautics and Space Administration (2012).

[132] M. Nakamura, Y. Kawakatsu, C. Hirose, T. Imamura, N. Ishii, T. Abe, A. Yamazaki, M. Yamada, K. Ogohara, K. Uemizu, T. Fukuhara, S. Ohtsuki, T. Satoh, M. Suzuki, M. Ueno, J. Nakatsuka, N. Iwagami, M. Taguchi, S. Watanabe, Y. Takahashi, G. L. Hashimoto, H. Yamamoto, Return to Venus of the Japanese Venus Climate Orbiter AKATSUKI, Acta Astronautica 93 (2014) 384–389. doi:10.1016/j.actaastro.2013.07.027.

[133] P. Drossart, G. Piccioni, A. Adriani, F. Angrilli, G. Arnold, K. H. Baines, G. Bellucci, J. Benkhoff, B. Bézard, J.-P. Bibring, A. Blanco, M. I. Blecka, R. W. Carlson, A. Coradini, A. Di Lellis, T. Encrenaz, S. Erard, S. Fonti, V. Formisano, T. Fouchet, R. Garcia, R. Haus, J. Helbert, N. I. Ignatiev, P. G. J. Irwin, Y. Langevin, S. Lebonnois, M. A. Lopez-Valverde, D. Luz, L. Marinangeli, V. Orofino, A. V. Rodin, M. C. Roos-Serote, B. Saggin, A. Sanchez-Lavega, D. M. Stam, F. W. Taylor, D. Titov, G. Visconti, M. Zambelli, R. Hueso, C. C. C. Tsang, C. F. Wilson, T. Z. Afanasenko, Scientific goals for the observation of Venus by VIRTIS on ESA/Venus express mission, Planet. Space Sci.55 (2007) 1653–1672. doi:10.1016/j.pss.2007.01.003.

[134] A. Mahieux, A. C. Vandaele, E. Neefs, S. Robert, V. Wilquet, R. Drummond, A. Federova, J. L. Bertaux, Densities and temperatures in the Venus mesosphere and lower thermosphere retrieved from SOIR on board Venus Express: Retrieval technique, Journal of Geophysical Research (Planets) 115 (E14) (2010) 12014. doi:10.1029/2010JE003589.

[135] B. Häusler, M. Pätzold, G. L. Tyler, R. A. Simpson, M. K. Bird, V. Dehant, J.-P. Barriot, W. Eidel, R. Mattei, S. Remus, J. Selle, S. Tellmann, T. Imamura, Radio science investigations by VeRa onboard the Venus Express spacecraft, Planet. Space Sci.54 (2006) 1315–1335. doi:10.1016/j.pss.2006.04.032.

[136] D. V. Titov, H. Svedhem, D. McCoy, J.-P. Lebreton, S. Barabash, J.-L. Bertaux, P. Drossart, V. Formisano, B. Haeusler, O. I. Korablev, W. Markiewicz, D. Neveance, M. Petzold, G. Piccioni, T. L. Zhang, F. W. Taylor, E. Lellouch, D. Koschny, O. Witasse, M. Warhaut, A. Acomazzo, J. Rodrigues-Cannabal, J. Fabrega, T. Schirmann, A. Clochet, M. Coradini, Venus Express: Scientific goals, instrumentation, and scenario of the mission, Cosmic Research 44 (2006) 334–348. doi:10.1134/S0010952506040071.

[137] ESA, ESA science missions continue in overtime (2013).
URL http://sci.esa.int/jump.cfm?oid=51944

[138] B. Häusler, M. Pätzold, G. Tyler, R. Simpson, D. Hinson, M. Bird, R. Treumann, V. Dehant, W. Eidel, S. Remus, et al., Atmospheric, Ionospheric, Surface, and Radio Wave Propagation Studies with the Venus Express Radio Science Experiment VeRa, ESA Scientific Publication ESA-SP.

[139] A. Migliorini, D. Grassi, L. Montabone, S. Lebonnois, P. Drossart, G. Piccioni, Investigation of air temperature on the nightside of Venus derived from VIRTIS-H on board Venus-Express, Icarus 217 (2012) 640–647. doi:10.1016/j.icarus.2011.07.013.

[140] R. Haus, D. Kappel, G. Arnold, Self-consistent retrieval of temperature profiles and cloud structure in the northern hemisphere of Venus using VIRTIS/VEX and PMV/VENERA-15 radiation measurements, Planet. Space Sci.89 (2013) 77–101. doi:10.1016/j.pss.2013.09.020.

[141] R. Haus, D. Kappel, G. Arnold, Atmospheric thermal structure and cloud features in the southern hemisphere of Venus as retrieved from VIRTIS/VEX radiation measurements, Icarus232 (2014) 232–248. doi:10.1016/j.icarus.2014.01.020.

[142] A. Mahieux, A. C. Vandaele, S. Robert, V. Wilquet, R. Drummond, F. Montmessin, J. L. Bertaux, Densities and temperatures in the Venus mesosphere and lower thermosphere retrieved from SOIR on board Venus Express: Carbon dioxide measurements at the Venus terminator, Journal of Geophysical Research (Planets) 117 (2012) 7001. doi:10.1029/2012JE004058.

[143] J.-L. Bertaux, D. Nevejans, O. Korablev, E. Villard, E. Quémerais, E. Neefs, F. Montmessin, F. Leblanc, J. P. Dubois, E. Dimarellis, A. Hauchecorne, F. Lefèvre, P. Rannou, J. Y. Chaufray, M. Cabane, G. Cernogora, G. Souchon, F. Semelin, A. Reberac, E. Van Ransbeek, S. Berkenbosch, R. Clairquin, C. Muller, F. Forget, F. Hourdin, O. Talagrand, A. Rodin, A. Fedorova, A. Stepanov, I. Vinogradov, A. Kiselev, Y. Kalinnikov, G. Durry, B. Sandel, A. Stern, J. C. Gérard, SPICAV on Venus Express: Three spectrometers to study the global structure and composition of the Venus atmosphere, Planet. Space Sci.55 (2007) 1673–1700. doi:10.1016/j.pss.2007.01.016.

[144] M. Rengel, P. Hartogh, C. Jarchow, Mesospheric vertical thermal structure and winds on Venus from HHSMT CO spectral-line observations, Planetary & Space Science 56 (2008) 1368–1384. arXiv:0809.2743, doi:10.1016/j.pss.2008.07.004.

[145] M. Rengel, P. Hartogh, C. Jarchow, HHSMT observations of the Venusian mesospheric temperature, winds, and CO abundance around the MESSENGER flyby, Planetary & Space Science 56 (2008) 1688–1695. arXiv:0810.2899, doi:10.1016/j.pss.2008.07.014.

[146] R. T. Clancy, B. J. Sandor, G. Moriarty-Schieven, Thermal structure and CO distribution for the Venus mesosphere/lower thermosphere: 2001-2009 inferior conjunction sub-millimeter CO absorption line observations, Icarus217 (2012) 779–793. doi:10.1016/j.icarus.2011.05.032.

[147] D. Crisp, V. S. Meadows, B. Bézard, C. de Bergh, J.-P. Maillard, F. P. Mills, Ground-based near-infrared observations of the Venus nightside: 1.27-μm $O_2(a\Delta_g)$ airglow from the upper atmosphere, Journal of Geophysical Research 101 (1996) 4577–4594. doi:10.1029/95JE03136.

[148] J. Bailey, V. S. Meadows, S. Chamberlain, D. Crisp, The temperature of the Venus mesosphere from O $_2$ (aΔg1) airglow observations, Icarus 197 (2008) 247–259. doi:10.1016/j.icarus.2008.04.007.

[149] R. K. Kakar, J. W. Waters, W. J. Wilson, Venus - Microwave detection of carbon monoxide, Science 191 (1976) 379. doi:10.1126/science.191.4225.379.

[150] R. T. Clancy, B. J. Sandor, G. H. Moriarty-Schieven, Observational definition of the Venus mesopause: vertical structure, diurnal variation, and temporal instability, Icarus161 (2003) 1–16. doi:10.1016/S0019-1035(02)00022-2.

[151] P. Connes, J. F. Noxon, W. A. Traub, N. P. Carleton, O2/1 Delta/ emission in the day and night airglow of Venus, Astrophysical Journal, Letters 233 (1979) L29–L32. doi:10.1086/183070.

[152] D. Allen, D. Crisp, V. Meadows, Variable oxygen airglow on Venus as a probe of atmospheric dynamics, Nature 359 (1992) 516–519. doi:10.1038/359516a0.

[153] S. Ohtsuki, N. Iwagami, H. Sagawa, Y. Kasaba, M. Ueno, T. Imamura, Ground-based observation of the Venus 1.27-μm O $_2$ airglow, Advances in Space Research 36 (2005) 2038–2042. doi:10.1016/j.asr.2005.05.078.

[154] S. Ohtsuki, N. Iwagami, H. Sagawa, M. Ueno, Y. Kasaba, T. Imamura, K. Yanagisawa, E. Nishihara, Distributions of the Venus 1.27-mum O airglow and rotational temperature, Planetary & Space Science 56 (2008) 1391–1398. doi:10.1016/j.pss.2008.05.013.

[155] A. I. F. Stewart, J.-C. Gerard, D. W. Rusch, S. W. Bougher, Morphology of the Venus ultraviolet night airglow, Journal of Geophysical Research 85 (1980) 7861–7870. doi:10.1029/JA085iA13p07861.

[156] A. J. Kliore, G. M. Keating, V. I. Moroz, Venus international reference atmosphere (1985), Planetary & Space Science 40 (1992) 573–573. doi:10.1016/0032-0633(92)90255-M.

[157] V. I. Moroz, L. V. Zasova, VIRA-2: a review of inputs for updating the Venus International Reference Atmosphere, Advances in Space Research 19 (1997) 1191–1201. doi:10.1016/S0273-1177(97)00270-6.

[158] A. Seiff, D. B. Kirk, R. E. Young, R. C. Blanchard, J. T. Findlay, G. M. Kelly, S. C. Sommer, Measurements of thermal structure and thermal contrasts in the atmosphere of Venus and related dynamical observations - Results from the four Pioneer Venus probes, Journal of Geophysical Research 85 (1980) 7903–7933. doi:10.1029/JA085iA13p07903.

[159] M. Yamamoto, M. Takahashi, Superrotation and equatorial waves in a T21 Venus-like AGCM, Geophysics Research Letters 30 (2003) 1449. doi:10.1029/2003GL016924.

[160] H. F. Parish, G. Schubert, C. Covey, R. L. Walterscheid, A. Grossman, S. Lebonnois, Decadal variations in a Venus general circulation model, Icarus212 (2011) 42–65. doi:10.1016/j.icarus.2010.11.015.

[161] N. Hoshino, H. Fujiwara, M. Takagi, Y. Takahashi, Y. Kasaba, Characteristics of planetary-scale waves simulated by a new venusian mesosphere and thermosphere general circulation model, Icarus 217 (2012) 818–830. doi:10.1016/j.icarus.2011.06.039.

[162] J. L. Hollingsworth, R. E. Young, G. Schubert, C. Covey, A. S. Grossman, A simple-physics global circulation model for Venus: Sensitivity assessments of atmospheric superrotation, Geophysics Research Letters 34 (2007) 5202. doi:10.1029/2006GL028567.

[163] S. Lebonnois, F. Hourdin, V. Eymet, A. Crespin, R. Fournier, F. Forget, Superrotation of Venus' atmosphere analyzed with a full general circulation model, Journal of Geophysical Research (Planets) 115 (2010) 6006. doi:10.1029/2009JE003458.

[164] A. S. Brecht, S. W. Bougher, J.-C. Gérard, C. D. Parkinson, S. Rafkin, B. Foster, Understanding the variability of nightside temperatures, NO UV and O_2 IR nightglow emissions in the Venus upper atmosphere, Journal of Geophysical Research (Planets) 116 (2011) 8004. doi:10.1029/2010JE003770.

[165] S. W. Bougher, R. G. E. Roble, R. E. Dickinson, E. C. Ridley, Venus mesosphere and thermosphere. III - Three-dimensional general circulation with coupled dynamics and composition, Icarus 73 (1988) 545–573. doi:10.1016/0019-1035(88)90064-4.

[166] S. Lebonnois, *personal correspondance*, April (2014).

[167] A. K. Pierce, The McMath solar telescope of Kitt Peak National Observatory, Applied Optics 3 (1964) 1337. doi:10.1364/AO.3.001337.

[168] T. Kostiuk, Physics and chemistry of upper atmospheres of planets from infrared observations, Infrared Physics and Technology 35 (1994) 243–266. doi:10.1016/1350-4495(94)90084-1.

[169] A. J. Kantor, A. E. Cole, Mid-latitude atmospheres, winter and summer, Geofisica Pura e Applicata 53 (1962) 171–188. doi:10.1007/BF02007120.

[170] S. Tellmann, B. Häusler, D. P. Hinson, G. L. Tyler, T. P. Andert, M. K. Bird, T. Imamura, M. Pätzold, S. Remus, Small-scale temperature fluctuations seen by the VeRa Radio Science Experiment on Venus Express, Icarus221 (2012) 471–480. doi:10.1016/j.icarus.2012.08.023.

[171] S. Tellmann, *personal correspondance*, August (2012).

[172] D. Grassi, P. Drossart, G. Piccioni, N. I. Ignatiev, L. V. Zasova, A. Adriani, M. L. Moriconi, P. G. J. Irwin, A. Negrão, A. Migliorini, Retrieval of air temperature profiles in the Venusian mesosphere from VIRTIS-M data: Description and validation of algorithms, Journal of Geophysical Research (Planets) 113 (2008) 0. doi:10.1029/2008JE003075.

[173] A. Migliorini, *personal correspondance*, May (2014).

[174] A. Mahieux, *personal correspondance*, February (2014).

[175] M. Rengel, *personal correspondance*, April (2014).

[176] E. Bell, Photo Gallery Mars (2010).
URL http://nssdc.gsfc.nasa.gov/photo_gallery/photogallery-mars.html

[177] D. Williams, Mars Fact Sheet (2013).
URL http://nssdc.gsfc.nasa.gov/planetary/factsheet/marsfact.html

[178] M. T. Lemmon, M. J. Wolff, M. D. Smith, R. T. Clancy, D. Banfield, G. A. Landis, A. Ghosh, P. H. Smith, N. Spanovich, B. Whitney, P. Whelley, R. Greeley, S. Thompson, J. F. Bell, S. W. Squyres, Atmospheric Imaging Results from the Mars Exploration Rovers: Spirit and Opportunity, Science 306 (2004) 1753–1756. doi:10.1126/science.1104474.

[179] R. W. Zurek, Mars, The University of Arizona Press, 1992, Ch. Comparative aspects of the climate of Mars - an introduction to the current atmosphere, pp. 799–817.

[180] E. Millour, F. Forget, A. Spiga, T. Navarro, J.-B. Madeleine, A. Pottier, L. Montabone, L. Kerber, A. Colaitis, F. Lefèvre, F. Montmessin, J.-Y. Chaufray, M. A. López-Valverde, F. González-Galindo, S. R. Lewis, P. L. Read, M.-C. Desjean, J.-P. Huot, MCD/GCM Development Team, A new Mars Climate Database v5.1, in: F. Forget, M. Millour (Eds.), Mars Atmosphere: Modelling and Observation, 5th International Workshop, 2014, p. 1301.

[181] P. J. Schinder, F. M. Flasar, E. A. Marouf, R. G. French, C. A. McGhee, A. J. Kliore, N. J. Rappaport, E. Barbinis, D. Fleischman, A. Anabtawi, The structure of Titan's atmosphere from Cassini radio occultations: Occultations from the Prime and Equinox missions, Icarus221 (2012) 1020–1031. doi:10.1016/j.icarus.2012.10.021.

[182] C. A. Griffith, J. L. Mitchell, P. Lavvas, G. Tobie, Comparative Climatology of Terrestrial Planets, The University of Arizona Press, 2013, Ch. Titan's Evolving Climate, pp. 91–119. doi:10.2458/azu_uapress_9780816530595-ch004.

[183] S. Vinatier, B. Bézard, C. A. Nixon, A. Mamoutkine, R. C. Carlson, D. E. Jennings, E. A. Guandique, N. A. Teanby, G. L. Bjoraker, F. Michael Flasar, V. G. Kunde, Analysis of Cassini/CIRS limb spectra of Titan acquired during the nominal mission. I. Hydrocarbons, nitriles and CO $_2$ vertical mixing ratio profiles, Icarus205 (2010) 559–570. doi:10.1016/j.icarus.2009.08.013.

[184] R. Rüfenacht, N. Kämpfer, A. Murk, First middle-atmospheric zonal wind profile measurements with a new ground-based microwave Doppler-spectro-radiometer, Atmospheric Measurement Techniques 5 (2012) 2647–2659. doi:10.5194/amt-5-2647-2012.

[185] J. P. L. NASA, HORIZONS Web-Interface (2013).
URL http://ssd.jpl.nasa.gov/horizons.cgi

Acknowledgment

This work is the result of not only one person, but the accumulation of the ideas and the support of many people from all over the world. Without the contribution of the following persons, the work could not have been a success.

The first person to mention is Prof. Dr. Lucas Labadie. Thank you for supervising my thesis and supporting me during the last three years. Many thanks also to Prof. Dr. Susanne Crewell for co-revision of my thesis.

The THIS-team - Dr. Guido Sonnabend, Dr. Manuela Sornig, Dr. Dušan Stupar, Maren Herrmann, Pia Krause, Carolin Wischnewski and Moritz Wiegand! Thanks for four years of fun - at the telescopes in Arizona and Hawaii, during conferences in Rome, on volcanic-forced short trips to Madrid, on bike tours through Washington DC, on Public Outreach events in Cologne, at physicists-family-BBQ-occasions in Bonn and many, many other joyful activities. It was a great time and I wish the whole team success and happiness for the future!

A special thanks to PD. Dr. Martin Pätzold from the Rheinische Institut für Umweltforschung an der Universtität zu Köln, for hosting me during the first one and a half years as a PhD candidate at his institute. It was a pleasure to be a part of the RIU team!

A deep and grateful thanks to Dr. Tilak Hewagama, who has hosted me for five weeks in fall 2012 at the NASA Goddard Space Flight Center and who supported and helped me in developing the IFR. Without your incredible input and knowdledge on IDL and CODAT I would still be changing the temperatures by hand. Honor to whom honor is due! I also want to thank the rest of the GSFC IRHet group - Dr. Theodor Kostiuk, Dr. Timothy Livengood and Dr. Kelly Fast - for welcoming me in Greenbelt several times and for giving me the opportunity to use their instrument HIPWAC for observations at the IRTF. It was a pleasure to work with you!

I want to thank the Venus Express Radio Science team for their great support and

contribution. Without the close collaboration the coordinated campaign could not have been realized. Especially the input and help from Dr. Silvia Tellmann was important. Also I want to express my gratefulness for providing me with the greatest good a scientist has - the data. The comparison of my Venus profiles to the VeRa data was a milestone for the outcome of my thesis.

Observations would not have been possible without the great support of staff at site. I would like to thank the crew of the IRTF and Eric Galayda and Claude Plymate from the McMath-Pierce Solar Telescope.

Many thanks also to the other observers and modelers for their support. Namely, Dr. Alessandra Migliorini from the Istituto di Astrofisica e Planetologia Spaziali in Rome, Italy, who has provided the VEX VIRTIS data, Dr. Miriam Rengel, for sending me the ground based profiles from the working group of the MPI für Sonnensystemforschung in Lindau, Germany, Dr. Sébastien Lebonnois from the Laboratoire de Météorologie Dynamique in Paris, France, for calculating some model profiles for our observations, even though, they have not been used, Dr. Arnauld Mahieux from the Belgium Institute for Space Aeronomy, Brussels, Belgium, for the support on the SOIR data.

Special thanks go to Mareile Strücker for proof reading my thesis. I know that it must have been a tough time for an English teacher!

Besonderer Dank gebührt all meinen Freunden, die mich in all den Jahren begleitet haben und die unzertrennlich in allen Lebenslagen eng zusammen stehen. Mit euch ist das Leben lebenswert und es wird niemals langweilig! Insbesondere erwähnt sei an dieser Stelle Dr. Mario Zacharias, den ich an meinen ersten Tag an der Uni, dem 06. Oktober 2003, kennengelernt habe und der mich auf meinem Weg - meistens mit einer Flasche Bier in unseren Händen - stets begleitet hat.

Bedanken möchte ich mich aber auch bei meiner Familie - meinen Eltern Angelika und Udo und meinem Bruder Fabian. Ihr habt immer an mich geglaubt und mich in allen Entscheidungen unterstützt. Ohne Eure Zuversicht hätte ich es niemals so weit gebracht! Ich bin froh, dass es euch gibt!

Zum Schluss möchte ich mich selbstverständlich noch bei meiner Verlobten Carola bedanken. Danke für all die Zeit die ich mit dir verbringen durfte, danke für deine unermessliche Geduld, danke für dein Verständnis, einfach danke, dass du für mich da bist. Ich freue mich auf unsere gemeinsame Zukunft. Ich liebe dich!

This work was funded by the Deutsche Forschungsgemeinschaft (DFG), through Grant SO1044/1-1 and SO879/3-1.

Erklärung

Ich versichere, dass ich die vorgelegte Dissertation selbständig und ohne unzulässige Hilfe angefertigt, die benutzten Quellen und Hilfsmittel vollständig angegeben und die Stellen der Arbeit - einschließlich Tabellen, Karten und Abbildungen -, die anderen Werken im Wortlaut oder dem Sinn nach entnommen sind, in jedem Einzelfall als Entlehnung kenntlich gemacht habe, dass diese Dissertation noch keiner anderen Fakultät zur Prüfung vorgelegen hat, dass sie abgesehen von unten angegebenen Teilpublikationen noch nicht veröffentlicht worden ist und dass ich eine solche Veröffentlichung vor Abschluss des Promotionsverfahrens nicht vornehmen werde.

Die Bestimmungen der geltenden Promotionsordnung sind mir bekannt. Die von mir vorgelegte Dissertation ist von Herrn Prof. Dr. Lucas Labadie betreut worden.

(Datum) (Unterschrift)

Teile dieser Arbeit sind bzw. werden in folgenden Publikationen veröffentlicht:

T. Stangier, G. Sonnabend, M. Sornig, Compact Setup of a Tunable Heterodyne Spectrometer for Infrared Observations of Atmospheric Trace-Gases, Remote Sensing 5 (2013) 3397–3414. doi:10.3390/rs5073397.

T. Stangier, T. Hewagama, M. Sornig, G. Sonnabend, T. Kostiuk, M. Herrmann, T. A. Livengood, Thermal Structure of Venus' Nightside Mesosphere as Observed by Infrared Heterodyne Spectroscopy at 10 µm, *accepted by Planetary and Space Science - SI: Exploration of Venus* (2015)

G. Sonnabend, D. Stupar, M. Sornig, T. Stangier, T. Kostiuk, T. A. Livengood, A search for methane in the atmosphere of Mars using ground-based mid infrared heterodyne spectroscopy, Journal of Molecular Spectroscopy 291 (2013) 98–101. doi:10.1016/j.jms.2013.05.009.